Energy Consumption Prediction for Electric City Buses

ENERGY CONSUMPTION PREDICTION for ELECTRIC CITY BUSES

Using Physics-Based Principles

Camiel Beckers

Energy Consumption Prediction for Electric City Buses

Using Physics-Based Principles

Camiel Beckers

disc

TU/e EINDHOVEN
UNIVERSITY OF
TECHNOLOGY

EVERLASTING

Energy Consumption Prediction
for Electric City Buses

Using Physics-Based Principles

Dit proefschrift is goedgekeurd door de promotoren en de samenstelling van de promotiecommissie is als volgt:

voorzitter:	prof.dr.ir. A.A. van Steenhoven	
1^e promotor:	prof.dr. H. Nijmeijer	
2^e promotor:	dr.ir. I.J.M. Besselink	
leden:	dr.ir. G.M. Bonnema, PDEng	(Universiteit Twente)
	prof.dr.ir. O. Hegazy	(Vrije Universiteit Brussel)
	dr.ir. T. Hofman	
	dr. K. Tammi	(Aalto University)
adviseur:	ir. P. Blom	(VDL ETS)

Summary

Energy Consumption Prediction for Electric City Buses Using Physics-Based Principles

DRIVEN by climate change, the present-day transportation sector is transitioning to electrically powered mobility. In this transition, the battery electric bus is a key solution that is already employed on a large scale in many cities. Compared to conventional diesel-powered buses, these new energy vehicles offer the possibility of a lower total cost of ownership due to lower fuel expenses and maintenance costs. Even though electric buses are more energy-efficient than conventional vehicles, the available energy is generally less due to the limited energy density of present-day battery cells. This results in a limited driving range that varies with vehicle, road, and weather conditions. Because of the uncertainty regarding the future energy consumption, electric buses are often scheduled more conservatively than conventional buses. In this dissertation, the energy consumption of a battery electric bus is modeled to more accurately predict the required powertrain power in advance.

An electric vehicle energy consumption prediction model is developed using physics-based principles. The model consists of a velocity prediction algorithm and an energy consumption model. The velocity prediction algorithm uses the maximum legislated speed, the road corner radius, traffic light locations along a route, and the previously measured average acceleration. The energy consumption model is based on the longitudinal dynamics of the vehicle and includes expressions for rolling resistance, aerodynamic drag, and road gradient. The combined two parts of the model are a function of route information, weather conditions, and road slope, each of which are obtained from databases via the internet. The model is applied to an electric delivery van and has an error ranging from 4.3% to 12% when compared to measurements. Given the correct model parameters, the physics-based model can be applied to any electric road vehicle.

Next, physics-based extensions of the baseline energy consumption model are developed. A nonlinear steady-state cornering model shows that both lateral and longitudinal slip of the tires cause additional energy losses during cornering of the

vehicle. This model is validated by comparing the results to steady-state cornering tests conducted with a 12 meter battery electric bus. Even though this effect is rarely considered in the literature, these additional tire losses can account for up to 5.8% of the powertrain energy consumption on city bus routes with many turns.

A second model extension involves the vertical dynamics of a bus. Simulation results from a validated quarter car model indicate that the energy dissipated in the dampers is equal to the work performed by the resistance force in the longitudinal direction. The quarter car model is used to relate road roughness to damper losses. Vehicle coast-down measurements reveal that the damper losses explain most of the increase in rolling resistance when changing from a smooth to a rough road. This is a solid motivation for including a road-type dependent rolling resistance coefficient in a microscopic energy consumption model.

A challenge in most physics-based models is the selection of the correct model parameters. In the longitudinal dynamics model the road-type dependent rolling resistance and an accurate road gradient are challenging to determine. A method is presented to estimate these parameters from the powertrain data of previous vehicles traversing the same route, thereby creating a position-dependent resistance profile. Using this profile to predict the future powertrain power reduces the error by 1.7 percent point compared to a conventional method and does not require the availability of a digital elevation model.

The physics-based energy consumption model requires knowledge of the future vehicle speed. Two methods are explored to increase the accuracy of the future forward velocity prediction. Firstly, during a hardware-in-the-loop test, an onboard velocity prediction algorithm gives an improved up-to-date energy consumption prediction by including the current vehicle speed and position in the prediction. Secondly, based on measurement data of a bus fleet, it is shown that the longitudinal vehicle acceleration, as a function of vehicle speed, is a good characterization of the driver. This concept is applied by defining driver-specific acceleration and deceleration curves. When applied in an energy consumption prediction, these curves clarify the majority of the powertrain energy difference measured between two drivers.

The methods presented in this thesis serve as the next step toward more accurate energy and power prediction for electric buses and electric vehicles in general. These predictions can be used to design onboard energy management controllers, perform preliminary vehicle design studies, and provide driver dashboard information.

Keywords: Battery electric bus, Energy consumption prediction, Physics-based modeling, Vehicle dynamics, Electric powertrain efficiency, Rolling resistance

Publiekssamenvatting

OM klimaatverandering tegen te gaan, is de vervoersector aan het overschakelen op elektrisch aangedreven mobiliteit. In deze overgang is de batterijelektrische bus een belangrijke oplossing die in veel steden al op grote schaal wordt toegepast. Vergeleken met conventionele diesel bussen is de actieradius van elektrische bussen nog beperkt en varieert deze naar gelang van voertuig-, weg- en weersomstandigheden. Om deze variaties in het energieverbruik beter te kunnen voorspellen, en zo de bruikbaarheid van elektrische bussen te verhogen, worden in dit proefschrift modellen gepresenteerd en experimenteel gevalideerd die het energieverbruik van een elektrische bus in detail simuleren.

Allereerst wordt een model beschreven voor het voorspellen van de belangrijkste fysische mechanismen die tot energieverbruik leiden in elektrische voertuigen. Het model beschrijft rolweerstand, luchtweerstand, hellingsweerstand en aandrijflijnverliezen en kan gebruikt worden om het energieverbruik van een elektrisch voertuig voor een willekeurige route te bepalen.

Vervolgens is gezocht naar nieuwe fysische mechanismen welke verantwoordelijk zijn voor energieverbruik. Ten eerste is vastgesteld dat tijdens het maken van bochten de banden van het voertuig extra slip ervaren, wat leidt tot extra energieverliezen. Voor stadsbussen kan dit tot wel 5% van het energieverbruik van de aandrijving zijn. Ten tweede is vastgesteld dat de invering van de wielophanging tijdens het rijden over oneffen wegdekken leidt tot energieverliezen in de schokbrekers van het voertuig. Voor stadsbussen is dit effect verantwoordelijk voor wel 13% van het gemiddelde energieverbruik. Ten derde is er een methode ontwikkeld waarmee rolweerstand en wegdekhelling, welke beide een duidelijk effect hebben op het energieverbruik, nauwkeurig kunnen worden bepaald uit meetdata van meerdere elektrische stadsbussen. Tenslotte worden twee methoden gepresenteerd waarmee de voertuigsnelheid voorspeld kan worden met inachtneming van 1) de huidige positie en snelheid en 2) het bestuurdersgedrag.

Gecombineerd vormen deze methoden een volgende stap naar een meer accurate energie- en vermogensvoorspelling voor elektrische bussen en elektrische voertuigen in het algemeen. Deze voorspellingen kunnen worden gebruikt om energiebeheer regelaars te ontwerpen, ontwerpstudies uit te voeren en uiteindelijk de kosten van het openbaar vervoer te verlagen.

Contents

Nomenclature

Acronyms

ABS	Anti-lock Braking System
AC	Alternating Current
API	Application Programming Interface
BEB	Battery Electric Bus
BEV	Battery Electric Vehicle
CAN	Controller Area Network
CDF	Cumulative probability Density Function
CFD	Computational Fluid Dynamics
CoP	Coefficient of Performance
CO_2	Carbon dioxide
CoG	Center of Gravity
DC	Direct Current
DEM	Digital Elevation Model
ECAS	Electronically Controlled Air Suspension
ECP	Energy Consumption Prediction
EU	European Union
EV	Electric Vehicle
FCEB	Fuel-Cell Electric Bus
FD	Final Drive
FVPP	Forward Velocity Profile Prediction
GPS	Global Positioning System
GVW	Gross Vehicle Weight
HiL	Hardware-in-the-Loop
HVAC	Heating, Ventilation and Air Conditioning
HV	High Voltage
ICE	Internal Combustion Engine
IMU	Inertial Measurement Unit
IRI	International Roughness Index
LFP	Lithium-Iron-Phosphate

LTO	Lithium-Titanate-Oxide
LV	Low Voltage
LiPo	Lithium Polymer
MPD	Mean Profile Depth
MPV	Multi Purpose Vehicle
NCA	Nickel-Cobalt-Aluminium
NMC	Nickel-Manganese-Cobalt
NO_x	Nitrogen Oxides
OC	Opportunity Charging
OEM	Original Equipment Manufacturer
PE	Prediction Error
PHEB	Plug-in Hybrid Electric Bus
PSD	Power Spectral Density
RMS	Root Mean Square
SRTM	Shuttle Radar Topography Mission
SoC	State of Charge
TCO	Total Cost of Ownerschip
WAPE	Weighted Average Prediction Error
WGS84	World Geodetic System 1984
ZEB	Zero-Emission Bus

1
Introduction

1.1 Background

SINCE the end of the industrial revolution in the mid-19th century, the concentration of CO_2 and other greenhouse gasses have been rising at unprecedented rates, leading to a global rise in temperature [1], see Figure 1.1. The transport sector is partly responsible for this climate change, producing one quarter of the global CO_2 emissions [2] and 30% of NO_x emissions in the European Union (EU) [3]. Even though the city bus sector is responsible for only a small part of the global pollution, it contributes 20% to the local emission in city centers [4]. Due to the frequent acceleration and low average speed of these vehicles, the diesel engines in city buses emit relatively large amounts of particle matter and NO_x [5, 6]. Electric buses minimize local pollution and offer reduced global emissions if the CO_2 intensity of the charging electricity is sufficiently low [7].
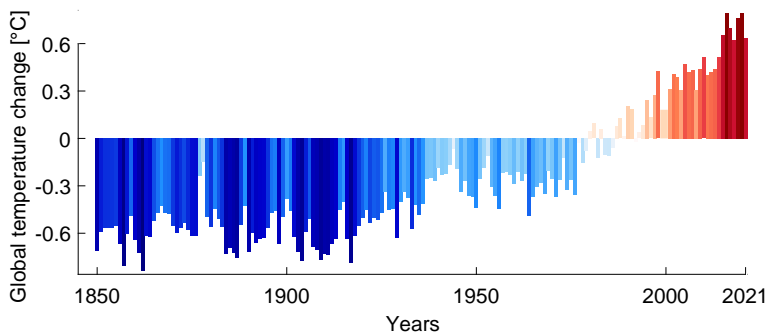
Figure 1.1. Global temperature change relative to the average of the period 1971-2000. Visualization inspired by [8] and based on data from [9].

Governments create incentives to accelerate the transition towards zero-emission vehicles through subsidies and legislation. The most significant subsidy benefiting Zero-Emission Buses (ZEBs) is China's new-energy vehicle subsidy scheme, which has been running since 2009 and includes a separate category for Battery Electric Buses (BEBs) [10, 11]. While the United States of America currently has no explicit legislation to promote ZEBs, California aims to achieve 100% ZEB sales by 2029 [12]. Another example is the EU's Clean Vehicles Directive, which sets national targets for each of the EU member states, defined as a minimum percentage of newly procured buses to be zero-emission [13]. This percentage varies between the member states from 24% to 45% in 2025 and from 33% to 65% in 2030. In the meantime, individual EU countries have specified targets that go even further, such as the Dutch government's goal to achieve 100% public transport ZEB sales by 2025 and 100% public transport ZEB stock by 2030 [14].

Due to these kinds of governmental incentives, the total number of electric buses in use globally, i.e., the global vehicle stock, has been rising since 2010. This is visualized in Figure 1.2. The figure also indicates that battery electric buses are the most commonly used of the available electric powertrain options. Deployment of other technologies, such as hydrogen Fuel-Cell Electric Buses (FCEBs), is increasing at a slower rate. In most analyzed cases, the Total Cost of Ownership (TCO) of FCEBs is higher compared to BEBs, mainly due to the cost related to hydrogen production and storage [15]. The TCO represents the total sum of money required to attain and operate a vehicle over its entire lifetime and is an important factor that public transport operators base their technology choice on. However, it should be noted that BEBs are still unable to compete with diesel buses on cost without governmental incentives due to the high cost of the large battery packs [16].

Trolleybuses, which run on electric power directly transferred to the vehicle via overhead cables, are another noteworthy zero-emission alternative. In theory, these vehicles are approximately 17% more energy-efficient than BEBs, because the energy conversion step associated with the battery is omitted [17]. However, the number of trolleybus networks is steadily decreasing [18]. A reason for this could be the large initial costs and maintenance of infrastructure required operate a trolleybus network. Although no recent yearly data is readily available, there were an estimated 40.000 trolleybuses operational at the beginning of this century [19], some of which are actually diesel-hybrid [20].

For a complete comparative analysis of the different electric bus powertrains in terms of energy consumption, reference is made to [18]. This thesis focuses on BEBs specifically because the BEB is currently the leading technology in terms of market share. Additionally, the fact that multiple large-scale BEB fleets are operational results in industry interest and the availability of large quantities of measurement data. Furthermore, both FCEBs and trolleybuses rely on an electric powertrain similar to a BEB, making the powertrain analyses of these vehicles interchangeable to a certain extent.
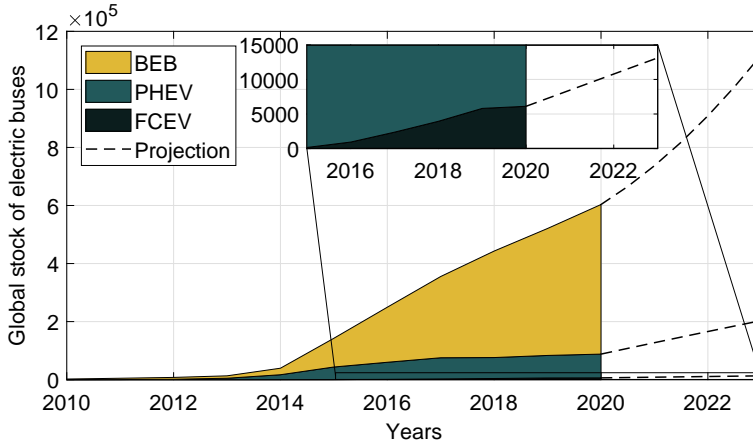
Figure 1.2. The global stock of electric buses, subdivided into Battery Electric Buses (BEB), Plug-in Hybrid Electric Buses (PHEB), and Fuel-Cell Electric Buses (FCEB) [2].

1.2 Battery electric bus developments

Battery electric buses are vehicles that draw their traction and auxiliary energy primarily or exclusively from an onboard electric accumulator or battery. An overview of specifications of recent BEBs on the market is supplied in Appendix A.

1.2.1 Historic overview

The use of battery electric vehicles in (semi-)public transport is not new. As early as 1895, tests were undertaken with electric taxi-cabs running in London, Paris, and various American cities [21, pp. 64-93]. In Amsterdam 12 electric taxi-cabs were introduced in 1909 to replace horse-driven carriages [22, p. 14]. One of the major advantages with respect to Internal Combustion Engine (ICE) vehicles of that time was that electric vehicles were significantly easier to drive because there was no clutch pedal, no changing of gears, and no hand crank. Therefore, they required less skill to drive, lowering the average driver salaries and thereby reducing the TCO. Secondly, battery-powered vehicles were considered less complicated and thus more reliable than their combustion engine counterparts.

Around 1900–1905 the first electric buses emerged in the larger European and American cities [21, pp. 181-182][23, pp. 66-67]. Whereas Berlin, Paris, and New York had smaller streetcar companies that each put several vehicles in operation, London, in particular, was notable because of the size of its fleet and the large number of different operating companies. One of these was the London Electrobus Company, which at its peak operated 20 buses. The Electrobus, displayed in Fig-

Figure 1.3. The London Electrobus. Photo taken on the Embankment, in London, on 18 April 1906. Reproduced with permission from [25].

ure 1.3, featured a driving range of 60 km and a 1.75 tonne battery that could be swapped in 3 minutes [24]. The vehicles were praised for their low noise and lack of fumes. However, the company went bankrupt in 1910 due to financial mismanagement and the last Electrobus was decommissioned in 1917. Other companies failed to compete with the rapidly innovating gasoline engine and low oil prices.

In the mid-1920s, city buses mostly ran on gasoline, sometimes as a series-hybrid with an electric motor. Also, electric trolleybuses kept operating in several cities [17]. Since then, only a few initiatives have existed that operated buses independently without the use of fossil fuels.

One example is the Gyrobus designed in 1950, which, although technically not a battery electric bus, is noteworthy because of its use of opportunity charging [26]. The vehicle featured a 1500 kg flywheel spinning at 3000 rpm as the primary energy accumulator. This flywheel was spun-up using power from a 52 kW pantograph

connection during standstill and stored sufficient kinetic energy to drive the vehicle 5 to 6 km between stops at speeds up to 55 km/h and carrying up to 70 passengers.

Interest in the BEB was further renewed during the oil crisis at the beginning of the 1970s. As a result, several vehicles were put into operation on a small scale in Germany [27], the United Kingdom [28], and, later, in the USA [29]. However, none of these were ever produced on a large scale [30], and the city road transport in Europe continued to be governed predominantly by diesel vehicles [17].

Since 2010, modern BEBs have been gaining market share in the city transport sector. So far, this transition has mostly taken place in China, where more than half a million BEBs are in operation in 2020 [11, 12]. In recent years, European and American cities are also starting to employ larger fleets of BEBs [31].

1.2.2 Energy consumption of battery electric buses

Environmental impact comparisons between BEBs and other modes of transport are often based on a well-to-wheel analysis [15, 32]. In this type of analysis, the entire energy consumption chain is considered from the energy source to the vehicle's wheels, as indicated in Figure 1.4. These results are also required for conducting a life-cycle assessment that quantifies the cost and environmental impact over the entire vehicle lifetime, including manufacturing and end-of-use [7]. Another essential analysis to the operation of electric vehicles is the assessment of the vehicle's driving range given a particular battery State of Charge (SoC) [33, 34]. This type of analysis concerns the modeling of the battery and all systems drawing power from it during driving. These systems include auxiliary components, such as the climate and pneumatic systems, and the powertrain. The powertrain is of special interest because it consumes approximately 70% of the energy supplied by the battery [35]. Additionally, the power request of the powertrain is highly variable depending on environmental factors, vehicle parameters, and driver behavior [36]. Therefore, this thesis focuses primarily on models that support the battery-to-wheel analysis of a BEB by modeling the energy consumption of the powertrain. These models do not represent the complete energy consumption of a BEB yet are essential for the other overarching types of analyses.

Figure 1.4 indicates the main components of the powertrain of a BEB. The vehicle features an electrochemical battery that can be charged via an off-board charger that draws power from the grid. While driving, the battery powers the traction inverter that converts the Direct Current (DC) electrical power to three-phase Alternating Current (AC), which is then converted to mechanical power by the motor. A final drive reduces the rotational speed of the output shaft and transfers power to the driven wheels. If regenerative braking is applied, power flows in the reverse direction: from the wheels to the battery. Additionally, the energy contained in the battery is used to power the different auxiliary components of the vehicle. These include the climate system, the pneumatic system, hydraulics, powersteering, and the low-voltage electronics such as lights and public transport
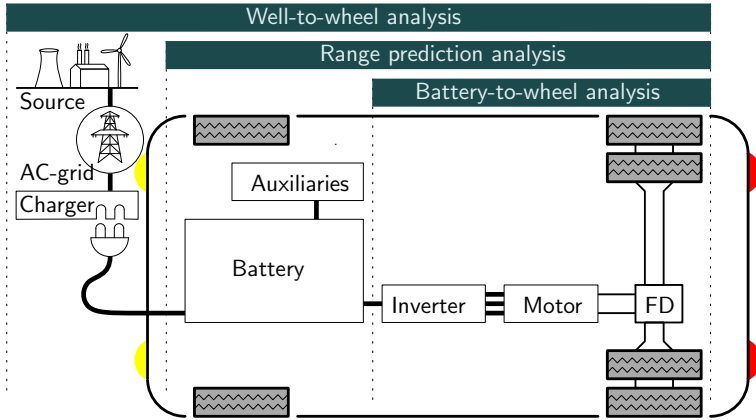
Figure 1.4. Schematic overview of the main powertrain components in a battery electric bus, including the Energy Source, AC-grid, Charger, Battery, Auxiliary Components, Inverter, Electric Motor, and Final Drive (FD).

electronics. While Figure 1.4 displays a driveline topology with one central motor and a final drive containing a differential, other topologies exist. An example is a 'drive-axle' where hub motors drive the wheels. Nevertheless, the basic powertrain components, i.e., inverter, motor, and final drive, remain present.

The electrification of the city bus sector is happening faster than the consumer passenger car market. City bus transport has several advantages with regard to electrification: the vehicles drive at relatively low average velocities, experience many stops, and drive in a restricted geographic area. Therefore, charging can happen overnight at the central vehicle depot or through fast charging at bus stops or other central locations. Nevertheless, similar to electric passenger cars, BEBs have a more limited driving range than ICE vehicles due to the limited energy capacity of modern-day batteries [37]. This limited driving range makes knowledge on the energy consumption more important. Because the intended driving distances are closer to the vehicle's maximum driving range, the inherent variations in the energy consumption have a more significant influence on whether or not a trip can be completed. Electric buses are often scheduled more conservatively to account for this uncertainty, resulting in more vehicles being required to operate a public transport network. As a result, conserving and predicting the remaining available energy of BEBs is essential to improving their viability compared to ICE vehicles.

The energy consumption of BEBs can be reduced both through vehicle design choices and vehicle control strategies. Vehicle design considerations include the type of powertrain topology, the type and sizing of the climate system, tire choice, and vehicle weight minimization [38, 39]. In addition, control strategies to minimize BEB energy consumption exist on a vehicle level and on a fleet level. On a

vehicle level, these control strategies include eco-driving [40], which supports the driver in driving the vehicle in an energy-efficient manner, or onboard energy management and eco-comfort strategies [41, 42], which control powertrain and auxiliary systems to minimize energy consumption. For BEBs, additional applications of energy consumption models are found in solving fleet scheduling problems [43, 44] and designing eco-routing and eco-charging strategies [45, 46]. Fleet scheduling is often performed to minimize the number of redundant vehicles, reduce peak grid load during charging, or minimize battery degradation [47]. In the future, dynamic scheduling offers a possible solution to make vehicle schedules flexible based on traffic conditions [48], electricity pricing [49] or battery degradation [50].

All the aforementioned methods rely on models that simulate the battery-to-wheel energy consumed by BEBs. By improving these models and providing more insight into the dynamics involved with the energy dissipated, both vehicle design and vehicle control strategies can be improved. Ultimately, more accurate and realistic energy consumption models can benefit BEB manufacturers by building more specialized products, public transport operators by lowering the operational expenses and number of redundant vehicles, and city residents by providing a locally clean and cost-efficient mode of transport.

1.3   Problem statement

As described in Section 1.2.2, the driving range of battery electric buses, and electric vehicles in general, is inherently variable. Because the driving range is limited with respect to conventional vehicles, numerous control strategies either minimize the energy consumption per driven distance, e.g., eco-driving or onboard energy management, or optimize the deployment of vehicles, e.g., eco-routing or fleet scheduling. These control strategies rely on models to either predict the energy consumption over a particular route or to predict the expected future power requested from the battery as a function of time. In the context of this thesis, prediction is referred to as the calculation of a physical value, e.g., energy consumption or vehicle speed, over a certain route, without explicitly using previous measurements of that value over the same route.

While plenty of literature exists on electric vehicle energy consumption prediction, only a selection focuses specifically on BEBs [51, 52]. This BEB-related literature concentrates mainly on data-driven models, which often rely on large, low-resolution datasets. These macroscopic models, with a temporal resolution of more than 1 s, aim to predict the energy required to traverse a route or a section of a route [53]. In contrast, microscopic models predict the power requested from the battery as function of time, which is required for onboard energy management or eco-driving strategies. There are physics-based methods that predict energy consumption [54], but these often contain the implicit assumption that the vehicle only drives straight, thereby neglecting part of the vehicle dynamics. Therefore,

a framework is required that supplies microscopic energy consumption prediction for BEBs, to be used in future eco-driving or energy management strategies. In summary, the objective of this thesis is:

> *To improve the accuracy of electric vehicle energy consumption prediction methods by considering the vehicle dynamics of a battery electric bus.*

The basis of this work is formed by the physics-based energy consumption prediction model developed in [55]. This model is microscopic and is of the 'backward-facing' type: the model predicts a vehicle speed and, given this speed, calculates the resistance forces at the wheels and propagates these backward via the powertrain to determine the required battery power. This physics-based energy consumption model was revised and integrated into a MATLAB tool. The tool is interfaced with online information services to obtain road-, weather-, elevation data and is published as the 'TU/e Microscopic Energy Consumption PRedictino tOol (MECPRO) 0.1' [56].

1.4   Research challenges and contributions

The main contributions of the research in this thesis, aimed at addressing three research challenges, are:

Physics-based model extensions.   In the majority of the energy consumption studies where a physics-based approach is followed, a backward-facing longitudinal dynamics model is used. After reconstructing the vehicle speed, the model considers the forces acting longitudinally on the vehicle, often including rolling resistance, aerodynamic resistance, the longitudinal component of gravity, and the force required to accelerate the vehicle. Although these forces comprise the main contributors to the energy dissipated by the vehicle's powertrain, other physical effects can play a role, yet are often neglected. In this scientific search for different physical effects that contribute to the dissipated energy, the first two contributions of this thesis are defined:

> **Contribution I.** *A method to assess the slip losses occurring at the tires of a battery electric bus during cornering, using a validated, nonlinear steady-state cornering model.*

> **Contribution II.** *A method to assess the damper losses occurring in the suspension of a battery electric bus, using a validated, nonlinear quarter car model.*

Contribution I pertains to the lateral vehicle dynamics, and **Contribution II** pertains to the vertical vehicle dynamics. In both cases, a vehicle dynamic model is first defined and validated by demonstrating a favorable comparison between simulations and dedicated vehicle tests. The validated model is then applied to quantify energy losses affiliated with the effects of interest for a realistic operation scenario with a battery electric bus. These analyses indicate that both the lateral and vertical vehicle dynamics contribute to the power requested from the battery and cannot be overlooked when accurate energy consumption predictions are required.

Parameter estimation. Even though the parameters of physics-based energy consumption models often describe physical quantities, the exact values can be challenging to ascertain. The rolling resistance coefficient is one of the parameters that is notoriously difficult to determine accurately because it depends on numerous factors, including tire design, tire inflation pressure, road roughness, and suspension characteristics.

The local road slope is a parameter that is especially relevant if the power request is to be predicted as a function of time. While various information sources exist that report the local road gradient, these are often not sufficiently accurate or restricted to certain countries or regions. In this context, the third contribution of this thesis is defined as:

> **Contribution III.** *A method to recursively estimate the combined rolling resistance and road gradient as function of position for a route that is traversed repeatedly by a battery electric bus.*

This method relies on the fact that both the rolling resistance and the road slope are position-dependent for a fixed route. By calculating the difference between the measured and modeled powertrain power, an estimate for these parameters can be provided in the shape of a position-dependent road-resistance profile. By describing this resistance profile using basis functions, measurements from multiple vehicles traversing the same route segments can be combined. This route-specific resistance profile includes all position-dependent resistance forces, including possible additional resistance in corners and rolling resistance due to rough roads. **Contribution III** thereby provides a method to also capture the physics described by **Contribution I** and **Contribution II** in the longitudinal dynamics model.

Forward velocity prediction. The longitudinal dynamics model describes the power requested from the battery of the vehicle when driving a certain forward velocity as function of time. To accurately predict the future power request, infor-

mation on the future forward vehicle velocity is required for the route of interest. While methods exist to predict the forward velocity based on route information, the vehicle velocity is uncertain and can change based on unexpected traffic circumstances and driver behavior. Thus, up-to-date vehicle and driver information is required to predict the remaining trip velocity and energy consumption online, which is enabled by increasing computing power on-board modern-day vehicles. This results in the final contribution of this thesis:

> **Contribution IV.** *A method to adapt the predicted forward vehicle velocity online by including current vehicle position and forward velocity and by performing driver characterization based on previous vehicle accelerations.*

This method predicts the forward velocity for the remaining part of a route. Besides route information that is conventionally used in these predictions, the algorithm includes:

- the current position and speed of the vehicle,
- the previously measured acceleration and deceleration realized by the driver.

The resulting online prediction adapts to unexpected changes in vehicle speed, providing an up-to-date estimate of the powertrain power and energy required to complete a predetermined route. Furthermore, a fleet-monitoring experiment indicates the potential of characterizing different drivers based on measured acceleration and using this information to make driver-specific speed predictions.

1.5   Outline

This thesis discusses the physics-based energy consumption prediction of electric vehicles, with a focus on battery electric buses. Including this introduction, the thesis consists of seven chapters.

Chapter 2 presents a backward-facing physics-based energy consumption prediction model, which forms the basis of this work. This model is adapted from [55] and applies longitudinal vehicle dynamics to predict the powertrain power as function of vehicle speed, vehicle parameters, and environmental factors. The model is demonstrated on an electric delivery van and can be generalized to different types of electric vehicles. In Chapter 3 the lateral vehicle dynamics are considered to assess the energy losses occurring during cornering of the vehicle by accounting for the slip losses occurring at the tires of the vehicle. In Chapter 4 the vertical vehicle dynamics are considered to assess the energy lost in the dampers of the suspension during traversal of rough roads. Chapter 5 presents a method to estimate the rolling resistance and road slope resistance of a route that is repeatedly traversed by an electric vehicle. Chapter 6 focuses on online forward

velocity prediction, including a method to make driver-specific acceleration predictions. Finally, Chapter 7 closes the main body of the thesis by summarizing the conclusions presented in Chapters 2-6. Furthermore, recommendations for future research are presented in this chapter. The Appendices A, B, and C of this thesis present extensions and additional findings on the matter presented in the main chapters.

Note for the reader. Chapters 2-6 are all based on research articles and can therefore be read independently. A reference to the corresponding research paper is included at the beginning of each chapter. At the end of Chapters 2, 3, and 6 a supplementary discussion is provided to mention relevant additional results and highlight the connection to other chapters. An overview of how the chapters relate to the contributions mentioned in Section 1.4 is provided in Table 1.1.

Table 1.1. Overview of contents.

Chapter 1	**Introduction**
Chapter 2	**A physics-based energy consumption model**
Chapter 3	**Contribution I** A method to assess the slip losses occurring at the tires of a battery electric bus during cornering, using a validated, nonlinear steady-state cornering model.
Chapter 4	**Contribution II** A method to assess the damper losses occurring in the suspension of a battery electric bus using a validated, nonlinear quarter car model.
Chapter 5	**Contribution III** A method to recursively estimate the combined rolling resistance and road gradient as function of position for a route that is repeatedly traversed by a battery electric bus.
Chapter 6	**Contribution IV** A method to adapt the predicted forward vehicle velocity online by including current vehicle position and forward velocity and by performing driver characterization based on previous vehicle accelerations.
Chapter 7	**Conclusions & recommendations**

1.6   List of publications

Peer-reviewed journal articles

- C. J. J. Beckers, I. J. M. Besselink, and H. Nijmeijer, "Assessing the impact of cornering losses on the energy consumption of electric city buses," *Transp. Res. Part D: Transp. Environ.*, vol. 86, p. 102360, Sep. 2020, doi: 10.1016/j.trd.2020.102360.

- C. J. J. Beckers, I. J. M. Besselink, and H. Nijmeijer, "Analysis of energy losses in suspension dampers on rough roads," *submitted*, 2022.

- C. J. J. Beckers, I. J. M. Besselink, and H. Nijmeijer, "Combined Rolling Resistance and Road Grade Estimation Based on EV Powertrain Data," *submitted*, 2022.

Conference contributions

- C. J. J. Beckers, I. J. M. Besselink and H. Nijmeijer, "On-line Test of a Real-Time Velocity Prediction for E-bus Energy Consumption Estimation," *2021 IEEE Veh. Power Propuls. Conf. (VPPC)*, Gijón, Spain, 2021, pp. 1-5, doi: 10.1109/VPPC53923.2021.9699205.

- C. J. J. Beckers, I. J. M. Besselink, and H. Nijmeijer, "The State-of-the-Art of Battery Electric City Buses," presented at the 34th Int. Electric Veh. Symp. and Exhib. (EVS34), Nanjing, China, Jun. 2021.

- C. J. J. Beckers, M. Paroha, I. J. M. Besselink, and H. Nijmeijer, "A Microscopic Energy Consumption Prediction Tool for Fully Electric Delivery Vans," in *33rd World Electr. Veh. Symp. & Expo. (EVS33)*, Sep. 2020, doi: 10.5281/zenodo.4023302.

- C. J. J. Beckers, I. J. M. Besselink and H. Nijmeijer, "Modeling of Energy Losses During Cornering for Electric City Buses," in *2019 IEEE Intell. Transp. Syst. Conf. (ITSC)*, Auckland, New-Zealand, Oct. 2019, pp. 4164-4169, doi: 10.1109/ITSC.2019.8917232.

- C. J. J. Beckers, I. J. M. Besselink, J. J. M. Frints, and H. Nijmeijer, "Energy consumption prediction for electric city buses," presented at the 13th ITS Eur. Congr., Brainport, The Netherlands, Jun. 2019.

Open-access datasets

- C. J. J. Beckers, T. A. G. H. Geraedts, I. J. M. Besselink, and H. Nijmeijer, "TU/e Microscopic Energy Consumption PRediction tOol 0.1 (TU/e MECPRO 0.1)," 4TU.ResearchData, Jan. 2021, doi: 10.4121/12764732.

- C. J. J. Beckers, I. J. M. Besselink, and H. Nijmeijer, "MATLAB-scripts describing a nonlinear steady-state cornering model for an electric city bus," 4TU.ResearchData, Mar. 2020, doi: 10.4121/12717902.

Ancillary publications

Besides the above mentioned work, the author has contributed to the following publications that are not discussed explicitly in this thesis.

- M. Ponchant, A. Li, C. J. J. Beckers and M. Paroha, "Battery Management System Evaluation within a Complete Electric Vehicle Model with Software-in-the-Loop and Hardware-in-the-Loop Approaches," *2021 23rd Eur. Conf. Power Electron. Appl. (EPE'21 ECCE)*, Ghent, Belgium 2021, pp. P.1-P.10.

- G. P. Padilla, C. Pelosi, C. J. J. Beckers, and M. C. F. Donkers, "Eco-Driving for Energy Efficient Cornering of Electric Vehicles in Urban Scenarios," *IFAC-PapersOnLine*, vol. 53, no. 2, pp. 13816-13821, 2020, doi: 10.1016/j.ifacol.2020.12.891.

1.7   List of supervised projects

- L. Trimbach, "Modeling of an Electric City Bus for Energy Consumption Estimation," M.S. thesis DC 2021.035 (Confidential), Eindhoven Univ. of Tech., Eindhoven, May 2021.

- D.T. van Blijderveen, "Real-Time Driver Characterization for Energy Consumption Prediction of Electric City Buses," Internship report DC 2021.006 (Confidential), Eindhoven Univ. of Tech., Eindhoven, Jan. 2021.

- A. Sundarrajan, "Range prediction algorithms and a stamina mode strategy for battery electric trucks: Estimating and extending the range ahead of an electric truck from a fuel economy perspective," PdEng thesis (Confidential), Eindhoven Univ. of Tech., Eindhoven, Nov. 2020.

- K. Van den Boom, "Sensitivity Analysis of an EV Energy Consumption Prediction Model," B.S. thesis DC 2020.071, Eindhoven Univ. of Tech., Eindhoven, Jun. 2020.

- O.F. Hulsebos, "Driver Behaviour Analysis for Energy Consumption Prediction in Electric Buses," M.S. thesis DC 2020.008 (Confidential), Eindhoven Univ. of Tech., Eindhoven, Jan. 2020.

- K. Basu, "An Online Powertrain Power Request Predictor for Electric City Buses," M.S. thesis DC 2019.103 (Confidential), Eindhoven Univ. of Tech., Eindhoven, Nov. 2019.

- T.A.G.H. Geraedts, "Programming of an Energy Consumption Prediction Algorithm for an Electric Vehicle," B.S. thesis DC 2019.071, Eindhoven Univ. of Tech., Eindhoven, Jul. 2019.

- M.P.A. Verwijlen, "Determination of road load parameters of a fully electric Voltia eVAN by means of coast-down tests," B.S. thesis DC 2019.016, Eindhoven Univ. of Tech., Eindhoven, Feb. 2019.

- K. Basu, "Characterization of Suspension Energy Losses due to Road Unevenness," Internship report DC 2018.102 (Confidential), Eindhoven Univ. of Tech., Eindhoven, Nov. 2018.

2

A Microscopic Energy Consumption PRediction tOol (MECPRO)

Abstract - *For cost-optimal utilization of battery electric delivery vans, energy consumption prediction is important. This chapter presents a microscopic energy consumption tool, which requires the intended route as input. Both the forward velocity profile prediction algorithm and the subsequent energy consumption model are based on data obtained from dedicated vehicle tests. Secondly, up-to-date environmental data on the weather, the road slope profile, and local speed legislation are obtained through APIs via the internet. The results show good correspondence with the measured energy consumption. Validation with several measured trips shows that the energy consumption is predicted with an error that rarely exceeds 10%.*

Figure 2.1. The Voltia eVan.

2.1   Introduction

MOTIVATED by the increasing awareness of global warming, the cargo transport sector is making a transition towards electric mobility. One example of such an electric vehicle is the Voltia eVan. The Voltia eVan is a fully electric delivery van with a swappable traction battery. Converted from a Citroën Jumper, the vehicle keeps all functional, safety, and driver-comfort features of the donor vehicle, while enhancing its driving characteristics thanks to the 160 kW (peak) electric motor. The capacity of the traction battery can vary between 40 and 90 kWh per vehicle. The Voltia eVan is also used as the carrier vehicle of a demonstrative batterypack with novel battery management system (BMS) features, which is developed within the scope of the H2020 project EVERLASTING [57].

Despite the battery capacity options and battery swapping capabilities, an accurate energy consumption prediction tool is essential for efficient utilization of these vehicles. An example of such a prediction methodology can be found in [58], where extensive fleet data is used to predict the energy consumption of electric taxi's. However, in case no large amount of fleet data is available, for instance before initial vehicle deployment, other methods are required to make accurate predictions.

In this chapter, a microscopic energy consumption prediction tool for the Voltia eVan is presented. The tool consists of two parts: a forward velocity profile prediction (FVPP) algorithm and an energy consumption prediction (ECP) model. Both parts follow a physics-based approach in order to provide reliable extrapolation to unknown geographic regions and operating conditions. The models rely on up-to-date weather, road, and elevation data. The tool [56], developed in MAT-LAB, is connected via APIs to OpenWeatherMap [59], OpenStreetMap [60], and
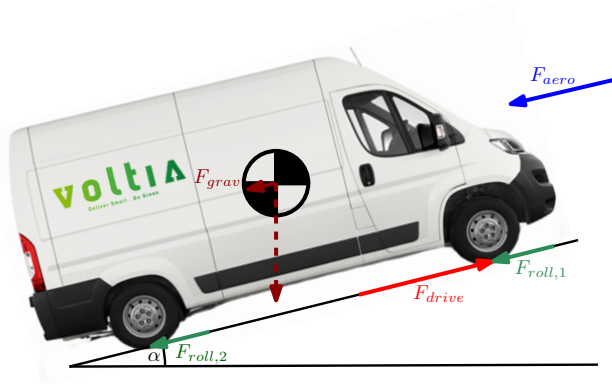
Figure 2.2. Schematic side-view of the Voltia eVan with all longitudinal forces indicated by arrows.

the SRTM elevation model [61], respectively, to obtain these data.

The outline of this chapter is as follows. In Section 2.2 the model and methods underlying the prediction are explained. In Section 2.3 the results of the energy consumption prediction tool are presented and compared to measurements. In Section 2.4 the results are discussed and the conclusions are presented in Section 2.5.

2.2 Methodology

2.2.1 Model

The energy consumption of the vehicle is modeled using a physics-based approach, i.e., by modeling the longitudinal dynamics of the vehicle, as shown in Figure 2.2. By applying Newton's second law we can write

$$m_{eff} \frac{dv}{dt} = F_{drive} - F_{roll,1} - F_{roll,2} - F_{aero} - F_{grav} . \tag{2.1}$$

In this equation, m_{eff} is the effective mass, which also includes rotational inertia of the wheels and driveline and v is the forward vehicle velocity as function of time t. Furthermore, F_{drive}, F_{aero}, and F_{grav} represent the driving force, aerodynamic drag force, and longitudinal gravity component, respectively. The rolling resistance experienced by the front axle $F_{roll,1}$ and the rear axle $F_{roll,2}$ are indicated individually in Figure 2.2. These are aggregated into one combined rolling resistance force for the remainder of this chapter.

By modeling each of these forces, the power required by the powertrain P_{pt}

can be calculated as [55]

$$P_{pt} = \left(m_{eff} \frac{dv}{dt} + f_r mg \cos(\alpha) + \frac{1}{2}\, \rho\, C_d A_f\, v_{wind,rel}^2 + mg \sin(\alpha) \right) v$$
$$+ P_{loss}(\omega_{wheel}, T_{wheel})\,. \quad (2.2)$$

This expression is first of all a function of the forward vehicle velocity v. Secondly, there are several vehicle parameters, such as vehicle mass m, rolling resistance coefficient f_r, aerodynamic drag coefficient C_d, frontal area A_f, and powertrain losses P_{loss} as function of wheel speed ω_{wheel} and wheel torque T_{wheel}. Lastly, also several environmental conditions are required, such as the gravitational acceleration g, the air density ρ, the local road slope α, and the relative wind velocity $v_{wind,rel}$. The total energy consumption E_{tot} for a trip can be calculated by adding the auxiliary power P_{aux} and integrating over the trip time:

$$E_{tot} = \int_{t_0}^{t_{end}} (P_{pt} + P_{aux})\ dt\,. \quad (2.3)$$

While the physics of the methodology is captured by (2.2) and (2.3) alone, the challenge lies in the accurate determination of all these vehicle and environmental parameters.

2.2.2   Identification of vehicle parameters

The model requires knowledge of several vehicle-specific parameters. Because it is generally difficult to determine these coefficients based on physical modelling alone, dedicated vehicle tests are performed.

Rolling resistance and aerodynamic drag

Coast-down tests are performed to determine both the rolling resistance coefficient and the aerodynamic drag coefficient. During such a coast-down test, the vehicle is accelerated to a certain speed, after which the propulsion power is removed, e.g., $P_{pt} = 0$, causing the vehicle to decelerate. By conducting this experiment on a level surface during low-wind conditions (2.2) reduces to

$$m_{eff} \frac{dv}{dt} + f_r mg + \frac{1}{2}\rho C_d A_f v^2 = 0\,. \quad (2.4)$$

Therefore, measurement of the forward velocity v and its time derivative dv/dt during deceleration yields enough information to estimate both f_r and C_d, as described in [62]. Because the rolling resistance coefficient will also vary as function of road surface, the tests are repeated for different road surfaces; good asphalt, medium quality asphalt, and bad asphalt. Approximately 10 coast-down maneuvers are performed on each road surface type in two directions.

Table 2.1. Measured average rolling resistance coefficient f_r for different road surfaces together with the applicable speed range for usage of the value in the energy consumption prediction model.

Road surface quality	Average measured f_r [-]	Prediction speed range [km/h]
Good asphalt	0.0088	>80
Medium asphalt	0.0092	30-80
Bad asphalt	0.0112	0-30
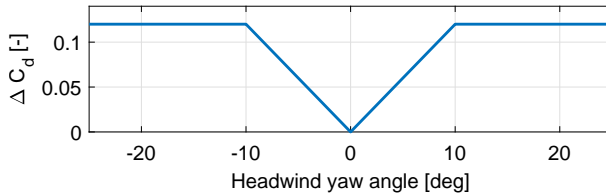
Figure 2.3. Increase in aerodynamic drag coefficient ΔC_d as function of headwind yaw angle β.

The results are listed in Table 2.1 and show that the rolling resistance coefficient f_r ranges between 0.0088 and 0.0112 and increases for decreasing road quality. This road surface quality dependency is also taken into account in the energy consumption prediction. The simulation value for f_r is considered a piecewise constant function of vehicle speed, as indicated in the last column of Table 2.1. The underlying assumption is that the road quality is generally better on high-speed roads, such as highways.

The aerodynamic drag coefficient is also a result of the coast-down tests. Because in theory the C_d of the vehicle does not change as function of road surface, the results of all the coast-down tests are averaged resulting in a C_d value of 0.36. As will be explained in Section 2.6, information about the apparent wind yaw angle β may be available. In that case, the aerodynamic drag coefficient is considered to increase due to crosswind effects and can be calculated by

$$C_d = 0.36 + \Delta C_d\left(\beta\right) \ . \tag{2.5}$$

Here, the increase in drag coefficient ΔC_d is a function of headwind yaw angle β. Because only little research is available on the cross-wind aerodynamics of medium-duty vehicles, such as the Voltia eVan, ΔC_d is assumed to be roughly similar as for a large Multi Purpose Vehicle (MPV), as is described in [63]. Therefore, $\Delta C_d\left(\beta\right)$ is considered a piecewise linear function shown in Figure 2.3 and is assumed to be constant for $|\beta| > 10\,\mathrm{deg}$.

Lastly, the vehicle mass is determined by weighing the empty vehicle and adding the mass of the cargo and drivers, resulting in $m = 2800\,\mathrm{kg}$. Addition-
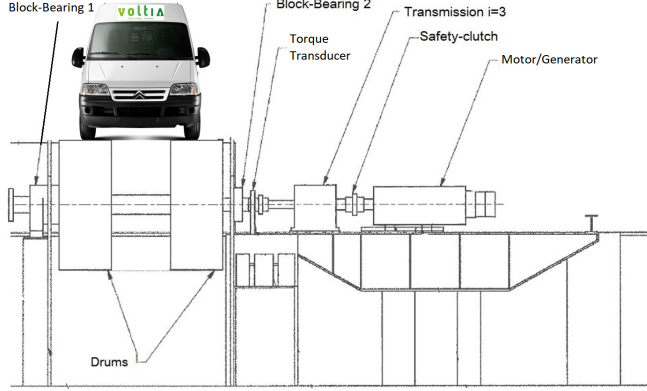
Figure 2.4. Schematic view of the Voltia eVan placed on the TU/e Heavy Duty Chassis Dynamometer.

ally, the effective mass is calculated based on the known inertia of the tires and motor rotor, resulting in $m_{eff} = 2880\,\text{kg}$.

Powertrain losses and regenerative braking

The powertrain loss P_{loss} is difficult to determine based on physical modeling. This term represents all the power lost between the vehicle's traction battery and the wheels, and includes both electrical losses in the inverter and motor, as well as mechanical losses in the gearbox, bearings, and driveshafts. Therefore, the choice is made to measure the lumped powertrain losses using vehicle tests. The TU/e Heavy Duty Chassis Dynamometer, displayed in Figure 2.4, allows for the measurement of the mechanical power output at the driven wheels of the vehicle P_{wheel}. Simultaneously, the electrical power P_{DC} at the DC-side of the vehicle's powertrain inverter is measured. This way, the powertrain losses can be determined as

$$P_{loss} = P_{DC} - P_{wheel} \,. \tag{2.6}$$

By operating the vehicle in steady-state at several combinations of velocities and torques, the powertrain loss is mapped for the entire operating range of the powertrain. The results are visualised as efficiency values in Figure 2.5a, and represent the efficiency of the inverter, motor, gearbox, and axle combined. The efficiency is calculated separately for the driving situation η_{drv} and the regenerative braking situation η_{brk}:

$$\eta_{drv} = \frac{P_{wheel}}{P_{wheel} + P_{loss}} \qquad \eta_{brk} = \frac{|P_{wheel}| - P_{loss}}{|P_{wheel}|} \,. \tag{2.7}$$

In the case of braking, η_{brk} is applied to the regenerated energy. If this energy is that supplied again to the powertrain, additional losses occur, represented by
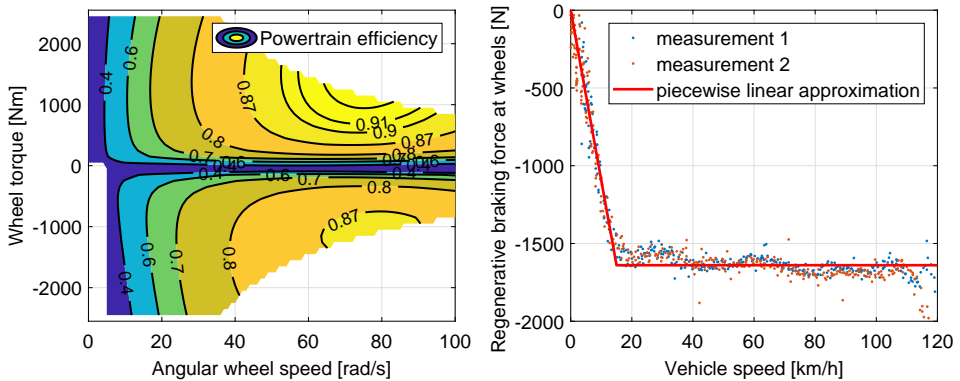
(a) Powertrain efficiency from battery to wheels.

(b) Maximum regenerative braking force.

Figure 2.5. Results of the TU/e Heavy Duty Chassis Dynamometer tests.

the battery efficiency and η_{drv}. Therefore, the overall efficiency applicable to regenerated energy is lower than η_{brk}.

The measured powertrain losses are implemented in the energy consumption prediction algorithm as P_{loss} in (2.2) and are considered to vary as function of wheel angular velocity ω_{wheel} and wheel torque T_{wheel}. Furthermore, coast-down experiments are conducted on the dynamometer with the goal of identifying the regenerative braking characteristics of the vehicle. The moment of inertia of the dynamometer is known, thus the braking force exerted by the vehicle on the drum can be determined during such a coast-down test. The results are displayed in Figure 2.5b and show a regenerative braking force that is approximately constant, except at lower velocities. In the energy consumption prediction model this force is modeled by a piecewise linear function, also indicated in Figure 2.5b. During normal operation of the vehicle the applied braking force up until this piecewise linear function is assumed to be regenerative. Any additional braking force exceeding this limit is applied using the hydraulic friction brakes and is therefore excluded from the regenerative braking gain. Lastly, the auxiliary power is considered to be constant based on measurements, resulting in $P_{aux} = 650\,\mathrm{W}$.

2.2.3 Identification of environmental parameters

The longitudinal dynamics model in (2.2) requires knowledge of several environmental parameters. While some of these parameters are assumed constant, such as the gravitational acceleration $g = 9.81\,\mathrm{m/s^2}$, others might vary as function of location and/or time. Therefore, relevant information is obtained for an arbitrary route through use of online Application Programming Interfaces (APIs).
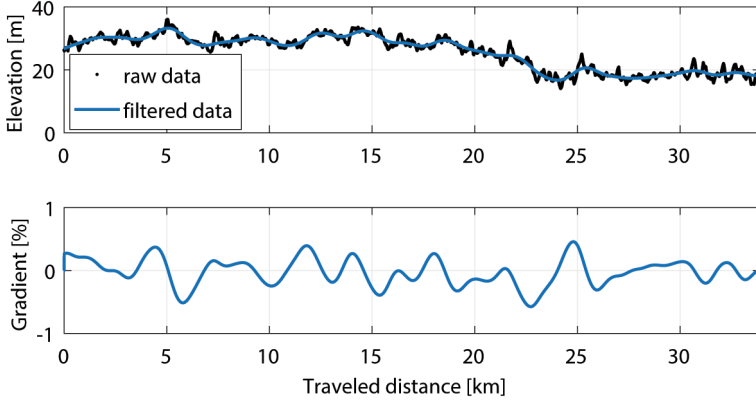
Figure 2.6. Elevation and gradient for one of the driven routes with the Voltia eVan.

Road slope

The local road slope α is determined from the SRTM elevation database [61]. By making use of the `readhgt` toolbox [64] relevant sections of the elevation map are downloaded and queried. The resulting elevation, as function of travelled distance, is filtered by a 3rd order Butterworth low-pass filter with cut-off spatial frequency $1/\lambda_c = 1/2000 \, \frac{1}{\text{m}}$, and differentiated numerically to obtain the local road gradient α, see Figure 2.6. This specific λ_c indicates that all features smaller than approximately $2 \, \text{km}$ are filtered out of the elevation profile. This step is essential, as otherwise short wave length variations in the elevation model will result in unrealistic road gradients, which can severely impact the accuracy of the energy consumption prediction.

Weather data

The energy consumption prediction algorithm takes up-to-date weather information into account. To this end, temperature T, air pressure p_a, wind magnitude, and wind direction are obtained from OpenWeatherMap [59]. The temperature and air pressure are used to calculate the air density $\rho(T, p_a)$ [65].

The wind magnitude and direction are represented by the vector $\vec{v}_W$, which indicates the direction the wind is blowing towards with respect to the north. This vector is used together with the vehicle velocity vector $\vec{v}_V$, whose direction is calculated from the vehicle heading, to determine the apparent wind vector $\vec{v}_A$

$$\vec{v}_A = f_w \vec{v}_W - \vec{v}_V \, , \tag{2.8}$$

which is also depicted in Figure 2.7. Practise shows that it is beneficial for the energy consumption prediction to scale the wind magnitude by choosing the con-
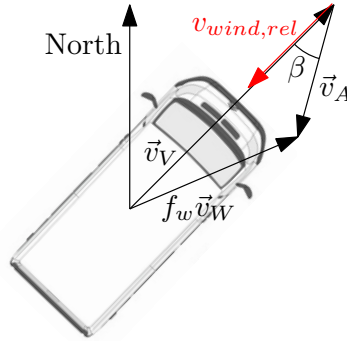
Figure 2.7. Top view of the Voltia eVan with the vehicle velocity vector $\vec{v}_V$, the scaled wind velocity vector $f_w \vec{v}_W$, the apparent wind vector $\vec{v}_A$ and the relative longitudinal wind velocity $v_{wind,rel}$.

stant factor $f_w < 1$. This factor is also used to compensate for the fact that the obtained wind magnitude is specified at an altitude of $10\,\text{m}$ above the road surface instead of $1\,\text{m}$, where the vehicle drives. To compensate for this altitude difference an f_w of approximately 0.28 is expected [66, p. 56]. For the result presented here, $f_w = 0.2$ was used, because it results in the most accurate predictions for the analysed trips. A likely reason that $f_w < 0.28$ is that the vehicle rarely drives in an open field where it is subject to the full influence of the wind. More often the vehicle is sheltered from the wind by road-side structures, trees, or buildings. As last step, the apparent wind direction β is calculated, which is used to determine $\Delta C_d(\beta)$ as described in Section 2.2.2. Furthermore, β is used to calculate the relative longitudinal wind direction $v_{wind,rel}$

$$v_{wind,rel} = |\vec{v}_A| \cos(\beta) \,, \tag{2.9}$$

which is used in (2.2).

2.2.4 Prediction of the forward velocity profile

The expression in (2.2) also requires knowledge of the forward velocity profile of the vehicle. A velocity predicting algorithm is developed, based on [55], that requires GPS coordinates of an intended route as input.

By use of the `OpenStreetMap Functions` toolbox [67], the algorithm queries relevant road information from OpenStreetMap [60]. This includes the local speed legislation and traffic light locations. The information is visualised in Figure 2.8 for the route that will also be discussed in Section 2.3. In the first step of the forward velocity profile prediction, the local speed legislation is considered to dictate the maximum speed along the route. Next, further speed constraining locations are identified. These include traffic light locations and corners. The vehicle is assumed to make a full stop at every encountered traffic light. The reduced speed in a
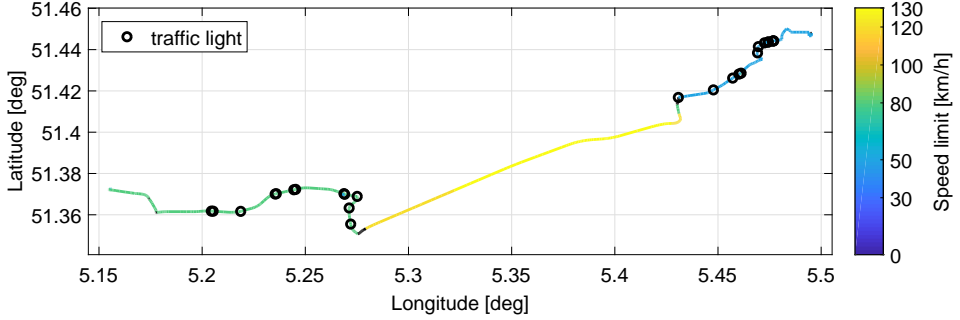
Figure 2.8. Legislated maximum speed and traffic light location according to OpenStreetMap.
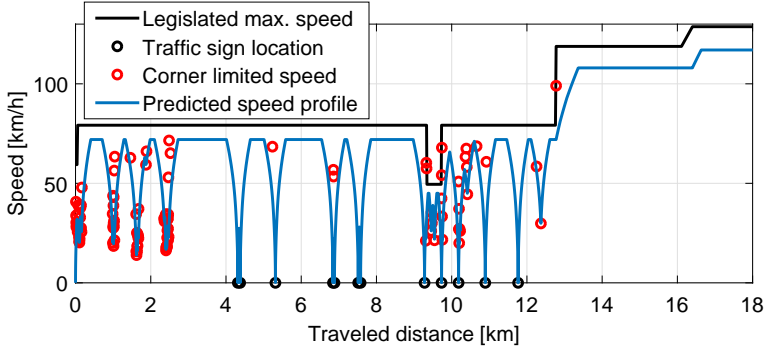
Figure 2.9. Detail of the determined speed constraining locations and the resulting predicted velocity profile.

corner is a function of the corner curvature calculated using the GPS-points and an assumed maximum lateral acceleration of $2\,\text{m/s}^2$. The result is a profile dictating the upper-bound of the forward velocity v_{max} as function of travelled distance s, which is discretized as

$$s = [s_1, s_2, ..., s_i, ..., s_N] \quad \text{for} \quad i = 1, 2, ..., N \ , \tag{2.10}$$

where N is the total number of coordinates along the route.

The final forward velocity profile is determined by including a limited vehicle acceleration and deceleration. Because these limits are mainly dictated by the driver, they are referred to as the driver model. The preferred cruising speed is also assumed to be driver specific and is calculated as factor of the legislated maximum speed. The three driver specific parameters; acceleration, deceleration, and cruising speed, are tuned based on recorded data to represent the average driving behavior of a particular driver, as shown in Figure 2.10a.
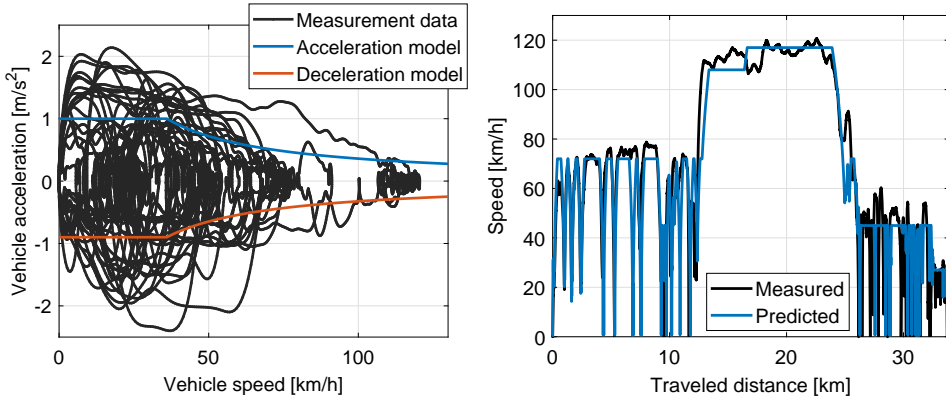
(a) Measured and modeled longitudinal vehicle acceleration.

(b) Measured and modeled speed profile.

Figure 2.10. Driver model that is used as input for the forward velocity profile prediction (**a**) and the resulting predicted forward velocity profile (**b**), both compared to measured data (black).

In order to include the acceleration limit, numerical time integration is performed in between each of the points of the distance grid s, while also taking the upper-bound of the forward velocity v_{max} into account:

$$v(s_{i+1}) = \min \left(\int_{t(s_i)}^{t(s_{i+1})} a_{x,lim}(v)dt + v(s_i) \, , \, v_{max}(s_{i+1}) \right) \text{ for } i = 1, 2, ..., N - 1 \, ,$$

(2.11)

where $a_{x,lim}$ is the acceleration limit, displayed in Figure 2.10a. This procedure is performed once in forward direction, as shown in (2.11), and once in backward direction, to include the deceleration limit. Using the now known forward velocity, the velocity profile as function of distance is interpolated to a time grid. The resulting forward velocity profile in Figure 2.10b shows a fair correspondence with a measured forward velocity profile. The prediction algorithm contains multiple assumptions, such as the completely deterministic driver model, and the fact that the vehicle stops at every traffic light. Even though not all realistic details are represented, the resulting forward velocity profile is accurate enough for the goal of energy consumption prediction.

2.3 Energy consumption prediction results

Having knowledge about the forward velocity profile and the vehicle and environmental parameters, the energy consumption can be predicted for a given route. To
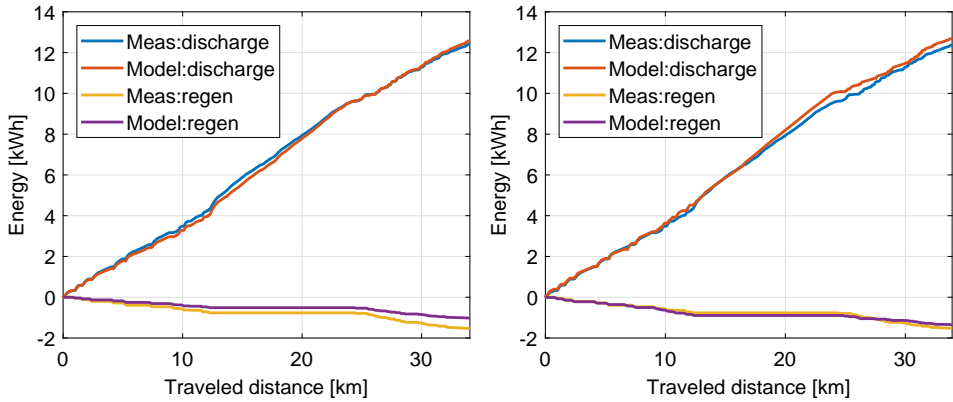
(a) Energy based on measured forward velocity.

(b) Prediction based on predicted forward velocity.

Figure 2.11. Predicted energy consumption compared to the measured energy consumption. In (**a**) the measured forward velocity $v(t)$ was used, whereas in (**b**) the predicted forward velocity profile was used.

this end, the forward velocity profile is first predicted, as described in Section 2.2.4. The predicted forward velocity profile $v(t)$ is then used as input for (2.2) and (2.3), together with all the parameters described in Sections 2.2.2 and 2.2.3.

In order to validate both parts of the model, a comparison with measured data is made. A 33.9 km route is used as input. Data for the same route are also displayed in Figures 2.6, 2.8, 2.9, and 2.10. First of all, the energy consumption model is validated by using the measured speed, also shown in Figure 2.10b as input to (2.2) and (2.3). The results, displayed in Figure 2.11a, show a good correlation between model and measurement, except for a slight under-estimation of the regenerated energy.

Next, the same calculations are performed by taking the predicted forward velocity profile, shown in Figure 2.10b, as input for the energy consumption model. The result is presented in Figure 2.12, which displays the power described by each of the terms in (2.2) as function of time. By comparing the individual contributions, it can be concluded that for this particular trip 49% of the energy is dissipated by aerodynamic drag, 25% on powertrain losses and 22% on rolling resistance. The remaining 4% is lost due to occasional dissipative braking. Furthermore, Figure 2.13 shows the total predicted power compared to the measured power. The comparison indicates that the position and shapes of most, but not all, of the power peaks caused by acceleration and deceleration events are predicted correctly.Integrating and summing these powers, according to (2.3), results in the total energy displayed in Figure 2.11b. The result shows a correct estimation of the regenerated energy and a slight over-estimation of the dissipated energy. Ul-
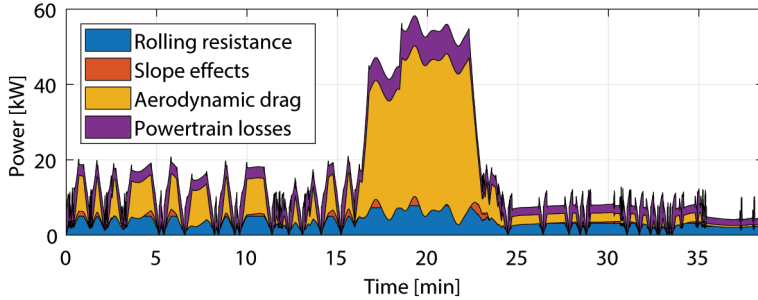
Figure 2.12. Overview of the power lost due to each of the terms in (2.2), excluding acceleration.
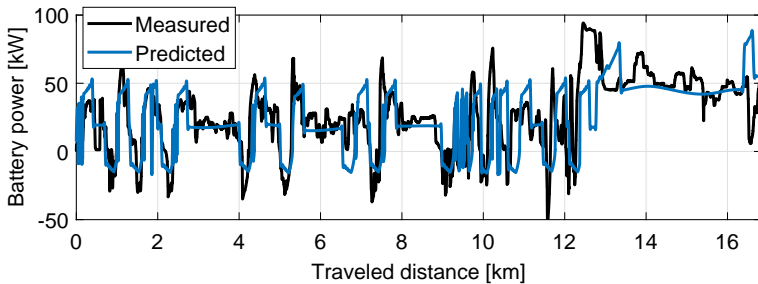
Figure 2.13. Comparison of the predicted battery power and the measured battery power for the first half of the trip.

timately, the difference between the measured and predicted energy consumption at the end of the trip is 4.3%.

The results of several trips are listed in Table 2.2. All trips are conducted in and around the city of Eindhoven, the Netherlands. The longer distance trips, e.g., trip 1, 3 and 4, include highway driving. All trips contain city driving. Based on five analysed trips with an average length of 17.6 km, the tool is fairly accurate and stays mostly below 10% with respect to the measured energy consumption. Trip number 5 is an exception. Most probably, the rolling resistance coefficient described in Section 2.2.2 is not in accordance with the real type of road along this short route. For short routes like this one, a deviation of one of the model parameters, which are often position-dependent, can result in large relative errors. In contrast, on longer routes any local errors are averaged.

2.4 Discussion

In theory, the model includes the influence of road slope and wind in the energy consumption. However, because the validation sets were recorded in the Nether-

Table 2.2. Results of the energy consumption prediction tool for five different trips. Data from Trip 4 is detailed in other figures throughout this chapter.

	Distance [km]	Measured Energy [kWh]	Predicted Energy [kWh]	Error [%]
Trip 1	16.2	3.89	3.68	-5.3
Trip 2	6.8	1.54	1.41	-8.6
Trip 3	29.7	9.17	9.98	8.9
Trip 4	33.9	10.90	11.30	4.3
Trip 5	1.7	0.34	0.38	12.0

lands during relatively low-wind conditions of $|\vec{v}_W| \leq 3\,\mathrm{m/s}$, the model should still be validated for more extreme situations.

Analysis of the predicted trips also shows that traffic can have a significant influence on the forward velocity profile and consequently on the energy consumption. Because at the time of writing, no free up-to-date traffic data was available, this effect is not included in the tool. Nevertheless, including information related to the traffic flow would probably increase the accuracy of the forward velocity profile and thus the energy consumption prediction.

Furthermore, the energy consumption prediction depends on several tunable parameters, such as f_w, λ_c and the chosen acceleration limits that capture the driver behavior. These are typically tuned based on measured data from an arbitrary route. Therefore, some vehicle data and knowledge related to the driver behavior will always be beneficial to get a good prediction accuracy for future trips.

2.5   Conclusions

The microscopic energy consumption prediction tool can be used for any predetermined route and shows a fair correspondence with the available measurements. For most of the analysed trips the deviation between predicted and measured energy consumption stays below 10%.

During development of the tool, it was concluded that the most accurate results are obtained by only partially taking the wind velocity into account and that filtering the STRM elevation profile is important. Validation of the tool with more extreme slope and weather conditions is considered future work. However, decent extrapolability is expected, based on the usage of a physical model and up-to-date map data. The full MATLAB-code for the tool, including connection to the aforementioned APIs is freely available in [56].

2.6 Supplementary discussion

This chapter demonstrates the application of a physics-based energy consumption prediction method on an electric delivery van. The method is derived from [33, 55], where it is applied to an electric passenger vehicle. In a comparison of 30 trips with this passenger vehicle, the physics-based method is demonstrated to have an offline energy consumption prediction error that is generally less than 10% [55, Figure 23].

With respect to this previous study, this chapter adopts a more complex aerodynamics model, with a relative wind velocity defined by (2.9) and an aerodynamic drag coefficient that varies as a function of apparent wind direction as defined in (2.5). In [55], the OpenStreetMap road-type information is applied to scale the rolling resistance coefficient. In this chapter, a pragmatic approach is followed, where the rolling resistance is assumed to be correlated with the legislated speed according to Table 2.1. This has the advantage that no road-type information is required. The rolling resistance depends on several factors, including the roughness of the road. This effect is discussed in detail in Chapter 4, revealing that the energy losses in the suspension depend on road roughness. Because road roughness information can be challenging to obtain, a method is presented in Chapter 5 to estimate the position-dependent rolling resistance from powertrain measurement data.

Both in [55], and in Section 2.2.4 of this chapter, the influence of corners on the forward velocity profile acknowledged. However, the lateral vehicle dynamics are not considered in detail. An analysis is presented in Chapter 3, where additional resistance forces during cornering are quantified. These forces can be added to the resistance forces in (2.1) to arrive at a model that better represents the position-dependent cornering losses.

The forward velocity profile prediction, as discussed in Section 2.2.4 is extended to an online algorithm in Chapter 6. The prediction is updated online by considering the current vehicle position and speed. Secondly, as also indicated by [55], model accuracy can be improved by adapting the predicted forward velocity profile to a specific driver. Therefore, in Chapter 6 a method is proposed to adapt the modeled accelerations $a_{x,lim}(v)$ in (2.11) to past acceleration data from a specific driver.

A note on battery modeling

The energy consumption prediction model presented in this chapter focuses specifically on the battery-to-wheel energy consumption of the vehicle. The results of the simulations are therefore represented as discharged and regenerated energy without making any explicit statements on battery efficiency. In case range prediction of a vehicle is desired, a battery model will be required to compute the remaining energy onboard and include losses occurring in the battery. These aspects are con-

sidered in the original model of [33], where an empirical equivalent circuit model is employed. However, detailed battery modeling is considered beyond the scope of this thesis.

2.6.1 Battery electric bus specifics

While this chapter's physics-based energy consumption model is demonstrated on an electric delivery van, different vehicles can be simulated by adapting the vehicle parameters $m_{eff}, m, f_r, C_d, A_f, P_{loss}$, and P_{aux} accordingly. By focussing on the use-case of the electric delivery van, this chapter highlights the general applicability of the model. Appendix B illustrates how a more basic version the model can be applied to a battery electric bus and provides details on the empirical powertrain losses map and determining the rolling-resistance values. Depending on the purpose and the required accuracy of the model, several further additions can be considered when aiming to predict the energy consumption of a battery electric bus. One major addition is the modeling of the auxiliary components, which is discussed in brief below.

Auxiliary components[1]

One main difference between the vehicle discussed in this chapter and an electric city bus is that the average forward velocity of the latter is relatively low. Consequently, the non-traction systems, i.e., the auxiliaries, play a significant role in the energy consumption of city buses [38, 68, 69]. Additional to an extensive Heating, Ventilation, and Air Conditioning (HVAC) system, other auxiliary systems are present on a bus that would typically not be present on a passenger vehicle or mid-size delivery van. These auxiliaries include a pneumatic system that supplies air to the pneumatic brakes and air suspension, a hydraulic system that provides power steering, and a 24 V low-voltage system that powers the lights and the public-transport electronics, such as information signs and ticket machines. All these systems draw power from the main battery via a set of power inverters, as visualized in Figure 2.14. These inverters convert the battery's High-Voltage (HV) direct-current power to HV alternating-current power or low-voltage direct-current for the respective auxiliary system. A traction-cooling system is present to cool these auxiliary inverters, the pneumatic air-compressor, and the components of the powertrain, which is also indicated in the figure.

    An overview of the energy consumption shares of these BEB subsystems is given in Figure 2.15. It can be observed that, for this particular case, the powertrain is the primary energy consumer, consuming 81% of the vehicle's energy, and the HVAC subsystem is the second-largest consumer, at 14%. These numbers are obtained under favorable weather conditions. In case of lower or higher ambient

---

[1]The results in this section are based on:
L. Trimbach, "Modeling of an Electric City Bus for Energy Consumption Estimation," M.S. thesis DC 2021.035 (Confidential), Eindhoven Univ. of Tech., Eindhoven, May 2021.
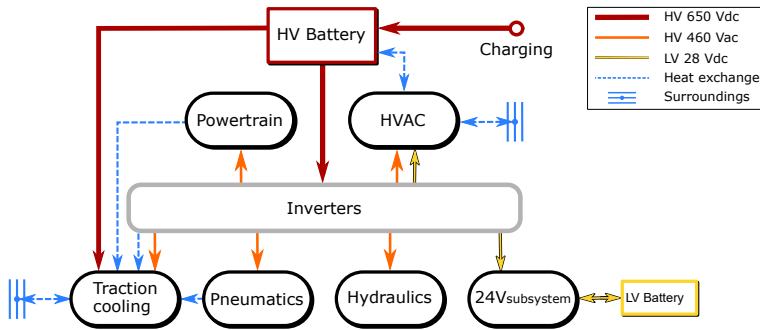
Figure 2.14. Schematic view of the energy flow between the main auxiliary components of a BEB[1].

temperatures or lower average forward velocities, the share of energy consumed by the HVAC system can be two or three times larger [70]. City bus HVAC systems can consume large amounts of energy because significantly more cabin space needs to be climatized compared to passenger cars. Additionally, the doors open and close regularly, losing precious warm or cool air to the ambient environment. The remaining auxiliary subsystems in the figure also account for a part of the total energy consumption, with the pneumatics and traction cooling accounting for the majority of the remaining 5%. It should be noted that Figure 2.15 represents an exemplary situation and that these ratios can change depending on driving cycle and environmental conditions.

Some research has been done regarding complete vehicle modeling for energy consumption estimation of BEBs, including modeling of the auxiliary components. In [34], the auxiliaries are modeled in detail, additional to the battery and the powertrain. Similar to the physics-based method described in this chapter, the powertrain model includes the longitudinal dynamics and an efficiency map of the traction motor. The cabin thermal behavior is modeled, considering the passenger heat and the effect of opening doors. The heat pump is modeled in detail in [71]. Furthermore, in [34], the air ventilation is modeled, concerning the ambient air input flow. The steering pump consumption is considered decreasing as function of the vehicle speed. For the pneumatic braking system, the airflow for a certain braking torque is modeled. The resulting air tank volume is captured and controlled with an on/off strategy. The remaining auxiliaries, e.g., the doors, parking brakes, lighting, and windshield wipers, are captured by constant powers. Overall, this is a detailed energy consumption model, including the auxiliaries with a physical approach; however, the model not validated or compared to any measured data. Therefore, no assessment of its energy prediction accuracy can be made. Instead, the model is applied for sensitivity studies and battery-sizing comparisons [72]. Similar studies exist that model BEB auxiliaries in detail. One example is [73], which includes models for the HVAC, the hydraulic power steer-
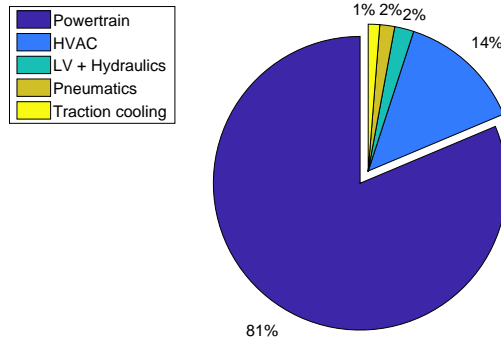
Figure 2.15. Share of the total energy consumption of a battery electric bus for each of the onboard systems. The data was gathered driving the route displayed in Figure 6.4 in Chapter 6. During this measurement, the weather conditions were dry and sunny with a light breeze at an ambient temperature of 22°C. In the test vehicle, the hydraulics are powered via low voltage (LV), and no public transport electronics are present.

ing, and the pneumatic braking of the vehicle. Here again, the model is applied to compare various auxiliary control strategies without making any statements on the model accuracy with respect to measurements. Furthermore, in [70] a physics-based HVAC model is presented, taking into account the loss of climatized air due to the opening of doors. In a validation against low-frequency measurements data, the model is shown to be an improvement compared to a reference model that attributes a fixed energy consumption ratio to the auxiliaries. Regardless, it is acknowledged that high-frequency data, including passenger occupancy, is essential for improving performance.

The fact that the available literature seldomly compares its models to measured data indicates the difficulty of auxiliary modeling. While macroscopic models of the auxiliary energy consumption exist, often establishing a single dependency of P_{aux} on ambient temperature [54, 74], microscopic auxiliary models, such as described in [34, 73] require a multitude of input signals. The HVAC system alone depends on temperature, density, and humidity of the ambient air, solar irradiance, passenger occupancy, bus-stop frequency, and the control strategy of the respective HVAC system. When aiming to predict the HVAC power as function of time, the additional challenge arises to predict each of these variables. Similar difficulties exist for the pneumatic system power, which is mainly affected by the lowering of the air suspension at bus stops, and the power steering hydraulics, which depends on the number of steering actions and vehicle forward velocity. Because of the complexity of the auxiliary systems, a possible solution might be found in data-driven methodologies. Nevertheless, in this case, the challenge is shifted towards gathering a dataset that contains sufficient data over the entire range of input variables.

3

Assessing the impact of cornering losses on the energy consumption of electric city buses

Abstract - *In view of the increasing electrification of public city transport, an accurate energy consumption prediction for Battery Electric Buses (BEBs) is essential. Conventional prediction algorithms do not consider energy losses that occur during turning of the vehicle. This is especially relevant for electric city buses, which have a limited battery capacity and often drive curvy routes. In this chapter, the additional energy consumption during steering of a BEB is modeled, measured, and assessed. A nonlinear steady-state cornering model is developed to establish the additional energy losses during cornering. The model includes large steer angles, load transfer, and a Magic Formula tire model. Model results show that both cornering resistance and tire scrub of the rear tires cause additional energy losses during cornering, depending on the corner radius and vehicle speed. The energy consumption model is validated with full scale vehicle tests and shows an average deviation of 0.8 kW compared to the measurements. Analysis of recorded real-world bus routes reveals that on average these effects constitute 3.1% of the total powertrain energy. The effect is even more significant for routes crossing city centers, reaching values up to 5.8%. In these cases, cornering losses can be significant and should not be neglected in an accurate energy consumption prediction.*

A supplementary discussion is provided in Section 3.7.

3.1   Introduction

I N the recent transition towards electric mobility, Battery Electric Buses (BEBs) are one of the first public transport solutions deployed on a large scale in many city centers [11, 75]. BEBs offer the advantage of zero local emissions and a possibility for a reduced total cost of ownership, due to the relatively low operational expenses [76].

Even though the electric drives of BEBs are more energy efficient than the internal combustion engines of conventional vehicles, the available energy stored in the vehicle is rather limited. This is mainly a consequence of the energy density of batteries still being low compared to fossil fuels [77]. Also, there is often little space available for batteries, as using maximum space for passengers still has priority. As a result, most current BEBs have a limited driving range. Moreover, the driving range can vary depending on several environmental and vehicle conditions, such as usage of vehicle auxiliaries, vehicle mass, and road conditions [78]. Practise shows that these effects result in conservative time table scheduling and use of redundant vehicles, and consequently in an increased total cost of ownership.

To migitate the problems posed by the limited and uncertain driving range of BEBs, energy consumption prediction methods are discussed extensively in literature. The proposed models can be subdivided into physics-based methods [33, 35, 79] and data-driven methods [80, 81]. Most models consider a multitude of dependent variables, ranging from road slope and road roughness, to losses of individual powertrain components, and detailed weather information. However, a common assumption in most of these methods is that the vehicle is driving in a straight line, i.e., only the longitudinal vehicle dynamics are accounted for. This is not necessarily true, especially when city buses are considered. The city routes contain many corners, which potentially cause additional tire wear and energy losses. The goal of this chapter is to model, measure, and assess the energy losses that occur in the tires when cornering a BEB.

3.1.1   State-of-the-art

There are some energy consumption prediction studies that consider the influence of corners. For example Ojeda, Chasse, and Goussault [82], who successfully identified the curves and roundabouts along a route and included these in the speed profile generation for heavy-duty trucks. However, the vehicle dynamic model that is used to predict energy consumption neglects the effects of tire slip.

Early research indicates that additional energy losses occur in the tires of road vehicles during cornering. This was modeled by Hales [83] and later experimentally confirmed by Gyenes, Williams, and Simmons [84]. Both studies focus on heavy-duty articulated vehicles and recognize that lateral tire forces result in additional resistance during cornering, which in later research is referred to as *cornering resistance*. Gyenes, Williams, and Simmons [84] estimate that a maximum of 3%

of the total fuel consumption of long haul articulated freight trucks can be ascribed to this effect.

There are several studies that recognize the relevance of cornering losses, and aim to minimize these through the development of vehicle dynamic models and application of control. An exemplary study is [85], where a linear bicycle model is used to find an expression the for the total power required to corner a vehicle. The validated model is used to develop a control strategy that minimizes the cornering resistance by yaw moment control. Likewise, Ikezawa, Fujimoto, Kawano, Goto, Takeda, and Sato [86] use a linear bicycle model to find an explicit expression for the cornering resistance force. This resistance is included in the total energy losses, which are minimized through optimization of the speed profile under time constraints. A bicycle model with linear tire forces is also used in [87] to explore various ways to minimize the power required for cornering an over-actuated vehicle. The model is later extended to a double-track model with nonlinear tire forces to expose the potential of active camber control [88]. This model then is extended to a full six degree of freedom model, including body roll, to investigate the possible energy savings of rear axle steering and torque vectoring [89]. The extension towards more complex models enables an accurate description of the nonlinear dynamics a vehicle might experience in tight cornering situations.

There are further studies that use more complex double-track models to describe the nonlinear dynamics that occur during cornering and relate these to energy losses. Maclaurin [90] analyses the steering characteristics of a heavy-duty six wheeled military vehicle. The author uses a steady-state double-track cornering model of the vehicle to compare different steering geometries, also taking energy consumption into account. In [91], a double-track model with load transfer is used for the development of a computationally-efficient control strategy to minimize cornering resistance. Lastly, in [92], an energy efficient torque vectoring control strategy is developed, also taking into account the energy efficiency of the individual electric motors. The cornering resistance is calculated using the IPG Carmaker model. This model is detailed more extensively in [93] and includes several nonlinear effects, such as large angle assumptions and weight transfer.

This brief survey reveals that the energy losses in the tires due to cornering are acknowledged in literature. Models of varying complexity are used to describe these effects. Even though some models manage to describe the elaborate nonlinear dynamics involved in a cornering a road vehicle, many studies still use linear models without load transfer. Moreover, only few of the described studies validate the energy consumption predicted by the models. While the models are mostly used to minimize the energy consumption through control, only little effort is focussed on the impact of these losses on the total energy consumption. The contribution of the cornering losses has not yet been compared to the total energy consumption in a range prediction context. Finally, little of the cornering related research is focussed on city buses, which drive curvy routes, often have double mounted tires, and have a high center of gravity.

3.1.2   Contribution

This chapter assesses the impact of the energy losses experienced by battery electric buses during cornering. Hereto, a nonlinear double-track steady-state cornering model is used. The model includes double tires on the rear axle to resemble the lay-out of a two-axle, 12 meter city bus without articulation. Furthermore, it includes relevant dynamic effects, such as nonlinear tire forces, longitudinal and lateral load transfer, and large steer angles. Two effects that contribute to the energy consumption are considered: *cornering resistance* and *tire scrub*.

Novelty of this work can be found in the fact that the model is validated on an energy consumption level by comparing it to the results of full-scale steady-state cornering tests. The energy-level validation and the inclusion of load transfer effects, make the model suitable to assess the cornering losses for electric city buses. Additionally, 62 hours of recorded real-world vehicle data from multiple routes are used to establish the relative impact of the cornering losses on the measured total energy consumption of the vehicles.

The outline of this chapter is as follows. In Section 3.2, the nonlinear double-track steady-state cornering model of a BEB is presented. The model is used to calculate the cornering losses for a typical BEB. Next, in Section 3.3, the model is validated with results from experiments. In Section 3.4, the validated model is applied to a set of recorded real-world electric bus routes to establish the significance of cornering losses. A discussion of the results is provided in Section 3.5 and the conclusions are given in Section 3.6.

3.2   Nonlinear double-track steady-state cornering model

A vehicle dynamic double-track model is developed with the goal of accurately identifying the tire forces and resulting energy loses during cornering of a BEB. The model is presented first in [94] and is recapped here to make this work self-contained. Throughout the model description, a multibody dynamics approach is used to easily add additional tires to a standard double-track model, thereby simulating double tires on the rear axle. Furthermore, the model includes longitudinal and lateral load transfer caused by the elevated center of the gravity of the vehicle. Angles are assumed to be large and the tire forces are represented by Pacejka's Magic Formula [95]. As a consequence, the four equations of motion resulting from the model are highly nonlinear. Therefore, a steady-state solution is found using Newton iterations. The complete code for the model presented in this section is publicly available in [96]. Data related to the experimental validation in Section 3.3 and to the route analysis in Section 3.4 are not included, because these are subject to a confidentiality agreement.

A schematic top view of a BEB is displayed in Figure 3.1. The figure shows
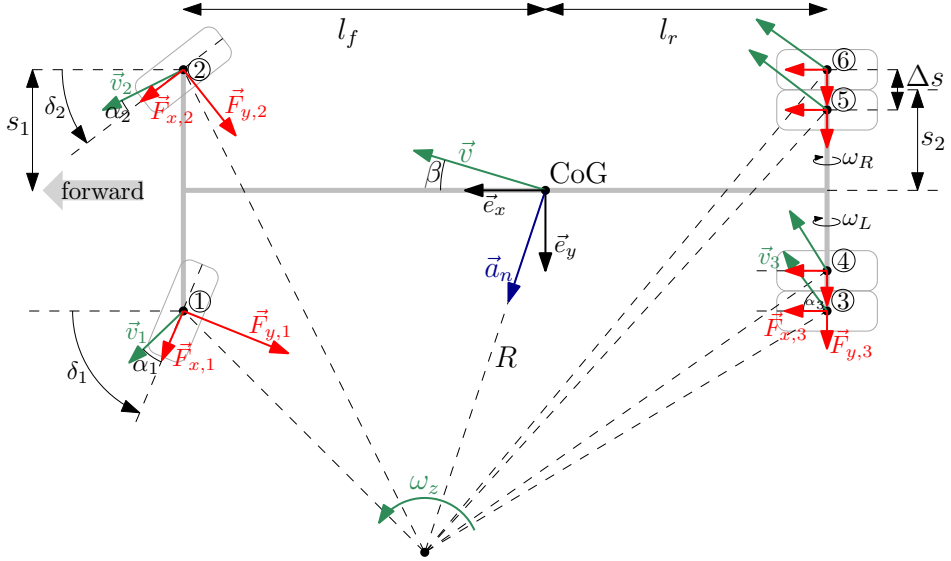
Figure 3.1. Schematic view of the steady-state cornering model. The tire locations are defined by the dimensions l_f, l_r, s_1, s_2, and Δs. The positive definitions of the velocity vector $\vec{v}_i$, the longitudinal force $\vec{F}_{x,i}$, the lateral force $\vec{F}_{y,i}$, and the side-slip angle α_i are indicated for each of the six tires ($i = 1, ..., 6$). In the CoG, a vehicle fixed axis system ($\vec{e}_x, \vec{e}_y$) is located. The normal acceleration vector is indicated with $\vec{a}_n$.

relevant dimensions, individual tire velocity vectors, and tire force vectors. The tires at each side of the rear axle are assumed to have the same angular speed, i.e., tires 3 and 4 rotate at a speed ω_L and tires 5 and 6 at a speed ω_R. The figure depicts a steady-state cornering situation. This implies that both the vehicle speed $v = |\vec{v}|$ and the cornering radius R are constant. The vehicle's left and right front wheels are steered and have individual steer angles δ_1 and δ_2 respectively, which are also constant. An average steer angle is defined as $\delta = \frac{1}{2}(\delta_1 + \delta_2)$. Furthermore, the vehicle has a constant yaw-rate ω_z, a constant vehicle side-slip angle β, and a constant lateral acceleration $a_n = |\vec{a}_n|$. The degrees of freedom of the model are defined as $\underline{s} = [\delta, \beta, \omega_L, \omega_R]^T$. The goal of the model is to find a quasi-static solution for a given forward speed v and corner radius R.

3.2.1 Kinematics

The calculation of the equations of motion starts by defining the velocity components of the center of gravity (CoG) as

$$v_x = v \cos(\beta) \qquad v_y = -v \sin(\beta) \qquad \omega_z = \frac{v}{R}, \tag{3.1}$$

where v_x and v_y are respectively the longitudinal and lateral CoG velocity. According to the used multibody dynamics approach, the velocity coordinates are stored in a column $\underline{v}$ such that

$$\vec{v} = \underline{v}^T\, \underline{\vec{e}} = \begin{bmatrix} v_x & v_y & 0 \end{bmatrix} \begin{bmatrix} \vec{e}_x \\ \vec{e}_y \\ \vec{e}_z \end{bmatrix} \,, \tag{3.2}$$

where $\underline{\vec{e}}$ represents the column of unit vectors that describe a vehicle-fixed axis system with its origin in the CoG. The same notation is used to define the position of each of the six tires with respect to the CoG as

$$\vec{p}_i = \underline{p}_i^T \underline{\vec{e}} \qquad i = 1, 2, ..., 6 \,, \tag{3.3}$$

where $\underline{p}_i$ is the column containing the position coordinates of tire i. These coordinates depend solely on the vehicle dimensions l_f, l_r, s_1, s_2, and Δs. Here, l_f and l_r are the distances between the vehicle CoG and the front and rear axle respectively, and s_1, s_2, and Δs define the track widths as indicated in Figure 3.1.

The local tire velocity vectors can be expressed in each tire-fixed axis system respectively, according to

$$\underline{v}_i = \underline{A}(\delta_i) \left(\underline{v} + \begin{bmatrix} 0 \\ 0 \\ \omega_z \end{bmatrix} \times \underline{p}_i \right) \quad i = 1, 2, ..., 6 \,, \tag{3.4}$$

where

$$\underline{A}(\delta_i) = \begin{bmatrix} \cos(\delta_i) & \sin(\delta_i) & 0 \\ -\sin(\delta_i) & \cos(\delta_i) & 0 \\ 0 & 0 & 1 \end{bmatrix} \tag{3.5}$$

denotes the direction cosine matrix that rotates the velocity vector from the vehicle-fixed frame to the tire-fixed frame as function of the steer angle δ_i. The front wheel steer angles δ_1 and δ_2 are assumed to be related through the Ackermann steering relation [97, p. 924],

$$\delta_1 = \tan^{-1}\left(l \left(\frac{l}{\tan\delta} - s_1 \right)^{-1} \right) \quad \text{and} \quad \delta_2 = \tan^{-1}\left(l \left(\frac{l}{\tan\delta} + s_1 \right)^{-1} \right) \tag{3.6}$$

with $l = l_f + l_r$ the wheelbase of the vehicle. Because the rear wheels are not steered, the direction cosine matrices corresponding to these wheels are $\underline{A}(\delta_3) = \underline{A}(\delta_4) = \underline{A}(\delta_5) = \underline{A}(\delta_6) = \underline{I}$, where $\underline{I}$ is the 3×3 unity matrix.

The coordinates of the local velocity vector with respect to the tire-fixed axis system are contained in the column $\underline{v}_i$. The first and second component of this column are denoted as $v_{x,i}$ and $v_{y,i}$, respectively. From these velocity components, the tire side-slip angle α_i and the longitudinal slip ratio κ_i can be determined;

$$\alpha_i = \tan^{-1}\left(\frac{-v_{y,i}}{|v_{x,i}|} \right) \quad \text{and} \quad \kappa_i = -\frac{v_{x,i} - r_{e,i}\omega_i}{|v_{x,i}|} \qquad i = 1, 2, ..., 6 \,. \tag{3.7}$$

3.2. Nonlinear double-track steady-state cornering model

In these calculations, the effective tire radius $r_{e,i}$ is considered to be linearly dependent on the vertical force $F_{z,i}$ acting on the tire. Furthermore, longitudinal slip of the front tires, which are not driven, is neglected.

3.2.2 Dynamics

In order to include load transfer both in longitudinal and lateral direction, the CoG accelerations in these directions are expressed respectively as

$$a_x = \sin(\beta)\frac{v^2}{R} \qquad a_y = \cos(\beta)\frac{v^2}{R} \; . \tag{3.8}$$

Next, the pitch moment M_{pitch} and roll moment M_{roll} are defined:

$$M_{pitch} = -h\,a_x\,m \qquad M_{roll} = h\,a_y\,m \tag{3.9}$$

with h the CoG height and the m the total vehicle mass. A positive pitch moment M_{pitch} redistributes part of the total vertical force from the rear axle to the front axle. This difference in vertical force is indicated by

$$\Delta F_{z,pitch} = \frac{M_{pitch}}{l_f + l_r} \; . \tag{3.10}$$

Similarly, a roll moment results in a difference in the total vertical force between the left and right track of the model. The roll moment distribution k_{dist} determines the distribution of this moment between the front and rear axle. The difference in vertical force between the left and right track is therefore described by

$$\Delta F_{z,front} = k_{dist}\frac{M_{roll}}{2s_1} \qquad \Delta F_{z,rear} = (1 - k_{dist})\frac{M_{roll}}{2s_2} \; . \tag{3.11}$$

The total vertical force on each of the tires is a result of the static vertical force plus the effects of the two types of load transfer, resulting in

$$F_{z,1} = \frac{l_r}{2l}m\,g - \Delta F_{z,front} + \frac{1}{2}\Delta F_{z,pitch} \tag{3.12a}$$

$$F_{z,2} = \frac{l_r}{2l}m\,g + \Delta F_{z,front} + \frac{1}{2}\Delta F_{z,pitch} \tag{3.12b}$$

$$F_{z,3} = F_{z,4} = \frac{l_f}{4l}m\,g - \frac{1}{2}\Delta F_{z,rear} - \frac{1}{4}\Delta F_{z,pitch} \tag{3.12c}$$

$$F_{z,5} = F_{z,6} = \frac{l_f}{4l}m\,g + \frac{1}{2}\Delta F_{z,rear} - \frac{1}{4}\Delta F_{z,pitch} \tag{3.12d}$$

with g the gravitational acceleration. As can be seen from (3.12c) and (3.12d) it is assumed that the vertical load is equal for two tires that are double mounted, e.g. $F_{z,3} = F_{z,4}$.

To model the tires, a simplified version of Pacejka's Magic Formula [95, p. 7] is used. The Magic Formula is an established tire model that accurately captures the nonlinear tire behaviour that occurs while taking sharp corners. The input parameters required for this tire model are included in the code [96] and describe typical bus or truck tires. The tire model expresses the longitudinal and lateral tire force, $F_{x,i}$ and $F_{y,i}$ respectively, as function of the slip conditions κ_i and α_i and the vertical tire force $F_{z,i}$:

$$F_{x,i} = f_{MF,x}(\kappa_i, F_{z,i}) + f_{mon,x}(\kappa) \quad \text{and} \quad F_{y,i} = f_{MF,y}(\alpha_i, F_{z,i}) \quad i = 1, 2, ..., 6 .$$
(3.13)

The longitudinal force expression in (3.13) is slightly altered with respect to the original Magic Formula by adding $f_{mon,x}(\kappa)$. This mathematical function is used in other contexts to model mechanical freeplay [98] and is described by

$$f_{mon,x}(\kappa) = \frac{50000}{\pi} \left((\kappa + \kappa_c) \left(\tan^{-1} \left(\frac{-1}{\kappa_e} (\kappa + \kappa_c) \right) + \frac{\pi}{2} \right) + \right.$$
$$\left. (\kappa - \kappa_c) \left(\tan^{-1} \left(\frac{1}{\kappa_e} (\kappa - \kappa_c) \right) + \frac{\pi}{2} \right) \right) .$$
(3.14)

The function is linear for large slip values ($|\kappa| \gg \kappa_c$) and approximately zero for $-\kappa_c < \kappa < \kappa_c$, where κ_c is chosen 0.6 and the smoothness is determined by $\kappa_e = 0.02$. This addition is made to ensure monotonicity of the longitudinal force with respect to κ and aids the performance of the used Newton scheme, which will be described in Section 3.2.3. The modified Magic Formula expression for the longitudinal force is visualised in Figure 3.2. Because the final steady-state solution of the model, also indicated in Figure 3.2, generally has low slip longitudinal values, it is not affected by the discussed modification.

Before summation, the individual tire forces are transformed back to the vehicle-fixed axis system described by $\vec{e}$;

$$\begin{bmatrix} \sum F_x \\ \sum F_y \\ \sum F_z \end{bmatrix} = \sum_{i=1}^{6} \underline{F}_i = \sum_{i=1}^{6} \underline{A}^{-1}(\delta_i) \begin{bmatrix} F_{x,i} \\ F_{y,i} \\ F_{z,i} \end{bmatrix} .$$
(3.15)

Four equations describe the steady-state solution. First of all, in accordance with the assumption of a constant yaw-rate ω_z, there is a moment equilibrium around the vertical axis:

$$\sum M_z = \sum_{i=1}^{6} \underline{p}_i \times \underline{F}_i = 0 .$$
(3.16)

Secondly, the force equilibrium should hold for both the tangential and normal direction:

$$\Sigma F_t = \qquad \cos(\beta) \, \Sigma F_x - \sin(\beta) \, \Sigma F_y = 0$$
(3.17)

$$\Sigma F_n = \qquad \sin(\beta) \, \Sigma F_x - \cos(\beta) \, \Sigma F_y = \frac{mv^2}{R} .$$
(3.18)
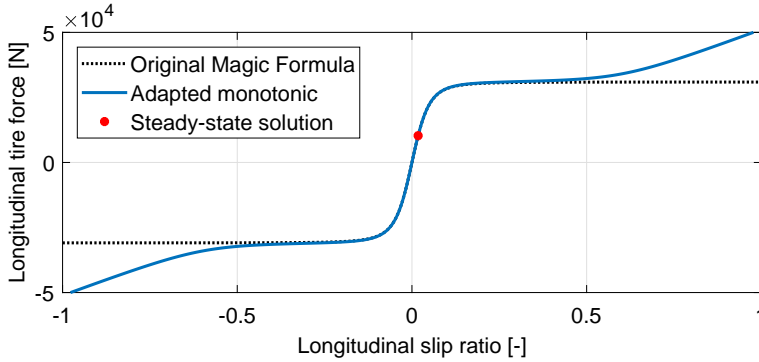
Figure 3.2. Magic Formula function describing the longitudinal tire force as function of the slip ratio. The function used in this study is adapted to be a monotonic function of the slip ratio. The steady-state solution for $v = 22.5\,\mathrm{km/h}$ and $R = 10\,\mathrm{m}$, corresponding to results of the inner right rear tire (tire 5) is also indicated.

The last equilibrium equation is a moment equilibrium between the left and right rear wheels. This results from the assumption that a mechanical differential distributes the torque produced by the powertrain evenly and without losses between the left and right wheels:

$$M_L - M_R = 0 \quad \text{with} \quad M_L = (F_{x,3}r_{e,3} + F_{x,4}r_{e,4}) \quad M_R = (F_{x,5}r_{e,5} + F_{x,6}r_{e,6}) \ . \tag{3.19}$$

3.2.3 Newton iterations

To find a solution for a given value of v and R, (3.16), (3.17), (3.18), and (3.19) are to be solved simultaneously for the degrees of freedom $\underline{s} = [\delta, \beta, \omega_L, \omega_R]^T$. In this case, unconstrained adapted Newton iterations [99] are used to find the solutions numerically. Hereto,

$$\underline{s}_{k+1} = \underline{s}_k + \gamma \left(-\underline{J}(\underline{s}_k)^{-1} \underline{\varepsilon}(\underline{s}_k) \right) \quad k = 0, 1, 2, \dots \ . \tag{3.20}$$

is evaluated repeatedly. In this equation, $\underline{\varepsilon}_k$ is the column containing the errors in the four equilibrium equations in respectively [N] and [Nm] as function of the current degrees of freedom $\underline{s}_k$. Furthermore, γ is the adapted Newton step size. The matrix $\underline{J}$ represents the Jacobian matrix of $\underline{\varepsilon}_k$ with respect to the degrees of freedom $\underline{s}_k$ and is determined numerically using the central difference approximation. The solution of the linearized single track model at low speed is used as the

Table 3.1. Typical vehicle parameters of a partially laden BEB.

Parameter	Symbol	Value
Vehicle mass (incl. passengers)	m	$15000\,\mathrm{kg}$
Wheelbase	l	$6\,\mathrm{m}$
Longitudinal CoG position	l_f	$3.5\,\mathrm{m}$
CoG height above road	h	$1.5\,\mathrm{m}$
Average track width	$2s_1 = 2s_2 + \Delta s$	$2\,\mathrm{m}$
Roll moment distribution	k_{dist}	$1/4$

starting point for the iterative scheme [95];

$$
\underline{s}_0 = \begin{bmatrix} \tan^{-1}(l/\sqrt{R^2 - l_r}) \\ \tan^{-1}(-l_r/\sqrt{R^2 - l_r}) \\ v/r_e \\ v/r_e \end{bmatrix} .
\tag{3.21}
$$

3.2.4 Model results for a city bus

Using this model, the tire forces and the work performed by these forces can be calculated for any realistic cornering situation defined by the vehicle speed v and corner radius R. The model is solved for an exemplary cornering situation of $v = 22.5\,\mathrm{km/h}$ and $R = 10\,\mathrm{m}$, using typical BEB parameters of a partially laden vehicle with approximately 30 passengers, as listed in Table 3.1. The velocity and force vectors of the obtained solution are shown in Figure 3.3. From the results of this particular cornering situation, it becomes evident that the side-slip angles differ for the individual tires. Also the vertical forces the tires, shown in Figure 3.4, show great variation. Both effects result in different longitudinal and lateral forces being generated by each individual tire.

The force vectors originating from the front tires are rotated with respect to the velocity direction, due to the vehicle side-slip angle and the significant steer angles. As a result, the lateral tire forces are partially directed in the rearward direction. These tangential rearward components of the lateral tire forces are often referred to as *cornering resistance*. To maintain a steady-state situation, this cornering resistance is countered by a net longitudinal force produced by the rear tires. Therefore, the cornering resistance power P_{cRes} can be calculated according to

$$
P_{cRes} = \sum_{i=3}^{6} F_{x,i} v_{x,i} \ ,
\tag{3.22}
$$

where $F_{x,i}$ and $v_{x,i}$ are the longitudinal tire force and velocity of the respective rear tires.
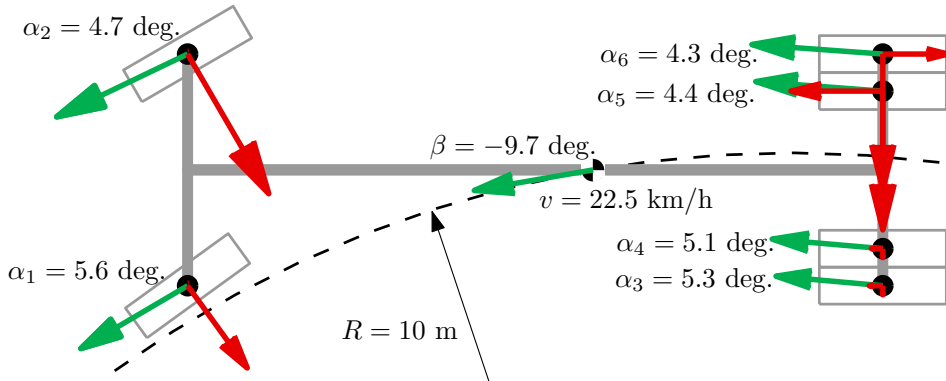
Figure 3.3. Schematic top view of the vehicle and wheels (gray) with the solution of the steady-state cornering model for the parameters $v = 22.5\,\mathrm{km/h}$ and $R = 10\,\mathrm{m}$. The dashed line indicates the path of the CoG. Velocity vectors are indicated in green and force vectors are indicated in red. The size of the arrows corresponds to the magnitude of the vectors. This figure is directly generated by the MATLAB-script provided in [96].
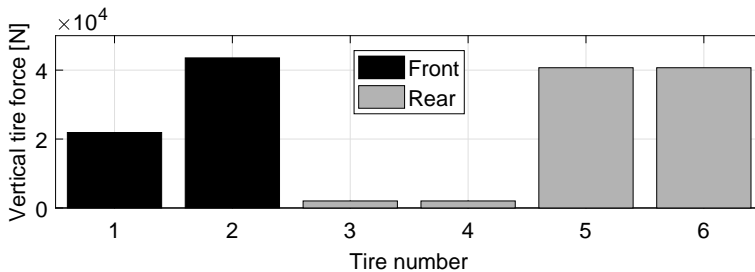
Figure 3.4. Vertical tire force of the steady-state solution for each of the six tires in case $v = 22.5\,\mathrm{km/h}$ and $R = 10\,\mathrm{m}$.

At the rear tires, additional longitudinal forces exist. Of each set of double rear wheels, the tire closest to the corner center develops a forward force, while the tire furthest from the center generates a smaller rearward force. This effect is caused by the fixed rotational speed of each set of double wheels and the fact that each wheel has a slightly different radius with respect to the corner center. This effectively results in additional *tire scrub*, which also results in additional energy losses. The power lost due to this effect can be calculated by multiplying the local slip velocity with the longitudinal tire force:

$$P_{scrub} = \sum_{i=3}^{6} F_{x,i} \left(-v_{x,i} + r_{e,i} \omega_i \right) \ . \tag{3.23}$$

Overcoming the cornering resistance force and the tire scrub losses requires additional work, which is ultimately delivered by the powertrain of the vehicle. Using the described model, the work required to overcome each of these effects is determined for varying cornering situations (v, R). Figure 3.5 shows the resulting cornering resistance power P_{cRes} and the power lost due to tire scrub P_{scrub}.

The results indicate that both effects vary as function of cornering situation, and are most profound for tight, fast corners. P_{cRes} is the more significant effect for the majority of the cornering situations and can reach values of up to $20\,\mathrm{kW}$. P_{scrub} is more relevant for low speed, small radius situations and can still exceed $1\,\mathrm{kW}$. Therefore, both effects are taken into consideration for further analysis and are together indicated as the *combined cornering losses* P_{loss}, which are equal to the total power requested from the vehicle's motor to overcome the considered losses;

$$P_{loss} = P_{cRes} + P_{scrub} = M_L \omega_L + M_R \omega_R \ . \tag{3.24}$$

3.3   Model validation

In order to verify whether the combined cornering losses predicted by the described cornering model are realistic, dedicated steady-state cornering tests have been conducted with an electric city bus. The goal of the experiment is to correlate the measured energy consumption of the vehicle during a tight cornering situation to the energy consumption as predicted by the cornering model described in Section 3.2.

3.3.1   Experimental setup

The experiment was conducted with a two-axle, $12\,\mathrm{m}$ BEB, fitted with C3 class tires of energy efficiency class D according to EU regulations [100]. Since the test was performed using a specific vehicle, the vehicle parameters of this vehicle are
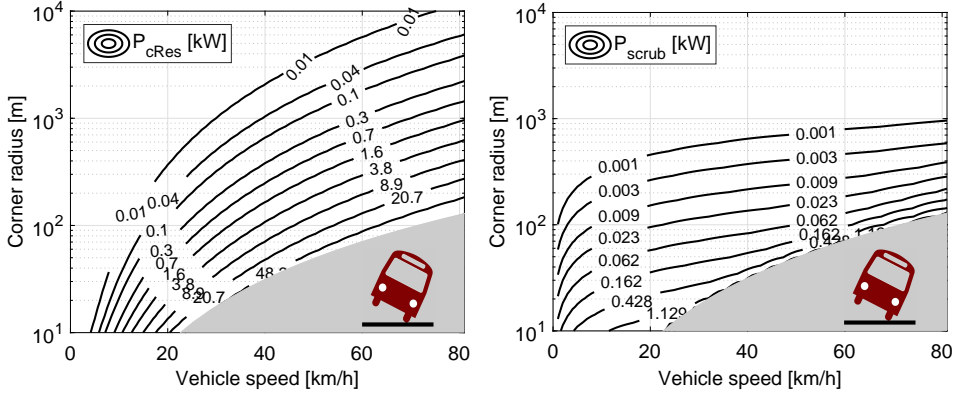
(a) Power lost due to cornering resistance   **(b)** Power lost due to rear wheel tire scrub

Figure 3.5. Resulting energy losses due to cornering resistance (**a**) and rear wheel tire scrub (**b**) for a range of vehicle speeds and corner radii. Solutions for high lateral accelerations ($a_y > 0.4g$) are not considered as the vehicle is close to roll over in this region [94].

used for the subsequent simulation results. These are slightly different from the parameters described in Table 3.1, also because the vehicles was largely unladen during the test. The vehicle was equipped with a CAN-logging device to enable the recording of several relevant sensors. Most importantly, all wheel velocities, the steering wheel angle, and the powertrain Direct Current (DC) power consumption were recorded. The test was conducted on a level piece of concrete of 80×360 m. Before start of the tests, the vehicle was driven for approximately 1 hour to reach steady-state temperatures in all powertrain components and tires.

The experiment consists of two parts. First the base power request of the powertrain of the vehicle was established by driving the vehicle in a straight line at various speeds. Secondly, the vehicle was driven in circles at the same speeds, thereby achieving steady-state cornering situations. By comparing the average power request of the powertrain between both situations, the additional power required for cornering can be determined.

3.3.2   Straight line driving results

The straight line driving power request of the vehicle is determined by driving at a constant speed in a straight line. This maneuver is conducted multiple times for velocities ranging from 5 km/h to 35 km/h, with intervals of 5 km/h. Results of such a test are displayed in Figure 3.6a. These show that during the 120 second measurement the vehicle speed ranges between 5 km/h and 7 km/h and is not exactly constant. This is mainly due to the absence of a cruise control on the test
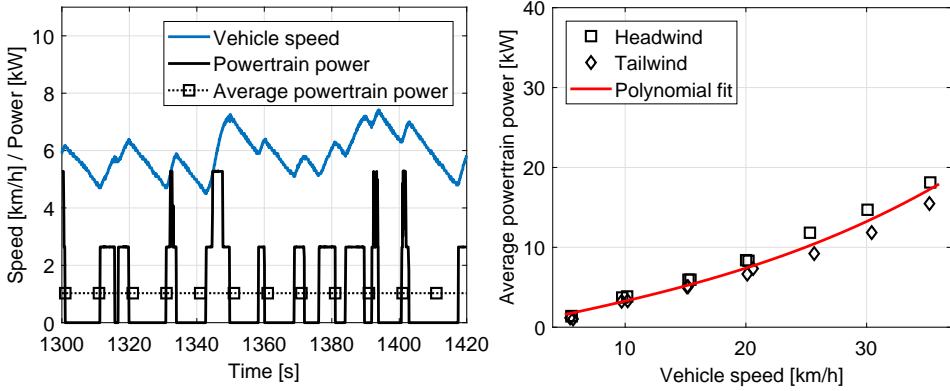
(a) Powertrain power and vehicle speed during straight line driving.

(b) Average powertrain power as function of speed.

Figure 3.6. Measured powertrain power and vehicle speed as function of time (**a**) and average powertrain power as function of vehicle speed while driving in a straight line (**b**). The measurement was performed in two directions, one direction against the wind (headwind) and one direction along the wind direction (tailwind). A third order fit of the measurements is indicated in red.

vehicle and the fact that the powertrain seems to operate at discrete power levels. Therefore, average values for both speed and powertrain power are obtained by averaging over a 120 second time interval. The same procedure is repeated for multiple vehicle velocities. The duration of the measurement interval is limited by the length of the available driving area. Therefore, tests at higher velocities have shorter durations. The tests are conducted in two directions to average possible slope and wind effects. Due to the presence of significant wind during the test, the directions are labeled 'headwind' and 'tailwind', accordingly. The results are combined in Figure 3.6b. These results show that the power consumption increases with speed and confirm that the average power consumption is slightly higher in the headwind situation. The tests up until 20 km/h are performed twice and show good repeatability.

Also in Figure 3.6b, a polynomial fit is applied to express the average powertrain power as function of vehicle speed in the straight line driving situation. The used polynomial is of third order, with coefficients constrained to be positive, in order to represent the power due to rolling resistance (mostly $\propto v$) and aerodynamic resistance ($\propto v^3$). This fit represents the power consumption for straight line driving due to rolling resistance, aerodynamic drag, and the internal powertrain losses.

3.3.3 Cornering results

For the second part of the test, the vehicle was driven at a constant speed in circles of varying radii. The steer angle was kept constant during each measurement, thereby achieving a steady-state cornering situation. Measurements where performed both clockwise (right-hand turn) and counter-clockwise (left-hand turn) and each measurement lasted approximately 60 seconds. Again, both vehicle speed and powertrain power are averaged over each measurement interval.

As the steer angle and the vehicle speed are controlled during the experiment, the resulting corner radius has to be measured or determined otherwise. In this case, the corner radius is determined from the individual wheels speeds. The vehicle yaw-rate ω_z is calculated from the front wheel velocities by

$$\omega_z = \frac{v_2 - v_1}{2s_1 \cos(\delta)} \ , \tag{3.25}$$

where v_1 and v_2 are the velocities of the front left and right wheel, respectively. Furthermore, s_1 is half of the front track width and δ is the average front steer angle, which is derived from the measured steering wheel angle. From the yaw rate, the corner radius R is determined according to

$$R = \frac{v}{\omega_z} \ , \tag{3.26}$$

where v is the speed of the CoG, which is approximated as the unweighted average of the four individual wheel speeds. Experiments were conduced at four different radii, as displayed in Figure 3.7.

Figure 3.7 shows the measured average power request while performing the steady-state cornering maneuver (markers), as well as the straight-line driving power request determined earlier (red). It is evident that the measured power request of the vehicle during cornering is significantly higher than the straight line power request. This difference can reach values of up to 15 kW at higher velocities. Furthermore, based on the measurements there seems to be little difference between data from a left-hand turn and a right-hand turn, indicating that the vehicle is symmetric.

The experimental data of the straight line driving measurements and the results of the cornering model are combined in the black line in Figure 3.7. For the corner radii 7.5 m, 11 m, and 25.5 m the model results seem in good agreement with the measured power consumption. The model appears to predict the increased power consumption during cornering accurately, both for low velocities and for higher velocities. However, when analysing the results for the minimal corner radius, $R = 7.5$ m, the measurements at $v = 20$ km/h fall far below the predicted energy consumption. The tests performed in this situation show very high lateral accelerations (near $4\,\mathrm{m/s^2}$) and are on the edge of the cornering capabilities of the vehicle. This is also indicated by velocity peaks in the individual tire velocities, shown in Figure 3.8a. These peaks indicate a loss of traction of the outer rear

(a) Corner radius: 7.5 m.

(b) Corner radius: 11 m.

(c) Corner radius: 18 m.

(d) Corner radius: 25.5 m.
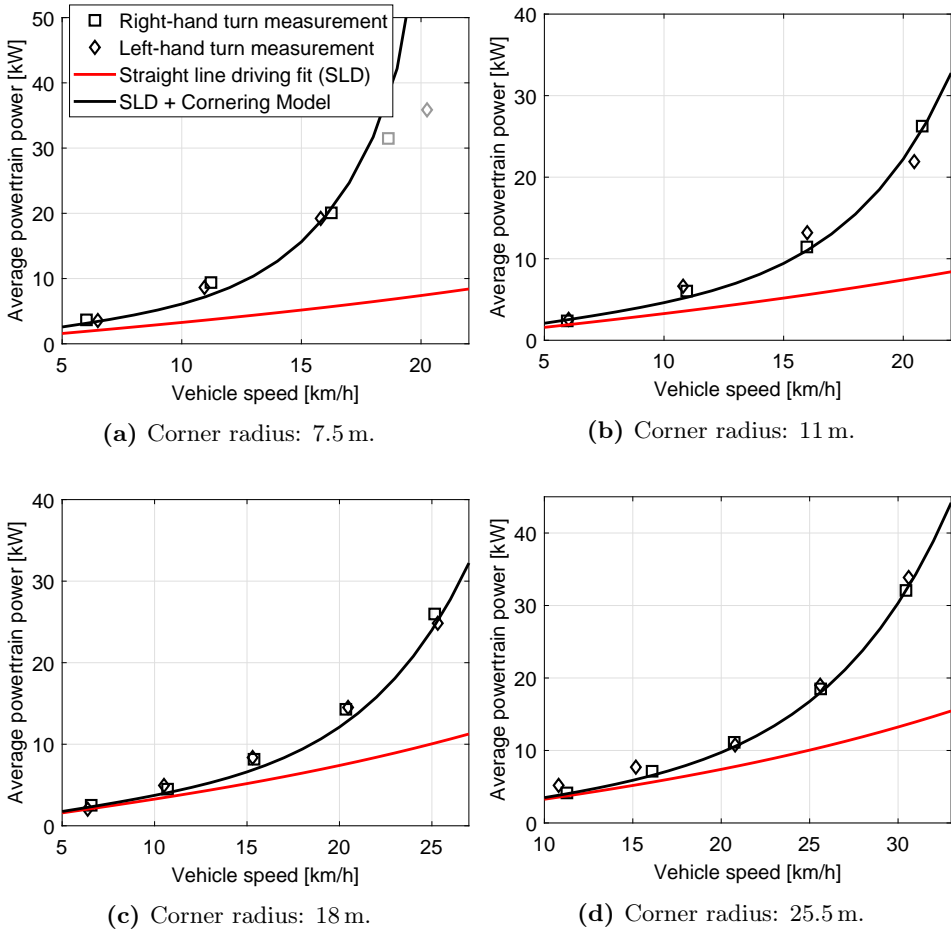
Figure 3.7. Average powertrain power as function of vehicle speed as measured during steady-state cornering. Both measurements for right-hand turns and left-hand turns are shown. The straight line driving power and the power as predicted by the cornering model are also indicated. Data of four different corner radii is shown: 7.5 m (a), 11 m (b), 18 m (c), and 25.5 m (d). Outliers are marked gray.
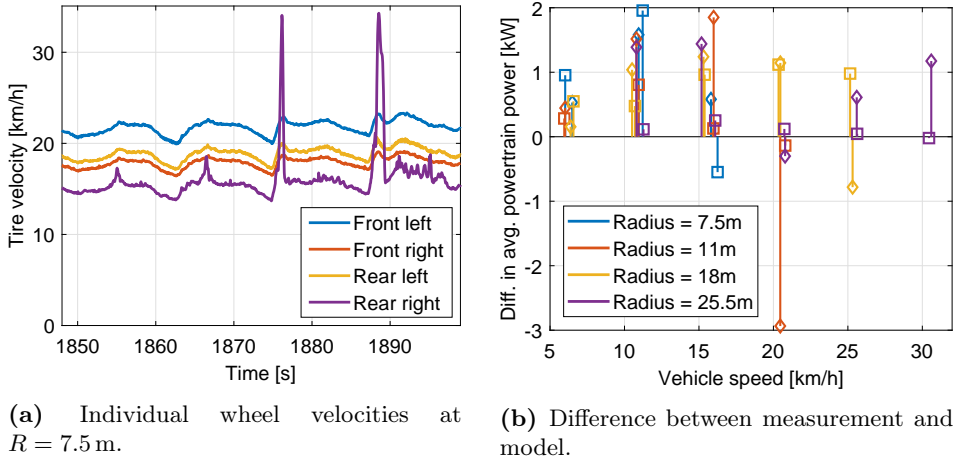
(a) Individual wheel velocities at $R = 7.5$ m.

(b) Difference between measurement and model.

Figure 3.8. Detail of the recorded wheel speeds during one of the measurements (a). Difference between measured and modeled average powertrain power request for all different corner radii and different velocities (b).

wheels and a subsequent interaction of the vehicle's electronic stability control system. Because these measurements are not steady-state, they are treated as outliers for the remainder of the analysis.

The difference between the measured and modeled power is visualised in detail in Figure 3.8b. This figure shows that generally, the model underestimates the increase of the measured power request. Only between 15 km/h and 26 km/h, the model overestimates the power request in some instances. On average, the deviation between model and measurement is 0.8 kW, which corresponds to approximately 0.5% of the maximum powertrain power of the considered vehicle. Even though the error of the model is not completely random, suggesting some structural deviation, the overall error is very small. The deviation could be caused by the fact that the tire parameters used are only estimates and are not matched to the exact tires that were used during the experiments. However, the power estimated by the model tends to be on the conservative side, resulting in slightly lower values than those that were measured.

In general, the model shows a good correlation with the measurement results for these relatively tight cornering situations, up until a radius of 25.5 m. Larger corner radii could not be tested due to the limited size of the available test area. As the model properly describes the most tight cornering situations it is assumed to be valid for larger corner radii as well.

(a) Radius calculation.

(b) Resulting curvature.
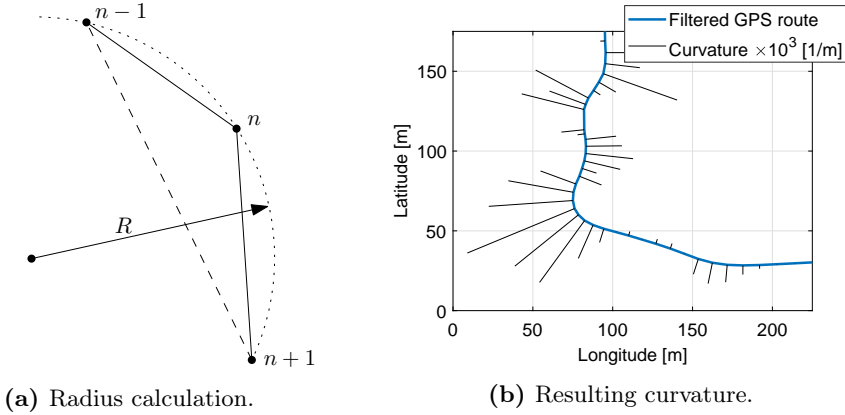
Figure 3.9. Schematic view of the corner radius calculation based on GPS-coordinates (**a**) and the resulting corner curvature (**b**), indicated by the length of the black lines.

3.4   Cornering losses on real bus routes

It has been established that the combined cornering losses are significant for fast, sharp corners. Therefore, the question remains whether a BEB encounters these type of cornering situations often during normal driving. To provide an answer, real-world bus fleet data is analysed. Four BEBs, each driving a different route on different locations were monitored for one day, thus collecting 62 hours of data. Of each vehicle, GPS position, wheel-based vehicle speed, and powertrain power consumption were measured with a sampling rate of 0.5 Hz. During the measurements, the vehicles were normally operated as part of a public transport fleet.

Because a steering wheel angle sensor is not present on the vehicles, the radius of the turns is estimated from the GPS-signal. Preprocessing of the signal is performed by removing GPS-points with little intermediate distance and by subsequently applying a Savitzky-Golay low-pass filter [101] to remove signal content with a high spatial frequency. These steps minimize the influence of GPS-sensor noise in the estimated corner radii. After preprocessing, the corner radius is calculated as the radius of circle circumscribing the triangle spanned by a GPS-coordinate n and its two neighbouring points $n - 1$ and $n + 1$, as indicated in Figure 3.9a. In Figure 3.9b, the resulting corner radius is visualized as a curvature [1/m] for a section of the analysed route. The results show that the algorithm correctly identifies corners of different curvature.

The resulting radii can be displayed as function of the vehicle speed, as shown in Figure 3.10. Additionally, the combined cornering losses P_{loss} as defined in (3.24) are included in the figure. While calculating P_{loss} as displayed here, vehicle parameters are used that exactly represent the vehicles under consideration. These

parameter values vary only slightly from the typical values mentioned in Table 3.1. The vehicles are assumed to be 50% laden. The results of four different routes are presented: a city route, a city route that also included rural driving to a nearby suburban area, a purely rural route between several small villages, and a rural route that includes a section of highway.

Overall, the results show that all kinds of corner radii can be observed, ranging from sharp corners $R \approx 10\,\mathrm{m}$ to straight line driving. When analysing the city route specifically, as displayed in Figure 3.10a, it becomes evident that the corner radius is positively correlated to the vehicle speed. Therefore, smaller corner radii of $R < 50\,\mathrm{m}$ are only reached at lower vehicle velocities $v < 30\,\mathrm{km/h}$. A similar trend is visible in Figure 3.10b, which shows the results for a city/rural route. In this case, the distribution of corner radii is wider. When analysing a rural route, as displayed in Figure 3.10c, velocities up to $80\,\mathrm{km/h}$ are reached, which is the extra-urban speed limit. Lastly, in the route containing mainly rural and highway driving, shown in Figure 3.10d, the vehicle regularly drives either roughly $50\,\mathrm{km/h}$ or its maximum speed of $80\,\mathrm{km/h}$.

In the high speed region of Figure 3.10c, a pattern becomes visible in the distribution of determined corner radii. This is a side-effect of the limited resolution of the available GPS-data and the fact that the analyzed route is largely aligned with the WGS84-coordinate grid used to describe the GPS measurements. Combined, these effects results in a erroneous discretization of the corner radii at higher velocities. As this effect only occurs at large radii, the influence on the energy consumption is considered to be small.

The total energy lost due to the described cornering effects is assessed. Hereto, the nonlinear steady-state cornering model is evaluated for each of the measured cornering situations as displayed in Figure 3.10. Integrating the resulting power gives the energy loss due to cornering resistance E_{cRes} and tire scrub E_{scrub}. This energy is compared to the measured total energy consumption of the powertrain of the vehicle E_{tot} in Table 3.2. This E_{tot} is obtained by integrating the recorded DC voltage and current from the powertrain inverter, while also taking the limited battery efficiency into account.

The comparison reveals that, in general, the scrub energy E_{scrub} is relatively small compared to the cornering resistance energy E_{cRes}. This is to be expected, as it was already observed from the model results in Figure 3.5 that the power-loss due to this effect is comparably small. Nevertheless, tire scrub constitutes approximately 9% of the combined cornering losses.

When analysing the specific trips, it becomes clear that the contribution of the cornering losses with respect to the total energy consumption depends on the type of route. Whereas the contribution of cornering losses is relatively minor for the rural/highway route, the effect is more profound in case of the city route and the city/rural route. A possible cause is found in a combination of the street layout and the local speed legislation. The rural/highway route contains many straight roads, while the average vehicle speed, and thus also the total powertrain
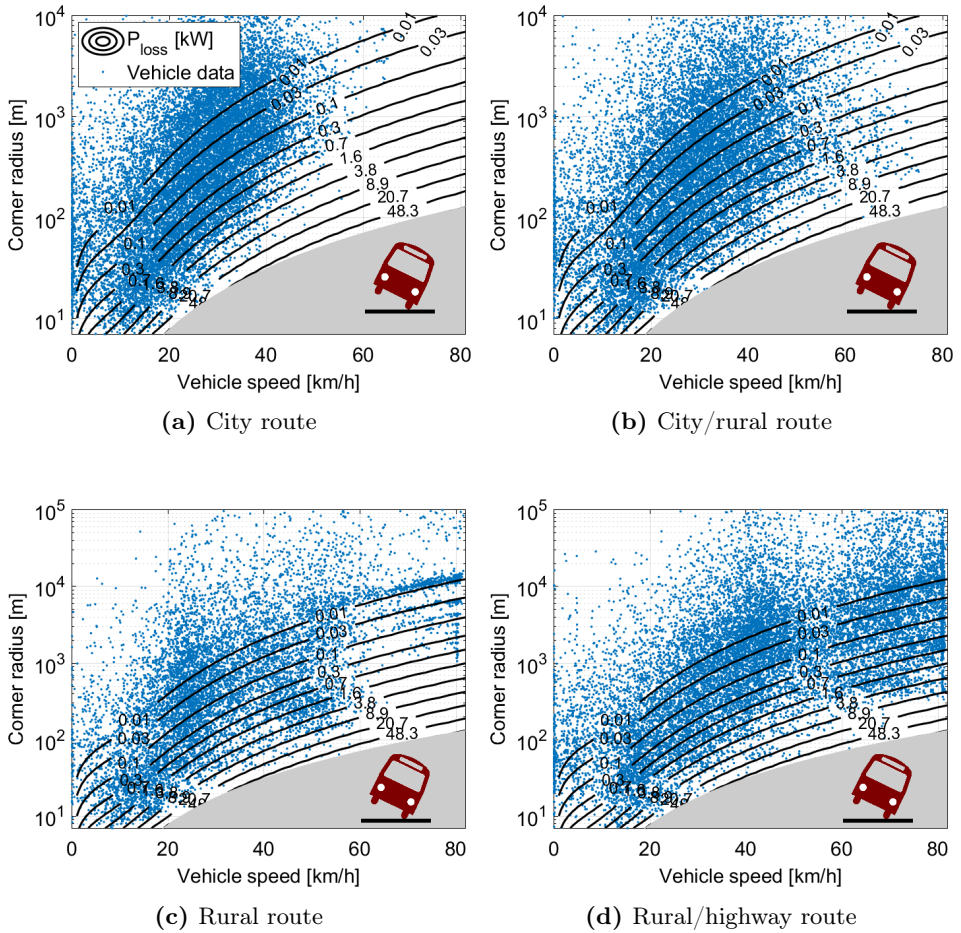
Figure 3.10. Combined cornering losses calculated by the model as function of vehicle speed and corner radius. Recorded data from electric buses operating in the field indicate the occurrence of these situations. Data of four different routes are shown: city (a), city/rural (b), rural (c), and rural/highway (d). Solutions for lateral accelerations of $a_y > 0.4g$ are not considered as the vehicle is close to roll-over in these situations.

Table 3.2. Calculated cornering resistance energy E_{cRes} and tire scrub energy E_{Scrub} with respect to the total powertrain energy E_{tot} for several electric bus routes.

Route	E_{tot} [kWh]	$\frac{E_{cRes}}{E_{tot}}$ [%]	$\frac{E_{Scrub}}{E_{tot}}$ [%]	$\frac{E_{cRes}+E_{Scrub}}{E_{tot}}$ [%]
City	139.7	2.82	0.39	3.21
City/Rural	131.9	5.32	0.43	5.75
Rural	150.5	2.11	0.18	2.29
Rural/Highway	393.2	1.25	0.07	1.32
Average	**203.8**	**2.86**	**0.27**	**3.14**

power consumption, is relatively high. This reduces the impact of cornering losses. In contrast, the city/rural route was mainly driven around a city center that contains many curved roads. Additionally, this specific route contained a high number of roundabouts, on average one every 1.8 km, increasing the influence of the considered effects. Based on the unweighted average over the four considered routes, the combined cornering losses compose more than 3% of the powertrain energy consumption.

3.5 Discussion and limitations

A nonlinear steady-state cornering model for a BEB has been developed. Although the model contains many nonlinear effects, such as individual, large steer angles, load transfer, and a Magic Formula tire model, not all possible physics are included. The current tire model does not include combined slip, turn slip, or camber. The influence of these phenomena is expected to be small, since the corner radius R is large compared to the tire width (turn slip) and the longitudinal tire forces are small (combined slip). Furthermore, the influence of camber angles on the lateral force is neglected. Also, while load transfer due to the elevated center of gravity is included in the model, body roll is not considered. Nevertheless, the validation show a close resemblance between model and measurement. Therefore, it can be concluded that the considered level of detail in the model is sufficient for the purposes considered here.

The model aims to quantify the additional forces involved when cornering the vehicle. Therefore, conventional road-load forces, such as aerodynamic drag or rolling resistance, are not considered in the model. The effect that these forces might have on the slip conditions of the tires is neglected. Consequently, the results presented here do not allow for any relations between the presented cornering losses and the rolling resistance properties of the tires. Furthermore, the energy consumption due to deceleration into the corner and acceleration out of the corner are not included in the study presented here.

Most of the vehicle parameters of the buses described in Section 3.4 are known. One exception is the loading condition of the vehicles. For city buses this can change throughout the day, or even throughout a single trip. The vehicle mass is therefore based on the assumption that the vehicles are 50% laden on average. In order to get an indication of the influence the mass variation might have the final result, the expression for the cornering resistance power derived from the linear bicycle model [85, 86] can be used;

$$
P_{cRes,lin} = \left(\left[\frac{l_r^2}{2l^2} \frac{1}{C_{F\alpha,f}} + \frac{l_f^2}{2l^2} \frac{1}{C_{F\alpha,r}} \right] m^2 a_y^2 \right) v
$$
$$
= \left[\frac{l_r^2}{2l^2} \frac{1}{C_{F\alpha,f}} + \frac{l_f^2}{2l^2} \frac{1}{C_{F\alpha,r}} \right] \frac{m^2 v^5}{R^2} \; , \quad (3.27)
$$

where $C_{F\alpha,f}$ and $C_{F\alpha,r}$ are the front and rear cornering stiffness respectively. The cornering stiffness is a tire property describing the lateral force a tire generates per unit of side-slip angle. As a first approximation, the cornering stiffness is a linear function of the normal load on the tires, and thus of the vehicle mass, i.e. $C_{F\alpha} \propto m$ [95]. Therefore, it can be concluded that the cornering resistance power, which is the most significant of the combined cornering losses, increases linearly with vehicle mass:

$$
P_{cRes} \propto m \; . \tag{3.28}
$$

Nevertheless, the used vehicle mass m is considered to be accurate enough on average. Only approximately 15% of the mass is determined by the passenger loading, and the remainder is vehicle weight, which is accurately known.

Results from a specific cornering situation show that both cornering resistance and tire scrub of the rear double tires cause additional cornering losses. The former of these effects is much more profound. Therefore, cornering losses are also significant for heavy-duty vehicles not equipped with double rear tires. Furthermore, the detailed results in Figures 3.3 and 3.4 show the variation in side slip angles and vertical tire forces between the individual tires. This emphasizes the importance of using a nonlinear double-track model to accurately simulate these tight cornering situations with a heavy-duty vehicle. If only a linear bicycle model were used, the differences in tire load, local velocity, and side-slip angle between the left and right side of the vehicle would not have been modeled in sufficient detail. Also the additional effect of tire scrub can only be studied in case the track width of the vehicle is not neglected.

Recordings from four real-world BEB routes are analysed. From recorded CAN-bus data, the corner radius could only be determined through analysis of the GPS-trace. Even though the analysis shows plausible results, some deviations are expected due to the noise and limited resolution of the considered GPS-sensor. These errors are expected to not introduce any bias and therefore still results in

a realistic corner radius distribution nonetheless. Lastly, it is assumed a realistic cornering situation can be represented by a sequence of different steady-state results generated by the model.

The final results show that the cornering effects described here account on average for 3.1% of the powertrain energy of the considered vehicle. It is also shown that the combined cornering losses can momentarily reach values of several kW's. These results seem to be in accordance with previous research by [90], who simulated vehicles of similar dimensions, and [84], who concluded that for long freight trucks the cornering losses would by bound to roughly 3% of the total energy consumption. Our results indicate that for BEBs driving in a city environment, the relative contribution of these cornering losses can even be as high as 5.8%. Considering the limited available energy of most BEBs, and electric vehicles in general, it seems that cornering losses have a significant impact on the driving range and should not be neglected. In contrast, literature shows that in many energy consumption prediction analyses cornering of the vehicle is not considered. It is likely that in these cases the cornering losses are implicitly included as part of the rolling resistance. According [35, Fig. 1], approximately 40% of the powertrain energy is ascribed to rolling resistance. Therefore, the indicated share of 3.1% cornering losses corresponds to a change in rolling resistance of approximately 7.75%.

3.6   Conclusions

In this chapter, the additional energy losses that occur due to tire slip while cornering are assessed using a nonlinear steady-state cornering model. From the model, *cornering resistance* losses and *tire scrub* losses from the rear double tires are identified, where the latter are less significant yet still relevant. The outcome of the model matches the additional power consumption as measured during full scale steady-state cornering tests and the model shows an average deviation of only $0.8\,\mathrm{kW}$, i.e., approximately 0.5% of the maximum power of the vehicle.

Using the validated model, various routes are analysed. By comparing the simulated cornering losses with the measured energy consumption of the vehicle powertrain, it is shown that the cornering losses on average constitute 3.1% of the powertrain energy consumption. The effect varies depending on route type. While cornering losses are less profound for rural or highway routes, the contribution of these losses can reach values of up to 5.8% for routes in a city environment. Considering the fact that BEBs are currently mostly deployed in city centers, it seems relevant to take the described effects into consideration in the development of accurate range prediction algorithms. Therefore, a topic of future research is the inclusion of the described effects in a physics-based energy consumption prediction model for electric city buses.

Due to the employed multibody approach in the model description, the wheel

configuration of the modeled vehicle can be changed easily. Consequently, different types of heavy-duty vehicles can be simulated by adapting the parameterized wheel locations and the vehicle parameters. Therefore, the model presented here, and for which the code is provided in [96], can be used to research the described cornering losses for different types of vehicles, such as electric semi trailer-trucks.

3.7   Supplementary discussion

This chapter presents two physical phenomena that contribute to additional energy losses during the turning of a bus: cornering resistance and rear wheel tire scrub. While the former has been acknowledged in literature since the 1980s [102], the latter effect is not often considered because it only affects heavy-duty vehicles. In summary, the results indicate that both cornering losses are the largest in high-speed, small-radius corners. Therefore, routes exhibiting these characteristics, such as city routes with faster sections, will show relatively large cornering losses, as indicated in Table 3.2. These results depend on vehicle mass. The cornering resistance scales linearly with mass, as indicated in (3.28), and the rear wheel tire scrub also increases with vertical tire force. However, because the powertrain energy consumption generally scales linearly with mass as well, the ratios mentioned in the table are approximately mass-independent.

The results in this chapter provide a clear motivation to include cornering losses in a microscopic energy consumption prediction model, especially when accurate power-request prediction as a function of time or distance is required. This can be done by including the linearized cornering resistance, as described in (3.27), as part of the conventional road-load forces, e.g., rolling resistance and aerodynamic resistance. However, this does not capture the rear-wheel-tire scrub. Additionally, knowledge is required on the vehicle's weight distribution and cornering stiffness to apply this method, and this information is not always available. Therefore, Chapter 5 of this dissertation provides a method to estimate position-dependent resistance forces from measured powertrain data. These forces implicitly include the cornering losses described here, which are a function of road curvature R and thus of the position along the route. Furthermore, the cornering resistance is shown to scale linearly with the vehicle mass, similar to the rolling resistance estimated in Chapter 5.

The vehicle described in this chapter is a 12 m unarticulated city bus. Even though these are the most occurring type, other vehicle configurations exist, such as the 18 m articulated city bus, see Figure A.1 and Table A.1 in Appendix A. These longer vehicles consist of a front body, with two axles, which connects via a revolute joint to a rear section with one axle. In theory, the nonlinear steady-state cornering model presented here can be extended to include these types of articulated vehicles. In that case, equations of motions will have to be

extended to also describe the three degrees of freedom of the rear body and the three constraint equations representing the revolute joint. Although the results of such an analysis cannot exactly be predicted, the resulting cornering losses are likely still proportional to the vehicle mass, as in (3.28). Since the powertrain energy consumption scales approximately linear with mass, the share of the energy consumption ascribed to cornering losses is likely to be similar for these 18 m vehicles.

Besides the effects described in this chapter, i.e., cornering resistance and rear wheel tire scrub, other physical phenomena can potentially influence the energy consumption during cornering. One example is the additional losses in a mechanical differential. When cornering, a difference in rotational speed arises between the left and right output shafts of the differential, causing additional movement of the smaller planet bevel gears. This effect is modeled and discussed in Appendix C. However, the results suggest that this effect is negligible compared to the other cornering losses.

4

Analysis of energy losses in suspension dampers on rough roads

Abstract - *The energy consumption of battery electric buses, and electric vehicles in general, depends to a large extent on rolling resistance. Although often aggregated into one, the energy lost due to rolling resistance can be subdivided into hysteric tire losses, vertical tire losses, and losses occurring in the shock absorbers of the vehicle suspension. In this chapter, the energy dissipated by the dampers of a battery electric bus is quantified in an energy consumption context. The analysis is based on a description of the vertical vehicle dynamics using a quarter car model with a nonlinear dashpot. The model is validated by comparing suspension deflection with a measurement on a known road surface. It is shown that 73% of the energy dissipated in the dampers occurs at road frequencies between 3 and 12 Hz. Model simulations on different simulated ISO 8608 road surfaces reveal that damper losses are in the order of 100 W on smooth roads (classes A and B), yet can reach values of 6.8 kW on rough roads (class D) at 40 km/h. A comparison with rolling resistance coefficients obtained from coast-down tests shows that the damper losses can explain the majority of the rolling resistance difference between road surfaces with a different roughness.*

4.1   Introduction

IN an effort to electrify inner-city transport, battery electric buses (BEBs) are introduced in ever more city centers around the world [12]. These vehicles offer reduced noise and local pollution without the cost and maintenance of overhead power lines. However, similar to electric passenger cars, the driving range of BEBs is smaller compared to Internal Combustion Engine (ICE) vehicles. Accurate modeling of the energy consumed by a BEB is therefore essential to maximize and predict the vehicle's driving range and reduce operational costs.

A physics-based approach to this energy consumption analysis involves modeling the individual longitudinal forces acting on the vehicle; rolling resistance, aerodynamic resistance, slope resistance, the force accelerating the vehicle, and the powertrain losses. The rolling resistance is responsible for up to 30% of the energy consumption of a BEB [35] and is often modeled as a constant coefficient multiplied by the vertical tire force. In reality, the rolling resistance is a consequence of different physical mechanisms, including hysteresis losses due to the repeated deformation of the tire tread. This effect is already studied extensively for bus and truck tires [103, 104]. This chapter focuses on the contribution of road irregularities to the rolling resistance for heavy-duty vehicles.

The relation between the power required to move a vehicle forward and suspension shock absorbers precedes the introduction of modern electric vehicles. At the beginning of the 1980s, road roughness was a topic of interest [105], and the link between fuel consumption and suspension stroking was made by various authors [102, 106, 107]. According to these sources, there are four mechanisms associated with vertical vehicle dynamics that contribute to additional energy losses:

1. Stroking of the suspension shock absorbers
2. Dynamic deflection of the visco-elastic tire, including obstacle enveloping
3. Impact between tire and road [108]
4. Micro slip associated with angular accelerations of the wheel due to a varying effective tire radius under dynamic wheel load [108] .

Since the loss of contact between tire and road is assumed to be unlikely on paved roads where BEBs drive, and the energy effects of 4. are shown to be negligible [108], only mechanisms 1. and 2. are considered in this study.

To the best of the authors' knowledge, suspension losses are studied first in [106], using a mass-spring-damper model. Later, a complete analysis of the entire tire-wheel-suspension system is presented in [102]. The latter study includes a radial spring-damper tire model and performs analyses for realistic road inputs. This model is later extended to include loss of tire-road contact and is compared to drum tests in [109]. In the 1990s, the observation that dampers dissipate energy led to the idea that active dampers could be used to harvest part of the energy that usually would be dissipated [110, 111]. Furthermore, simulation studies have

been done that employ quarter car models to quantify damper losses, but often without a comparison of the result to measurement data [112].

Most of these earlier studies employ linear quarter car models in combination with a variety of tire models. However, it is established that automotive shock absorbers have nonlinear characteristics [113, 114]. A linearized damper only achieves comparable results to nonlinear dampers for constant excitation amplitudes [115]. Therefore, when analyzing a variety of road roughnesses, a nonlinear damper model is required.

Damper losses are not always considered when discussing rolling resistance. Detailed empirical and finite element models exist that aim to model the resistance experienced by an individual rolling tire [104, 116–118]. The tire models in these studies that only concern the tire are often compared with measurements from a tire-test setup.

The rolling resistance can also be studied using empirical methods. These studies often focus on estimating the colling resistance coefficient based on data without considering the details of the physical mechanisms through which energy is dissipated. [119] and [120] are examples of empirical models for the rolling resistance of truck tires based on tire measurements. The resulting models describe a statistical relation between the rolling resistance coefficient and the road roughness, typically indicated by Mean Profile Depth (MPD) or International Roughness Index (IRI). Other studies directly relate the road roughness to fuel consumption through regression analysis [121], without considering the rolling resistance coefficient in detail.

This chapter presents a quantitative analysis of the energy dissipated in the suspension dampers due to road irregularities and evaluates the results in an energy-consumption context. The contributions of this chapter are threefold: First, a quarter car model with nonlinear suspension damper characteristic is validated by comparison to multiple vehicle tests. Secondly, to support this validation, road-profile measurements are augmented with data from a Digital Elevation Model (DEM) to arrive at an accurate road description over a wide frequency range. Lastly, using the validated nonlinear quarter car model, the energy dissipated in the dampers of a BEB is quantified for different road conditions and is compared to experimentally determined rolling resistance coefficients.

This chapter is organized as follows. In Section 4.2 a quarter car model is introduced to describe the vertical dynamics of a battery electric city bus. Model validations are provided in Section 4.3 using experimental data recorded on two different road surfaces. In Section 4.4 the validated quarter car model is used to quantify the damper losses in the suspension of a battery electric bus. The results are compared to coast-down tests conducted with a similar vehicle. Lastly, in Section 4.5 the conclusions of the work are summarized and the prospects of future work are discussed.
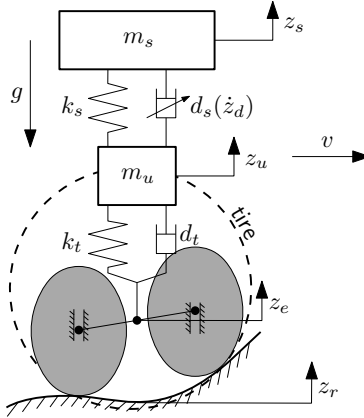
Figure 4.1. Schematic view of the quarter car model with a nonlinear shock absorber and a tandem-cam enveloping model.

4.2   Quarter car vehicle model

An often employed model in vehicle dynamics literature is the quarter car model [122, p. 194-196]. This model describes the vertical displacement of one corner of the vehicle, with sprung mass m_s and unsprung mass m_u, as visualized in Figure 4.1. Both masses are subject to the gravitational acceleration g and are interconnected by a spring with stiffness k_s and, in this case, a nonlinear damper. The unsprung mass m_u is connected to the road via the tire, which is represented by a linear spring with stiffness k_t and a linear damper with damping constant d_t. The tire-road contact is modeled using a tandem model with elliptical cams according to [123, Chapter 4]. Two cams, a longitudinal distance apart, follow the road profile z_r, thereby simulating the enveloping of small objects by the tire and generating an effective road profile z_e that is perceived by the quarter car model. The model does not include the rolling resistance due to hysteric tire losses.

The model features a nonlinear damper, where the damper force $F_d(\dot{z}_d)$ is a function of the suspension deflection rate $\dot{z}_d$, with

$$\dot{z}_d = \dot{z}_s - \dot{z}_u \ . \tag{4.1}$$

Automotive shock absorbers generally have a nonlinear characteristic, with damper forces typically being larger during extension than during compression [113, 114], as visualized in Figure 4.2. This damper characteristic is realized in a passive way using a series of internal chambers, orifices, and check valves through which hydraulic oil can flow. To describe the nonlinear damper force, a nonlinear damping coefficient is considered in the model, according to

$$F_d(\dot{z}_d) = d_s(\dot{z}_d) \cdot \dot{z}_d \ . \tag{4.2}$$
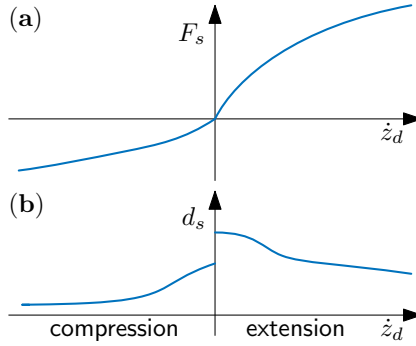
Figure 4.2. A typical force-velocity diagram of an automotive shock absorber (**a**), with corresponding nonlinear damping coefficient (**b**).

Secondly, linear tire damping d_t, although small compared to the suspension damping, is included here because it contributes to the total energy dissipated in the system.

Based on Figure 4.1, the following equations of motion can be defined for the quarter car model;

$$m_s \ddot{z}_s = -k_s (z_s - z_u) - d_s (\dot{z}_d) \cdot (\dot{z}_s - \dot{z}_u) - m_s g \ ,$$
$$m_u \ddot{z}_u = -k_t (z_u - z_e) + k_s (z_s - z_u) - d_t (\dot{z}_u - \dot{z}_e) + d_s (\dot{z}_d) \cdot (\dot{z}_s - \dot{z}_u) - m_u g \ .$$
$$(4.3)$$

These two second-order differential equations are rewritten to a system of first-order differential equations by defining the state column $x(t)$ and input column $u(t)$ according to:

$$x(t) := \begin{bmatrix} \dot{z}_s & \dot{z}_u & z_s & z_u \end{bmatrix}^\top \qquad u(t) := \begin{bmatrix} \dot{z}_e & z_e \end{bmatrix}^\top \ . \qquad (4.4)$$

In contrast to a quarter car model without tire damping, the input column includes the time derivative of the effective road height $\dot{z}_e$, which is required to calculate the tire damping force. Using the definitions in (4.4), (4.3) can be written as a first-order ordinary differential equation:

$$\dot{x}(t) = f(x(t), u(t)) \qquad (4.5)$$

with

$$f(x(t), u(t)) =$$
$$\begin{bmatrix} \frac{1}{m_s} \left(-d_s (\dot{z}_d) (x_1 - x_2) \quad + k_s \ x_4 - k_s x_3 \qquad\qquad\qquad\qquad \right) - g \\ \frac{1}{m_u} \left(\ \ d_s (\dot{z}_d) (x_1 - x_2) - (k_t + k_s)x_4 + k_s x_3 - d_t x_2 + d_t u_1 + k_t u_2 \right) - g \\ x_1 \\ x_2 \end{bmatrix} \ .$$
$$(4.6)$$
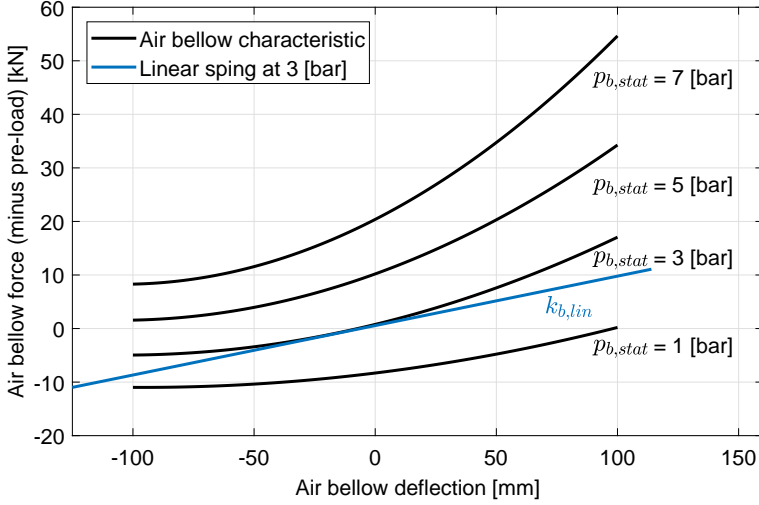
Figure 4.3. Air bellow force-displacement characteristic for different nominal pressures. A deflection of 0 mm corresponds to the nominal ride height of the vehicle. Data according to manufacturer specification.

To perform the simulations presented in this chapter, the system of equations described by (4.5) is implemented in Simulink and integrated with respect to time using an explicit numerical solver, in this case MATLAB's `ode3` [124], with a fixed time step of 1 ms. A fixed-step solver is used here because an equidistant time vector will allow easy analysis of the model outputs in the frequency domain later. At the start of every simulation, the system is assumed to be at rest. This implies that all time derivatives are zero and the initial positions represent the static deflections of suspension and tire due to gravity, with the road height z_r being equal to zero:

$$x(t=0) = \begin{bmatrix} 0 & 0 & -\frac{m_s g}{k_s} & -\frac{(m_s+m_u)g}{k_t} & -\frac{(m_s+m_u)g}{k_t} \end{bmatrix}^\top . \qquad (4.7)$$

4.2.1   Air suspension characteristics

Most modern battery electric buses are equipped with Electronically Controlled Air Suspension (ECAS), where air bellows are integrated into the suspension to support the sprung mass. The pressure in the individual bellows is controlled through a central electro-pneumatic actuator. This system enables the possibility to control the vehicle's ride height to be approximately constant under varying passenger occupancy conditions. Secondly, it allows the vehicle to 'kneel' at bus stops by lowering one side of the vehicle, or even the whole vehicle, to reduce the entry step height for boarding passengers.

The air bellow possesses a slightly progressive force-displacement characteristic, as displayed in Figure 4.3. Furthermore, the bellow force is a function of the air pressure inside the bellow. In this work, the air bellow is modeled as a quasi-linear spring with stiffness $k_{b,lin}$, which depends linearly on the static bellow pressure $p_{b,stat}$. This is visualised in the figure, where $k_{b,lin}$ is shown for a static bellow pressure of $p_{b,stat} = 3\,\mathrm{bar}$.

The static bellow pressure is determined as

$$p_{b,stat} = \frac{m_s\,g}{A_b\,n_b}\;,\tag{4.8}$$

where A_b is the horizonal cross-sectional area of one air bellow and n_b is the number of air bellows per corner of the vehicle. Typically for a bus, $n_b = 1$ at the front axle of the vehicle and $n_b = 2$ on the second- and possibly third axle. In this research, A_b is determined empirically based on static measurements where both the vehicle weight per vehicle corner and the bellow pressure have been measured.

After $k_{b,lin}$ is determined based on the bellow characteristic shown in Figure 4.3, the suspension stiffness is calculated as

$$k_s = n_b\,k_{b,lin}(p_{b,stat}(m_s))\;.\tag{4.9}$$

According to (4.9), the suspension stiffness k_s is a linear function of the sprung mass m_s. Consequently, the sprung mass resonance frequency ω_s of the system remains approximately constant under changing masses m_s:

$$\omega_s = \sqrt{\frac{k_s}{m_s}}, \quad \text{with} \quad k_s \propto m_s\;.\tag{4.10}$$

Any damping or hysteresis that the air bellow provides is assumed to be negligible compared to the damping force of the hydraulic shock absorbers.

4.3 Model validation

In this section, two experiments are discussed that compare the output of the quarter car model to measured suspension deflections. First, in Section 4.3.1 the specific vehicle used for these validation tests is described. Next, Sections 4.3.2 and 4.3.3 describe experiments where the vehicle is driven over a specific road, and the suspension deflection is compared to the quarter car simulation results.

4.3.1 Vehicle parameters

An articulated, three-axle, $18\,\mathrm{m}$ diesel bus is used for the validation experiments. Even though the vehicle has no electric powertrain, the suspension is similar to that of a battery electric bus. The second axle of the vehicle is considered. This is a non-driven, non-steered axle, with two air bellows, two shock absorbers, and two tires

Table 4.1.   Model parameter of the quarter car model that represents the vehicle used in the validation tests.

Parameter	Symbol	Value	Unit
Sprung mass (unladen)	$m_{s,unlad}$	1310	kg
Sprung mass (laden)	$m_{s,lad}$	3042	kg
Unsprung mass	m_u	600	kg
Bellow stiffness (unladen)	$k_{s,unlad}$	92000	N/m
Bellow stiffness (laden)	$k_{s,lad}$	154000	N/m
Damper force	$F_d(\dot{z}_d)$	Figure 4.4	N
Tire stiffness	k_t	$2.3 \cdot 10^6$	N/m
Tire damping	d_t	600	Ns/m

per corner of the vehicle. The axle is instrumented with potentiometers positioned parallel to each of the four shock absorbers. This allows for measurement of the shock absorber deflection z_d with an accuracy of 0.2 mm at a sampling rate of 500 Hz.

The parameters of the quarter car model simulating this vehicle are listed in Table 4.1. The damper and spring characteristics originate from the respective manufacturer information, except for the vertical tire damping, which is taken from [125]. The unsprung mass originates from component specifications of the axle and tires, and the sprung masses for both a laden and an unladen vehicle are determined by measurements. Because the air bellow stiffness depends on the sprung mass according to (4.9), this parameter is also reported for both loading conditions. Enveloping model parameters for a 245/75 R16 tire are taken from [123, Table 4.4], as these are geometrically closest to a bus tire.

The force $F_d(\dot{z}_d)$ for this axle is visualized in Figure 4.4. This is the combined force of two dampers that act in parallel. The damper characteristic shows that the damping force is approximately a factor five higher for extension than it is for compression at equal deflection rates.

4.3.2   Road bump test

In a first test, the laden vehicle is driven with a constant speed of 30 km/h over a well-defined obstacle. The road section of interest is a bump with a relatively steep increase and a more gradual decrease, as is displayed in Figure 4.5. The bump is measured and subsequently modeled using a piecewise affine road-height profile, as shown in Figure 4.6.

The results of the measurement are presented in Figure 4.7, together with the simulated deflection from the quarter car model. The instance the second axle of the vehicle encounters the bump is visible in the figure as t_1, and after this moment, the suspension is compressed 60 mm. The axle reaches the top of the
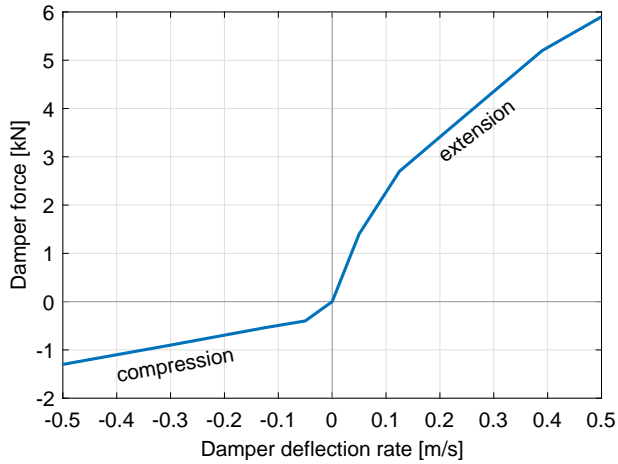
Figure 4.4. Damper force F_d versus damper deflection rate $\dot{z}_s$ for the vehicle used in the validation tests. Values represent the damping of two shock absorbers combined. Data according to manufacturer specification.

Figure 4.5. Photo of the road bump with laser sensor.

bump at t_2, after which the rebound of the suspension occurs and the dampers extend to approximately -80 mm. The results show that the quarter car model accurately simulates this initial compression and the subsequent rebound. At t_3, the third axle of the vehicle encounters the bump. After this moment, the simulation and measurement no longer coincide because the load transfer between
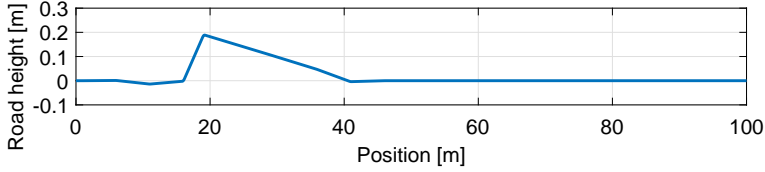
Figure 4.6. Road height z_r of the road bump as function of position x.
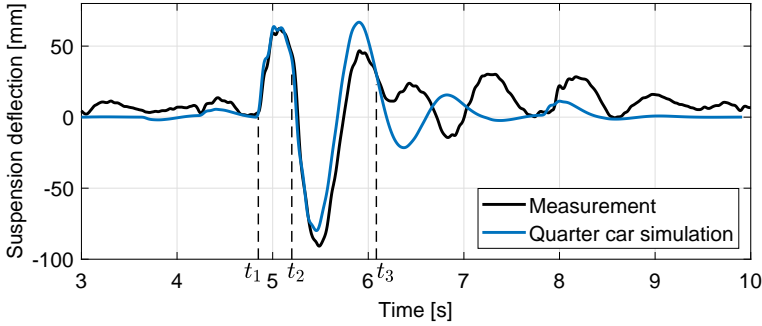
Figure 4.7. Measured and simulated suspension travel of the second axle. Time instances t_1, t_2, and t_3 respectively indicate the start of the bump, the top of the bump, and the instance the third axle encounters the start of the bump.

different axles is not included in the simulation. Nevertheless, from the data in the range $t = [t_1\ t_3]$ it can be concluded that the model matches the measurements well.

Energy decomposition

After simulating the road bump, the full state of the system $x(t)$ is known for all time instances. This information can subsequently be used to construct the system's energy balance. Firstly, the kinetic energy is calculated as

$$E_{kin}(t) = \frac{1}{2}m_s\dot{z}_s^2(t) + \frac{1}{2}m_u\dot{z}_u^2(t) \ . \tag{4.11}$$

Secondly, the potential energy of the system equals

$$E_{pot}(t) = \frac{1}{2}k_s\left(z_s(t) - z_u(t)\right)^2 + \frac{1}{2}k_t\left(z_u(t) - z_e(t)\right)^2 + m_s z_s(t)g + m_u z_u(t)g \ . \tag{4.12}$$

Lastly, the energy dissipated due to non-conservative forces acting on the system is calculated according to

$$E_{dis}(t) = E_{damp}(t) + E_{tir}(t) = \int_{t=0}^{t} F_d(\dot{z}_d(\tau))\cdot\dot{z}_d(\tau)\,\mathrm{d}\tau + \int_{t=0}^{t} d_t\left(\dot{z}_u(\tau) - \dot{z}_e(\tau)\right)^2\,\mathrm{d}\tau. \tag{4.13}$$
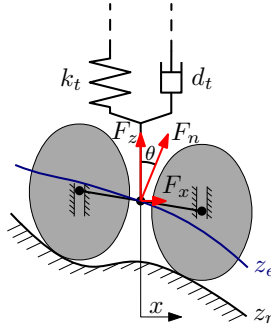
Figure 4.8. Schematic view of the tire-road contact point with the effective road profile z_e indicated in blue, and forces indicated in red.

According to conservation of energy, the sum of these energies ΣE should be equal to the work exerted on the system $W(t)$:

$$\Sigma E(t) = E_{kin}(t) + E_{pot}(t) + E_{dis}(t) = W(t) \ . \tag{4.14}$$

This work is derived by examining the tire-road contact point, as detailed in Figure 4.8. The modeled contact exerts a normal force F_n on the vehicle, which is decomposed in a vertical dynamic tire force F_z and a longitudinal force F_x. If the vehicle is moved at a constant longitudinal velocity, this force F_x exerts work on the system, which can be calculated according to:

$$W(t) = \int F_x(t)\mathrm{d}x \quad \text{with} \quad F_x(t) = F_z(t)\tan(\theta(t)) \ , \tag{4.15}$$

where $\theta(t) = -\arctan(\mathrm{d}z_e(t)/\mathrm{d}x)$ and F_z is the dynamic tire force, which can be calculated according to

$$F_z(t) = -k_t \left(z_u(t) - z_e(t)\right) - d_t \left(\dot{z}_u(t) - \dot{z}_e(t)\right) \ . \tag{4.16}$$

The potential, kinetic and dissipated energy resulting from the bump simulation are visualized in Figure 4.9. At the start of the simulation, the system is in its initial position, and the internal energy is zero. At t_1, the axle encounters the bump, resulting in an increase of the potential energy E_{pot} first and then also of the kinetic energy E_{kin}. Note that the energy dissipated in the dampers is still low at this point. Only after t_2, when the axle has reached the top of the bump and the rebound starts, most energy is dissipated. The oscillations in E_{pot} and E_{kin} disappear again, and, at the end of the simulation, both are zero. In contrast, E_{dis} is non-zero at the end, indicating that $1.8\,\mathrm{kJ}$ was dissipated in the tire and the damper. The majority of this dissipation happens during the rebound, just after t_2. Lastly, simulated values for $\Sigma E(t)$ and $\int F_x dx$ show the conservation of energy in the model.
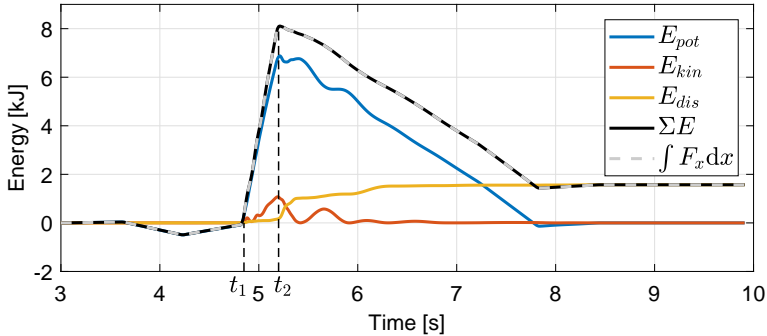
Figure 4.9. Energy decomposition of the bump simulation. Time instances t_1 and t_2 respectively indicate the start of the bump and the top of the bump.

4.3.3   Belgian blocks test

In the second test, the vehicle is driven over several strips of Belgian blocks. This specific road has been designed to represent a worst-case situation regarding the loading of the suspension and is generally used in durability tests. The measured section consists of two strips of Belgian blocks, one with a length of $306\,\mathrm{m}$ and one of $714\,\mathrm{m}$, connected by a section of smooth asphalt. These strips are traversed at a constant speed of $v = 40\,\mathrm{km/h}$ using the vehicle described in Section 4.3.1, resulting in a measurement with a duration of approximately $100\,\mathrm{s}$.

Simulated road input

To simulate a stretch of Belgian blocks, information on the road height z_r is required. Because the road considered is part of a test track, a profile of the Belgian-block section is available. The frequency content of the road height is visualized in Figure 4.10. The road classes according to ISO 8608 [126] are also indicated in the figure and show that the Belgian-block road is of class D or E for the higher frequencies. However, for frequencies below $0.1\,\mathrm{m}^{-1}$, the measurement seems to indicate class C or lower. The measurement of the road height is compared to data from a high-resolution digital elevation model [127]. This DEM has a horizontal resolution of $0.5\,\mathrm{m}$, and a vertical accuracy of approximately $10\,\mathrm{cm}$. The strips of Belgian blocks are located on the DEM and the resulting height-profile is also visualized in Figure 4.10.

Several observations can be made from Figure 4.10. First of all, for the spatial frequency range from $0.04\,\mathrm{m}^{-1}$ to $0.2\,\mathrm{m}^{-1}$, the DEM and the measured road profile coincide well, indicating that both sources of information are in agreement. For spatial frequencies larger than $1/\lambda_2 = 0.2\,\mathrm{m}^{-1}$, the DEM seems to deviate from the measured road profile. The likely cause is that the road profile oscillations are nearing the accuracy limit of the DEM. Lastly, for frequencies below $1/\lambda_1 = 0.04\,\mathrm{m}^{-1}$,
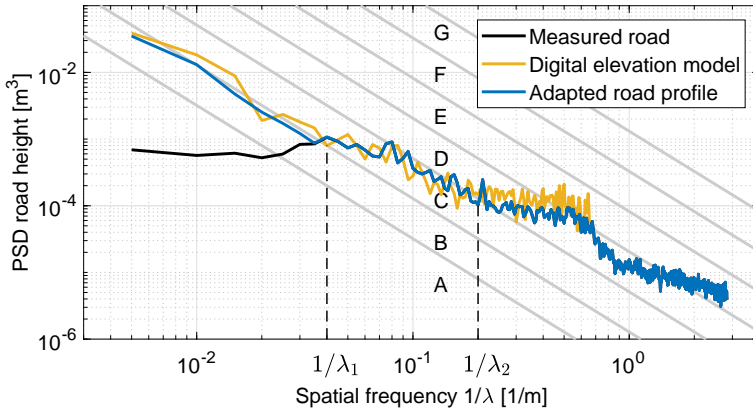
Figure 4.10. Power spectral density of the Belgian blocks, based on measurements, based the elevation model, and the resulting adapted road profile. Road classes according to ISO 8608 are indicated as well.

the DEM indicates that the road is of class B or C, whereas the measurement predicts barely any low-frequency oscillations. In this lower frequency range, the DEM is likely to be the more trustworthy source of information, as the measured road profile may have been filtered.

The measured road profile is adapted to construct a road input that is realistic over the entire frequency range. A synthetic random-road profile of road class B is generated. This profile is then low-pass filtered with a cut-off frequency of $1/\lambda_1 = 0.04\,\mathrm{m}^{-1}$, and the filtered signal is added to the measured road profile. The result is indicated in Figure 4.10. For low frequencies, this signal has a similar energy content as the DEM, and for higher frequencies, it is equal to the measured road profile.

Results

The road profile, as described in Section 4.3.3, is used as input to the quarter car model described in Section 4.2 with the vehicle parameters of Section 4.3.1. The simulated road input has similar spectral characteristics as the actual surface the vehicle was driven on. Therefore, the frequency content of the simulation and measurement results can be directly compared.

Figure 4.11 shows the results of both measurement and simulation of an unladen vehicle traversing the Belgian blocks. The top figure displays the simulated road input as function of temporal frequency. The middle figure shows the estimated transfer function magnitude based on the input and output signals of the quarter car model. Both the vehicle bounce eigenfrequency, around 1.3 Hz and the wheel hop eigenfrequency at 10 Hz are clearly visible. Lastly, the bottom figure
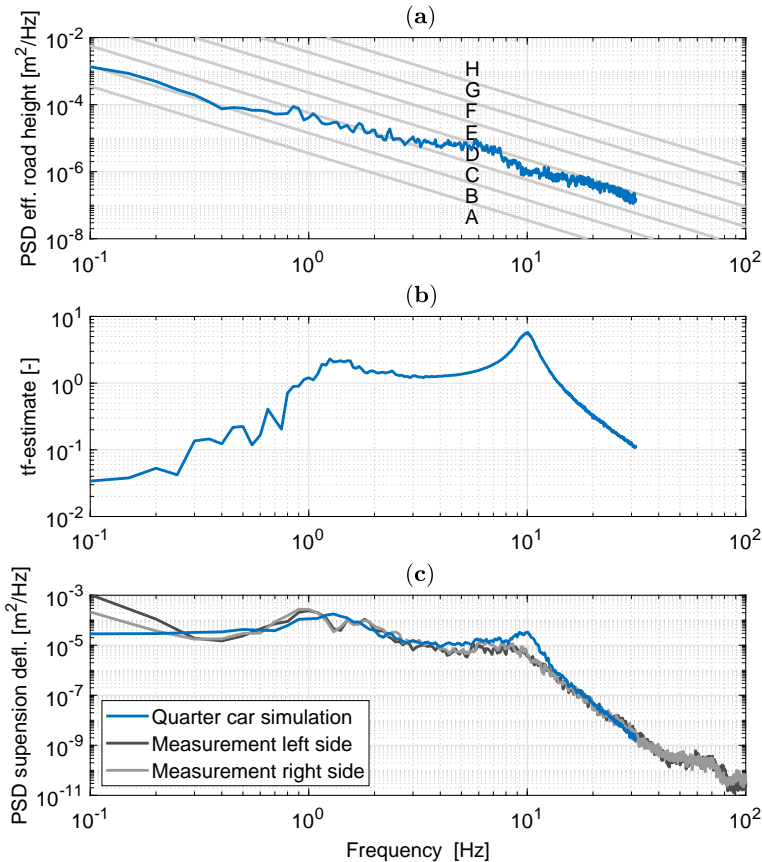
Figure 4.11. Input road profile (**a**), estimated transfer function from road to suspension deflection (**b**), and resulting suspension deflection (**c**) of an unladen vehicle at $v = 40\,\text{km/h}$.

in Figure 4.11 shows the Power Spectral Density (PSD), determined via Welch's method [128], of both the simulated suspension deflection and the measured suspension deflection signals. Again, the two eigenfrequencies are visible. It can be seen that the simulated suspension deflection is in the same order of magnitude as the measured signals. A difference can be observed around the $10\,\text{Hz}$ eigenfrequency. Here, the measurement data shows more damping than the model. A possible reason for this is that, for example, friction in the suspension, which is not modeled, results in additional damping. Alternatively, the possibility exists that the tire damping coefficient in Table 4.1 is lower than the actual tire damping.

Results of the Belgian blocks tests with a laden vehicle are displayed in Figure 4.12. These results are similar to those presented in Figure 4.11. The main
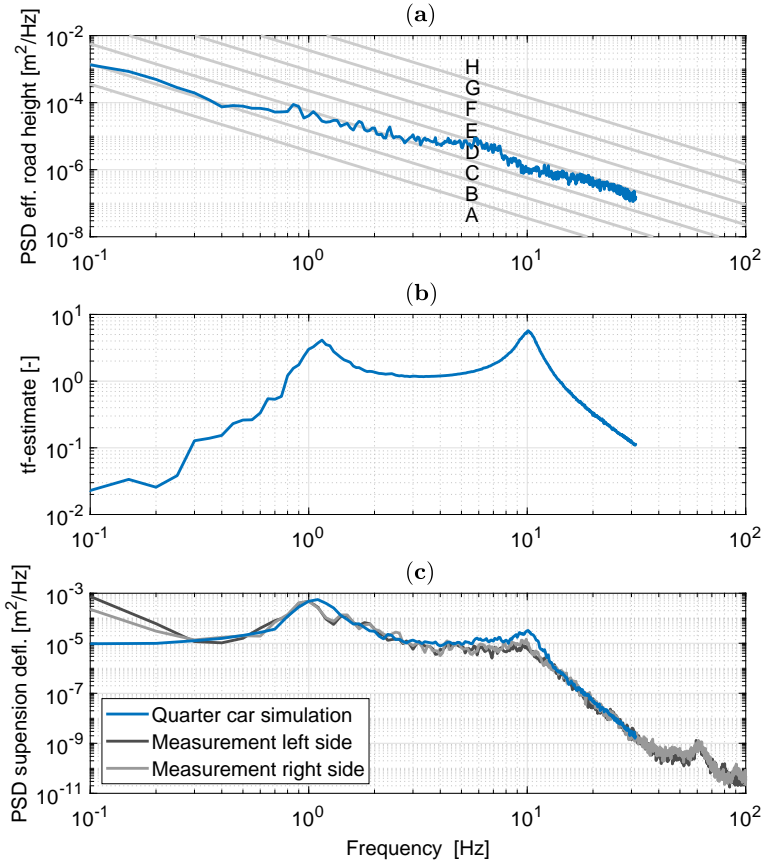
Figure 4.12. Input road profile (**a**), estimated transfer function from road to suspension deflection (**b**), and resulting suspension deflection (**c**) of a laden vehicle at $v = 40\,\text{km/h}$.

difference is the vehicle bounce resonance peak, which shows a larger amplitude in the loaded vehicle situation. Because the air bellow stiffness changes according to (4.9), the frequency at which this peak occurs barely changes between the two loading situations. Again, it can be concluded that the PSD of the measured and modeled suspension deflection z_s are very similar.

4.4 Quantification of damper losses

The quarter car model that has been validated with measurement data of a diesel bus in Section 4.3 is used here to assess the energy dissipated in the dampers of

Table 4.2. Model parameters of the quarter car models that represent the front and rear axle of a battery electric bus.

Parameter	Symbol	Value Front Axle	Value Rear Axle	Unit
Sprung mass (unladen)	$m_{s,unlad}$	2390	3685	kg
Sprung mass (laden)	$m_{s,lad}$	3018	5037	kg
Unsprung mass	m_u	425	695.5	kg
Bellow stiffness (unladen)	$k_{s,unlad}$	151000	175000	N/m
Bellow stiffness (laden)	$k_{s,lad}$	182000	236000	N/m
Damper force	$F_d(\dot{z}_d)$	Figure 4.13	Figure 4.13	N
Tire stiffness	k_t	$1.15{\cdot}10^6$	$2.3{\cdot}10^6$	N/m
Tire damping	d_t	300	600	Ns/m

a battery electric bus. The battery electric bus is described in Section 4.4.1. The results of the quarter car model simulations are presented in Section 4.4.2 and compared to the results of coast-down tests in Section 4.4.3.

4.4.1   Vehicle parameters

The model parameters representing the battery electric bus are listed in Table 4.2. Separate sets of parameters are used to represent both the front and rear axle of the vehicle. The damper force characteristic for both axles is visualized in Figure 4.13. Again, two loading conditions are considered; an unladen vehicle and a laden vehicle.

With respect to the diesel vehicle in Section 4.3.1, the electric bus shows a higher sprung mass and consequently a higher air bellow stiffness. The unsprung mass of the rear axle is slightly higher here, because the rear axle here is driven and contains a final drive. Also the parameters for the front axle are presented, which has only one air bellow, one damper, and one tire per corner of the vehicle. The stiffness and damper characteristics presented in Figure 4.13 represent the effective values, after accounting for suspension kinematics.

4.4.2   Random road input

As input to the simulation, random road profiles of classes A, B, C, and D will be considered. Higher road classes are of such poor quality that these are unlikely to be encountered by electric city buses. The resulting profiles are shown in Figure 4.14. Tire enveloping is taken into account in the roads displayed in the figure according to the method described by [123]. This results in a dip in the frequency content of the road profiles, as objects of this spatial dimension are enveloped by the tire.
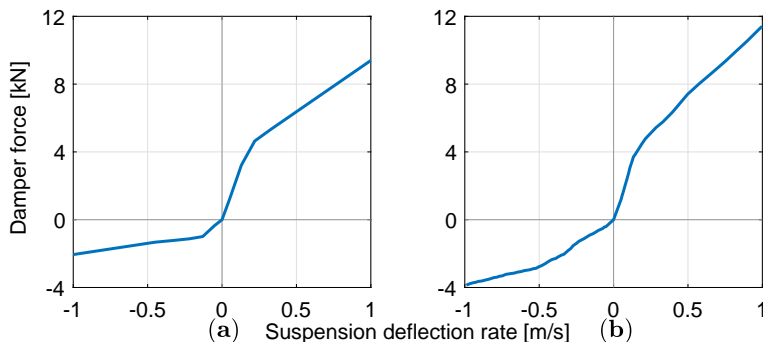
Figure 4.13. Damper force F_d versus damper deflection rate $\dot{z}_s$ for both the front (**a**) and rear (**b**) suspension of the battery electric bus. The values represent the damping force per corner of the vehicle according to manufacturer specification.
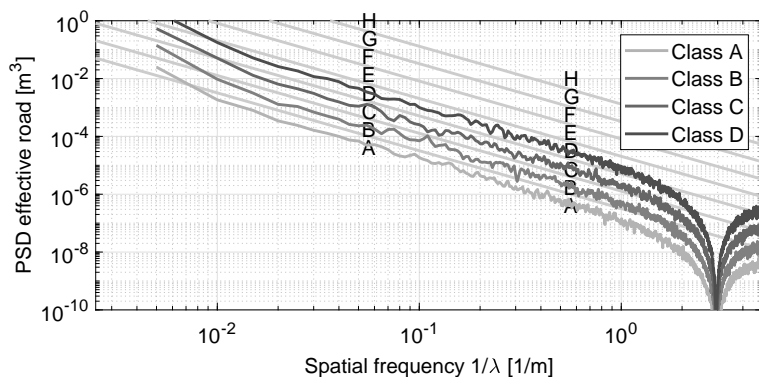
Figure 4.14. Power spectral density of the four effective random-road profiles used for the simulation study, each representing one road-roughness class.

The quarter car model with nonlinear damper, as described in Section 4.3 is used to simulate the front and rear axle of the battery electric bus. The random-road profiles of Section 4.4.2 are used as input for these simulations.

For each road class A, B, C, and D, a 3 km section of road is simulated. The vehicle forward velocity is assumed to be constant at $v = 40\,\text{km/h}$. The front and rear axle analyses are conducted independently with the same road profile. The effect of any coupling between the dynamics of the front and rear-axle is thereby assumed to be small. The resulting energy dissipated per axle for both dampers and tires is displayed in Figure 4.15.

The results for road class A, displayed in Figure 4.15a, show that the total dissipated energy increases linearly with time. The majority of this energy is dis-
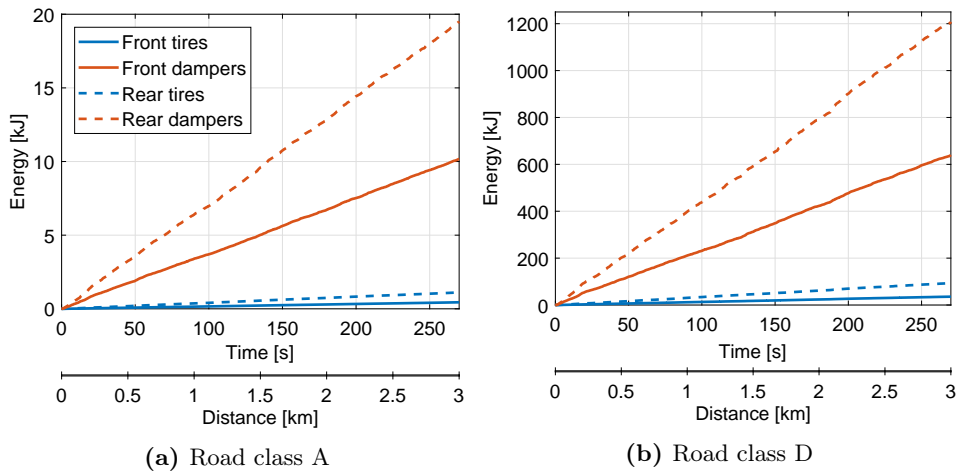
Figure 4.15. Simulated cumulative energy dissipated in dampers and tires, indicated for both the front and rear axles for road classes A (**a**), and D (**b**). Results are for an unladen vehicle driving 40 km/h.

sipated by the dampers, where the rear dampers dissipate almost twice as much energy as the dampers in the front suspension. This is in accordance with the fact that the rear axle is equipped with double springs, dampers, and tires. By dividing the total dissipated energy by time, the front and rear dampers in this simulation dissipate 110 W combined on average. The dissipated energy increases with increasing road classes. Consequently, the most energy is dissipated on the class D road, where all dampers combined account for 6.8 kW, as shown in Figure 4.15b. Given the vehicle has six dampers, this is about 1.1 kW per damper.

An overview of the average specific dissipated energy, expressed in kWh/km, is presented in Figure 4.16. The dissipated energy is partitioned into energy dissipated in the shock absorbers and energy dissipated in the tires. This shows that the contribution of the tire damping is relatively small. Data is shown for both a laden and an unladen vehicle. Surprisingly, the energy dissipated in the dampers in these two situations is very similar. This observation is likely a consequence of air bellow stiffness increasing with sprung mass, resulting in dynamics that are approximately mass-independent. Nevertheless, the literature suggests that even for vehicles with constant suspension stiffness, the dissipated damper energy mainly depends on tire stiffness and is independent of other suspension parameters [112].

When comparing the different road classes, we see again that the dissipated energy increases exponentially for increasing road classes. At 0.0027 kWh/km, the total dissipated energy is lowest for road class A. For road class D, the total distance-specific energy amounts to 0.17 kWh/km, which is approximately 13% of
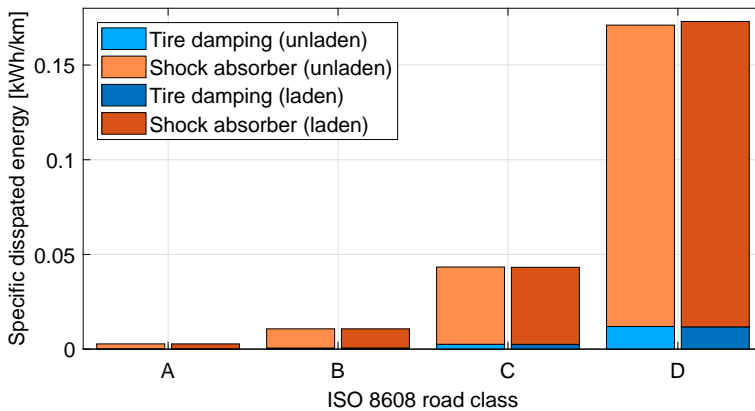
Figure 4.16. Total specific energy dissipated in the dampers and tires of a battery electric bus for different road classes. Results are shown for both an unladen and laden vehicle driving 40 km/h.

a representative energy consumption for a battery electric bus (= 1.3 kWh/km), see Figure A.5a in Appendix A.

The simulation results presented here are obtained at a simulated forward velocity of 40 km/h. Considering that the road PSD is effectively represented by a -2 slope, as shown in Figure 4.14, and assuming that the constant forward velocity only affects the vertical tire excision and no other vehicle dynamics, a doubling of the forward velocity is equivalent to increasing the road class by +1. In other words, the results presented for class B in Figure 4.16 would also approximately represent the losses on a class C road at 20 km/h.

Frequency analysis

As previously shown in Figure 4.14, the random-road inputs have a broad frequency content that is representative of a realistic road. The question arises which frequency range is responsible for most of the energy consumption. To this end, the random-road profile is filtered with a low-pass filter of varying cut-off frequencies. This results in a set of different road profiles that range from profiles with only low-frequency content to the original road profile with its full frequency content.

Each low-pass filtered profile is used as input to the quarter car model representing the battery electric bus. The resulting dissipated energy is expressed as a percentage of the energy dissipated for the original road profile in Figure 4.17. The results show that the frequencies below 0.7 Hz do not contribute to the energy dissipation in the damper and tire. The frequencies related to vehicle bounce, ranging from 0.7 to 3 Hz contribute 27% to the total dissipated energy. However, the majority of the energy, 73%, is dissipated due to road inputs in the 3 to 12 Hz frequency range. Only as of 7 Hz, tire damping starts to become significant.
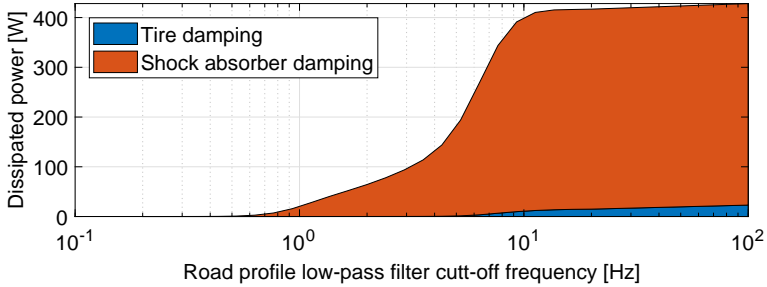
Figure 4.17. Dissipated power due to vertical damping in shock absorbers and tires for different low-pass cut-off frequencies of the road profile. Simulation represents a BEB driving $40\,\text{km/h}$ on a road of class B.

4.4.3   Coast-down tests

The dissipative damper losses described by the quarter car model represent only part of the rolling resistance experienced by the bus. Energy is also dissipated due to hysteresis effects in the deformation of rubber in the tire-road contact patch, micro-slip between tire and road, and, in case of a wet road, due to displacement of water [103, 129]. Because these effects are challenging to model based on first principles, the tire rolling resistance is often measured on a drum test setup or through a vehicle test. In this case, the rolling resistance is determined from coast-down tests with a $12\,\text{m}$ battery electric bus on various roads.

The coast-down tests are conducted in accordance with NEN-ISO 10521-1 [62]. During each test, the vehicle is accelerated to a certain speed, after which propulsion is removed, and the vehicle is allowed to slow down under the influence of rolling resistance and aerodynamic resistance. By analyzing forward velocity as function of time, an estimate can be provided for both rolling resistance coefficient c_r and aerodynamic drag coefficient c_d. Measurements are repeated five times in both directions on each road to arrive at average values for both these parameters. The tests are conducted with an unladen vehicle on four different road surfaces: Smooth asphalt, standard asphalt, rough asphalt, and Belgian blocks. These four road surfaces correspond to the first classes of the random road profiles, respectively: A, B, C, and D.

In order to compare these results, the energy dissipated in the dampers E_{damp} and tires E_{tir} as described in (4.13), is determined for all $i = 1, ..., 4$ corners of the vehicle and scaled with the vehicle mass and travelled distance to arrive at a rolling resistance coefficient contribution, respectively,

$$c_{r,damp} = \frac{\sum_{i=1}^{4} E_{damp,i}(t)}{m\,g\,v\,t} \qquad c_{r,tir} = \frac{\sum_{i=1}^{4} E_{tir,i}(t)}{m\,g\,v\,t} \,, \qquad (4.17)$$

where m is the total vehicle mass. The resulting rolling resistance contributed both due to shock absorber losses and vertical tire damping losses are shown in
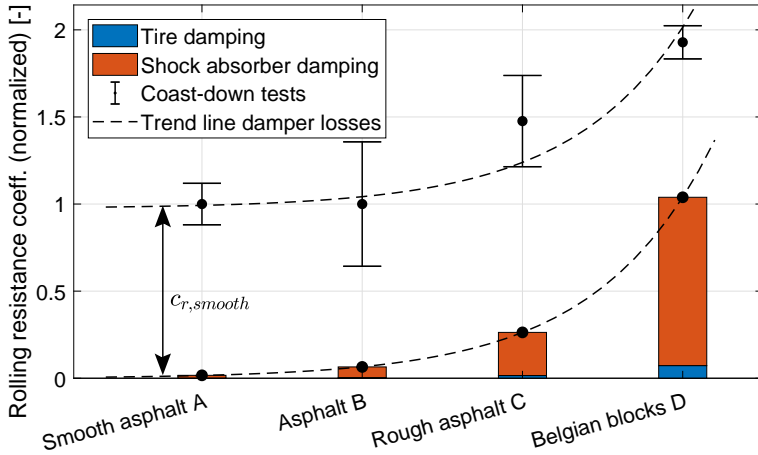
Figure 4.18. Tire damping and shock-absorber damping expressed as rolling resistance coefficient contribution. Trend line indicates increasing damper losses and is shown once with and once without offset of $c_{r,smooth}$. The error bars indicate the maximum and minimum rolling resistance measured using coast-down tests.

Figure 4.18. The results of the coast-down tests are shown as well, where the error bars indicate the maxima and minima of all parameter estimates.

The results in Figure 4.18 show that the rolling resistance obtained from coast-down tests approximately doubles when going from smooth asphalt to Belgian blocks. This rolling resistance can be perceived as the sum of the rolling resistance on a smooth surface, $c_{r,smooth}$, and the rolling resistance contributed due to shock absorber and tire damping losses. The trend line in Figure 4.18 indicates that the road-roughness dependency of the coast-down test results and the damper losses predicted by the quarter car model have a similar order of magnitude and trend. Therefore, it is concluded that the majority of the rolling resistance increase on rough roads is caused by energy dissipation in the dampers and, to a lesser extent, by energy dissipation in the tires. Although it is acknowledged that the rolling resistance of a tire on a smooth surface can increase for speeds above $100 \, \text{km/h}$ [129], the damper losses described here are the dominant reason for increasing resistance while increasing road roughness or increasing vehicle speed.

4.5 Conclusion

The energy lost due to stroking of the suspension shock absorbers when driving over road irregularities is quantified. A quarter car model with nonlinear damper and tire enveloping is validated based on data of an $18 \, \text{m}$, three-axle city bus. Two

known road inputs are used; a road bump and Belgian blocks. The simulated road bump compares well to measurements during compression and rebound, and the energy balance of the quarter car model is demonstrated. The Belgian block simulations, performed with both a laden and an unladen vehicle, compare well to the measured suspension deflection in the frequency domain.

The validated model is employed to calculate the damper energy losses for a set of generated random-road profiles. For all of these profiles, the energy dissipated in the rear axle is roughly twice as large as the energy in the front axle. The energy dissipated due to vertical damping of the tire is one order of magnitude smaller than that of the suspension. The road roughness significantly affects the total dissipated power, which can reach 6.8 kW, or 0.17 kWh/km, on roads of class D at 40 km/h. This corresponds to approximately 13% of the nominal energy consumption of a battery electric bus. These results are independent of vehicle mass, which is likely a consequence of the mass-dependent air bellow stiffness. Comparing the results to rolling resistance coefficients determined from coast-down tests indicates that the effects described here are responsible for the majority of the road-surface dependency of the rolling resistance coefficient. Lastly, by low-pass filtering the road input, it is established that the road frequencies between 3 and 12 Hz constitute 70% of the dissipated energy.

Several improvements to this study are conceivable. Firstly, this work only concerns the losses attributed to the suspension dampers and the vertical damping of the tire. If a complete first-principles rolling resistance model is desired, a model representing the hysteric tire losses on a smooth surface should be added. Secondly, to more accurately simulate large vertical excitations of the suspension, the nonlinear thermodynamic effects of the compressed air in the bellows should be considered, thereby more closely resembling the characteristics in Figure 4.3. Likewise, the inclusion of bump- and rebound stops might be considered. Furthermore, making the damper force position-dependent, $F_d = F_d(\dot{z}_d, z_d)$, allows for the modeling of the hysteresis that is often present in shock absorbers [114]. Lastly, it remains an open topic to simulate the dissipated damper power in both front and rear axle and correlate these to the vehicle's powertrain power in the time domain. While the results presented here indicate a clear trend in average rolling resistance, making a rolling resistance force prediction for a particular road profile involves more detailed tire- and powertrain dynamics.

5

Combined rolling resistance and road grade estimation based on EV powertrain data

Abstract - *Energy consumption prediction is increasingly important for eco-driving, energy management, and charging scheduling of electric vehicles. Detailed knowledge of the rolling resistance and road grade, combined here in a road-resistance profile, improves the accuracy of these predictions. This chapter presents a recursive method to identify the position-dependent road-resistance coefficient using GPS position, powertrain power, and vehicle speed. The calculations make explicit assumptions regarding the spatial continuity of both road gradient and rolling resistance by defining road segments. A recursive least-squares method with Gaussian basis functions allows the estimates to be updated whenever a route segment is traversed anew. The method is tested on data gathered by a 12 m battery electric bus. The resulting road-resistance profile shows a strong resemblance to the road slope and captures changes in rolling resistance well, including a dependency on ambient temperature, which is in accordance with literature on tire rolling resistance. Including the resistance profile in a vehicle model reduces the error of the predicted powertrain power with 1.7 percent point compared to a conventional method, without the limitation of requiring a high-resolution digital elevation model.*

5.1   Introduction

TO reduce global climate change and local air pollution, the transportation sector is transitioning to electric mobility [12]. Electric Vehicles (EVs) are already a key solution in this transition, and in the next decade, the total share of EVs is expected to keep growing exponentially [12, p. 75]. The shift towards electric propulsion is also taking place in the public transport sector, where inner-city transport is electrified, mostly by introducing Battery Electric Buses (BEBs) [43]. The shorter routes with relatively low average velocities, together with the need to reduce local air pollution, make the city centers a suitable use case for BEBs [130].

The limited driving range is an important technical challenge still stalling the dominance of EVs with respect to conventional Internal Combustion Engine (ICE) vehicles. For EVs, the available energy stored in the battery is generally far less than is available in the fuel tank of an ICE vehicle. Even though electric power-trains operate more efficiently, the resulting net driving range is lower. A secondary result of the relatively high and constant efficiency of the electric powertrain is that the road loads, i.e., aerodynamic resistance, rolling resistance, and the longitudinal force due to road gradient, have a larger effect on the vehicle's driving range. Therefore, the driving range can vary significantly when these resistance forces change from route to route or day to day. Even though progress is made both in increasing the available battery capacity and reducing the energy consumed per driven distance, the variability of the driving range is inherent to the efficient powertrain of the EV.

Accurately modeling the energy consumed by an EV powertrain remains an essential requirement to predict the driving range and apply energy-saving control algorithms. Examples of these control strategies include eco-driving [40], look-ahead cruise controllers [131], on-board energy management [41], and eco-routing algorithms [45]. For BEBs, additional uses of energy consumption models are found in solving fleet scheduling problems [43, 44] and exploring the vehicle design space [38, 39], often to minimize Total Cost of Ownership (TCO).

There are generally two types of EV energy consumption models. The first type is a data-driven approach where historical measurements are used to predict the energy consumption of a future trip under similar conditions [132, 133]. Evermore often, machine learning-type methods are used for this purpose. Alternatively, a physics-based approach can be employed, where the longitudinal dynamics of the vehicle are reconstructed to determine the energy that will be required to traverse a route at a certain forward velocity [33]. This method typically relies on models of the different road load forces; aerodynamic resistance, rolling resistance, the longitudinal component of gravity due to road gradient, the acceleration force, and the powertrain losses. Compared to data-based models, physics-based models offer an increased understanding of the energy losses and better extrapolatability to different routes and operating conditions. However, the parameters of the physics-

based model can be challenging to obtain.

The rolling resistance is an important physical effect that is challenging to model accurately. Rolling resistance is a function of tire-design parameters, tire inflation pressure, tire temperature, road wetness, and road roughness [129, 134]. A second component strongly influencing the EV power request is the road gradient. In any prediction, the quality of road gradient data is detrimental to the accuracy of the energy prediction [135]. Road gradient profiles can be obtained from GPS [136, 137], Inertial Measurement Units (IMUs) [138] or Digital Elevation Models (DEMs) [139]. However, each of these methods brings its own disadvantages; GPS is considered inaccurate for elevation measurements, IMU measurements require additional sensors, and DEMs are often of limited spatial resolution or only locally available. Furthermore, DEMs provide no data for parts of the route consisting of tunnels or obscured by overpasses.

5.1.1   Literature overview: online rolling resistance and road grade estimation

Because of the increasing number of sensors in road vehicles, interest arose in the 1990s to identify vehicle parameters online [136, 140, 141]. Most of these earlier studies, both in simulation and experimentally, use an ICE vehicle as a case study [142–145]. In the presented estimator algorithms, engine torque is often required to be measured. Because direct measurement of this torque is challenging, most studies employ static engine maps to express this signal as a function of speed and fuel rate. In the last decade, more EVs have appeared as subject in parameter estimation studies [55, 146, 147]. These vehicles offer the advantage of measurement of the motor current, which directly relates to motor torque. Alternatively, the powertrain power can be used [55]. Except for engine or motor torque, additional sensors are often employed to base the estimation on. These include GPS [136, 137, 143, 146], which is often used to assess the road grade, or IMUs [138, 142, 145]. In most studies, the vehicle speed signal is also required and measured using wheel-speed sensors or a tachograph.

Most studies focus on the estimation of either road grade or rolling resistance. Road grade estimators are often combined with simultaneous estimation of the vehicle mass [142, 144–146, 148]. This is possible because the vehicle mass affects the longitudinal acceleration of the vehicle, which can easily be measured directly with an IMU or indirectly via the vehicle speed. Online rolling resistance estimators are also described in literature [147, 149, 150] and are sometimes combined with estimations for the aerodynamic coefficient [151, 152] or the vehicle mass [55]. Combined estimation of rolling resistance and road grade is seldomly encountered [143].

Different techniques are used for the various online estimators. An often encountered choice in the automotive industry is the Kalman filter [136, 142] or extended Kalman filter [131]. Secondly, more general observer-based methods

are used [148–150], often in the context of estimating the rolling resistance. The method encountered most often in the literature of interest is Recursive Least-Squares (RLS) algorithm [55, 140, 143–146, 151]. This algorithm is intuitive and computationally efficient.

While the applied methods can give a good indication of the rolling resistance or road grade of past a route, this gives no direct information on any future conditions the vehicle might encounter. This aspect is left undiscussed in most studies, where results are presented as a function of time or traveled distance with respect to the start of a measurement. Some studies, e.g., [138] and [147], make the first step towards combining data from multiple vehicles by visualizing the estimated parameter as function of position on a map. One other exemplary study, [153], proposes a detailed method to combine data from a connected fleet of vehicles to estimate rolling resistance and wind influence, yet is only applied to simulated data. To the best of the authors' knowledge, only in [131] multiple measurements from multiple vehicles are combined to arrive at a single estimate for the road gradient. Multiple measurements are averaged using a spatial Kalman filter resulting in a road gradient that compares favorably to a reference profile.

5.1.2   Contribution

Although previous studies exist that estimate the rolling resistance or road gradient online, only a few account for the location-dependency of both these parameters and use this to combine data from multiple measurements. Additionally, other studies rarely estimate rolling resistance and road grade combined. This chapter presents a novel approach to the problem by defining route segments to include both the continuous nature of road gradient and the spatial discontinuities introduced by the rolling resistance. Recursive least-squares with Gaussian basis functions is applied to iteratively evaluate the measured powertrain power of a battery electric bus that is repeatedly driving the same route. The resulting parameter estimates are subsequently used in a physics-based longitudinal vehicle model to predict the power request of a future vehicle traversing the same route.

This chapter is organised as follows. In Section 5.2 the physics-based longitudinal dynamics model that is at the basis of this work is explained. In Section 5.3 the theory behind the proposed recursive identification method is detailed. This method is evaluated with measurement data obtained from a 12 m electric bus, as described in Section 5.4. The results of this experiment are presented in Section 5.5. Lastly, conclusions and future work are described in Section 5.6.

5.2   Vehicle model

This chapter follows a physics-based approach to energy consumption prediction. This implies that the longitudinal dynamics of the vehicle are considered, as described in Section 5.2.1. Notably, this model includes an empirically determined
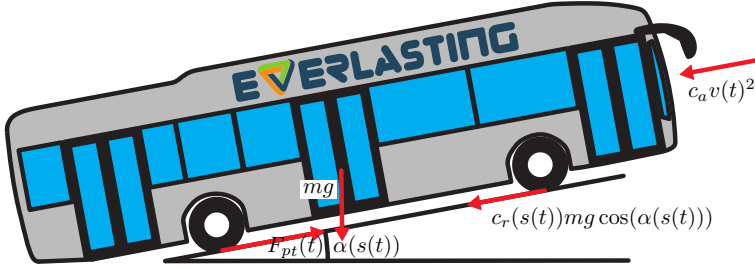
Figure 5.1. A schematic view of the longitudinal forces acting on the vehicle.

map to represent the powertrain losses as discussed in Section 5.2.2 and accounts for the temperature-dependency of the aerodynamic drag force as discussed in Section 5.2.3.

5.2.1   Longitudinal vehicle dynamics

The energy consumption of the electric vehicle is assumed to adhere to the road-load equation [33], which describes the longitudinal dynamics of the vehicle, as seen in Figure 5.1, according to:

$$m_{eff}\frac{dv(t)}{dt} = F_{pt}(t) - \cos(\alpha(s))c_r(s)mg - \sin(\alpha(s))mg - c_a(T_{amb})v(t)^2 \ , \quad (5.1)$$

where constants m_{eff} and m are respectively the effective vehicle mass, which includes rotational inertia of wheels and driveline, and the vehicle mass, $c_a(T_{amb})$ is the aerodynamic resistance coefficient as function of ambient temperature T_{amb}, $c_r(s)$ is the rolling resistance coefficient, $\alpha(s)$ is the road gradient, and g is the gravitational acceleration. $F_{pt}(t)$ represents the driving force applied at the driven wheels, which can be determined according to

$$F_{pt}(t) = \frac{P_{pt}(t) - P_{loss}(T_{mot}(t), v(t))}{v(t)} \ , \quad (5.2)$$

where $P_{pt}(t)$ is the electric powertrain power supplied by the high-voltage battery, and $P_{loss}(T_{mot}(t), v(t))$ is the energy lost between wheel and battery as function of motor torque $T_{mot}(t)$ and forward vehicle velocity $v(t)$. In these equations, the forward velocity $v(t)$, powertrain losses $P_{loss}(t)$, and the powertrain power $P_{pt}(t)$ are functions of time t. In contrast, the road gradient $\alpha(s)$, and the rolling resistance $c_r(s)$ are assumed functions of the vehicle position $s(t)$, which by itself is a function of time. This time-dependency of s, will be dropped hereafter for brevity.

Next, (5.1) is rewritten as

$$\frac{1}{mg}\left[F_{pt}(t) - m_{eff}\frac{dv(t)}{dt} - c_a v(t)^2\right] = c_{road}(s(t)) \ . \quad (5.3)$$

From this equation, we define the *road-specific resistance coefficient* $c_{road}(s)$ as

$$c_{road}(s) := \cos \alpha(s)\, c_r(s) + \sin \alpha(s) \; , \tag{5.4}$$

which represents the combined effect of rolling resistance and road grade. Using (5.1) and (5.2), the variables in left term of (5.3) are either measured ($P_{pt}(t)$, $T_{mot}(t)$, $v(t)$) or known constants (g, m, m_{eff}, c_a). Therefore, it is possible to calculate $c_{road}(s)$ when measurements on these signals are available.

There are two conditions under which direct calculation of the road resistance is not possible. Firstly, because (5.3) does not contain any term for the dissipative friction brakes of the vehicle, $c_{road}(s)$ can only be calculated if these brakes are not engaged. Secondly, because (5.2) is badly conditioned for low velocities, $c_{road}(s)$ is only calculated in case $v(t) > 5\,\text{km/h}$.

The constants in (5.3) are subject to several assumptions. In practice, the vehicle mass m of an electric bus can change due to differences in passenger occupancy. However, modern vehicles are equipped with an Electronically Controlled Air Suspension (ECAS) that enables estimates of the vehicle mass by measuring the air bellow pressure. Given the availability of these sensors, the vehicle mass is assumed a known piecewise constant parameter that changes when the vehicle is halted at a bus stop. Furthermore, while the aerodynamic resistance coefficient c_a is dependent on the ambient temperature, as described in Section 5.2.3, these changes are typically slow. Therefore, during a single trip, c_a is treated as a constant.

5.2.2   Empirical powertrain losses model

The term $P_{loss}(T_{mot}(t), v(t))$ in (5.3) represents the combined losses of the inverter, motor, possible driveshafts, the final drive, and bearings. Because modeling these components in detail requires extensive knowledge about the powertrain, an empirical method is followed. To this end, the losses between battery and wheels are measured on a heavy-duty chassis dynamometer for different velocities and torques. The resulting power losses map is visualized in Figure 5.2, and is described in more detail in Appendix B. The map is a function of the wheel torque $T_{whl}(t)$, which here is determined from the motor torque $T_{mot}(t)$ that is reported by the motor controller during the measurements and the known final-drive gear ratio.

5.2.3   Temperature-dependent aerodynamics

The aerodynamic resistance coefficient c_a consist of

$$c_a = \frac{1}{2}\, \rho(T_{amb}, h_{rel}, p_{atm})\, c_d A_f \; , \tag{5.5}$$

where c_d and A_f describe respectively the aerodynamic drag coefficient and frontal area of the vehicle. Both these parameters are assumed constant, indicating that
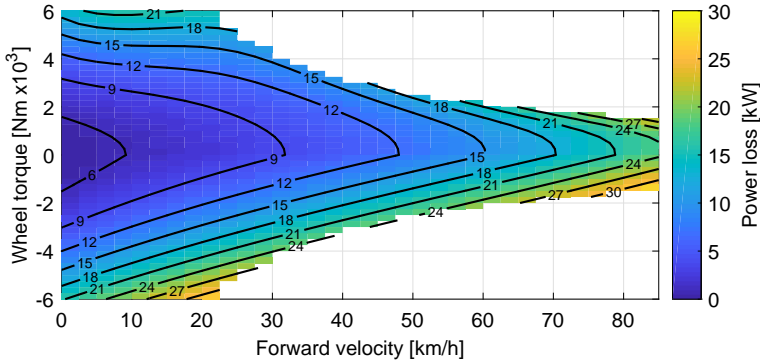
Figure 5.2. The powertrain losses model originating from dynamometer measurements.

no side-wind effects are considered here. The expression for the air density ρ is based on [65], which describes a static relation as function of temperature T_{amb}, relative humidity h_{rel}, and the atmospheric pressure p_{atm}. The values for these three parameters are obtained from openly accessible databases of nearby weather stations [154]. The time-resolution of this weather data is 1 hr, and is matched to the start time of each trip.

5.3 Recursive least-squares identification

Having defined the road-resistance coefficient $c_{road}(s)$, this section describes the system identification method used to combine multiple observations of this coefficient in a single position-dependent road-resistance profile. Assumptions regarding the position-dependency are summarized in Section 5.3.1 and the used recursive least-squares method is detailed in Section 5.3.2.

5.3.1 Route segmentation

The road resistance $c_{road}(s)$, as defined in (5.4), combines the influence of the road gradient $\alpha(s)$ and the rolling resistance coefficient $c_r(s)$. While $\alpha(s)$ can typically be considered a continuous function of position s, the rolling resistance depends strongly on the road surface [134] and can thus be discontinuous as function of s. Therefore, it is assumed here that roads consist of shorter *road segments* that each contain a specific road-surface type. Road segments are defined based on the following criteria that can be obtained for any road via OpenStreetMap:

- The road name, e.g., 'Station Road' [155].
- The road type, e.g., 'motorway' or 'primary' [156].

Figure 5.3. Top view of a road network where each of the road segments are indicated by individual colors. The segments indicated by ③...⑥ are included in the test route.

- Whether or not the road is part of a junction [157].

Sections of the route with the above three properties in common are defined as part of a single road segment, which is assumed to have a constant rolling resistance c_r. This implies continuity of $c_{road}(s)$ within every route segment. Discontinuities in $c_{road}(s)$ are assumed possible on points between road segments to represent a possible change in road-surface. In Figure 5.3 an exemplary highway overpass is shown, with colors indicating the different route segments.

Besides realizing specific assumptions regarding the position-dependency of $c_{road}(s)$, the above segment-based definition of the route offers the advantage that at any location two roads meet, a new road segment is defined. This opens up the ability to combine resistance profiles of vehicles that have several segments, but not the entire route, in common.

5.3.2   Recursive least-squares with Gaussian basis functions

A vehicle is considered that traverses several route segments $i = 1, ..., N_s$, while measuring $P_{pt}(t)$, $T_{mot}(t)$, $v(t)$, and GPS position. Thereby, $c_{road}(s(t))$ can be determined through (5.3) and (5.2), which is referred to as an observation of $c_{road}(s(t))$. Whenever a similar vehicle drives the route the next time, a second set of observations of $c_{road}(s(t))$ can be made. These sequential batches of observations are indicated by $k = 1, ..., N_t$, where N_t is the number of trips. In this section, a single road segment i, defined by the criteria in Section 5.3.1, is considered. To this end, the subscript i will be dropped in the subsequent explanation.

Every time a vehicle traverses this route segment for the kth time, a batch of measurements of the powertrain power $P_{pt,k}(t_1, ..., t_{N_{m,k}})$, motor torque $T_{mot,k}(t_1, ..., t_{N_{m,k}})$, and forward vehicle velocity $v_k(t_1, ..., t_{N_{m,k}})$ are made, where $N_{m,k}$ is the total number of measurements in the kth trip. The total number of measurements $N_{m,k}$ can vary and is a function of the route segment length d, the vehicle speed $v(t)$, and the sampling rate of the measured signals. The measured signals are used to calculate $N_{o,k}$ observations of $c_{road,k}(t_1, ..., t_{N_{o,k}})$ using (5.3) and (5.2). Note that this calculation is only valid if the dissipative brakes of the vehicle are
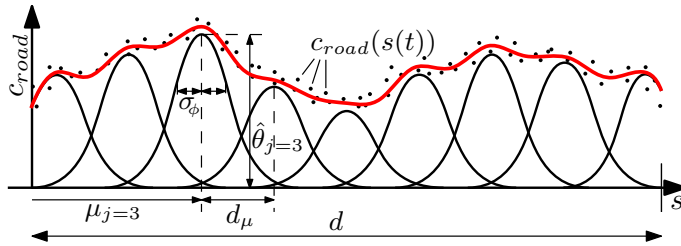
Figure 5.4. Schematic view of Gaussian basis functions approximating the road-resistance profile for a single route segment of length d.

not engaged and $v(t) > 5\,\text{km/h}$. These conditions are checked by monitoring the brake-pedal position and forward vehicle velocity, and invalid data is excluded from further processing. Therefore, $N_{o,k} \leq N_{m,k}$. The resulting observations for $c_{road}(\underline{s}_k)$ are gathered in a column $\underline{c}_{road,k}$, along with the positions $\underline{s}_k$ at which these are captured;

$$\underline{c}_{road,k} = \begin{bmatrix} c_{road,k}(t_1) \\ \vdots \\ c_{road,k}(t_{N_{o,k}}) \end{bmatrix} \qquad \underline{s}_k = \begin{bmatrix} s_k(t_1) \\ \vdots \\ s_k(t_{N_{o,k}}) \end{bmatrix} \qquad (5.6)$$

If the route segment is traversed the next time $(k+1)$, a new set of observations: $\underline{c}_{road,k+1}$ at possibly different locations $\underline{s}_{i,k+1}$ is generated. Therefore, the challenge arises to determine an average c_{road}-profile from the spatially non-equidistant observations of c_{road}, and subsequently add new observations to this profile in a recursive manner.

Gaussian basis functions

The positions at which the road resistance is measured $\underline{s}_k$ are not equidistant due to the non-constant forward velocity of the vehicle. Additionally, in the next set of observations, the positions $\underline{s}_{k+1}$ are likely to differ. Gaussian basis functions are proposed in the position-domain, as shown in Figure 5.4, to parameterize the road-resistance profile and achieve a definition for the road resistance that does not depend on sensor sampling time or forward vehicle velocity. Gaussian functions are chosen because these are non-periodic, C^1 continuous, and vanish at infinity, which are all properties that apply to a local road gradient measurement. Additionally, by using the amplitudes of the functions as the unknown parameters, physical interpretation of the parameter values is maintained.

Figure 5.4 shows that the basis functions are spatially distributed along the length of the road segment. The number of basis functions per road segment N_ϕ depends on the road segment length d and a pre-defined inter-basis function

distance d_μ;

$$N_\phi = \left\lceil \frac{d}{d_\mu} \right\rceil . \tag{5.7}$$

For the results generated in this chapter, $d_\mu = 66\,\text{m}$ is taken. The midpoints of the Gaussian curves μ_j for the basis functions $j = 1, 2, ..., N_\phi$ are chosen to be uniformly distributed over the length of the road segment:

$$\mu_j := (j-1)d_\mu + \frac{(N_\phi d_\mu) - d}{2} \quad \text{with} \quad j = 1, 2, ..., N_\phi , \tag{5.8}$$

where the latter term ensures symmetry with respect to the center of the segment, which is convenient if the segment is traversed in both directions. Lastly, the basis function width σ_ϕ, is constant and is taken $\sigma_\phi = 44\,\text{m}$ in this chapter. The values described here result in approximately $1000/d_\mu \approx 15$ basis functions per kilometer and are sufficiently small to capture any gradient changes in the measurement data, such as those that will be described in Section 5.5.2. Additionally, the fact that $\sigma_\phi = 2/3d_\mu$ ensures that the different basis functions partially overlap, enabling even relatively constant profiles to be approximated.

The Gaussian basis functions are defined as [158]

$$\underline{\phi}_j(\underline{s}_k^T) := \begin{cases} \exp\left(-\frac{\underline{s}_k^T - \mu_j}{2\sigma_\phi^2}\right) & \text{if } N_\phi > 1 \\ \underline{J}_{1 \times N_{o,k}} & \text{if } N_\phi = 1 . \end{cases} \tag{5.9}$$

The lower condition in (5.9) ensures that if $d < d_\mu$, e.g., when only one basis function fits the road segment, a matrix of ones $\underline{J}$ is used and thus $c_{road}(s)$ is assumed constant over the entire road segment. If $d \geq d_\mu$, multiple basis functions are required. A regressor matrix $\underline{\Phi}(\underline{s}_k)$ is constructed by ordening the N_ϕ basis functions as

$$\underline{\Phi}(\underline{s}_k) := \begin{bmatrix} \underline{\phi}_{j=1}(\underline{s}_k^T) \\ \vdots \\ \underline{\phi}_{j=N_\phi}(\underline{s}_k^T) \end{bmatrix} \quad \text{with} \quad j = 1, 2, ..., N_\phi . \tag{5.10}$$

The regressor matrix is used in a linear regression model defined as

$$\underline{c}_{road,k}(\underline{s}_k) = \underline{\Phi}(\underline{s}_k)^T \underline{\theta} + \underline{\varepsilon}_k(\underline{s}_k) , \tag{5.11}$$

where $\underline{c}_{road,k}(\underline{s}_k)$ is the data-vector containing the observed values for c_{road}, $\underline{\Phi}(\underline{s}_k)$ is the previously defined regressor matrix, containing basis functions that are a function of measured positions $\underline{s}_k$, $\underline{\theta}_k$ is the column containing the individual amplitudes of the basis functions, and $\underline{\varepsilon}_k(\underline{s}_k)$ is the error term. The positions $\underline{s}_k$ at which the c_{road}-observations are made are based on GPS-measurements, as is explained in Section 5.5.1. The assumption is made that any error in $\underline{s}_k$ is negligibly small compared to the width of the basis functions, thereby making $\underline{\Phi}(\underline{s}_k)$ completely known. Also assuming that the errors $\underline{\varepsilon}_k(\underline{s}_k)$ are zero-mean, the parameter estimates in this least-squares problem can shown to be unbiased.

Combining multiple observations

Having defined the regressor matrix $\underline{\Phi}$, next, parameter estimates $\hat{\underline{\theta}}$ are sought that minimize the errors $\underline{\varepsilon}_k(\underline{s}_k)$ in (5.11) in a least-squares sense for all available N_t trips, i.e.,

$$\hat{\underline{\theta}}_{N_t} = \underset{\underline{\theta}}{\operatorname{argmin}} \frac{1}{N_t} \sum_{k=1}^{N_t} \left[\underline{c}_{road,k}(\underline{s}_k) - \underline{\Phi}(\underline{s}_k)^T \underline{\theta} \right]^2 . \tag{5.12}$$

A recursive least-squares algorithm is applied [159], by repeatedly evaluating

$$\underline{P}_k = \left(\underline{P}_{k-1}^{-1} + \underline{\Phi}(\underline{s}_k)\underline{\Phi}(\underline{s}_k)^T \right)^{-1} , \tag{5.13}$$

$$\underline{L}_k = \underline{P}_k \underline{\Phi}(\underline{s}_k) , \tag{5.14}$$

$$\hat{\underline{\theta}}_k = \hat{\underline{\theta}}_{i,k-1} + L \left(\underline{c}_{road,k}(\underline{s}_k) - \underline{\Phi}(\underline{s}_k)^T \hat{\underline{\theta}}_{i,k-1} \right) , \tag{5.15}$$

for $k = 1, ..., N_t$. Whenever new data becomes available in the form of $\underline{c}_{road,N_t+1}(\underline{s}_{N_t+1})$, (5.13), (5.14), and (5.15) can be re-evaluated to arrive at updated parameter estimates $\hat{\underline{\theta}}_{N_t+1}$.

During the first observation, i.e, $k = 1$, no prior information is available. Therefore, the following initial conditions are assumed:

$$\underline{P}_0 = a \cdot \underline{I} \quad \wedge \quad \hat{\underline{\theta}}_0 = \underline{0} , \tag{5.16}$$

with a a constant that should be sufficiently large compared to the covariance introduced by measurement data, and $\underline{I}$ the identity matrix, thereby assuming no prior knowledge. In these equations, the matrix $\underline{P}_k$ can be used to estimate the covariance of the parameter estimates according to [160, p. 74]

$$\operatorname{Cov} \hat{\underline{\theta}}_{N_t} = \hat{\sigma}_{\varepsilon,k}^2 \underline{P}_k, \tag{5.17}$$

where the estimated error variance is given by

$$\hat{\sigma}_{\varepsilon,k}^2 = \frac{1}{N_{o,k} - N_\phi} \underline{\varepsilon}_k(\underline{s}_k)^T \underline{\varepsilon}_k(\underline{s}_k) . \tag{5.18}$$

There are several arguments for choosing the above method over other function-estimation methodologies. First of all, the use of a parametric approach with basis functions allows the estimated profile to be stored efficiently, with only 15 parameters per km of road. Using nonparametric methods would result in significantly higher memory requirements. Secondly, the use of a recursive algorithm gives the ability to conveniently update c_{road}-profile any time new observations become available, i.e., when the same road segment is traversed again, by simply re-evaluating the covariance matrix $\underline{P}_k$ and the parameter estimates $\hat{\underline{\theta}}$ according to (5.13), (5.14), and (5.15). This is illustrated in Figure 5.5. The figure shows the
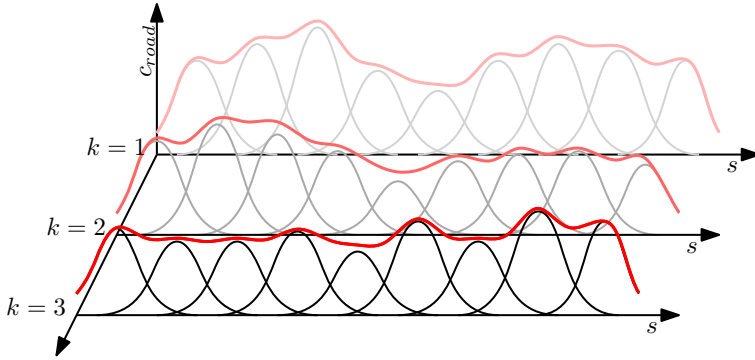
Figure 5.5. Schematic view of the road-resistance profile iteratively changing.

road-resistance profile, first shown in Figure 5.4, gradually evolving as function of the number of sets of observations k.

The above explanation describes the calculations for a single route segment i and is repeated for all segments constituting the route. In the end, the profiles of the individual road segments are aggregated into a total-route profile. Note that the resistance profile is defined as function of segment position s and not as function of traveled distance. As a result, data from vehicles with different start positions can be combined.

5.4   Battery electric bus experiment

The method described in Section 5.3 is tested on real-world data. A dedicated experiment is performed by driving a battery electric bus, as described in Section 5.4.1, repeatedly over a predefined route, as described in Section 5.4.2. The resulting dataset is summarized in Section 5.4.3.

5.4.1   Vehicle details

The used vehicle is a 12 m battery electric bus with a curb weight of 14 tonnes and a 160 kW central electric motor. The vehicle was fitted with the factory-default set of sensors which are logged via the CAN-bus. These measurement signals include the powertrain power $P_{pt}(t)$ and motor torque $T_{mot}(t)$ as reported by the powertrain inverter sampled at 20 Hz and the forward vehicle velocity $v(t)$ as measured by ABS-sensors sampled at 50 Hz. Additionally, for this test, a GPS sensor was added that reports the GPS coordinates of the vehicle at a sampling frequency of 10 Hz. Further vehicle details are provided in Table 5.1. To simulate different passenger loading conditions, the vehicle was loaded with sandbags resulting in vehicle weights also mentioned in Table 5.1.

Table 5.1. Vehicle parameters.

Parameter	Symbol	Value	unit
Vehicle weight empty	m_{empty}	14390	kg
Vehicle weight half laden	m_{half}	16355	kg
Vehicle weight fully laden	m_{full}	18350	kg
Aerodynamic coeff. ($T_{amb} = 20\,°\text{C}$)	c_a	3.36	Ns^2/m^2

5.4.2 Route details

The considered route is 9.5 km long and mainly includes a primary road and a highway. Figure 5.6 shows the route details.The route contains three longer, straight sections and is relatively flat except for two motorway links; an elevated highway on-ramp at 4-5 km and a highway off-ramp at 10 km. The figure also shows the road-type and -junctions as indicated by OpenStreetMap. Based on these, the route is divided into 7 route segments, indicated by $i = $ ①,...,⑦. Even though ② and ③ are both primary roads, these are considered separate route segments because they bear different names in OpenStreetMap. This is a result of the fact that these two roads are maintained by different municipalities, resulting in a difference in road surface between the two. The figure also shows that, based on the OpenStreetMap data, two roundabouts are identified and the two highway on/off-ramps are considered separately from the highway.

5.4.3 Resulting dataset

The instrumented vehicle described in Section 5.4.1 is driven on the route multiple times in the span of approximately one month. The vehicle adheres to normal traffic rules during driving without making any special maneuvers. The resulting dataset describes 12 trips, as detailed in Table 5.2. The trips vary in driver, vehicle load, and weather conditions. For each trip, the calculated air density is included in the last column [65]. Due to faulty measurement equipment, a part of the data is missing in trip #5. Nevertheless, this trip is still used because the presented method accepts non-equidistant data.

The signals measured continuously during each of the trips are the forward vehicle velocity $v(t)$, the powertrain power $P_{pt}(t)$, the motor torque $T_{mot}(t)$, the brake pedal position, and the GPS position. The measurements of the powertrain power also serve as a reference for the validation presented in Section 5.5.3. The brake pedal position is measured to distinguish when the dissipative brakes of the vehicle are used.

Table 5.2.   Resulting real-world dataset indicated by date, driver, average forward velocity, vehicle load incl. nr. of people on board, weather conditions, ambient temperature, and air density.

Meas.	Date	Driver	$\bar{v}$ [km/h]	Vehicle load		Weather	T_{amb} [°C]	ρ [kg/m³]
#1	2020-06-10	F.	69	m_{empty}	(+3 p.)	dry, overcast, light breeze	14	1.228
#2	2020-06-10	F.	73	m_{empty}	(+3 p.)	dry, overcast, light breeze	18	1.212
#3	2020-07-08	F.	65	m_{empty}	(+3 p.)	rain, overcast, gentle breeze	14	1.224
#4	2020-07-09	F.	74	m_{empty}	(+3 p.)	dry, overcast, moderate breeze	18.5	1.196
#5*	2020-07-09	F.	73	m_{empty}	(+2 p.)	dry, overcast, moderate breeze	21	1.190
#6	2020-07-10	H.	70	m_{empty}	(+3 p.)	dry, overcast, gentle breeze	17.5	1.210
#7	2020-07-13	F.	70	m_{half}	(+3 p.)	dry, sunny, light breeze	22	1.199
#8	2020-07-13	F.	74	m_{half}	(+3 p.)	dry, sunny, light breeze	24	1.192
#9	2020-07-14	E.	68	m_{half}	(+3 p.)	wet road, overcast, light breeze	19	1.213
#10	2020-07-15	F.	74	m_{half}	(+2 p.)	dry, overcast, light breeze	18.5	1.208
#11	2020-07-16	F.	66	m_{full}	(+2 p.)	light rain, overcast, light breeze	16	1.219
#12	2020-07-17	F.	73	m_{full}	(+5 p.)	dry, overcast, light air	18	1.213

*data missing for $s = [3.9, 4.5]$ km.
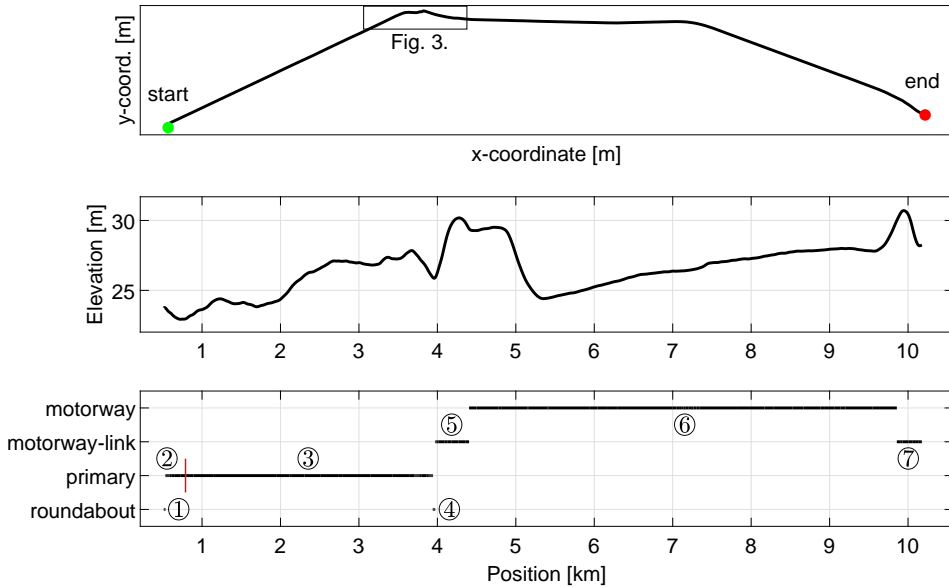
Figure 5.6. The considered route (top), including the elevation profile (middle) and the OpenStreetMap details (bottom). The numbers ①,...,⑦ indicate the route segments.

5.5 Results

This section summarizes the results of the experiments. Pre-processing of the measurement signals is explained in Section 5.5.1 and the first results are highlighted in Section 5.5.2. The resulting road-resistance profile is used in a power-request prediction in Section 5.5.3. Lastly, temperature effects are investigated in Section 5.5.4.

5.5.1 Data pre-processing and map matching

When driving over a road segment the vehicle provides data in the form of measurements of forward velocity $v(t)$, powertrain power $Ppt(t)$, motor torque $T_{mot}(t)$, and GPS coordinates. The position s_i of each measurement is determined by finding a point on the OpenStreetMap route that has the smallest Euclidian distance to the respective GPS measurement. Hereafter, the other measurement signals v, P_{pt} and T_{mot}, are interpolated to the GPS time-grid and can thereafter be defined as function of position; $v(s_i)$, $P_{pt}(s_i)$, and $T_{mot}(s_i)$. The vehicle acceleration $\frac{dv(t)}{dt}$, which is also required for (5.3), is calculated before this step, in the time-domain. To this end, the high-sampling rate forward velocity signal is fil-
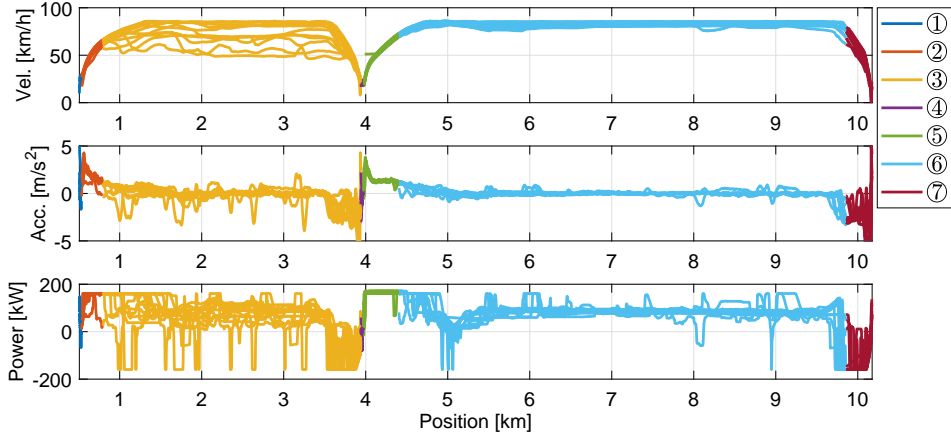
Figure 5.7. Forward velocity, acceleration, and powertrain power of the 12 trips as function of position. The seven road segments $i = ①,...,⑦$ are indicated by colors.

tered using a Savitzky-Golay filter with an approximate cut-off frequency of $0.6\,\mathrm{Hz}$ [101]. Advantages of the Savitzky-Golay filter are that it preserves high-frequency signal content well, at the cost of a limited noise reduction. Furthermore, it can be applied to non-equidistantly sampled data. Note that the filter is allowed to be non-causal, as the measurement information is processed in batches after the vehicle has completed the road segment i.

During pre-processing, all recorded CAN data is matched to the position s_i along the route segment. As a result, data from all trips can be visualized on a common position-axis, as seen in Figure 5.7. These results show that the 12 measured forward velocity profiles are similar for the majority of the route, except route segment $i = ③$, which is a primary road where more traffic might be encountered. This is also visible in the acceleration of route segment $③$. In contrast, on route segment $⑥$, which is a highway, the forward velocity is nearly constant and the vehicle can drive its maximum speed of $80\,\mathrm{km/h}$. Over the entire route, the powertrain power shows some correlation with the acceleration and often reaches the limits of $\pm\,160\,\mathrm{kW}$.

5.5.2   Resulting route-resistance profile

The measured signals $P_{pt}(s)$, $T_{mot}(s)$, and $v(s)$ of trips #1,...,#11 are used to calculate separate observations of $c_{road}(s)$ according to (5.3) and (5.2). Based on these, the method described in Section 5.3.2 is used to determine the parameters estimates $\hat{\underline{\theta}}_{N_t=11}$ for every road segment i.

After 11 iterations, i.e., $N_t = 11$, the estimated road-resistance profile $\hat{c}_{road}$ is
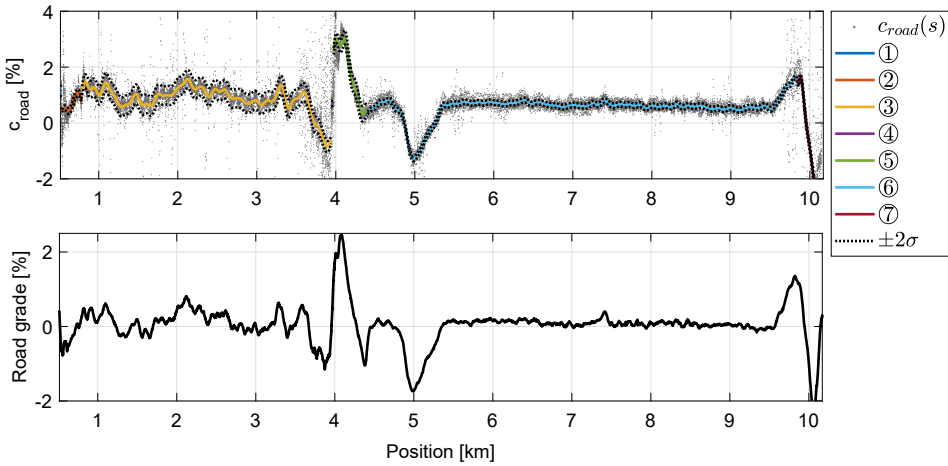
Figure 5.8. Road resistance coefficient $\hat{c}_{road}(s)$ for all seven route segments ①,...,⑦ after $N_t = 11$ trips. 95% confidence bounds are indicated by dashed lines. The road grade, as determined from the DEM [127], is also visualised.

reconstructed according to

$$\hat{c}_{road}(s) = \underline{\Phi}(s)^T \underline{\hat{\theta}}_{11} \; , \qquad\qquad (5.19)$$

and is displayed for the entire route in Figure 5.8. Also included in this figure is the road grade. The road grade is obtained from a high-resolution DEM [127], which has been low-pass filtered using a Savitzky-Golay filter, with a spatial cut-off frequency of approximately $1/50\,\mathrm{m}^{-1}$, and differentiated with respect to position using the forward difference method. The results in Figure 5.8 show that between $5.5\,\mathrm{km}$ and $9.5\,\mathrm{km}$, where the road is nearly level, $\alpha(s) \approx 0$, the c_{road}-profile is also nearly constant at $\hat{c}_{road} \approx \hat{c}_r \approx 0.56\%$, which is a plausible value for the rolling resistance coefficient c_r of bus tires on good asphalt [103]. In contrast, in regions of the route that are sloped, e.g., the highway on-ramp at $4.0\text{-}5.5\,\mathrm{km}$ and the highway off-ramp at $9.5\text{-}10\,\mathrm{km}$, the profile of $\hat{c}_{road}(s)$ deviates from this average value and shows strong similarity to the road gradient.

The gray dots in Figure 5.8 represent the individual observations of $c_{road}(s)$ of all 11 trips. Because the measurement signals $P_{pt}(t)$, $T_{mot}(t)$, and $v(t)$ are measured at a constant sampling frequency, there are more observations of $c_{road}(s)$ on sections of the route where the vehicle speed is low, for instance at the beginning of the route, around $s = 4\,\mathrm{km}$, and near the end of the route. However, because of the $1/v(t)$ term in (5.2) the accuracy of $c_{road}(s)$ decreases with forward velocity, resulting in a wider spread of the observations here. This again motivates the condition to not take into account measurements where $v(t) < 5\,\mathrm{km/h}$. Additionally, it is worth noting that if a complete route segment is to be analyzed, persistency
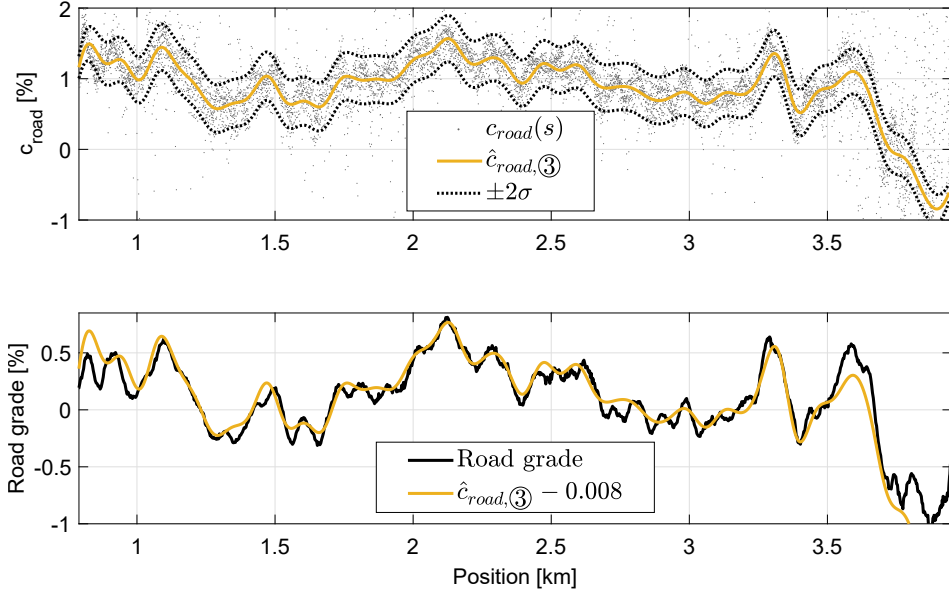
Figure 5.9. Road coefficient $\hat{c}_{road}(s)$ of road segment i $=$ ③ after $N_t = 11$ trips.

of excitation is required; the vehicle needs to be driven at a sufficiently high speed without the usage of the dissipative brakes at every position at least once.

Route segment ③ is of special interest. This section of road, which visually would be considered 'flat', displays gradient oscillations in the order of 0.5% ($\alpha \approx$ 0.3°). These small oscillations are reflected by the c_{road}-profile in this region between 0.8 and 3.9 km, which shows a strong correlation to the displayed road gradient. This is further highlighted in Figure 5.9. In the bottom part of this figure, the resulting estimated c_{road}-profile is visualized with a 0.8% offset and can be seen to coincide with the road gradient. This offset can be interpreted as an estimated rolling resistance coefficient $\hat{c}_{r,③} \approx 0.8\%$, because for small road grades $c_{road} \approx c_r + \alpha(s)$. Note that this rolling resistance value is larger than the earlier established average on road segment ⑥; $\hat{c}_{r,⑥} \approx 0.56\%$. This difference of $(0.8 - 0.56)/0.56 = 43\%$ is plausible, because rolling resistances obtained from previously conducted coast-down tests, see Appendix B, showed a similar difference between smooth asphalt and bad asphalt.

5.5.3 Leave-one-out cross-validation

As described in Section 5.5.2, 11 out of 12 trips are used to generate an estimate of the location-dependent road load coefficient $\hat{c}_{road}(s)$, as displayed in Figures
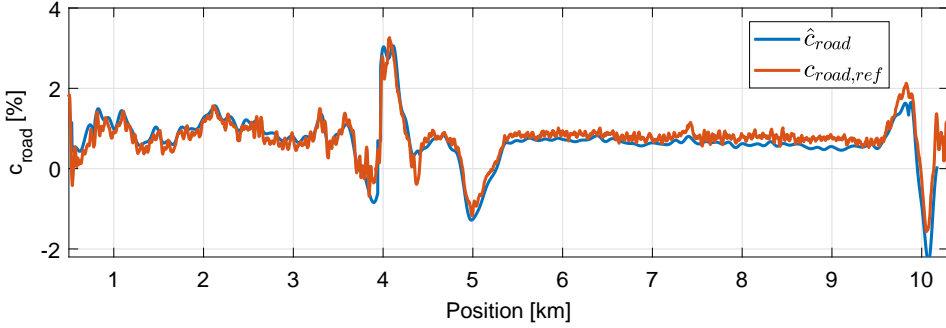
Figure 5.10. The estimated $\hat{c}_{road}(s)$ based on trips #1,...,#11 and the reference profile $\hat{c}_{road,ref}(s)$ for trip #12.

5.8 and 5.9. The 12th trip of the route is reserved for validation purposes. In the following validation, $\hat{c}_{road}(s)$ will be compared to a reference profile defined by

$$\hat{c}_{road,ref} := \cos\alpha(s)\,\hat{c}_{r,ref} + \sin\alpha(s), \tag{5.20}$$

where $\alpha(s)$ is the road gradient based on a high-resolution DEM [127], as also visualised in Figure 5.8, and $\hat{c}_{r,ref} = 0.72\%$ is an optimal constant rolling resistance, that is determined by minimizing the powertrain-power error. Taking the rolling resistance constant is a reasonable assumption because the road surface of the entire route is indicated as 'asphalt' in OpenStreetMap. Thus, no distinction can be made between the seven road segments based on this information. Both $\hat{c}_{road}(s)$ and $\hat{c}_{road,ref}(s)$ are visualised in Figure 5.10 and are shown to be similar. However, small offsets can be seen, for instance between 5.5 and 9.5 km, where $\hat{c}_{road,ref}(s)$ is consistently higher.

   Next, both $\hat{c}_{road}(s)$ based on trips #1,...,#11 and the reference profile $\hat{c}_{road,ref}(s)$ are used to predict the powertrain power request of trip #12. By substituting (5.1) in (5.2) the powertrain power request $\hat{P}_{pt}(t)$ can be calculated according to

$$\hat{P}_{pt}(t) = \left[m_{eff}\frac{dv(t)}{dt} + \hat{c}_{road}(s(t))mg + c_a v(t)^2\right]v(t) + P_{loss}(T_{mot}(t), v(t)), \tag{5.21}$$

where $v(t)$ and $T_{mot}(t)$ are the measured forward velocity and motor torque of the validation trip. This results in $\hat{P}_{pt}(\hat{c}_{road}(s))$ and $\hat{P}_{pt}(\hat{c}_{road,ref}(s))$, respectively. Both predictions are visualised in Figure 5.11 and are compared to the measured power during trip #12, $P_{measured}$. The error between prediction and measurement is also visualized and is slightly lower for $\hat{P}_{pt}(\hat{c}_{road,ref})$ in the first 4 km of the trip, and slightly higher for the remaining part of the trip. This indicates that for the first half of the trip, $\hat{P}_{pt}(\hat{c}_{road,ref})$, with its constant value for $\hat{c}_{r,ref}$, underestimates the rolling resistance, and over-estimates it for the second half of the trip. This larger error is confirmed when calculating the RMS power error defined
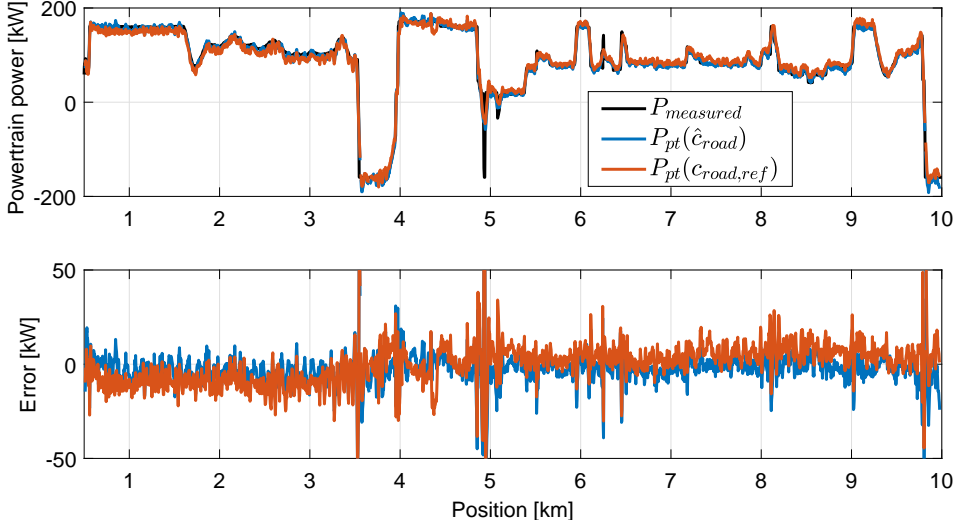
Figure 5.11. Estimated and measured powertrain power of trip #12 (top) and the error of both compared to measurements (bottom).

as

$$PE_{RMS}(\hat{c}_{road}(s)) := \frac{1}{160\,\mathrm{kW}} \sqrt{\frac{1}{N_{m,k}} \left(\hat{P}_{pt}(\hat{c}_{road}(s)) - P_{measured}(s)\right)^2}, \quad (5.22)$$

where $N_{m,k}$ is the total number of data points in the $k = 12$th trip, and the factor $1/160\,\mathrm{kW}$ is used to scale the error with respect to the maximum power of the vehicle. The resulting errors for the power predictions of trip #12 are

$$PE_{RMS}(\hat{c}_{road}(s)) = 6.0\% \quad PE_{RMS}(\hat{c}_{road,ref}(s)) = 8.2\% \,.$$

Note that the value for $\hat{c}_{r,ref} = 0.72\%$ in $\hat{c}_{road,ref}(s)$ has been obtained by minimizing $PE_{RMS}(\hat{c}_{road,ref}(s))$ and it is therefore the optimal average constant rolling resistance coefficient for this approach. Nevertheless, the results show that using the estimated road-resistance profile $\hat{c}_{road}(s)$ results in a lower power error, indicating that the rolling resistance is not constant over the entire route. For this particular route, the rolling resistance seems to be slightly higher on route segments ② and ③, which are primary roads, and slightly lower on route segment ⑥, which is a highway with relatively new, smooth asphalt. The proposed method captures these effects accurately and also includes gradient estimation without requiring a high-resolution DEM.

A leave-one-out cross-validation is performed by repeating the above validation procedure for different estimation and validation datasets combinations. In all cases, 11 trips are used to estimate the position-dependent road load profile

Table 5.3. Results of leave-one-out cross-validation.

Validation Set	$PE_{RMS}(\hat{c}_{road,ref}(s))$ [%]	$PE_{RMS}(\hat{c}_{road}(s))$ [%]	Difference [p.p.]
#1	8.5	6.7	-1.8
#2	7.4	4.5	-2.9
#3	7.6	6.9	-0.7
#4	8.8	5.5	-3.3
#5	8.7	7.3	-1.4
#6	10.4	8.5	-1.9
#7	8.9	7.3	-1.6
#8	8.6	7.1	-1.5
#9	6.3	5.6	-0.7
#10	6.9	5.2	-1.7
#11	9.8	8.5	-1.3
#12	8.2	6.0	-2.2
Average	8.3	6.6	-1.7

$\hat{c}_{road}(s)$ and the remaining trip is used as validation. The order of the 11 estimation trips is arbitrary because no weighting is applied in the RLS algorithm. For each validation dataset, the rolling resistance coefficient $\hat{c}_{r,ref}$ in $\hat{c}_{road,ref}(s)$ is determined by minimizing $PE_{RMS}(\hat{c}_{road,ref}(s))$ for the respective validation dataset. The results are displayed in Table 5.3. These clearly indicate that, irrespective of the validation dataset, the error consistently decreases when using the c_{road}-profile, compared to $\hat{c}_{road,ref}(s)$. On average, the proposed method reduces the RMS power error PE_{RMS} from 8.3% to 6.6%. This is a strong indication that using a constant rolling resistance results in a less accurate power-request prediction even when the optimized value is known. In contrast, the proposed RLS method with Gaussian basis functions captures the position-dependency of the rolling resistance. Furthermore, the estimated $\hat{c}_{road}(s)$ also includes the effect of road gradient, which is per definition position-dependent.

Likely, $\hat{c}_{road}(s)$ includes other physical effects or modeling errors that are correlated with position apart from rolling resistance and road gradient. One example is the energy lost due to additional tire slip when cornering, which only occurs in the corners of the route, as is described in Chapter 3. Even though these additional effects are technically not rolling resistance, the fact that additional unmodeled dynamics are included in $\hat{c}_{road}(s)$ can improve the power-request prediction because future vehicles are likely to experience these same effects.
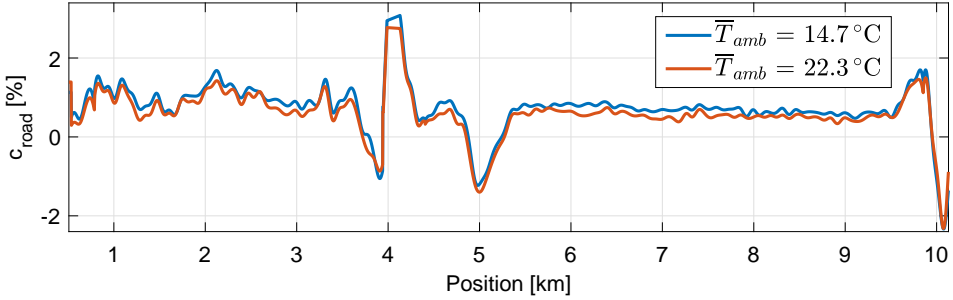
Figure 5.12. The estimated c_{road}-profile as result of analysing trips #1, #3, and #11 ($\overline{T}_{amb} = 14.7\,°\mathrm{C}$) and trips #5, #7, and #8 ($\overline{T}_{amb} = 22.3\,°\mathrm{C}$).

5.5.4   Temperature effects

Because $\hat{c}_{road}(s)$ includes the rolling resistance coefficient c_r, it is expected to have similar physical dependencies. After the road-surface type, the temperature has the second largest effect on the rolling resistance of pneumatic tires [55]. To evaluate if this effect is captured by the proposed method, the trips in Table 5.2, are divided into separate sets. Three trips with the lowest ambient temperatures, trips #1, #3, and #11 are combined, as well as the three trips with the highest ambient temperatures; #5, #7, and #8. This results in a low temperature dataset with an average ambient temperature $\overline{T}_{amb} = 14.7\,°\mathrm{C}$ and a high temperature dataset with an average ambient temperature of $\overline{T}_{amb} = 22.3\,°\mathrm{C}$. Both these datasets are each used to estimate a $\hat{c}_{road}(s)$ for the entire route, the result of which is visualised in Figure 5.12.

The results shown in Figure 5.12 indicate that the colder dataset results in an overall higher c_{road}-profile. This is also evident when the profiles are averaged over s, thereby averaging out the influence of the road gradient, resulting in:

$$\bar{c}_{road}\big|_{\overline{T}_{amb}=14.7\,°\mathrm{C}} = 0.69\% \qquad \bar{c}_{road}\big|_{\overline{T}_{amb}=22.4\,°\mathrm{C}} = 0.55\% \ .$$

The results indicate a decrease of 20% between the cold-weather and warm-weather datasets. This is more than the expected decrease based on literature [33], which dictates a rolling resistance decrease of 7% for passenger car tires over the same temperature interval. Note that the difference cannot be ascribed to a change in air density because this is included in the model as described in Section 5.2.3.

Several reasons can explain this exaggerated temperature effect. Firstly, two of the three cold-weather trips are driven on a wet road, which has an increasing effect on the rolling resistance c_r. Secondly, two of the three warm-weather trips were recorded as the second trip of that day, implying that the powertrain and tires are likely to have already reached operating temperature. Most other trips were driven at the beginning of the day, without prior heating of the vehicle. This difference in heating of the powertrain components, especially the drive-axle oil, can cause a
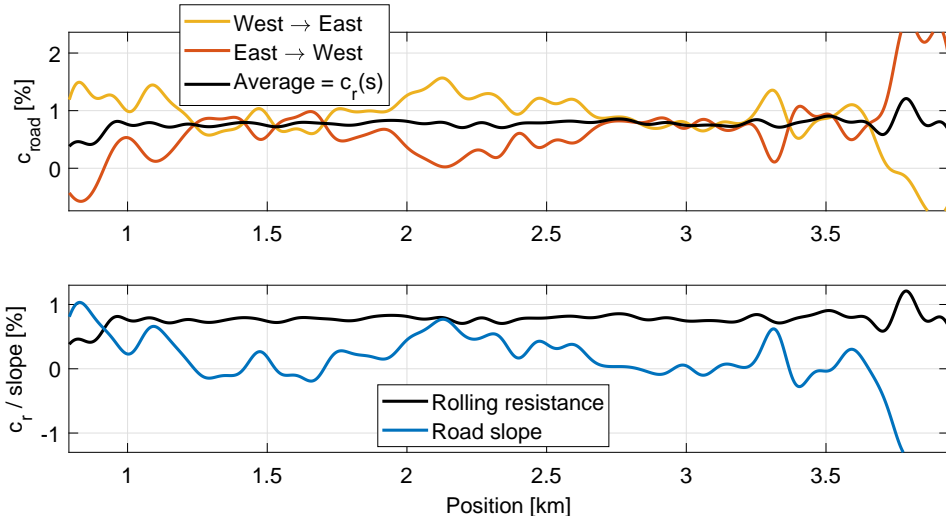
Figure 5.13. Road resistance profile of road segment ③ as determined from two different driving directions (top) and the resulting rolling resistande and road grad (bottom).

significant difference in the powertrain losses, which is reflected here as a change in $\hat{c}_{road}(s)$. Nevertheless, the results indicate that there is a strong temperature dependency in $\hat{c}_{road}(s)$, which reflects the change of the rolling resistance and also that of other physical effects.

5.5.5 Separating rolling resistance and road grade

Throughout this work, the rolling resistance and road grade are considered in a combined c_{road}. A possibility exists to separate the two parameters if a route segment is traversed in the opposite direction as well, because the sign of the road slope will change with respect to the rolling resistance. This is demonstrated in Figure 5.13, where the $\hat{c}_{road}$-profile of route segment ③, which was driven from west to east, is repeated. A road resistance profile is also shown based on two trips where the vehicle traversed the segment in the reverse direction, from east to west. Assuming that both lanes of the road are of the same surface type and have the same road slope, the average of these two profiles $\hat{c}_{average}(s)$ represents the rolling resistance, according to:

$$
\begin{aligned}
\hat{c}_{average}(s) &= 0.5\left(\hat{c}_{road}(s)_{W\rightarrow E} + \hat{c}_{road}(s)_{E\rightarrow W}\right) \\
&\approx 0.5\left(\hat{c}_r(s) + \hat{\alpha}(s) + \hat{c}_r(s) - \hat{\alpha}(s)\right) \\
&\approx \hat{c}_r(s)\,.
\end{aligned}
\tag{5.23}
$$

Subsequently, the a road slope estimate can be determined according to

$$\hat{\alpha}(s) = \hat{c}_{road}(s)_{W \to E} - \hat{c}_{average}(s) \ . \tag{5.24}$$

The resulting rolling resistance and slope profile are both displayed in Figure 5.13 and indicate that the rolling resistance is indeed constant over almost the entire segment, as is assumed in Section 5.3.1. Deviations at the beginning and end of the segment are likely due to a wider median strip at these locations causing the road slopes of both lanes to no longer be equal.

5.6   Conclusion

A recursive least-squares method with Gaussian basis functions is proposed to identify the position-dependent road resistance coefficient to accurately predict the powertrain power request of electric vehicles. Route segments are defined to include both the continuous nature of road gradient and the possible discontinuities due to changes in rolling resistance. The method is tested on data gathered by a 12 m battery electric bus, driving the same 9.5 km route 12 times, under varying conditions. The results indicate that including the estimated road-resistance profile improves the accuracy of the power-request prediction by from 8.3% to 6.6%, i.e., by 1.7 percent point, with respect to using a high-resolution elevation model and an optimized constant rolling resistance.

Based on the estimated road-resistance profile from 11 trips, it is shown that road gradient features, such as highway on-ramps and off-ramps, are easily recognizable. Furthermore, even small gradient oscillations, in the order of 0.5% are captured well. Also, the effect of a changing rolling resistance is recognizable in the results, ranging from 0.8% for route segment ③ to 0.56% for route segment ⑥. The road-resistance profile is shown to be strongly temperature dependent, displaying a 20% decrease for a 7.5 °C ambient temperature increase. This effect can partially be explained by the decreased rolling resistance at higher temperatures, yet also other unmodelled effects might be captured here, such as the temperature-dependent powertrain losses.

The used RLS parameter estimation method is computationally cheap and, because of its recursive aspect, allows for the easy addition of new observations of the same route segments. While the results in this chapter are based on data from electric buses, the underlying method can, in theory, be used to combine data from electric vehicles in general. In this case, vehicles from which data is combined should have the same expected rolling resistance coefficient, e.g., similar type of tires and suspension. Additionally, the mass and the powertrain losses of the considered vehicles should be known or determined otherwise.

Future work remains to prove that the method can be applied to data originating from different vehicles with possibly different powertrain characteristics. Assuming this is feasible, the method described in this chapter could be used to

estimate the road-specific resistance for an entire route network based on data from a fleet of similar electric vehicles. Secondly, weights can be introduced in the recursive-least squares method to empathize the importance of more recent trips, thereby enabling tracking of temporal changes due to weather influence or road maintenance in the road resistance.

6

Online and driver-specific velocity prediction for e-bus energy consumption estimation

Abstract - *To facilitate dynamic vehicle scheduling for battery electric city buses, a real-time online energy consumption prediction model is proposed. The model utilizes the current forward vehicle velocity and position, combined with knowledge of the remaining route, to predict the total trip energy. The model consists of a remaining forward velocity profile predictor and a longitudinal dynamics model. The algorithm is demonstrated in a Hardware-in-the-Loop experiment with a battery electric bus. The model has an average error of 3.1% with respect to the total trip energy and adapts in real-time to unexpected acceleration and deceleration events. In the supplementary section of this chapter, the forward velocity prediction is adapted to driver characteristics. Based on telemetry data from a fleet of electric buses, differences are established in the longitudinal vehicle acceleration realized by different drivers. Driver-specific acceleration curves are defined by describing the measured acceleration and deceleration per forward velocity using probability density functions. Using these driver-specific curves in an energy consumption model results in differences up to 17%, which is comparable to the measured energy difference between drivers of 14%.*

6.1   Introduction

BATTERY Electric Buses (BEBs) are increasingly used for inner-city public transport. The vehicles emit no local pollutants and potentially offer a lower Total Cost of Ownership (TCO) because of relatively low running expenses. However, adaptation is still relatively low, partially because, compared to conventional diesel vehicles, BEBs have a smaller driving range due to the limited energy density of their batteries [16]. Additionally, the driving range is uncertain, because it can vary as function of road, weather and vehicle conditions and the performed drivecycle [161]. This results in BEB schedules being conservative, sometimes even including redundant vehicles.

Dynamic vehicle scheduling offers a possible solution by no longer fixing time tables in advance, but rather making them flexible based on traffic conditions [48], electricity pricing [49] or battery degradation [50]. In the dynamic version of this vehicle scheduling problem, the schedule is based on both current information as well as predictions regarding the future [48]. In order to make optimal dynamic schedules for BEBs, it is beneficial to have up-to-date and accurate predictions regarding the energy that will be consumed for a trip and the remaining driving range.

Previous research indicates that using route information can be useful to predict the future energy consumption of an electric vehicle [55]. The same study also indicates that it is beneficial to include up-to-date estimations of rolling resistance and mass during driving to give a more accurate prediction during the trip. The same is suggested by [162]. However, most of this research focuses on predicting certain parameters of the vehicle model, based on the observed difference between measured and modeled energy consumption, while omitting the effect of the current forward vehicle velocity has on the prediction. While other studies do focus on online prediction of the future forward velocity [163, 164], many of these methods are data-driven and cover a limited horizon.

This chapter presents an online method to predict the future forward vehicle velocity, based on the current speed and route data, and uses this information for the energy consumption prediction (ECP) on a BEB. The method is tested by implementing a MATLAB Simulink model in Vector CANoe and performing real-time Hardware-in-the-Loop (HiL) tests.

This chapter is organized as follows. In Section 6.2 the method applied to predict the future forward velocity and energy consumption are explained. In Section 6.3 the experimental setup of the HiL test is explained, including route details and vehicle specifications. The results of this test are presented and discussed in Section 6.4. Conclusions are given in Section 6.5. Furthermore, additional results regarding the characterization of the acceleration behavior of different drivers are presented in Section 6.6. A supplementary discussion in Section 6.7 reflects on these results and summarizes the presented methods that perform online and driver-specific velocity-profile prediction.

6.2   Future energy consumption prediction

The model works in two steps to predict future energy consumption using a physics-based approach. Firstly, the forward velocity driven along the remaining part of the route is predicted. Secondly, a physics-based energy consumption model calculates the required energy to drive this velocity profile.

6.2.1   Future forward velocity profile prediction

The future forward velocity profile prediction is based on route information and the current position and speed of the vehicle. The entire route is discretized, consisting of N points. For each of these points $i = 1, ..., N$ along the route, the following information is assumed to be known:

- GPS coordinates $p_i \in \mathbb{R}^2$ [deg.]
- Cumulative distance from start d_i [m]
- Legislated maximum speed $v_{leg,i}$ [m/s]
- Local road curvature c_i [1/m]
- Boolean indicating (bus)stops b_i [-]

During operation, a vehicle will start at the beginning of the route, near p_1, and will subsequently pass all the points along the route, until arriving at the end of the route p_N. To make a prediction regarding the remaining part of the route, it is imperative to know the current position of the vehicle with respect to the route. To this end, a map matching algorithm is applied.

Map matching

The route is represented by $N - 1$ route sections, indicated by s_i in Figure 6.1. Each section s_i is defined by its vertices p_i and p_{i+1}. A straight-forward, computationally efficient map-matching algorithm is applied, which identifies the section the vehicle is currently traversing by calculating the shortest Euclidian distance l_i between the most current GPS measurement p_v and each of the sections s_i, as shown in Figure 6.1. The sections for which this distance l_i is shortest, is assumed to be the one where the vehicle is currently driving. This index, specifying the current location of the vehicle, is expressed as I;

$$I = \underset{i}{\operatorname{argmin}} \, l_i \, . \tag{6.1}$$

The speudocode to this map-matching algorithm is listed in Section 6.7.1.
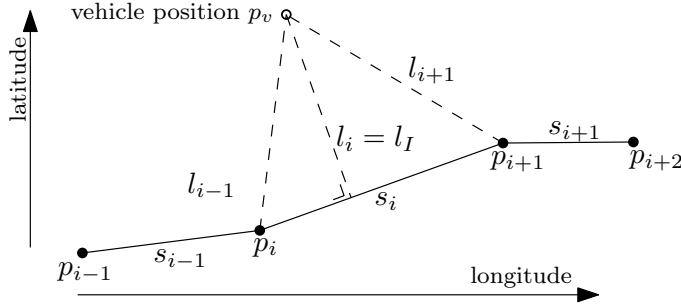
Figure 6.1. Map matching: Schematic view of the shortest Euclidian distances (l_{i-1}, l_i, l_{i+1}) between the vehicle position and the respective route sections (s_{i-1}, s_i, s_{i+1}).

Forward velocity prediction algorithm

Given the vehicle is currently at position p_I, the challenge is to predict the forward velocity v_i for all remaining route points $i = I, ..., N$. As first step, the velocity limitations due to corners are included by considering a maximum lateral acceleration $a_{y,max}$. This corner-limited forward velocity is determined as

$$v_{curv,i} = \sqrt{\frac{a_{y,max}}{|c_i|}} \quad \forall \quad i = I, ..., N \ . \tag{6.2}$$

Secondly, the vehicle is assumed to make a full stop at every bus stop. Therefore, the stop-limited speed is described as

$$v_{stop,i} = \begin{cases} 0 & b_i = 1 \\ \infty & b_i = 0 \end{cases} \quad \forall \quad i = I, ..., N \ , \tag{6.3}$$

where no speed limitations ($v_{stop,i} = \infty$) are imposed on the points that are not stops.

Lastly, the vehicle is assumed to adhere to the legislated maximum speed $v_{leg,i}$. Therefore, together with (6.2) and (6.3), a maximum forward velocity envelope v_{max} can be described;

$$v_{max,i} = \min(\, v_{leg,i}, \, v_{curv,i}, \, v_{stop,i}\,) \quad \forall \quad i = I, ..., N \ , \tag{6.4}$$

which the vehicle is assumed to never exceed.

This maximum forward velocity envelope is discontinuous, which is unrealistic, because the longitudinal vehicle acceleration and deceleration are finite. Therefore the forward velocity profile has to be adapted to include the finite acceleration. This is realized by step-wise forward time-integration of the profile with a limited
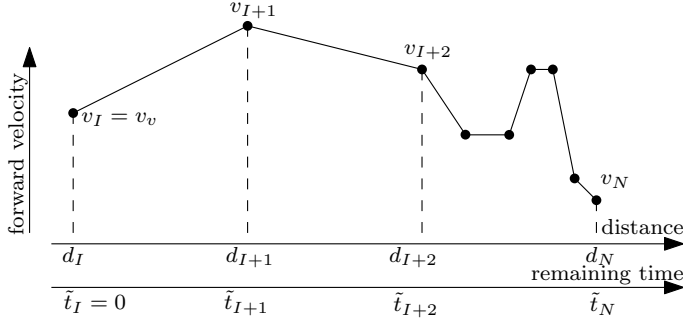
Figure 6.2. Predicted future forward velocity at the route points defined both as function of distance and remaining time.

longitudinal acceleration $a_{x,acc}$;

$$v_{i+1}^{acc} = \min \left\{ \int_{t_i}^{t_{i+1}} a_{x,acc} dt + v_i^{acc}, v_{max,i+1} \right\} \ \forall \ i = I, ..., N-1 \ . \qquad (6.5)$$

Important here is that the currently measured forward velocity v_v is used as starting point for this procedure, i.e.

$$v_I^{acc} = v_v \ , \qquad (6.6)$$

thereby including the current vehicle velocity in the prediction. Similarly, backwards time-integration is performed, starting at $v_N = 0$, to ensure that the decelerations do not exceed a maximum value $a_{x,dec}$;

$$v_{i-1} = \min \left\{ \int_{t_i}^{t_{i-1}} a_{x,dec} dt + v_i, \ v_{i-1}^{acc} \right\} \quad \forall \quad i = N, ..., I+1 \ . \qquad (6.7)$$

After applying (6.5) and (6.7) to $v_{max,i}$ described by (6.4), v_i represents a future velocity profile defined at each of the route points $v(p_i)$, and thus also as function of distance $v(d_i)$.

Distance-time conversion

For each of the future route points $i = I, ..., N$, the expected arrival time $\tilde{t}$ with respect to the current time t_I is calculated:

$$\tilde{t}_i = \sum_{k=I}^{i-1} \frac{2 \left(d_{k+1} - d_k \right)}{v_k + v_{k+1}}, \quad \forall \quad i = I+1, ..., N \qquad (6.8)$$

which is based on the assumption that the acceleration is constant between two route-points, as seen in Figure 6.2. Note that, because p_I signifies the current position of the vehicle, $\tilde{t}_I = 0$. Now, the forward velocity profile for all the future route points is defined as function of the remaining time: $v(\tilde{t}_i)$.

6.2.2   Remaining energy consumption prediction

A physics-based model is applied to predict the energy required to drive the future forward velocity profile $v(\tilde{t}_i)$. Because the model relies on knowledge regarding the acceleration, the calculations are performed per route section s_i. Therefore, forward velocity $v_{s,i}$ and acceleration $a_{s,i}$ are calculated for every route section $i = I, ..., N-1$:

$$v_{s,i} = 0.5 \left(v_i + v_{i+1} \right) \quad [\text{m/s}] \tag{6.9}$$

$$a_{s,i} = \frac{\left(-v_i + v_{i+1} \right)}{\left(-\tilde{t}_i + \tilde{t}_{i+1} \right)} \quad [\text{m/s}^2] . \tag{6.10}$$

By modelling the longitudinal dynamics of the vehicle, the average driving force at the wheels can be determined as

$$F_{wheel,i} = m_{eff} a_{s,i} + c_r \, m \, g + c_a v_{s,i}^2 , \tag{6.11}$$

where m_{eff}, m, c_r, and c_a are vehicle parameters described in Table 6.1. Note that, due tot the characteristics of the route described in Section 6.3.2, no road slope component is considered. From $F_{wheel,i}$, the electric power delivered by the traction inverter is determined as

$$P_{inv,i} = F_{wheel,i} v_{s,i} + P_{loss} \left(v_{s,i}, F_{wheel,i} \right) , \tag{6.12}$$

where P_{loss} represents a previously measured powertrain losses map, see Appendix B. By summing the inverter power over the remaining route, the remaining energy consumption is determined to be

$$E_{remaining} = \sum_{i=I}^{N-1} P_{inv,i} \cdot \left(\tilde{t}_{i+1} - \tilde{t}_i \right) . \tag{6.13}$$

Trip energy consumption prediction

Simultaneously, the consumed powertrain energy

$$E_{consumed} = \int_{t_0}^{t_I} U_{HV,measured} \, I_{HV,measured} \, dt . \tag{6.14}$$

is recorded by the model based on the measured traction inverter Direct-Current (DC) voltage $U_{HV,measured}$ and current $I_{HV,measured}$. In the calculation of both $E_{remaining}$ and $E_{consumed}$ the effects of the battery efficiency are assumed to be small. The total trip energy is determined by combining this measured energy with the predicted remaining energy:

$$E_{trip} = E_{consumed} + E_{remaining} . \tag{6.15}$$
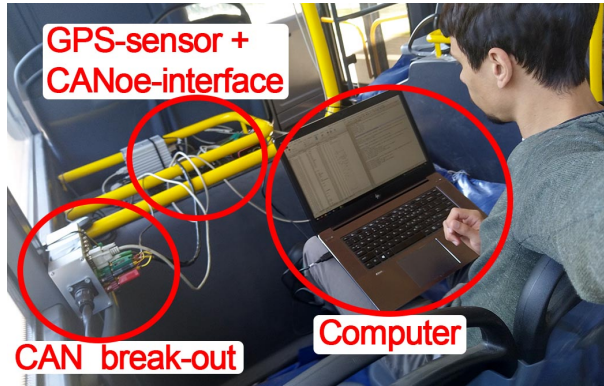
Figure 6.3. Photo of the HiL-setup in the vehicle, including the CAN break-out, GPS-sensor, CANoe-interface, and the computer.

6.3 Case study: bus trip

The online ECP algorithm, as described in Section 6.2, is implemented in MAT-LAB Simulink, and interfaced via Vector CANoe to the CAN-bus of a battery electric city bus, as seen in Figure 6.3. This HiL setup allows for real-time reading and processing of several sensor signals including:

- GPS position $p_v \in \mathbb{R}^2$ [deg.]
- Forward vehicle velocity v_v [m/s]
- Estimated vehicle weight m_{ECAS} [kg]
- Traction inverter voltage $U_{HV,measured}$ [V]
- Traction inverter current $I_{HV,measured}$ [A].

6.3.1 Test vehicle

The vehicle used for this test is a series-production $12\,\mathrm{m}$ battery electric city bus equipped with a $170\,\mathrm{kW}$ central motor and a $288\,\mathrm{kWh}$ battery pack. The vehicle is fitted with the factory-default set of sensors, and an additional GPS-sensor.

The vehicle features an Electronically Controlled Air Suspension (ECAS) that uses pressure measurements in the air-bellows to estimate the current weight of the vehicle. This estimate m_{ECAS} is used as indicated in Table 6.1. The estimated weight provided by the ECAS can vary incorrectly due to vehicle acceleration or suspension kneeling. Therefore a processed signal $\tilde{m}_{ECAS}$ is created that only registers the ECAS vehicle weight if the vehicle is 1) standing still, 2) not kneeled, and 3) the accelerator pedal is not pressed. The effective mass of the vehicle is

Table 6.1. Parameters used in the online ECP model.

Parameter	Symbol	Value	Unit
Vehicle weight	m	$\tilde{m}_{ECAS}$	kg
Effective vehicle mass	m_{eff}	$1.02\,m$	kg
Aerodynamic coefficient	c_a	3.36	kg/m
Rolling resistance coefficient	c_r	0.007	-
Acceleration limit in prediction	$a_{x,acc}$	0.9	m/s^2
Deceleration limit in prediction	$a_{x,dec}$	-0.8	m/s^2
Lateral acceleration in prediction	$a_{y,max}$	1.5	m/s^2
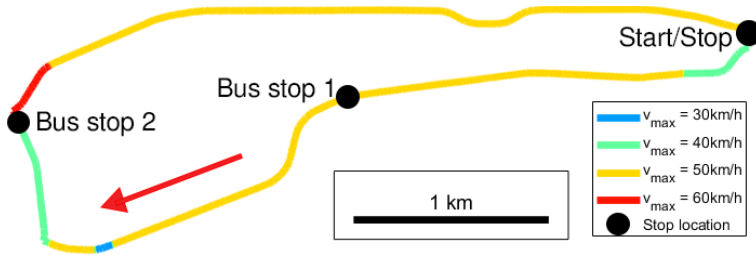
Figure 6.4. The used test route, driven clockwise, with bus stops indicated as black dots and the legislated maximum sped indicated by color.

assumed as 102% of the vehicle weight, where the 2% represents the contribution of the rotating mass of the vehicle drivetrain. This includes the rotor of the motor, drive-axles, and the six tires. Defining this rotating mass as ratio of the vehicle weight results in a rough estimate for the effective mass that is valid for 12 m as well as 18 m vehicles. During the measurements, the vehicle is loaded with sand bags to half of its maximum capacity to simulate passenger load.

Except the mass, all further vehicle parameters are assumed constant, as listed in Table 6.1. The rolling resistance coefficient c_r and aerodynamic coefficient c_a originate from coast-down tests performed with a similar vehicle. The table also shows the assumed acceleration limits $a_{x,acc}$, $a_{x,dec}$, and $a_{y,max}$ used in the prediction of the remaining forward velocity profile. These are based on previously measured speed profiles of the same vehicle.

6.3.2 Route information

For the HiL test, a route is defined to represent a typical city bus trip. The route is shown in Figure 6.4 and features several legislated maximum velocities ranging from 30 km/h to 60 km/h. Apart from the start/stop point, there are two further bus stops. At each of these stops, the driver is instructed to make a full stop,
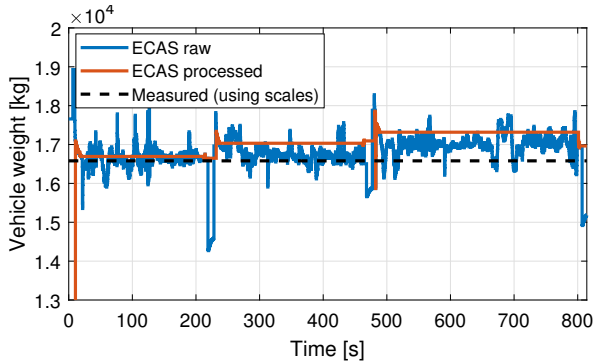
Figure 6.5. Vehicle weight according to the ECAS system for trip #4.

open the doors of the vehicle, and wait for 7 seconds before resuming the trip. In the online ECP algorithm, the 8.725 km route is discretized into $N = 1285$ points, resulting in an average section length $||s_i||$ of 6.8 m. The route is nearly flat, therefore no road slope component is included in (6.11).

The route is located in a rural area, to minimize the effect of traffic. Nevertheless, some disturbances due to oncoming vehicles or cyclists are observed. The driver is instructed to drive the route as he would normally assuming passengers are onboard, while adhering to the specified maximum velocities and stopping at the abovementioned bus stops. Before the start of the series of tests, the vehicle is driven for at least 20 minutes to achieve steady-state temperatures in the powertrain and tires.

6.4   Results and discussion

The route specified in Section 6.3.2 is driven six consecutive times, where the online ECP algorithm is restarted at the beginning of every route. This section discusses the detailed results of trip #4.

6.4.1   Vehicle weight estimation

Figure 6.5 shows the estimated value indicated by the ECAS system together with $\tilde{m}_{ECAS}$ as described in Section 6.3.1. Also indicated is the actual weight of the vehicle, as determined prior to the test by placing the vehicle on scales. The results show that the ECAS weight estimate varies during the trip and slightly over-estimates the actual weight by 1.9%. The processed ECAS weight $\tilde{m}_{ECAS}$ remains constant during driving, with an average error of 2.9%, and only varies during a stop, around $t = 220$ s and $t = 480$ s. The fact that $\tilde{m}_{ECAS}$ provides an over-estimate will results in more conservative energy predictions. Nevertheless,
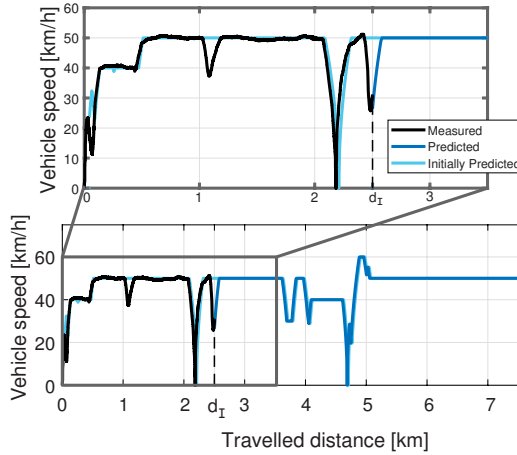
Figure 6.6. Measured and predicted forward velocity profile when the vehicle is at a travelled distance of $d_I = 2.5\,\mathrm{km}$ along the route for trip #4.

the processed signal is considered useful, because it greatly reduces unwanted fluctuations in the predicted trip energy.

6.4.2 Forward velocity profile prediction

During the experiment, the online model is repeatedly predicting the remaining forward velocity profile $v(d_i)$ as described in Section 6.2.1. All these calculations are happening online on a computer onboard the vehicle.

Figure 6.6 shows the results of this prediction at a point in time where the vehicle is 2.5 km along the route. In this situation, the forward velocity profile of the past 2.5 km is known, as indicated by the black line. For the remaining 6.2 km the forward velocity is predicted, based on the available route information and current vehicle velocity.

The results in Figure 6.6 indicate that the predicted forward velocity generally matches the measured velocity along the trip. Nevertheless, deviations due to unmodelled effects, such as traffic, can occur. In this case, the online ECP model predicts that the vehicle will accelerate before resuming the originally predicted profile, as demonstrated at $d_i = [2.5, 2.6]\,\mathrm{km}$ by the steeply increasing blue line. Note that prediction here does not include any future influence of traffic, and will always assume unobstructed driving from $\tilde{t}_I = 0$ onwards.

6.4.3 Energy consumption prediction

The predicted remaining energy, as described in Section 6.2.2, is visualised for this same trip #4 in Figure 6.7. This figure shows that dips in $E_{consumed}$, due to
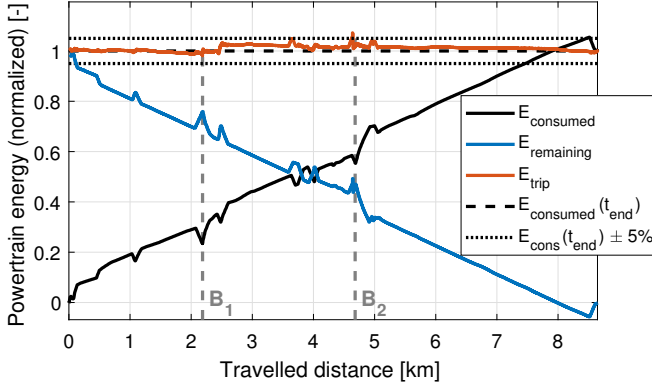
Figure 6.7. Measured and predicted energy consumption as function of travelled distance for trip #4. Bus stops are indicated by B_1 and B_2.

deceleration events, are largely compensated by peaks in $E_{remaining}$, ultimately resulting in a smooth estimate E_{trip} that generally stays within the 5% of the actually consumed energy. When the trip is finished, the predicted and measured energy consumption are per definition equal.

In case of an unexpected deceleration event, for instance at $d_I = 2.5\,\text{km}$, E_{trip} increases to compensate for the acceleration expected after the deceleration. Likewise, in the last $0.6\,\text{km}$ of the trip in Figure 6.7, E_{trip} remains lower than $E_{consumed}$, because the prediction already accounts for the energy regenerated during the final braking action of the route. This illustrates the predictive capabilities of the online ECP model.

6.4.4 Weighted average prediction error

In order to quantify the observed difference, the Prediction Error (PE) is introduced for a route point i, according to

$$\text{PE}(d_i) = \frac{|E_{trip}(d_i) - E_{consumed}(t_{end})|}{E_{consumed}(t_{end})} \tag{6.16}$$

The trip energy becomes easier to predict as the vehicle progresses along the route, because the prediction only concerns the remaining part of the trip. Therefore the error is weighted by remaining distance, resulting in the Weighted Average PE;

$$\text{WAPE} = \frac{\sum_{i=1}^{n} w_i \, \text{PE}(d_i)}{\sum_{i=1}^{N} w_i}, \quad \text{where } w_i = 1 - \frac{d_i}{d_N} \tag{6.17}$$

are the weight factors that decrease linearly as function of travelled distance d_i. This way, the prediction error at the start of the trip is weighted more than the

Table 6.2. Weighted Average Prediction Error (WAPE) for six trips.

Trip #	1	2	3	4	5	6	Average
PE(d_1) [%]	2.0	6.2	1.1	0.4	9.0	7.8	**4.4**
WAPE [%]	1.6	3.4	2.4	1.2	5.1	4.7	**3.1**

predictions near the end of the trip. Calculating this value reveals that the WAPE is 1.2% for the measurement presented in Figure 6.7. This is partially the result of the fact that the model parameters Table 6.1 seem to match particularly well for this trip.

The WAPEs for further trips are indicated in Table 6.2 and range between 1.2% and 5.1% among the various trips. This variation could be caused by influences that are not considered in the current algorithm, variation in the occurance of traffic between the individual trips or unmodelled dynamics in the longitudinal vehicle model. Also the variability introduced by the ECAS weight estimator is expected to have an influence on the end results. Nevertheless, on average the WAPE is 3.1%, and is shown to be generally lower than the offline prediction error that is made at the beginning of the trip PE(d_1).

6.5   Conclusions

This chapter presents an online energy consumption prediction model that in real-time predicts the remaining energy required to complete a trip. The results show that by using the current position and speed of the vehicle, a future forward velocity profile can be determined that accounts for future acceleration and deceleration events in the route. The remaining energy consumption predicted basted on this forward velocity profile complements the consumed energy to arrive at a predicted total trip energy that is close to the consumed energy. The results of a Hardware-in-the-Loop test show that the weighted average prediction error is 3.1% over six observed trips. This indicates that the proposed methodology could provide a reliable, real-time energy consumption prediction for future dynamic planning algorithms.

Future work includes further testing of the online model with more vehicle loading conditions, different drivers, varying weather conditions, and a route that includes road slope. In a realistic scenario, where passenger occupancy can change at each bus stop, an improved method for weight estimation, that could even predict vehicle weight changes at future stops, would be beneficial. Moreover, possibilities exist to make the algorithm adaptive by including online driver characterization via nonconstant acceleration limits $a_{x,acc}$ and $a_{x,dec}$ and an adaptive longitudinal dynamics model that iteratively estimates the rolling resistance coefficient c_r as function of distance.

6.6 Driver characterization[2]

Driver behavior is an uncertain factor that significantly influences the energy consumption of an electric vehicle. Besides defining the setpoints of several auxiliary components, such as reference temperature for the Heating, Ventilation, and Air Conditioning (HVAC) system, the driver controls the vehicle's powertrain. By adjusting the accelerator and braking pedal positions, the driver controls the longitudinal acceleration of the vehicle and governs the vehicle forward velocity as function of time.

Literature suggests that driver behavior can significantly impact the energy consumption of BEBs. Based on statistical analyses, the driver aggressiveness, which quantifies the speed changes realized by a driver, in combination with the number of stops, is found to explain 28% of the variation in energy consumption [165]. Furthermore, simulations in [166] indicate that approximately 17% of the powertrain energy consumption of a BEB could be saved by optimizing the forward velocity profile between stops. Measurement data suggests a similar effect, where [167] found average energy consumptions ranging from 0.62 kWh/km to 1.24 kWh/km, amongst drivers that were monitored over several months. It is noteworthy that the results of driver behavior research on Internal Combustion Engine (ICE) vehicles cannot directly be applied to BEBs. Compared to drivers of diesel buses, drivers of BEBs are shown to drive more aggressively, achieving both higher average velocities and higher accelerations [168]. This difference is likely caused by the silent operation of the electric powertrain, thereby providing less noise feedback to the driver, and by the large available torque at low velocities. This literature serves as an indication that driving behavior is relevant and should be incorporated in the prediction to achieve an accurate prediction of BEB energy consumption.

According to [169] driving behavior can be divided into three different activities: strategical activities, tactical activities, and operational activities. Strategical activities comprise knowledge-based choices such as route planning. Because city buses adhere to fixed timetables and drive on predetermined routes, strategical driver behavior variation is expected to be low. Tactical activities happen on a smaller time scale, in the order of seconds, and include actions like the decision to exceed the speed limit or to change lanes. Finally, on the smallest, sub-second timescale, operational activities mark the exact accelerator and braking pedal positions a particular driver will use given certain strategical and tactical choices. Assuming that strategical and tactical decisions are mostly fixed for city bus drivers, this section focuses on operational driver behavior.

To enable further analysis on the operational driver behavior, a dedicated experiment is set up that monitors small time-scale data of drivers that operate

---

[2]The results in this section are based on:
O.F. Hulsebos, "Driver Behaviour Analysis for Energy Consumption Prediction in Electric Buses," M.S. thesis DC 2020.008 (Confidential), Eindhoven Univ. of Tech., Eindhoven, Jan. 2020.

electric busses as part of a public transport fleet. First, the experiment and results are summarized in Section 6.6.1. Next, a suggested method to include the driver-specific differences in the forward velocity prediction is presented in Section 6.6.2.

6.6.1   Driver-monitoring experiment

A driver-monitoring experiment is conducted to analyze how BEB drivers operate vehicles in a real public-transport fleet. To this end, a student rode along aboard selected vehicles to monitor several parameters. These parameters included the driver identity, indicated by a number here, an approximation of the number of passengers aboard, and a log of any particular events that influence the driver's reaction, such as red traffic lights. This log is supplemented by data from an action camera mounted on the observed vehicle's windshield. The camera recorded video footage of the road in front of the vehicle, high-frequency GPS position, and longitudinal acceleration. This data is later synchronized to the telemetry data of the respective vehicles, which provides powertrain power, forward vehicle velocity, and again GPS position. The telemetry data is available at a sampling frequency of 0.5 Hz, while the action-camera data is recorded with at least 18 Hz.

Two routes are specifically selected for this experiment. The routes consist mainly of dedicated bus lanes to minimize the influence of traffic on driver behavior and minimize the variability in the resulting data. For both routes, trips in the 'onward' and 'return' directions are considered independently. Data is recorded in the mornings for four days within the span of one week. In this time period, 16 different drivers were monitored over 21 trips in total. All monitored vehicles are the same type 18 m BEB. This section presents the main findings and observations from these experiments.

To make a first assessment of the speed variation among drivers, the telemetry-recorded speed data is categorized according to three vehicle states: decelerating, accelerating, or cruising. The vehicle is considered to be cruising if the magnitude of the longitudinal acceleration is below the bound of $0.275 \, \text{m/s}^2$, which corresponds to a 1 km/h speed change per second. This is assumed to be the minimally noticeable acceleration, based on the resolution of the digital driver dashboard. Beyond these bounds, the vehicle is either accelerating or decelerating, depending on the sign of the acceleration signal. Based on this division, the powertrain energy and the distribution of the acceleration states can be visualized as presented in Figure 6.8.

First of all, the figure indicates that for this single route, the powertrain energy consumption varies from 7.0 kWh (Driver 16) to 11.7 kWh (Driver 10). While the relatively large energy consumption of Driver 10 might partially be explained by the large passenger occupancy of 30 persons, other trips with a similar occupancy rate, such as the one of Driver 15, do not show the same increase. The trip of Driver 10 is also noticeable because the vehicle spends only 25% of the driving
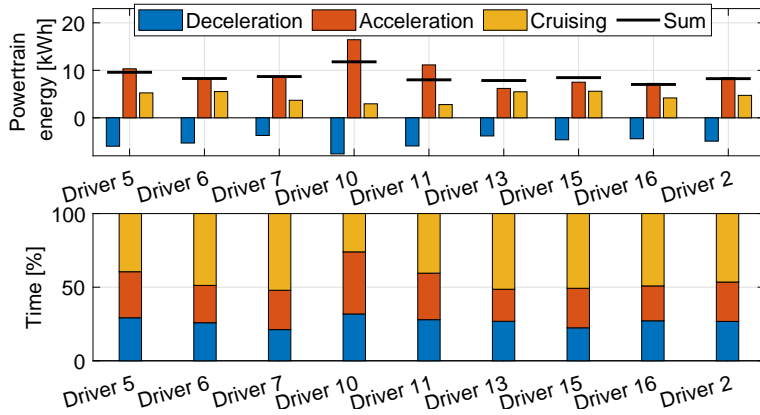
Figure 6.8. Powertrain energy measured during decelerating, accelerating, and cruising (**top**) and the percentage of driving time spent in each of these three states (**bottom**). Data shown for nine different drivers on route 1 in the 'onward' direction.

time cruising, with the remaining time either accelerating or decelerating.

Next, for a selection of drivers, the acceleration is visualized as function of forward velocity in Figure 6.9a. The data is sampled at a constant rate of $0.5\,\mathrm{Hz}$ and shows accelerations of up to $1.2\,\mathrm{m/s^2}$, and decelerations of up to $-2.3\,\mathrm{m/s^2}$. The measured forward velocity ranges from 0 to $60\,\mathrm{km/h}$, and the density of the points clouds suggests that $50\,\mathrm{km/h}$ is an often used cruising speed. When looking at the boundaries of the point clouds, it can be seen that below $10\,\mathrm{km/h}$, the maximum acceleration is limited by the motor controller, leaving little room for driver variation. However, as seen in Figure 6.9a, there is variation among drivers above $30\,\mathrm{km/h}$, with Driver 14 consistently showing slightly larger accelerations than, for instance, Driver 15. During braking, Driver 14 often decelerates at $-0.4\,\mathrm{m/s^2}$, which could indicate the default regenerative braking deceleration limit of the vehicle. On the other hand, Driver 15 often achieves larger decelerations, indicating more frequent use of the dissipative brakes. Figure 6.9b indicates similar measurements if the same driver is observed, even if the route direction changes.

6.6.2 Driver-specific acceleration prediction

The results in Section 6.6.1 indicate that the acceleration as function of forward velocity can vary amongst different drivers, yet shows good repeatability for a single driver. This supports the idea to use this data as a basis for a driver-specific velocity prediction. Therefore, a method is presented to model the acceleration characteristics specific to a driver using previous measurements of forward velocity and acceleration. The model is deterministic and is based on the method presented
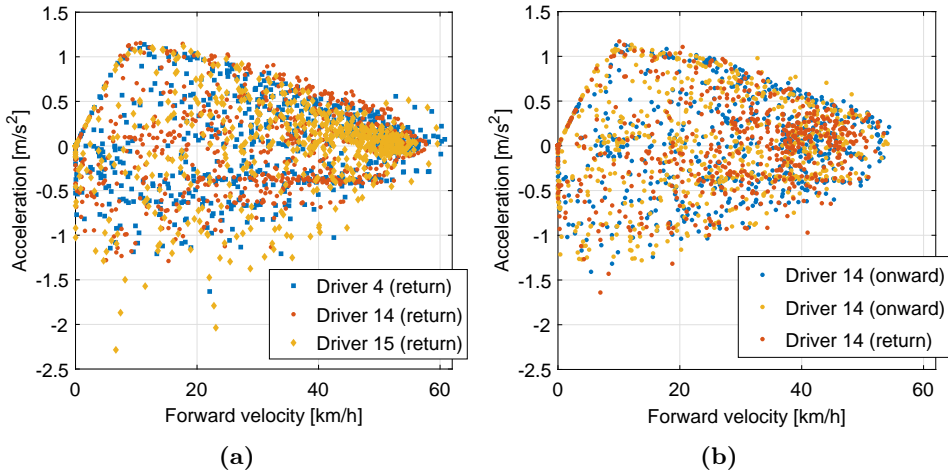
Figure 6.9.   Acceleration versus forward velocity graph for three different drivers (**a**) and for multiple trips from a single driver (**b**). Shown data is of route 1 in multiple directions.

in [170, p. 30–33] to define acceleration requirements for powertrain control.

The velocity range, as displayed on the horizontal axis of Figure 6.9, is discretized into $j = 1, ..., N_v$ intervals. This is also visualized in the top part of Figure 6.10, where instead of low-frequency telemetry data, high-frequency measurement data is used. The measured acceleration data is clustered according to these velocity intervals, as demonstrated by the histogram in the bottom part of Figure 6.10. Using this histogram, a probability density function is estimated per velocity interval j for acceleration and deceleration separately. Accelerations below a magnitude of $\pm 0.05 \,\text{m/s}^2$ are not considered for this high-frequency data and estimates are provided for acceleration and deceleration separately. A non-parametric kernel-based approach is applied to estimate these probability density functions because this requires no prior assumptions on the distribution of the data. Once an estimate is found, the accelerations indicating 90% of the Cumulative probability Density Function (CDF) are marked. These represent the values larger than 90% of all measured accelerations at this velocity. The value of 90% is chosen as this reflects a worst-case estimate of the driver acceleration with respect to energy consumption and visually matches well with the measurement data in Figure 6.10(top). Lastly, as in [170], the resulting acceleration is defined as function of forward velocity through the use of a polynomial function of v that approximates the values of the individual velocity intervals. The same procedure is repeated for the deceleration. This way, two polynomials are constructed that represents a driver-specific acceleration and deceleration as function of forward velocity.
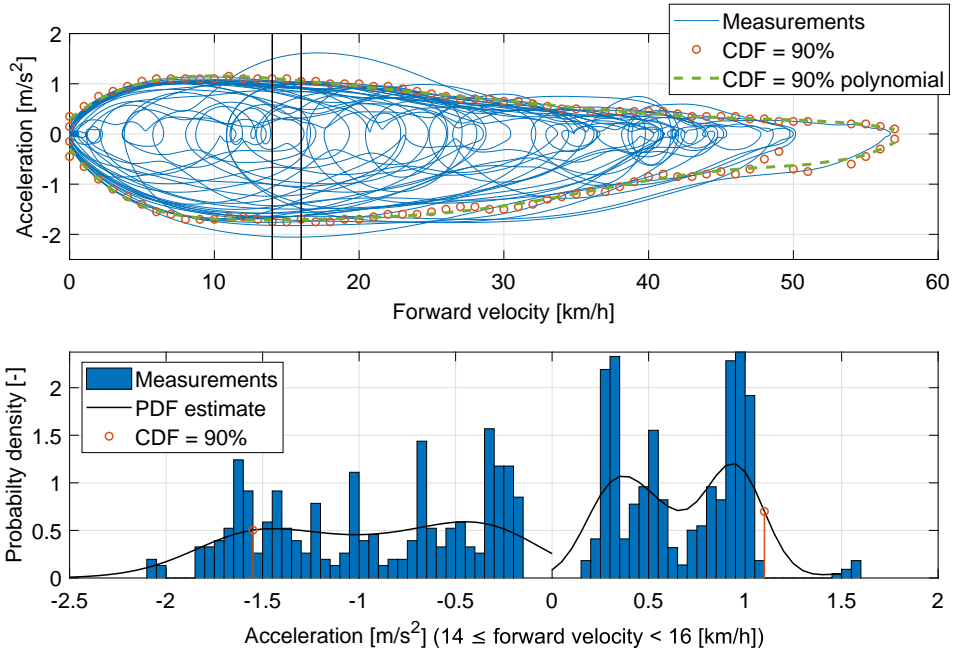
Figure 6.10. Measured high-frequency velocity data (**top**) with the estimated 90% cumulative probability accelerations of all velocity intervals, and the measured and estimated probability densities for the velocity interval $14 \leq v < 16$ [km/h]. (**bottom**).

Based on the data of Driver 14 and Driver 15, both measured in the 'onward' direction of route 1, a driver-specific acceleration function is constructed. The resulting driver characteristics are shown in Figure 6.11 and indicate that the models of Driver 14, although based on different measurements, are very similar. In contrast, the acceleration curve of Driver 15 clearly distinguishes itself, marked by a slightly lower acceleration at higher velocities and an overall higher deceleration. This difference is recognizable when a forward velocity prediction is made using these driver-specific acceleration functions.

The forward velocity profiles shown in Figure 6.11(bottom) are used as input to the longitudinal dynamics model described in Section 6.2.2. The vehicle parameters of the model are adapted to represent the 18 m vehicles that were monitored in the experiment. As a result, the dissipated and regenerated energy are visualized as function of trip distance in Figure 6.12.

The results show that both the dissipated and regenerated energy are similar for the two simulations of Driver 14. In contrast, Driver 15 discharges 4.2% more energy and regenerates 13.8% less energy than Driver 14. This is in accordance with Figure 6.11, which showed a smaller acceleration, but more substantial de-
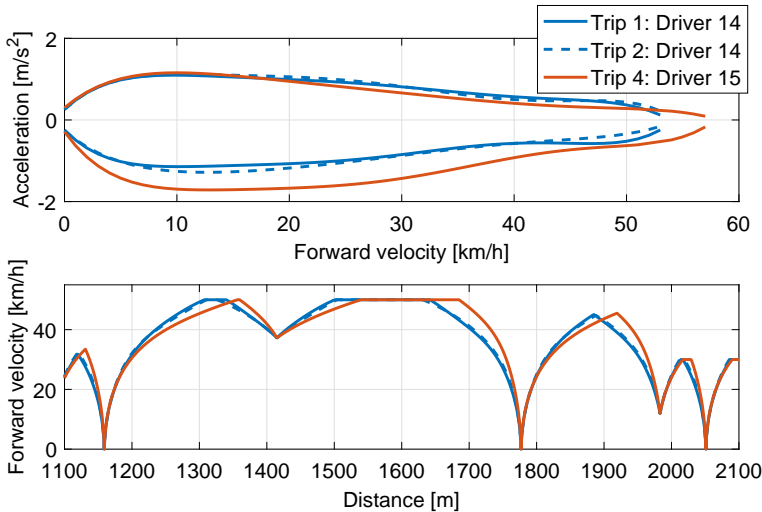
Figure 6.11. The estimated acceleration profile based on measured velocity data (**top**), and the simulated forward velocity profile using these acceleration profiles (**bottom**). Data is shown two times for driver 14 and once for driver 15.

Table 6.3. Energy consumption measured, simulated using measured forward velocity, and simulated using simulated forward velocity for two different drivers.

Energy →	Measured Energy	Measured Velocity	Simulated Velocity
Driver 14	7.45 kWh	7.03 kWh	7.50 kWh
Driver 15	8.52 kWh	8.00 kWh	8.78 kWh
Difference	+14%	+14%	+17%

celeration for Driver 15. The strong decelerations require the use of dissipative brakes, and therefore results in an overall lower regenerated energy. Summing the regenerated and dissipated energy, thereby neglecting any battery losses, reveals that the simulated energy consumption of Driver 14 and Driver 15 are respectively 7.50 kWh and 8.78 kWh. This is also listed in Table 6.3. These results are in accordance with the measured energy from the vehicle's telemetry data, which indicated that Driver 15 consumed 14% more energy than Driver 14. Even though this difference is at least partially due to other environmental factors, this exemplary result forms an indication that the provided method may be able to capture and predict part of the energy consumption variation caused by driver behavior.

Lastly, simulations using the measured forward velocity profile of Driver 14 are also indicated in Figure 6.11. Compared to the measured forward velocity,
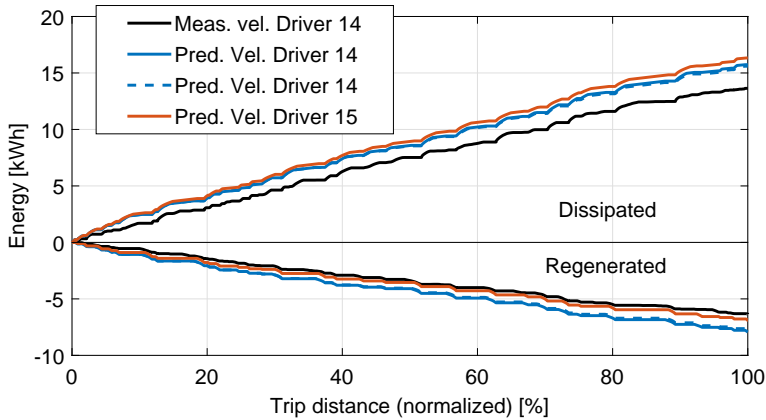
Figure 6.12. Simulation results indicating dissipated and regenerated powertrain energy. Results are shown for the three forward velocity profiles in Figure 6.11 and for the measured velocity of driver 14.

the results of the predicted forward velocity indicate a higher energy dissipation and more energy regeneration. This could be considered an indication that the predicted acceleration is conservative in terms of energy consumption, due to the fact that the simulation represents the 90% worst-case accelerations.

6.7 Supplementary discussion

The driver-specific acceleration prediction of Section 6.6.2, is applied offline to measurement data that was gathered in advance. It is also possible to apply the proposed methodology to acceleration data obtained online to characterize the driver while driving and include this information in the prediction for the remaining part of the trip. A first simulation study[3] of this online driver characterization reveals several practical issues that come along with online driver prediction. Examples of these issues are the definition of an initial driver model that is applied when no driver data is known, or a weighting function to average the measured acceleration data over time, for each of which conscious choices are to be made. A recommendation originating from this study is to use the maximum driven forward velocity as a driver-specific parameter. As the results in Figure 6.9 already suggest, this can vary among drivers, also influencing the energy consumption.

---

[3]D.T. van Blijderveen, "Real-Time Driver Characterization for Energy Consumption Prediction of Electric City Buses," Internship report DC 2021.006 (Confidential), Eindhoven Univ. of Tech., Eindhoven, Jan. 2021.

Ultimately, one could combine the online forward velocity prediction algorithm in the first half of this chapter and the driver-specific acceleration prediction of Section 6.6 to arrive at a forward velocity prediction that adapts both to the current vehicle velocity and to the specific driver operating the vehicle. However, before adding this additional model complexity, a comparative analysis should be performed to quantify the expected accuracy improvement of the energy consumption prediction when a driver-specific forward velocity profile is considered.

A remark on privacy

The driver-specific data presented in this chapter was gathered with the consent of the drivers and the public-transport operator owning the vehicles. The visualizations can purposefully not be traced back to the individual drivers. If the methods suggested here are implemented in a BEB fleet in the future, the data gathered and processed to make any driver-specific prediction should be considered 'sensitive,' as it might be used to quantify driver performance. This, however, is not the purpose of the presented work, which aims to improve the accuracy of energy consumption predictions.

6.7.1   Map-matching algorithm

The map-matching algorithm described in Section 6.2.1 is described by *Algorithm 6.1*. Given a vehicle position $p_v \in \mathbb{R}^2$ and a route defined by a list of route points $p_{1,\dots,N}$, the shortest Euclidian distance between the point p_v and the route segment s_i is determined for segment of the route. The segment for which this length l_i is shortest is considered to be the best match.

Algorithm 6.1 Map matching pseudocode.

1: **procedure** MAPMATCH($p_v \in \mathbb{R}^2$)
2:     $l_{I,min} = 999;$
3:     **for** $i \leftarrow 1$ to $(N-1)$ **do**
4:         $l_i \leftarrow$ Shortest Euclidian distance between p_v and line s_i.
5:         $|s_i| \leftarrow$ length of section s_i
6:         $l_{v1} \leftarrow |p_v - p_i|$ distance from p_v to vertex 1 of section s_i
7:         $l_{v2} \leftarrow |p_v - p_{i+1}|$ distance from p_v to vertex 2 of section s_i
                        ▷ Check whether p_v, p_{i-1}, and p_i form an acute triangle:
8:         **if** $l_{v1} + l_{v2} \leq \sqrt{|s_i|^2 + l_i^2} + l_i$ **then**
9:             **if** $l_i < l_{I,min}$ **then**
10:                 $l_{I,min} \leftarrow l_i$
11:                 $I_{min} \leftarrow i$
        return I_{min}

7

Conclusions and recommendations

7.1 Conclusions

The transportation sector is a significant contributor to global greenhouse gas emissions. City buses add to these global emissions and are responsible for a large part of the local air pollution in cities. Consequently, governments are spurring developments toward electric mobility. In these developments, Battery Electric Buses (BEBs) are one of the first solutions deployed on a large scale in city centers.

Similar to electric passenger cars, BEBs face a more limited and more critical driving range compared to conventional vehicles. To address these drawbacks, research is aimed at vehicle design and control strategies that minimize energy consumption and increase the economic viability of BEBs. Accurate models that predict the battery-to-wheel energy consumption are essential for the required analyses and potentially reduce the Total Cost of Ownership (TCO).

Achieving an accurate prediction of energy consumption is challenging due to the variability of the resistance forces and the influence of the driver. Following a physics-based approach to these predictions results in engineering insight and models that extrapolate well to new operating conditions. However, the difficulty of this approach is in achieving appropriate model complexity that accounts for the relevant physics at hand. In addition, the various model parameters have to be determined with sufficient accuracy. Therefore, the objective of this thesis is:

> *To improve the accuracy of electric vehicle energy consumption prediction methods by considering the vehicle dynamics of a battery electric bus.*

The conclusions regarding this objective are discussed according to the three research directions: 1.) physics-based extensions to the conventional energy consumption model that is described in Chapter 2, 2.) estimation of difficult-to-determine model parameters, and 3.) an adaptive forward velocity prediction algorithm. Within each of these challenges, the presented thesis aims to follow a physics-based approach with associated definitions and assumptions.

Physics-based model extension.   Extensions are found to the conventional longitudinal-dynamics model by evaluating both the lateral and the vertical vehicle dynamics. A nonlinear steady-state cornering model has been developed to assess the relevant energy losses associated with cornering. The model allows the calculation of the tire forces in different cornering scenarios and indicates that both *cornering resistance* due to the rearward component of the lateral tire force and *tire scrub* due to the double-mounted rear tires result in additional energy consumption. The model is validated against steady-state cornering tests with a 12 m BEB and is able to predict these combined cornering losses with an accuracy of 0.5%. Using data from a fleet of BEBs, it is established that cornering resistance is the most relevant of the two effects and that the cornering losses combined constitute up to 5.8% of the powertrain energy consumption on curvy city routes.

The vertical vehicle dynamics are considered by defining a quarter car model to simulate the suspension dynamics of a BEB. The simulated suspension deflection is validated against measurements of an 18 m bus traversing a known road surface. The validated model is applied in simulations of several realistic road classes. The results indicate that the power dissipated in the dampers on rough roads of class D can be up to 13% of the baseline powertrain power. While these *damper losses* are often attributed to the rolling resistance, the road-roughness dependency is emphasized by this result.

Parameter estimation.   The above findings are a prime example that model parameters, such as the rolling resistance, can vary along a route and that additional dynamics, such as cornering losses, can have a relevant impact on energy consumption. Both these effects are position-dependent. A method is proposed to estimate position-dependent model parameters in the form of the rolling resistance coefficient and local road grade based on measured powertrain data. The method employs recursive least-squares with Gaussian-basis functions in the position-domain to estimate a *road-resistance profile* along pre-defined route segments. Based on cross-validation of twelve measurements, the resulting road resistance is shown to improve a power-request prediction error from 8.3% to 6.6% with respect to a conventional method, without requiring a digital elevation model.

Forward velocity prediction.   An online algorithm is developed that predicts the expected forward velocity profile for the remaining part of a bus trip, which is an important variable that influences the energy consumption of a BEB. The

current vehicle position and speed serve as the initial value of this prediction. The *online forward velocity prediction* is used to predict the remaining powertrain energy required to complete the trip in real-time and responds to unexpected decelerations. The algorithm is demonstrated in a Hardware-in-the-Loop test with a 12 m BEB. The online prediction is shown to have an average error of 3.6% compared to the measured powertrain energy consumption, which is lower than the value of 4.4% originating from a similar offline prediction.

By controlling the vehicle speed, the driver can significantly impact the energy consumption of a BEB. By observing and measuring the driving behavior of several drivers operating 18 m BEBs in a city center, different drivers are characterized based on an acceleration-versus-velocity plot. This characterization can differentiate between drivers above a forward velocity of 30 km/h and is relatively constant for a single driver between trips. To *characterize the driver*, a driver-specific acceleration as a function of forward velocity is defined using data from these plots and used as input to an energy consumption simulation. The simulation results show an energy consumption difference of 17% between the two drivers, which is in accordance with a difference of 14% seen in the measurement data.

Remark.   Most of the percentages mentioned here refer explicitly to the power or energy of the powertrain. However, as already indicated in Section 2.6.1, the powertrain represents the majority, but not all, of the vehicle's energy consumption. Therefore, when projecting the contributions mentioned above to the total vehicle energy consumption, the resulting percentages will be approximately 70% to 80% of those mentioned here.

7.2   Recommendations

This thesis presents a physics-based approach to microscopic energy consumption prediction for battery electric buses, while focusing on the battery-to-wheels modeling. Naturally, there are several suggestions for future research and development beyond the scope of this work. These are as follows.

A complete validation on high-resolution vehicle data.   The methods described in this thesis highlight various aspects of physics-based battery-to-wheel energy consumption prediction, ranging from detailed model extensions, in Chapters 3 and 4, to a parameter estimation technique in Chapter 5 and online methods for forward velocity prediction in Chapter 6. Not all these extensions are integrated into one complete energy consumption model yet. Firstly, the required model complexity depends on the application in mind, ranging from eco-driving to life-cycle assessment. Secondly, the dynamics of some extensions, for instance the vertical dynamics model, occur on a small timescale, which can make the implementation in a microscopic energy consumption model challenging.

The extensions and suggestions in this thesis are evaluated individually using dedicated vehicle measurements. These dedicated tests allow the measurement of high-resolution, high-frequency data using non-default sensors while performing specific vehicle maneuvers and require the availability of test personnel and equipment. In contrast, fleet data can be gathered with little additional effort. However, this data often has a limited temporal resolution and a smaller number of signals, making the application of microscopic energy consumption models challenging.

Therefore, an extensive validation experiment is proposed to thoroughly assess the validity of the methods presented in this thesis on the overall prediction accuracy. A detailed dataset should be constructed by monitoring relevant signals for one or several vehicles during a prolonged time period, e.g., several months or one year, at a sufficiently high sampling rate. In this case, relevant signals would include the powertrain and auxiliary energy consumption, longitudinal, lateral and vertical vehicle acceleration, forward vehicle velocity, GPS position, and ideally passenger count or a different signal to base a vehicle weight estimate on. The availability of such a dataset would allow for the development of an extensive model based on Chapter 2 in combination with the contributions of Chapters 5 and 6. Additionally, it opens up the ability to follow a more data-driven approach to model extensions beyond the scope of this thesis, such as detailed modeling of the auxiliary components or prediction of the passenger occupancy.

Improved modeling of temperature effects. Several of the model parameters of the longitudinal dynamics model depend to some extent on temperature, as discussed in Chapter 2. In this model, and the vehicle model applied in Chapter 5, the temperature dependence of the air density is explicitly taken into account. Nevertheless, a similar approach could be followed for other parameters. This effect is included in the empirical rolling resistance estimation of Chapter 5, which is shown to vary with ambient temperature. While not considered in this thesis, the energy consumption of some auxiliary components, such as the climate system, are known to be heavily temperature-dependent. Including these effects is essential to achieve accurate range prediction.

Except for a static dependency on the ambient temperature, as described above, dynamic model extensions could be considered that introduce an internal temperature state. These could be used to model, for example, the powertrain losses and the rolling resistance, which are both known to experience a settling time of hours before reaching steady-state temperature. Including these thermal dynamics in a physics-based model is expected to increase accuracy.

Traffic influence. The forward velocity prediction discussed in Chapters 2 and 6 is based on route data, such as stop locations and maximum legislated speed, and a deterministic driver model. Even though the method presented in Chapter 6 allows the model to react to decelerations that are not predicted based on this information, it cannot predict traffic influence in advance. While the

presented framework allows for the addition of other information sources that limit the predicted forward vehicle velocity as a function of position, the challenge lies in predicting the influence of traffic in advance. This information could be estimated from historical fleet data or obtained from a commercial party.

Furthermore, including a waiting time at bus stops could be beneficial for the prediction accuracy of a possible range prediction model. Even though the powertrain dissipates little energy during these moments, the auxiliary components are active during standstill and are influenced by the opening of doors or kneeling of the vehicle.

Improved mass estimation. Vehicle mass is one of the most influential parameters in a physics-based energy consumption model. This parameter is especially relevant when considering city buses because these vehicles can experience a 40% difference in mass due to changes in passenger occupancy. This effect will only become more prominent in the future as manufacturers strive to construct lighter vehicles, while still maximizing passenger occupancy. In the baseline model, presented in Chapter 2, the mass appears in three terms of the road-load equation: the acceleration term, the rolling resistance term, and the longitudinal component of gravity. In Chapter 3 the cornering resistance scales linearly with the vehicle mass. In Chapter 5 the mass must be known to calculate the road-specific resistance. This allows for the data from different vehicles with different weights to be combined. Lastly, the mass influences the maximum longitudinal acceleration and deceleration as discussed in Chapters 2 and 6.

As discussed in Chapter 6, the vehicle mass is estimated based on the measured air bellow pressures in the Electronically Controlled Air Suspension (ECAS). However, the air bellows are subject to suspension compression due to road unevenness and longitudinal and lateral load transfer during driving. As a result, the estimated vehicle weights are not constant. To this end, the ECAS weight estimate was processed in Chapter 6 to remain constant except for certain situations where the vehicle is known to be stationary. Nevertheless, other aspects can influence the estimated weight, such as hysteresis caused by friction in suspension bushings or a sloped or banked road.

Other mass estimation methodologies could be investigated. A reference is made to [145] for a suggested list of mass estimation methodologies. The methods are based either on powertrain dynamics or on longitudinal, lateral, or vertical vehicle dynamics. While all these options are feasible, the vertical eigenfrequency of a bus with air suspension is shown to be mass-independent in Chapter 4, making the latter option the least applicable to BEBs. Ultimately, the method that requires minimal additional sensors is most likely to be adopted on a fleet level by manufacturers.

If energy consumption prediction is required for trips further in the future, the focus will shift from mass estimation to mass prediction. In this context, data-based methods that estimate the likely passenger occupancy based on historical

data could be used.

Rolling resistance and road slope estimation based on fleet data. Chapter 5 of this thesis provides a method to estimate the local rolling resistance and road slope based on power measurements of a vehicle that repeatedly travels the same route. In theory, this methodology can be applied to combine data from a fleet of similar vehicles. The introduced method already accounts for this by defining route segments that allow data from vehicles traveling different routes to be combined. Although theoretically a small step, this method still has to be tested with data from multiple vehicles with different vehicle parameters. The method can potentially be applied to monitor the rolling resistance of a road network traveled by a fleet of electric vehicles.

Model extension to range prediction. The scope of this thesis is explicitly restricted to predicting battery-to-wheel energy consumption. This type of analysis focuses on modeling the vehicle, thereby predicting the power requested from or, in the case of sufficient regenerative braking, delivered to the battery. Because the battery and its efficiency are not considered in this thesis, results are presented either as power as a function of time or as energy split up into dissipated and regenerated energy. Nevertheless, in case the driving range of the vehicle is to be predicted, a battery model will be required. Such a battery model dictates the available energy onboard and describes the efficiency applied to the regenerated and charged energy. Depending on the application of the model and required accuracy, a multitude of different battery models is available in the literature [171, 172], ranging from empirical equivalent-circuit models [173], to more physics-based electrochemical models [174].

Model applications in eco-driving and energy management strategies. Chapters 3 and 4 of this thesis highlight how the resistance forces experienced by the vehicle can be location-dependent down to a small scale, such as a single corner or a single road bump. These local resistance forces can be of importance for eco-driving methods or energy management strategies, where optimal speed profiles or auxiliary control references are sought based on model simulations. Including the local resistance forces in the evaluated model will result in different optimal solutions. An exemplary study is [175] where the optimal speed trajectory is found to reduce energy consumption if the cornering losses are included in the vehicle model.

Data-driven energy consumption prediction methods. The fact that modern BEBs are equipped with telemetry systems that gather and store data acquired by onboard sensors opens up the possibility to apply data-driven, or 'black-box', methods to the energy consumption prediction problem. Some studies predict BEB energy consumption using data-driven or machine-learning type

models [53, 176, 177]. These models are often macroscopic, with training data and predictions on a time scale of minutes or based on the time intervals between stops. In contrast, the physics-based methods presented in this thesis focus on microscopic energy consumption prediction on a sub-second time scale [52]. Although studies are directed towards making microscopic energy consumption predictions using black-box models [178], a combination of the two methods, e.g., a physics-based model structure with data-driven parameters could provide results in both the microscopic and the macroscopic domain.

Additional considerations. One of the main motivators to electrify mobility in public transport is the reduction of global emissions and local air pollution. Ultimately, the environmental impact of battery electric vehicles is largely determined by the origin of the power used to manufacture and charge the vehicle [7]. Therefore to fully exploit the environmental benefits of BEBs, a long-term goal should be to reduce the greenhouse gas intensity of the grid electricity mix in the regions where the vehicles are constructed and operated.

Appendices

A

A 2021 overview of battery electric city bus specifications

Abstract - *Driven by climate change, the public transport sector is currently transitioning to electric mobility. As part of this transition, many new battery electric buses have entered the market over the last decade. By organizing and categorizing the reported specifications of more than 130 battery electric buses, this appendix creates an overview of the state-of-the-art per 2021. The results give a distribution for the battery capacity per vehicle type and indicate that Lithium-ion Iron Phosphate and Nickel-Manganese-Cobalt are the most used cell chemistries. Central motor and wheel hub motor driveline topologies are encountered approximately equally often, and the average continuous driveline power is 7kW per tonne of vehicle weight. Based on the reported range and battery capacity, the energy consumption is 1.3 kWh/km when averaged over all vehicles. Therefore, at an occupancy rate of 38% (seated), battery electric buses offer the same energy consumption per person as an average electric passenger car. The current lack of standardization in the reported range makes direct comparison of individual vehicles difficult. Based on the charging rate and the battery capacity, depot charging and opportunity charging strategies can be distinguished in the vehicle specifications.*

A.1   Introduction

DRIVEN by climate change, the present-day transportation sector is undergoing a transition away from fossil fuels and towards electrically powered mobility [12]. In this transition, the Battery Electric Bus (BEB) is a key solution that is already employed on a large scale in many cities. Compared to conventional Internal Combustion Engine (ICE) vehicles, BEBs offer no local pollutants, reduced noise, less maintenance, and the potential of a lower Total Cost of Ownership (TCO) due to lower operational expenses [43, 130].

Since the recent revival of the BEB, both established and new Original Equipment Manufacturers (OEMs) have entered the BEB market. While these vehicles seem all similar in general terms, detailed specifications may vary. Exemplary, OEMs have a range of different battery types to choose from, which in turn can affect vehicle weight, passenger capacity, and driving range. Therefore, BEBs with various specifications exist.

There are scientific studies that focus on the general design of BEBs and reflect on the choices that OEMs and public transport operators have to make. In [44] a detailed energy consumption model of a BEB is applied to data from a fleet of diesel vehicles to consider the feasibility of electrifying the route. Using the model, different battery sizing and charging strategies are examined. As input to the model, typical BEB specifications are obtained by considering eight BEBs from different manufacturers. Similarly, in [39] a design methodology is proposed to calculate the TCO as function of the large BEB design space. This design space is explored by considering cell chemistry, vehicle size, driveline topology, auxiliary systems, and charging strategy. Typical values for each of these design parameters are combined from different OEM specification sheets and the ZeEUS eBus Report [75]. It shows that design studies such as these [39, 44, 72] require typical vehicle parameters, which are often gathered by the individual authors.

Some studies do create an overview of BEB driveline technology. [17] presents a detailed historical overview of the available bus driveline technologies and the state-of-the-art per 2015. However, the work only partially focuses on battery electric buses. More details specifically regarding BEBs are offered in [179]. However, one of the more recent of these kinds of overviews [180], dates from 2016, when the scale of the transition to BEBs has only just begun to become clear. The majority of the BEBs today have been introduced since.

More recent literature does exist but provides only few specifications on a vehicle level. [181] presents an in-depth technical overview of different zero-emission bus technologies available, also including fuel-cell buses, battery buses, and supercapacitor buses. Furthermore, other studies [43, 182] review BEBs from both a technological and economic perspective, listing current technologies and future challenges. Even though the latter study gives the specifications of an exemplary vehicle, most of these works focus more on providing an in-depth view of the various technological solutions, as opposed to reporting the current-day vehicle

specifications.

Although specifications of individual BEBs are abundantly available, there is little recent scientific work that combines this information in a single overview. This appendix aims to organize the specifications of BEBs available on the market today and list the characteristics of these vehicles. To this end, the specifications as provided by manufacturers are gathered and displayed graphically, similar to the methodology presented in [183] for electric trucks. Using this method, average values are quantified and trends in specifications are identified and discussed. This appendix is thereby an extension of a previously published conference paper [184].

The outline of this appendix is as follows. In Section A.2, the method employed to gather the vehicle specifications is explained. Next, the graphs resulting from this overview are presented and discussed in Section A.3. Furthermore, more extensive discussions on energy consumption, driving range standardization and charging strategy are presented in Section A.4. Lastly, the conclusions are summarized in Section A.5.

A.2   Methods

To give an indication of the current-day status of BEB technology, a specification overview is created. To this end, the specifications of over 130 individual BEBs are collected and indexed. The information for this overview is obtained from OEM webpages, brochures, and press releases, and also from secondary sources, such as news-websites reporting on BEB technology and the ZeEUS eBus Report [75]. A selection of the data is displayed in Table A.1.

The scope of the research is limited to battery electric city buses. Therefore, only vehicles that obtain all or most (Vehicles that use a fuel heater as HVAC solution are still included) of the energy required to independently operate the vehicle from an electric accumulator are included in the overview. Therefore, both ICE-electric hybrids and (hydrogen) fuel-cell vehicles are excluded from the overview, as well as electric trolleybuses. Furthermore, only vehicles of a Gross Vehicle Weight (GVW) of more than 8 tonnes that are specifically marketed as 'city bus' or 'transit bus' are included. Therefore, relatively small vehicles with a GVW below 8 tonnes, and vehicles used for inter-city transport, e.g., coaches, are excluded from the overview.

The information presented here is gathered by October 2021 and includes vehicles that are in production or announced to go into production later this year. The list distinguishes between prototype vehicles, which are typically only used for presentations at public events and for tests, and series-production vehicles, which are delivered to public transport operators and are operated in larger fleets.

Manufacturers included are those that are leading the market in 2020 in China [185], Europe [31, 186], North America [187] and India [188], together with several smaller OEMs. OEMs regularly launch new versions of existing vehicles or up-
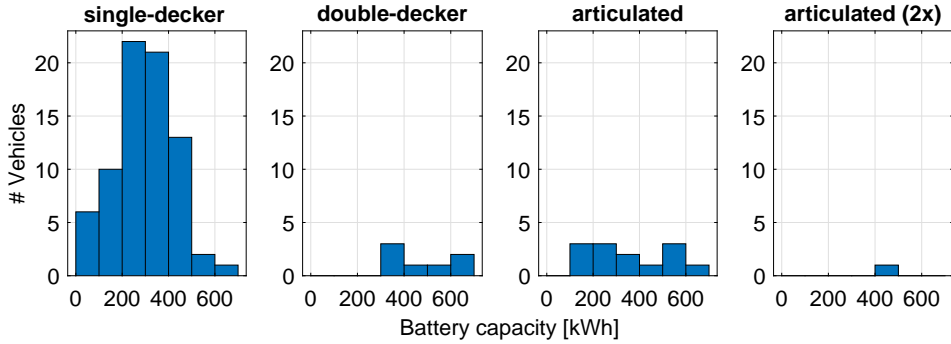
Figure A.1. Histograms of the reported battery capacity categorized per vehicle type.

date the specifications of existing vehicles. Therefore, the numbers found across different sources can be contradictory. Whenever this is the case, the most recent values are considered. Else, the data as provided by the manufacturers or news sources is used directly without making any statements on the accuracy of these numbers. Lastly, it should be noted that the majority of the indexed data originates from European and North-American manufacturers, because this information was more readily available to the English-speaking authors. In contrast, detailed specifications of Asian and Indian manufacturers are often challenging to find. Nevertheless, there are sufficient OEMs in the dataset to assume that the numbers represent the global battery electric bus market.

A.3   Results

This section presents the results of the BEB specification overview in a graphical way. Results are categorized according to battery technology in Section A.3.1, charging power in Section A.3.2, driveline topology in Section A.3.3 and Heating Ventilation and Air Conditioning (HVAC) in Section A.3.4. Because not all OEMs disclose the same specifications, the data for a single vehicle can be incomplete, as also illustrated by the blank spaces in Table A.1. Therefore, figures only display vehicles for which the specifications listed on both figure-axis are known. Figures presented in this section only include data from series-production vehicles, unless stated otherwise.

A.3.1   Battery technology

The total battery capacity is one of the main vehicle specifications of a BEB. It directly affects the vehicle's driving range and influences other important specifications, such as vehicle weight and space available for passengers. Therefore, the battery capacity as specified by the OEMs is assessed.

Table A.1. Overview of some of the indexed vehicles and some of their specifications. Vehicle Type: SD = single-decker, DD = double-decker, A = articulated. HVAC Type: HP = heat pump, FH = fuel heater, E = electric.

Vehicle	Vehicle Type	Country Manufacturer	Year Of Introduction	Overall Length [m]	Wheelbase [m]	Unladen Vehicle Weight [kg]	GVW [kg]	Capacity [passengers]	Capacity (seated) [passengers]	Reported Range [km]	Battery Chemistry	Battery Capacity [kWh]	Charging Power [kW]	Optional Fast Charging [kW]	DriveType	Power (cont.) [kW]	Power (peak) [kW]	# axles	# driven axles	HVAC Type	Source
ADL Enviro400EV 10.3m	DD	UK/China	2020	10.3		13300	19200	85	67	257	Li-ion (LFP)	339	80	112	Wheel hub motors		300	2	1	HP	[189]
Ankai 12m electric city bus	SD	China		12	6.1	18000	18000		38	290	Li-ion (unspecified)	314			Wheel hub motors			2	1	unknown	[190]
BYD K9 (june 2017)	SD	China	2017	12	3.1	13100	18000		35	250	Li-ion (LFP)	324	80		Wheel hub motors		300	2	1	unknown	[191]
Caetano E.City Gold 10.7m	SD	Portugal	2018	10.7				64		300	Li-ion (NMC)	385	150		Central motor		180	2	1	unknown	[192]
EBUSCO 3.0	SD	NL	2021	12	6.8	8530	18000	95		500	Li-ion (LFP)				Wheel hub motors		250	2	1	unknown	[193]
GAZ Electro bus	SD	Russia		12.4	6	12220	18000	85	31	56	Li-ion (LTO)	77	11	300	Wheel hub motors	120	250	2	2	unknown	[194]
Mercedes-Benz eCitaro	SD	Germany	2018	12.1	5.9		20000				Li-ion (NMC)	198		300	Wheel hub motors	125	250	2	1	unknown	[195]
Olectra K9	SD	India		12			18000		39	300	Li-ion (LFP)			80			180	2	1	unknown	[196]
Otokar e-KENT C	SD	Turkey	2019	12				100		300	Li-ion (NMC)	350			Wheel hub motors		340	2	2	unknown	[197]
Proterra ZX5+ 35ft.	SD	USA	2021	11.3	6.2	13453	19051		29	332		450	132	330	Wheel hub motors	252	410	2	1	unknown	[198]
Scania Citywide low floor	SD	Sweden	2020	13.3	7.1		20000	100	35	320	Li-ion (NMC)	330	150			250	300	2	1	HP / FH	[199]
Solaris Urbino LE 15 Electric	SD	Poland		15						200	Li-ion (unspecified)	250			Central motor		300	3	1	unknown	[200]
Tata Starbus EV	SD	India		12	6.3		19500		35		Li-ion (unspecified)						245	2	1	unknown	[201]
Temsa Avenue Elektron	SD	Turkey	2022	12.1	5.8		19000				Li-ion (NMC)		300		Central motor		250	2	1	unknown	[202]
VDL Citea SLFA-181 Electric	A	NL/BE	2015	18.2	12	19150	29000	133				216	320	480	Central motor	210	210	3	1	E / HP / FH	[203]
Volvo 7900 Electric A	A	Sweden	2019	18.7				150			Li-ion (unspecified)	396			Wheel hub motors		400	3	1	unknown	[204]
YUTONG E12	SD	China		12.2			18500	80	28		Li-ion (LFP)	423	90			120	240	2	1	unknown	[205]

In Figure A.1, a histogram details the battery capacity per vehicle type, i.e., single-decker, double-decker, or articulated vehicles. The results show that most of the indexed vehicles for which the battery capacity is known are single-decker-type vehicles. These buses, with a typical length ranging from 9 to 15 meter mostly have a reported battery capacity between 200 and 400 kWh. Furthermore, the dataset shows that articulated vehicles, which have a typical length of 18 m, and double-decker vehicles on average have a higher battery capacity. There is only one vehicle in the dataset with two articulations and a total length of 25 meter [206].

Across the indexed vehicles, various types of battery chemistry are used by the different manufacturers. If available, the reported battery chemistry is listed for every vehicle and ordered according to the number of OEMs using this technology, in Table A.2. Additionally, in Figure A.2, the distribution of observed battery capacities per vehicle is reported in a boxplot per battery technology.   Of the various

Table A.2. Overview of the battery chemistries categorized according to number of OEMs using the technology. OEMs who use multiple technologies are counted multiple times.

Cell Chemistry	# OEMs
Li-ion (LFP)	11
Li-ion (NMC)	9
Li-ion (unspecified)	8
Li-ion (LTO)	4
Li-ion (LFP, Solid-State)	2
Li-ion (LiPo)	1
Super capacitor	1
Unknown	17
Total	53

cell technologies observed, cells with Lithium-Iron-Phosphate (LFP) cathodes are the most common, followed by cells with Nickel-Manganese-Cobalt (NMC) cathode material. As can be seen from Figure A.2, battery packs with these two technologies exist in roughly the same capacity range. Smaller capacity battery packs with Lithium-Titanate-Oxide anodes (LTO) and Lithium Polymer cells (LiPo) are encountered less frequently. Also, one vehicle featuring super-capacitor-based energy storage is included in the overview [207]. Lastly, the results also show that there are already multiple OEMs that have vehicles with a solid-state electrolyte on the market [208, 209].

A.3.2   Charging power

Most OEMs offer multiple charging options for their range of vehicles. This includes a default charging option, which often consists of one - or two parallel - CCS
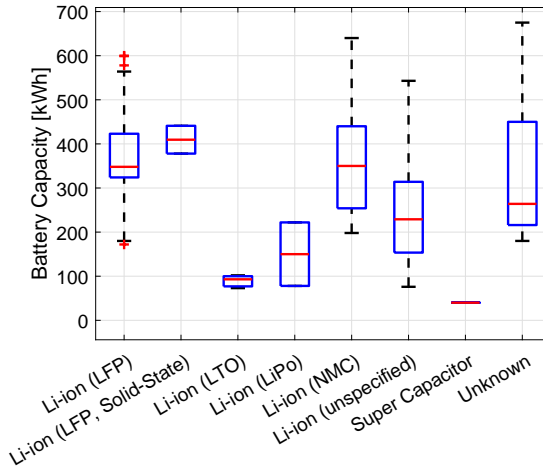
Figure A.2. Boxplots of the reported battery capacity per vehicle categorized according to battery technology.

Type 2 charger plugs, and an optional secondary charging option. The secondary charging option is typically marketed as 'fast charging' and often happens via an overhead pantograph. If available, the maximum power at which these charging options operate is recorded and visualized in Figure A.3a. In case a vehicle only supports fast (pantograph) charging, it is listed as the first charging option.

The results show that various charger powers are offered, ranging from 11 kW [194] to 480 kW [75, p. 155]. While it is difficult to recognize any trend in the maximum charger power, batteries rarely charge slower than $1/6$ C. This indicates that OEMs consider 6 hours to be the maximum charging time for any charging solution. By dividing maximum charger power by battery capacity, the maximum charging rate of the battery pack can be expressed, as shown in Figure A.3b. The results show that a C-rate below 1 is customary for most high-capacity battery packs and that there are several battery packs with lower capacities that can be charged relatively fast. This difference is further discussed in Section A.4.3

A.3.3 Driveline topology

Generally, two types of driveline topologies can be identified for BEBs; a central electric machine, which powers the wheels via a differential, or a drive-axle where the wheels are powered by two individual motors located in the wheel hubs. These same two principles are encountered in different configurations, where mostly one but also sometimes two of the vehicle's axles are driven.

In Table A.3, the two observed driveline technologies are ordered according
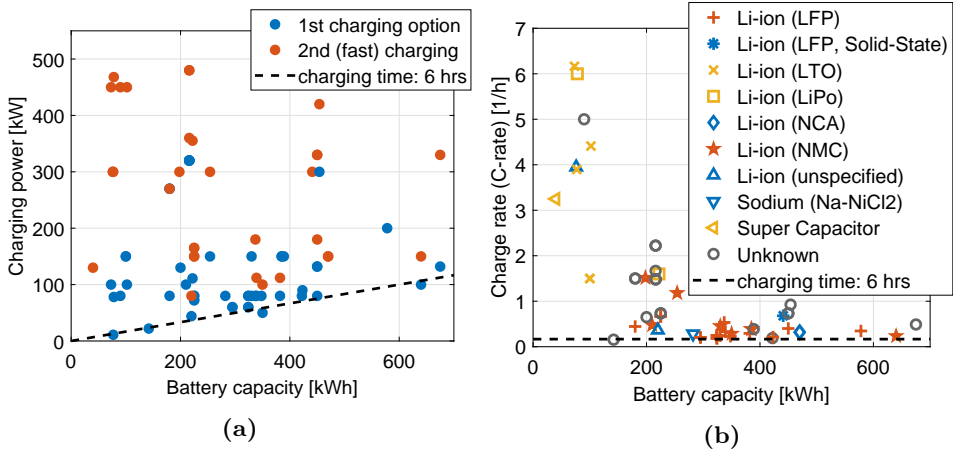
Figure A.3. **(a)** charger power (•), including optional secondary charging option (•), as function of battery capacity. **(b)** maximum charge rate as function of battery capacity for different cell chemistries. Here, typical fast charging chemistries are indicated yellow (×□◁), while typical slower charging chemistries are red (+★). In both plots, the dashed line (- -) indicates a nominal charging time of capacity/power = 6hrs. Data also includes prototype vehicles.

to the number of OEMs using this technology. Furthermore, in Figure A.4a the distribution of the reported continuous power and peak power per driven axle is visualized per topology. The results show that both driveline topologies are

Table A.3. Overview of the driveline type categorized according to number of OEMs using the technology. OEMs who use multiple technolgies are counted multiple times.

Driveline Topology	# OEMs
Central motor	16
Wheel hub motors	14
Unknown	26
Total	56

encountered approximately equally often in the group of vehicles indexed in this review. It is not uncommon for one OEM to use different topologies across their range of vehicles. Figure A.4a shows that the continuous power of both these systems is comparable and gives a slight indication that wheel hub motors offer a higher peak power.

The driveline power is generally higher for longer, heavier vehicles. This is
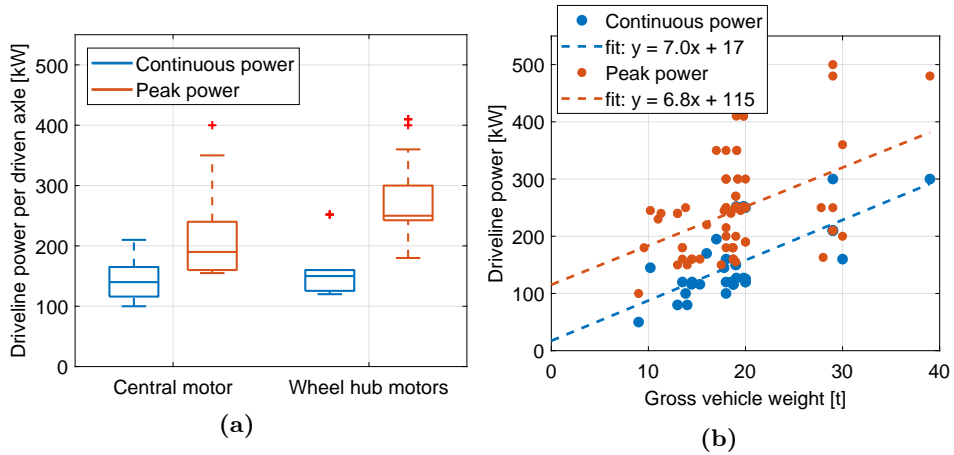
Figure A.4. Driveline power visualized in multiple ways. **(a)** shows boxplots of the driveline power per driven axle categorized according to driveline technology. **(b)** indicates the total driveline power per vehicle as function of gross vehicle weight. In both figures, both continuous power (• −) and peak power (• −) are indicated

confirmed by the data in Figure A.4b, which shows both the continuous and peak driveline power versus the gross vehicle weight. The results show that the continuous power-to-weight ratio is approximately 7 kW/t (0.009 hp/kg). The peak power shows a similar trend, with an additional 100 kW offset.

A.3.4 Heating, ventilation and air conditioning technology

The Heating, Ventilation, and Air Conditioning (HVAC) system consumes a significant part of the energy in a BEB. Compared to passenger cars, the HVAC system of a bus has to condition a larger air volume, which is made more challenging by the frequently opening doors through which both ambient air and new, unconditioned passengers enter the vehicle. After the driveline, the HVAC system consumes the most energy in a BEB [35].

In Table A.4 the type of HVAC system that is offered by the OEMs is listed. Generally, there are only three types of HVAC systems mentioned; a (diesel) fuel heater, an electric resistance heater, or an electric heat pump. As opposed to an electric heater, a fuel heater does not affect the driving range, however, it does require a separate, small diesel tank and negates the advantage that a BEB emits no local pollutants. A heat pump offers a higher Coefficient of Performance (CoP) than electric resistance heaters, thereby minimizing the negative effect on the driving range of the vehicle, while still releasing zero local emissions. The data in the table shows that only a small fraction of the OEMs are specific about the

Table A.4. HVAC type and the number of OEMs offering this technology. OEMs that offer multiple technolgies are counted multiple times.

HVAC type	#OEMs
heat pump	10
fuel heater	4
electric	3
unknown	37
Total	54

type of HVAC system that is used. Out of the manufacturers that do mention this in detail, most report to use a heat pump.

A.4   Discussions

Using the recent numbers provided in Section A.3, several topics related to BEB development are discussed here. Brief discussions are provided on topics related to energy consumption compared to consumer electric vehicles in Section A.4.1, driving range standardization in Section A.4.2, and charging strategy in Section A.4.3.

A.4.1   Energy consumption and driving range

Regardless of battery capacity, minimizing the vehicle energy consumption is relevant to maximize the driving range and minimize TCO. Figure A.5a shows the driving range reported by the manufacturers as function of the specified battery capacity. In the same figure, the GVW is indicated, which shows that the larger battery capacity is generally reserved for heavier vehicles. By taking the ratio of battery capacity and range, the average energy consumption averaged over all vehicles is found to be 1.3 kWh/km.

Next, the energy consumption per passenger is detailed in Figure A.5b, which is on average 1.5 kWh/100 km/person. Based on the values of 50 of the indexed vehicles, an average ratio between total passenger capacity and seated passenger capacity is determined to be

$$\frac{n_{passengers,total}}{n_{passengers,seated}} = 2.4 \ . \tag{A.1}$$

Using this number, the specific energy consumption per seated passenger can be derived from Figure A.5b, resulting in

$$\tilde{E}_{BEB} = 2.4 \cdot 1.5 = 3.6 \, [\text{kWh}/100 \, \text{km/pers.}] \ , \tag{A.2}$$

assuming all the seats are occupied, but no passengers are standing. This value can be compared to the average energy consumption of electric series production
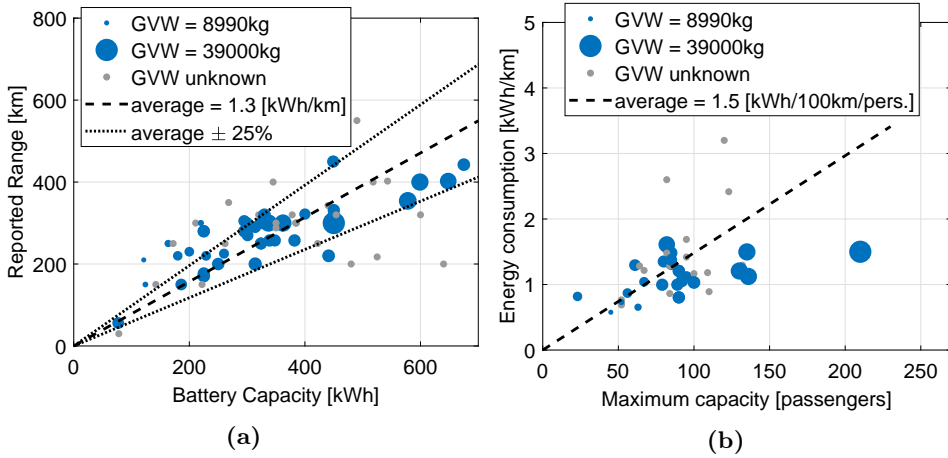
Figure A.5. Reported range versus battery capacity **(a)** together with the average energy consumption. Energy consumption is shown versus passenger capacity in **(b)**. Marker size (•) indicates vehicle weight. Also prototype vehicles are included.

passenger cars; 13.7 kWh/100 km [210, Fig. 3]. Together with the average number of occupants per vehicle: 1.45 [211], this results in

$$\tilde{E}_{car} = 13.7/1.45 = 9.4 \,[\text{kWh/100 km/pers.}] \,. \tag{A.3}$$

Therefore, a BEB offers approximately the same person-specific energy consumption as an electric passenger car if approximately $3.6/9.4 = 38\%$ of the BEB seats are occupied. Alternatively, if standing passengers are included, a fully occupied BEB transports passengers $9.4/1.5 = 6$ times more efficiently than the average electric passenger car.

The battery capacity and reported driving range of newly introduced vehicles can be visualized as function of time, see Figure A.6. Several trends can be distinguished from this figure. First of all, it can be seen that the battery capacity per newly introduced vehicle increases over time. As a result, the reported driving range increases as well. Nevertheless, this increase is not proportionate, resulting in a net increase in the reported energy consumption over time. Only in 2021 is the average energy consumption equal to the average as established in Figure A.5a: 1.3 kWh/km. For preceding years, it is generally less. This increase in reported energy consumption could be a consequence of the fact that more heavier vehicles were introduced in the later years, because most first-generation BEBs were of the 12 single-decker type, which are relatively light. A second hypothesis is that in later years OEMs are reporting more honestly about the driving range of their vehicles.
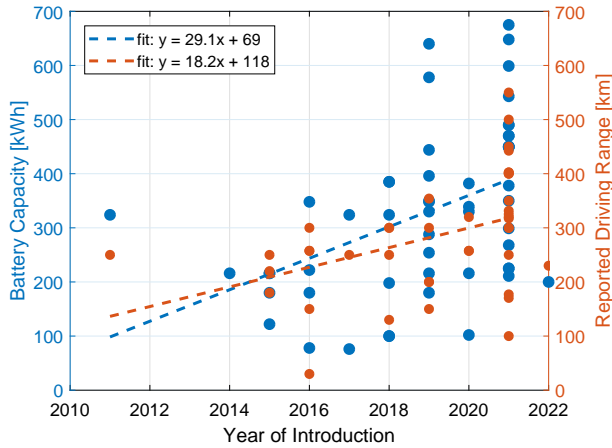
Figure A.6. The reported battery capacity (● —) and the reported driving range (● —) as function of the introduction year of the vehicle. Prototype vehicles are also included.

A.4.2   Driving range standardization

In Figure A.5a an uncertainty interval surrounding the average energy consumption by ±25% is indicated with dashed lines. This 25% is considered the approximate difference that could be caused by either including or excluding the HVAC consumption in the reported driving range number [35, Fig. 1]. Still, several vehicles exceed this boundary, indicating that there is a large spread in reported energy consumption.

Whereas some differences are expected due to design differences, part of the spread is likely caused by a lack of standardization surrounding the reported range. In the gathered dataset, only a handful of OEMs specify which driving cycles or environmental conditions are considered for the reported driving range or explain whether the value originates from simulations or driving tests. This makes a direct comparison of individual vehicles difficult.

Several standardized driving cycles exist specifically for BEBs [212, 213]. However, the variety of cycles is still large, and the usage of a particular cycle seems to correlate with the geographic region where the OEM operates. There are even examples of single public transport operators specifying their own standardized cycles [214]. Additionally, based on the data indexed here, these cycles are seldomly used when reporting driving range numbers publicly.

A.4.3   Charging strategy

When electrifying a city bus network, two main charging strategies can be considered. On one side, there is the depot-charging strategy, whereby vehicles are

charged only once or twice per 24h, typically at the bus depot. This strategy allows the vehicles to be operated similarly to diesel vehicles: driving for a large part of the day without interruption. On the other side, Opportunity Charging (OC), assumes the vehicles are charged additionally for brief intervals at some or all of the intermediate bus stops.

This choice of charging strategy has a defined influence on the vehicle design. For a depot-charging solution, the driving range should be relatively large, ideally comparable to diesel vehicles. In contrast, for OC functionality, a smaller driving range is allowed, but the vehicle should be able to recharge quickly. Some OEMs actively advertise their vehicle for either depot charging [193] or OC [207] strategies; however, the majority of the OEMs offer multiple versions of their product, thereby leaving the choice to the public transport operator. While there is scientific literature that takes a distinct stance towards a particular charging solution [39], the majority of the charging studies [44, 215] seem to indicate there is no absolute best option and the preferred solution depends on the nature of the bus routes and the optimization objectives, e.g., minimizing TCO, grid impact, or fleet size.

The two different charging strategies can be distinguished from the results presented in this appendix. First of all, the battery box plot in Figure A.2 shows clearly that LTO and LiPO cells are encountered in battery packs with a relatively small capacity. Because these cells are suitable for high-power applications, they are often used in vehicles that apply an OC strategy. This is confirmed by Figure A.3b, which shows that these cell types are also the ones boasting charging rates above 1 C. In contrast, the LFP and NMC cells are often encountered in larger capacity battery packs and have lower charge rates, making them more suitable for depot-charging strategies. Lastly, the fact that the smallest battery capacity encountered in a battery electric double-decker is still relatively large (314 kWh [216]), as seen in Figure A.1, indicates that this type of vehicle is mostly operated in a depot-charging strategy.

A.5 Conclusion

This appendix presents a specification overview of over 130 BEBs available on the market per 2021. Based on the numbers provided by OEMs and news sources, trends and average values are identified. It is established that both LFP and NMC are the most frequently encountered cell chemistries at this moment. Based on the reported charging power, a minimal charging time of 6 hrs across all vehicles can be identified. In the driveline design, central motors and wheel hub motors are encountered approximately equally often and the average nominal driveline power is 7 kW per tonne GVW. Unfortunately, only a few OEMs are specific about the used HVAC solution, but those that do, report using a heat pump.

Based on the reported specifications, it is revealed that the average energy con-

sumption of a BEB is 1.3 kWh/km, and that an occupancy rate of 38% (seated) is already enough for a BEB to match the specific energy consumption of an electric passenger car. Furthermore, during the study, it was found that the energy consumption varies significantly across vehicles, likely because standardization regarding these values is seldomly reported. Lastly, it is shown that, from the resulting graphs, vehicles that focus specifically on depot charging or opportunity charging can be identified.

B

Energy consumption prediction for electric city buses

Abstract - *Similar to electric vehicles for the consumer market, the driving range of battery electric city buses is still a limiting factor for market adoption. Furthermore, this driving range can vary depending on environmental conditions, the number of passengers, and driver behavior and is therefore often uncertain. This results in conservative charging strategies and an increased total cost of ownership of the vehicle. This appendix presents a physics-based energy consumption prediction model, aimed at electric city buses, with the goal of reducing the uncertainty regarding the energy consumption of the vehicle. The model is derived from first principles and complemented by dedicated measurements of an electric city bus, including dynamometer tests and coast-down measurements. Validation using real-world data shows that the model has the ability to accurately predict the consumed energy for the majority of the analyzed trip, although deviations, probably caused by road slope effects, do occur.*

B.1   Introduction

OVER the last decades, battery research advancements have led to increased energy density and reduced costs of battery packs [217]. These developments, together with the favorable legislation for electric mobility with respect to fossil fuel-based transportation [218], sparked a renewed interest in Battery Electric Vehicles (BEVs). The rate of adoption of BEVs varies across different markets. While diesel is generally still regarded as the most cost- efficient solution for long-distance road-freight transport, the passenger car sector is slowly evolving towards electric propulsion as the new standard. In the public transport sector, BEV implementation is also gaining traction [14]. In all sectors, the rate of adoption seems to be limited by the battery-powered alternatives having inferior driving range with respect to their fossil fuel counterparts. This results in 'range anxiety' experienced by BEV drivers and fleet operators, which is amplified by unreliable range predictions [219]. In the public transport sector, this uncertainty in range prediction gives rise to conservative charging strategies, resulting in unnecessarily long charging times, sub-optimal timetables, and the use of more (redundant) vehicles compared to a fossil fuel-powered fleet. While increasing the available battery capacity will resolve the range anxiety, this solution is not always trivial due to cost, weight, and space constraints. Therefore, until future generation batteries are developed, a more suitable method to decrease range anxiety can be found in developing more accurate energy consumption models to supply more reliable information to both drivers and public transport fleet operators. While the power drawn from the main battery of a BEV also includes the auxiliary components, such as the HVAC system, the pneumatic system, and low voltage electronics, this appendix focuses on predicting the power consumed by the powertrain, as this power varies significantly as function of a number of vehicle and environmental parameters and it is generally the most significant energy consumer of the vehicle.

B.1.1   EVERLASTING

The Horizon 2020 project EVERLASTING (Electric Vehicle Enhanced Range, Lifetime And Safety Through INGenious battery management) aims to develop innovative technologies to improve the reliability, lifetime, and safety of lithium-ion batteries by developing more accurate, and standardized, battery monitoring and management systems [57]. These novel battery technologies will be demonstrated in two vehicles, one of which is a battery electric city bus. This vehicle is also the subject of the study presented here and is henceforth denoted as the 'EVERLASTING demonstrator'. Among other technologies, the EVERLASTING demonstrator will be able to accurately predict the future power request and energy consumption of the driveline of the vehicle, as function of the route that will be driven.

B.1.2   Problem statement

While energy consumption models are widely researched for passenger cars [33, 78, 81], the available literature on electric city busses is more limited. Furthermore, much of the research that is available relies on historic data from a single vehicle or a fleet of monitored vehicles. This data dependency makes it difficult to apply the result to a specific vehicle, such as the EVERLASTING demonstrator. Therefore, this appendix presents a physics-based energy consumption model for the EVERLASTING demonstrator. In addition to the advantage of straightforward adaptation to different types of vehicles, the physics-based approach also yields more insight in the energy consumption processes and allows for better extrapolation of the results to more diverse operating conditions.

B.1.3   Approach

First, a literature overview on energy consumption models is presented in Section B.2. In Section B.3 the physics of the longitudinal dynamics of the vehicle are explained to derive an energy consumption model. Where a purely first-principles approach is difficult or impractical, dedicated measurements are supplied to provide realistic parameters for the model in Section B.4. The resulting energy consumption model is compared against real-world measurements in Section B.5, after which conclusions and future model extensions are summarized in Section B.6.

B.2   Literature overview

Vehicle energy consumption models are an extensively researched topic. The models serve different purposes, ranging from the development of eco-driving algorithms [220], to parameter sensitivity studies [78], driver behavior research [168], range prediction [33], and energy management and charging strategy studies [221]. Regardless of the purpose of the models, the aim is to predict the energy consumption of the vehicle, often as function of a set of vehicle and environmental parameters.

B.2.1   Literature on energy consumption models

There are generally two classes of energy consumption models: physics-based models and data-driven models. Physics-based models [33, 79, 221] apply the available knowledge of the energy-consuming physics. This often includes modeling the longitudinal dynamics of the vehicle and the powertrain, thereby aiming to accurately mimic the physical components of the vehicle. The models are often a 'backward simulation' of the actual power flow, starting from the dynamics of the vehicle to finally calculate the electrical power requirements at the battery terminals. While

the derivation of the model equations is generally straightforward and well understood, the challenge lies in accurately predicting or measuring the relevant input parameters for the models.

Data-driven methodologies [80] are based on statistical models describing correlations between certain input parameters and the vehicle's energy consumption. In general, the models are derived by identifying statistical relations in sets of real-world data. If this data is available, these models allow to capture complex relations between the parameters and the vehicle energy consumption. However, the quality of the model depends heavily on the available data and accuracy is not ensured in case the model is used to extrapolate outside the range of the available data. Furthermore, as the model parameters often no longer represent a physical quantity, insight into the underlying physics is lost. There are studies that combine a physics-based and data-driven approach, such as [81], where the applied methodology is mainly data-driven, but with a model structure that is strongly based on the underlying physics.

B.2.2   Energy consumption of electric city buses

In the energy consumption modeling field, some research is specifically aimed at energy consumption models for electric city buses. In [222], an electrical-mechanical road load model of an electric bus is developed and verified using real-world data. Different models for the electric drive are investigated, ranging from an efficiency map, wherein all the losses are lumped into one parameter, to a more complicated electric model of the inverter and motor. Results show a 5% error in energy consumption between measurement and simulation, in case an efficiency map is used.

B.3   A physics-based energy consumption model

In this section, the applied methodology is explained. The longitudinal equations of motion of the vehicle are used to derive expressions for the energy consumption of the powertrain. Furthermore, the relevant input parameters for the model are discussed.

B.3.1   Longitudinal vehicle dynamics

Figure B.1 shows a side-view of a vehicle with all longitudinal forces acting on it. The longitudinal dynamics of the vehicle can be described by

$$ m_{eff}\, a_x = F_x - F_{r,f} - F_{r,r} - F_{aero} - \sin(\alpha)F_g \;, \qquad (B.1) $$

where m_{eff} is the effective mass of the vehicle and a_x is the longitudinal acceleration. The effective mass includes the rotational inertia of the wheels and powertrain components that also experience rotational acceleration when a_x is non-zero.
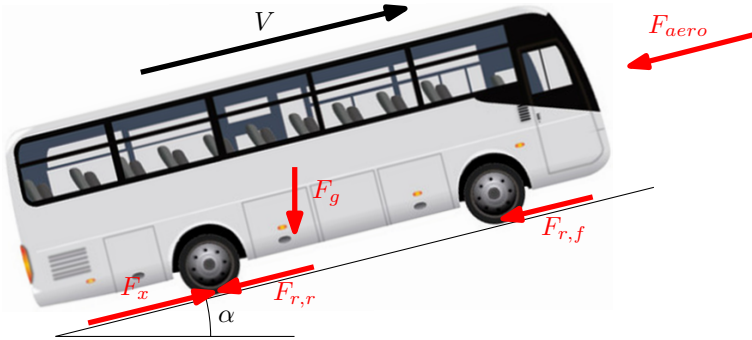
Figure B.1. Schematic side-view of a bus driving with a forward velocity V with acting forces in red.

For busses, the effective mass is typically 102% of the total vehicle mass. The right-hand side of (B.1) describes the various forces acting longitudinally on the vehicle and include the driving force F_x, the combined rolling resistance force $F_r = F_{r,f} + F_{r,r}$, the aerodynamic drag force F_{earo}, and the longitudinal component of gravity F_g. The driving force of the vehicle can be expressed as

$$F_x = \eta \, \frac{P_{DC}}{V} \ , \tag{B.2}$$

where η is the overall powertrain efficiency between battery and wheels, P_{DC} is the electrical DC power drawn from the battery by de powertrain and V is the forward vehicle velocity. The rolling resistance is modelled as

$$F_r = f_r \, F_g \cos(\alpha) \ , \tag{B.3}$$

where f_r is the rolling resistance coefficient, α is the local road gradient, and F_g is the gravitational force according to

$$F_g = m \, g \ , \tag{B.4}$$

where g is the gravitational acceleration and m is the vehicle mass. Lastly, the aerodynamic drag force is modelled as

$$F_{aero} = \frac{1}{2} \, \rho \, C_d \, A_f \, V^2 \ , \tag{B.5}$$

where ρ is the air density, C_d is the aerodynamic drag coefficient, and A_f is the frontal area of the vehicle.

Substituting the above relations into (B.1) and rearranging, results in

$$P_{DC} = \frac{V}{\eta} \left(m_{eff} \, a_x + f_r \, m \, g \cos(\alpha) + \frac{1}{2} \rho \, C_d \, A_f V^2 + \sin(\alpha) \, m \, g \right). \tag{B.6}$$

This is a closed-form expression for the power drawn from the battery by the powertrain, as function of the longitudinal velocity V and acceleration a_x, a set of vehicle parameters (η, m, C_d, and A_f), and a set of environmental parameters (f_r, α, ρ, and g). Assuming the motion of the vehicle, e.g. the forward velocity profile as function of time, is known, the challenge lies in accurately determining each of the model parameters.

B.3.2   Input parameters

In reality, the model parameters mentioned above are not constant, as is shown in Table B.1. Note that the variability of some model parameters changes with respect to research performed for passenger cars, such as [33], when electric city buses are considered. For this study, it is assumed that the constant model parameters g and A_f are easily measurable or known. However, other parameters might be more challenging to determine and are discussed below individually.

Table B.1. Model parameters and their variability for city buses, adapted from [33, Table 1].

Parameter	Dependency	Variability
g, A_f	-	constant
C_d	relative wind direction	low
ρ	weather	low
m	passenger load	high
η	velocity, torque, temperature	high
f_r	road, weather	high
α	road	high

Aerodynamic drag coefficient

Even though, as indicated in Table B.1, the aerodynamic drag coefficient is a function of the relative wind direction, this correlation is difficult to determine for a specific vehicle. Also, when driving at high velocities, the influence of the relative wind direction is reduced. Therefore, in this study, C_d is assumed to be constant. While it is possible to determine C_d using Computational Fluid Dynamics (CFD), this method requires exact knowledge of the geometry of the vehicle and extensive computational effort and knowledge. Therefore, a more pragmatic approach is used and coast-down measurements are used to determine C_d experimentally. These tests are discussed in Section B.4.2.
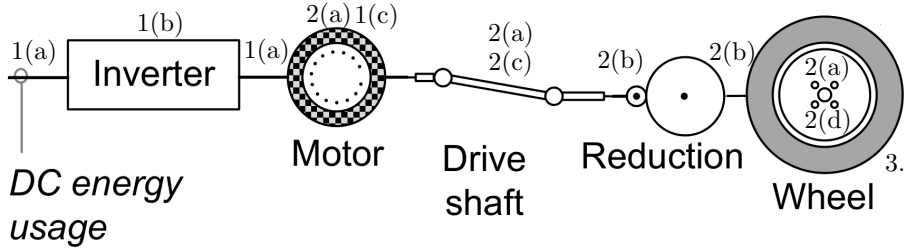
Figure B.2. Schematic overview of the powertrain with the various losses, indicated by numbers. Figure adapted from [33].

Air density

As already shown by [33], the variability of the air density can be taken into account in a vehicle energy consumption model. For this, the equations from [65] are used to express the air density as function of ambient temperature, ambient pressure, and relative humidity. These environmental weather variables are obtained from the Royal Netherlands Meteorological Institute (KNMI) [154].

Vehicle mass

In contrast to a passenger car, the total vehicle mass of a city bus can vary significantly during a route, due to variations in the number of passengers. However, exact real-time data on passenger loading is difficult to obtain. Therefore, in this initial study, the vehicle mass m is assumed to be constant.

Powertrain losses

In (B.6), the powertrain efficiency η summarizes the power losses that occur between battery and wheels. This single quantity actually represents multiple individual physical losses. Figure B.2 shows the topology of the powertrain of the considered vehicle. The power flow starts as DC current at the battery terminals and flows through the inverter to the electric motor. The resulting mechanical power is transferred through a driveshaft to the rear axle. This rear axle contains a differential gearing unit and additional reduction gears. Finally, the mechanical energy is transferred to the road through the tires. Note that the efficiency of the battery is not taken into account in this study. Inside and in between each of these powertrain components, energy losses can occur. These are summarized below:

1. **Electrical losses.** These include

   (a) **Ohmic losses** in both DC cables between battery and inverter and the 3-phase AC cables between the inverter and the motor.

(b) **Losses in the inverter**. The inverter suffers from ohmic and switching losses of the switch-mode converter, which can be approximately 3 to 4% of the total power [223, p. 266].

(c) **Losses in the motor**. These also include ohmic losses. For induction motors, these comprise 55 to 60% of the total motor losses at full load [223, p. 262]. Furthermore, there are magnetic core losses, these typically comprise 20 to 25% of the total motor losses. Further losses are due to mechanical friction in the motor (2.a) and other losses that are difficult to specify further.

2. **Mechanical friction.** Generally, all components that are lubricated experience friction and will heat up during driving, thus energy is lost here. These losses include

(a) **Bearings** in the motor, differential housing and uprights.

(b) Constant velocity **joints** of the driveshaft.

(c) **Gears**: in the rear axle.

(d) There can also be **unintended (dry) mechanical friction**, for instance in the brakes that are not fully released.

3. **Tire slip.** All tires experience slip. This can be longitudinal slip of driven or braked wheels but also lateral slip.

Because it is challenging to predict all these losses individually based on first principles, the lumped powerlosses of the powertrain is determined through measurements, as is described in Section B.4.1.

Rolling resistance coefficient

The vehicle experiences rolling resistance on all tires contacting the road. The rolling resistance force is caused by the continuous deformation at the tire-road contact patch of the rolling pneumatic tire. Due to the visco-elastic nature of the rubber in the tire, energy is lost in this process, resulting in a resistance force. This effect is captured by the rolling resistance coefficient f_r.

The physics that underly the rolling resistance are complex. Even though physics-based models exist that simulate the rubber deformation that results in rolling resistance, these models often include large finite element simulations of the tire and require extensive knowledge of the tire construction and material properties. Even if this information is available, the numerical models have difficulty finding accurate rolling resistance coefficient values, due to the many factors that can influence rolling resistance [103, p. 60]. These factors include the tire itself (dimension, structure, and material), tire temperature, tire pressure, and road condition, which further includes road surface roughness and wetness.

Due to the complexity of the rolling resistance phenomenon, it seems preferable to determine f_r in an alternative manner, that is representative of the real-world driving conditions of the vehicle. Therefore, the rolling resistance coefficient used
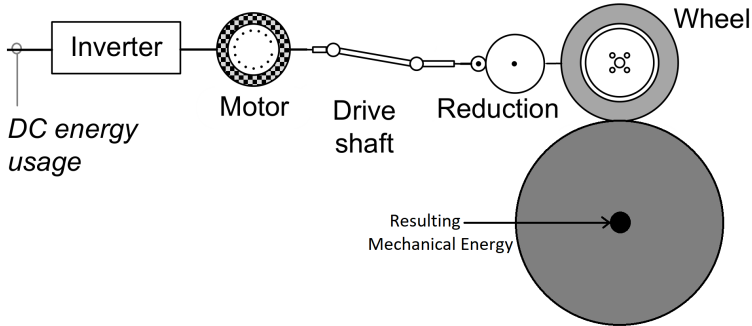
Figure B.3. Schematic of the dynamometer measurement. Adapted from [33].

in this study is determined through vehicle coast-down measurements, as is explained in Section B.4.2.

Road gradient

In (B.6) it can be seen that the road gradient has an influence on the energy consumption. However, in the current appendix, this effect is assumed negligible, because only relatively flat routes in the Netherlands are considered.

B.4 Dedicated measurements

As discussed in Section B.3, not all input parameters for the physics-based energy consumption model can be determined in a straightforward manner. Especially the powertrain efficiency, the aerodynamic drag coefficient, and the tire rolling resistance are parameters that represent the effect of complex physical processes. Therefore, this study deviates from its first-principles approach with respect to these three parameters and determines these through dedicated vehicle tests.

B.4.1 Dynamometer measurements

The combined powertrain efficiency η, as discussed in Section B.3.2, is measured for the EVERLASTING demonstrator. The methodology from [224] is used in these tests. The vehicle is fixed on the TU/e Heavy Duty Chassis Dynamometer, with the driven wheels of the vehicle in contact with the drum of the dynamometer. This drum can be powered or braked using a 260 kW electric motor. A schematic of this setup is shown in Figure B.3. During the measurement, various variables are recorded. A shunt sensor measures the DC electrical power transferred between the battery and the inverter P_{DC}. This gives an accurate value for the total power that is consumed or regenerated by the powertrain. Furthermore, the dynamometer

setup contains sensors to measure the rotational velocity of the drum and the torque applied to the drum. This allows for the calculation of the total mechanical power applied at the driven wheels of the vehicle P_{wheel}.

The purpose of the test is to determine the power loss in the powertrain P_{ptloss} as function of the motor torque and angular velocity. Assuming the powertrain of the vehicle is in steady-state, e.g. no forces/torques are required for the acceleration of masses or inertias, the power loss is defined as

$$P_{ptloss} = P_{DC} - P_{wheel} \; . \tag{B.7}$$

The powertrain efficiency η is then defined as the ratio between the power flowing out of the driveline and the power entering the driveline. As this powerflow is reversed when switching between driving and regenerative braking, two definitions for η are used:

$$\eta_{drv} = \frac{P_{wheel}}{P_{wheel} + P_{ptloss}} \qquad \eta_{brk} = \frac{|P_{wheel}| - P_{ptloss}}{|P_{wheel}|} \; , \tag{B.8}$$

where η_{drv} and η_{brk} apply for driving and regenerative braking situations, respectively.

Measurement results

The results of the dynamometer efficiency measurements are shown in Figure B.4a as function of motor angular velocity and motor torque. The figure shows the normalized powertrain efficiency η_{norm}, which is defined as

$$\eta_{norm} = \frac{\eta}{\max(\eta)} \; . \tag{B.9}$$

The results show that the powertrain efficiency varies significantly as function of motor torque and that the regenerative efficiency, e.g. the shown efficiency for negative torques, is generally lower than the driving efficiency. Due to torque limitations of the experimental setup, high torque regions of the efficiency map could not be measured. Therefore, the found relation for P_{ptloss} is extrapolated into these regions of the map, as shown in Figure B.4b. Furthermore, the figure shows that the operating points from the recorded validation data, discussed in Section B.5, are mostly within the measured part of the efficiency map.

B.4.2   Coast-down tests

Coast-down tests are performed to determine estimates for both the aerodynamic drag coefficient C_d and the tire rolling resistance coefficient f_r. During such a test, the vehicle is accelerated up to a certain speed, after which the propulsion force is removed, e.g. the vehicle is put into 'neutral gear'. During the coast-down that follows, the vehicle slows down under the influence of the road load forces

(a) Measured map   (b) Extrapolated map
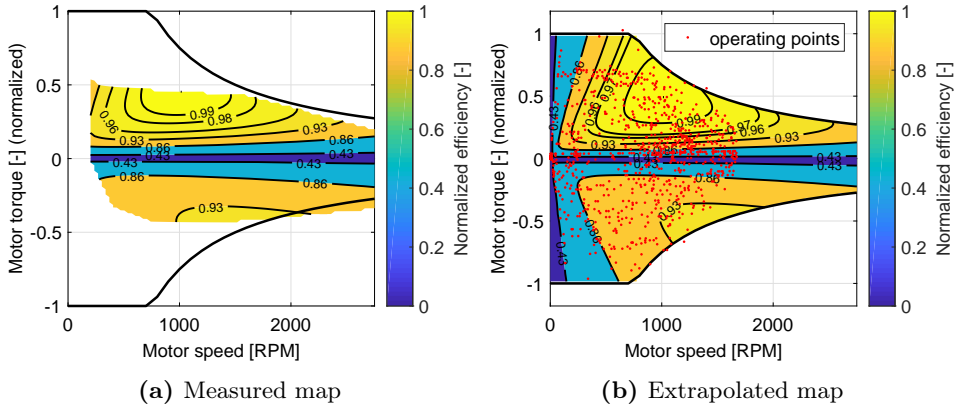
Figure B.4. Normalized efficiency map, as function of motor speed and normalized motor torque. The black lines indicate the motor torque limit.

summarized in Section B.3. From the forward velocity profiles recorded during several of such measurements, estimates for C_d and f_r can be derived.

Several of these coast-down measurements are performed using the EVERLASTING demonstrator. By performing the test at various geographical locations, thereby changing the road surface, the rolling resistance coefficient is determined for several road surfaces, ranging from Belgian blocks to good quality asphalt. A comparison between the measurement results and the rolling resistance coefficient provided by the tire manufacturer is shown in Figure B.5. It shows that the rolling resistance can vary according to the quality of the road. The figure also shows that the manufacturer-supplied value is roughly in accordance with the average value of the measurements. Both for f_r and C_d, the average value as obtained from the measurements is used for the energy consumption model.

B.5 Model validation

The energy consumption model is validated using measurement data from a real-world trip of a vehicle comparable to the EVERLASTING demonstrator. During the trip, the longitudinal vehicle velocity V is measured, along with the power consumption of the driveline. The measured velocity profile as function of time $V(t)$ and its time derivative $a_x(t)$ are used as input for the energy consumption model. Figure B.6 shows the energy discharged and regenerated by the powertrain, as measured on the vehicle and as estimated by the model. As expected, the total accumulated energies increase during the trip, where regenerated energy is defined as negative. The results show that the model closely approximates the measured discharged energy. However, there are larger deviations visible in the recharged energy profile. The majority of this error originates from the period between $370\,\mathrm{s}$
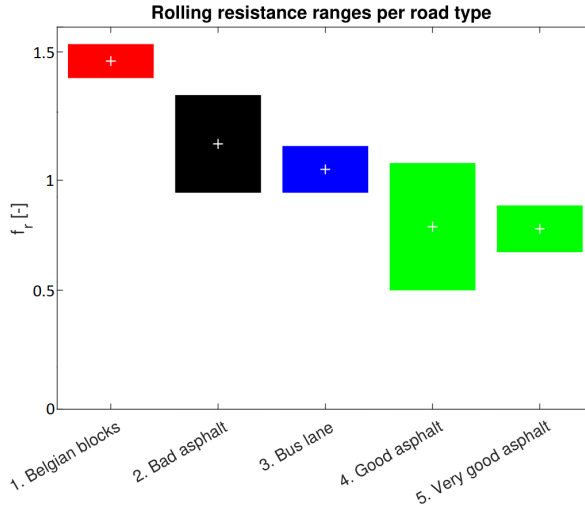
Figure B.5. Ranges for the normalized rolling resistance coefficient found on various road surfaces. Values are scaled such that the manufacturer provided value is $f_r = 1$.

and $400\,\mathrm{s}$.

Zooming in on this time period reveals that, while in reality a considerable amount of energy is regenerated, the model predicts barely any charging or discharging. A more detailed analysis of the driven route reveals that the driven road section during this time had a downward slope, which allowed the monitored vehicle to regenerate energy. Because road gradient effects are not included in the current version of the model, the regenerated energy is under-estimated.

B.6   Conclusions and outlook

An energy consumption model is derived for the EVERLASTING demonstrator, using a first-principles approach. For model parameters that are less trivial to determine, dedicated experiments are conducted.

The powertrain efficiency is measured using a chassis dynamometer and is mapped as function of motor speed and motor torque. Differences are visible between the efficiency for regenerating conditions compared to driving conditions. Secondly, the rolling resistance coefficient is measured on different road surfaces by use of coast-down tests. The measured rolling resistance coefficient is largely in agreement with the manufacturer-provided value, and shows small deviations depending on road surface quality. The coast-down test also yields an estimate for the aerodynamic drag coefficient.
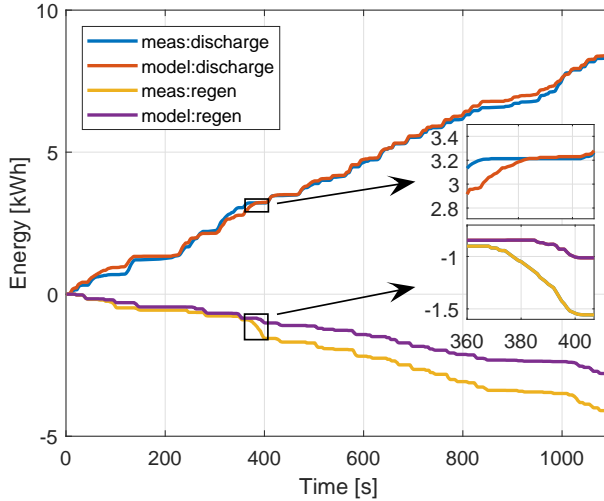
Figure B.6. Discharged and regenerated energy from the vehicle battery, from measurement and estimated by the energy consumption model.

With the measured parameters as input, the energy consumption model is validated using a recorded bus trip. The model output is compared to the measured energy consumption of the powertrain of the vehicle. The results show that for the majority of the trip, the model is able to approximate the measured energy consumption relatively closely. However, the deviations during one particular time period in the simulation indicate that road slope effects have a significant influence on the energy prediction.

B.6.1 Outlook

The validation in this appendix is based on real-world data from a single recorded trip. The resulting analysis shows that particular route characteristics can have a large influence on the model results. Therefore, to better assess the overall accuracy of the model, data from multiple trips, recorded under more varying conditions, should be used.

The energy consumption prediction model can be improved by supplying better estimates for several of the model parameters, as listed in Table B.1. As indicated by the model validation, including road height information to supply a road gradient to the model will improve the results. As the height profile from a GPS-signal is rather unreliable, it would be advisable to extract this information from a height map, was done by [33] for a passenger car. Further parameter estimates that could be improved are the rolling resistance coefficient, which could be adapted depending on road type. Also the aerodynamic model can be improved by taking into

account wind velocity and relative wind direction.

Additionally, if the model were to be implemented online, up-to-date information of the forward vehicle velocity and energy consumption could be used to further improve and adapt the model predictions. Furthermore, online prediction could also be used to estimate parameters from the additional sensor data available on the vehicle.

Supplementary remark

This appendix presents a preliminary study that demonstrates a physics-based energy consumption prediction model on a battery electric bus. While the model here focuses specifically on powertrain losses and rolling resistance measurements, other aspects are not considered, such as road-roughness variation, road gradient, and weather influence. These aspects are included in the study presented in Chapter 2, which demonstrates a complete energy consumption prediction model. Moreover, due to the physics-based nature of the model, it can easily be generalized to other types of electric vehicles.

C

Mechanical differential losses during cornering

C.1   Introduction

Electric vehicles with a central motor typically employ a mechanical differential to split the motor torque to both driven wheels while preserving independent freedom of rotation of both wheels. A simulation analysis is performed to quantify the possible additional losses that occur in this differential gear unit during cornering. First, in Section C.2, the nonlinear steady-state cornering model, presented in Chapter 3, is employed to determine the possible speed difference between the left and right axle. Next, Section C.3 details the methods and assumptions involved in calculating the additional gearing losses compared to straight-line driving.

C.2   Steady-state cornering vehicle model

As described in Section 3.2.3, the nonlinear steady-state cornering model has four degrees of freedom, the latter two of which represent the angular velocities of both the left and right rear wheels, respectively ω_L and ω_R. After iteratively solving the model for a particular forward vehicle velocity V and corner radius R, the solution of the model includes values for ω_L and ω_R, while accounting for nonlinear effects such as large angles, lateral load transfer, and tire slip.

The resulting speed ratio between left and right axle is defined as $r_{diff} = \frac{\omega_R}{\omega_L}$ and is visualized for different velocities and corner radii in Figure C.2a. Based on this figure, it can be seen that $r_{diff} \approx 1$ for large corner radii and gradually increases for tighter turns. The value is also slightly vehicle-speed-dependent due to the nonlinear effects, such as lateral load transfer and changing vehicle sideslip angles. Values of up to $r_{diff} = 1.32$ are found for realistic cornering situations,
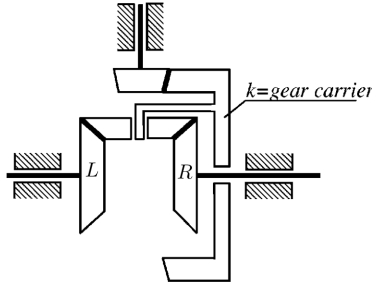
Figure C.1. Schematic view of the differential gear unit [225].

indicating a speed difference between the right and left axle of 32%.

C.3 Differential gear unit efficiency calculation

Given that the speed difference between the right and left axle exists, the challenge arises to estimate the effect this has on the energy losses in the differential. A differential gear unit, as in Figure C.1, is considered, where the gear carrier k is driven by the driveshaft connected to the motor, and L and R are the driven axles, connected to respectively the left and right rear wheels. Assuming the speeds of the wheels are known, the rotational velocity of the gear carrier can be calculated as the average of the two wheel velocities, according to:

$$\omega_k = \frac{1}{2}\left(\omega_L + \omega_R\right). \tag{C.1}$$

In a straight-line driving situation $\omega_R = \omega_L = \omega_k$. However, in a corner there will be a relative speed difference $\Delta\omega$ between the carrier and the wheels. Knowing that the carrier speed is the average of the two wheel velocities, we can write

$$\Delta\omega = \frac{1}{2}\left|\omega_R - \omega_L\right|. \tag{C.2}$$

An exemplary left-hand turn is considered. In a reference frame attached to the carrier, the left axle rotates with $\omega_{L,k} = -\Delta\omega$ and the right axle rotates with $\omega_{R,k} = \Delta\omega$, causing meshing of the planetary bevel gears. The torque on both axles is assumed known and is equal in steady-state: $M_L = M_R = 0.5M$, where M is the driving torque applied by the motor on the carrier. Next, the total power transferred through the bevel gears can be calculated as

$$P_{planet} = \Delta\omega \cdot M_L + \Delta\omega \cdot M_R = \Delta\omega M = \frac{1}{2}|\omega_R - \omega_L|M \tag{C.3}$$

The assumption is made that the meshing of the planetary bevel gears and the driven bevel gears has a constant efficiency $\eta_{mesh} = 98\%$, [225]. Therefore, the

(a) Rear axle speed ratio [-]

(b) Planetary gear efficiency [%]
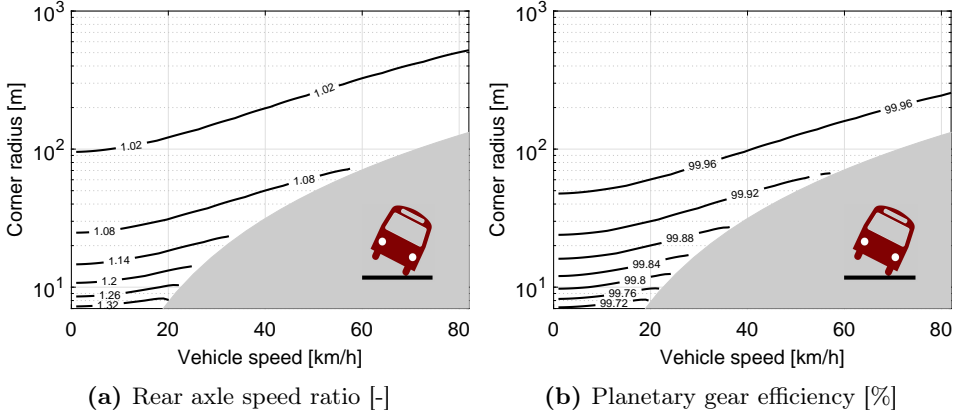
Figure C.2. The speed ratio between outer and inner axle r_{diff} **(a)** according to the nonlinear steady-state cornering model from Chapter 3 and the resulting efficiency of the planetary gears **(b)** for different corner radii and vehicle velocities. The gray area represents infeasible solutions where the vehicle is close to roll-over.

additional power lost due this meshing is given by

$$P_{loss} = (1 - \eta_{mesh}) \cdot P_{planet} = \frac{1}{2}(1 - \eta_{mesh}) |\omega_R - \omega_L| M \qquad (C.4)$$

As the total power transferred through the differential gear unit is given by $P_{total} = M_L\omega_L + M_R\omega_R = 0.5M(\omega_L + \omega_R)$, the efficiency of the bevel gears can be expressed as

$$\eta_{diff} = 1 - \frac{P_{loss}}{P_{total}} = 1 - (1 - \eta_{mesh})\frac{|\omega_R - \omega_L|}{\omega_L + \omega_R} = 1 - (1 - \eta_{mesh})\frac{|r_{diff} - 1|}{r_{diff} + 1}, \quad (C.5)$$

where the ratio $\frac{|\omega_R - \omega_L|}{\omega_L + \omega_R}$ indicates the ratio of the total driveline power that is transferred through the bevel gears. For instance, when $\omega_L = \omega_R$, $\frac{|\omega_R - \omega_L|}{\omega_L + \omega_R} = 0$, and when $\omega_L = 0$, $\frac{|\omega_R - \omega_L|}{\omega_L + \omega_R} = 1$. Reference is made to [226] for more details on analytical efficiency calculations of differential gear units.

Equation C.5 allows us to calculate the efficiency of the differential gear unit as function of r_{diff}. Therefore, the results presented in Figure C.2a can be translated to an efficiency value, as shown in Figure C.2b. These show that in the worst-case situation, the differential action reduces the drivetrain efficiency to 99.7% of its original value. Therefore, according to the results presented here, the effect of differential action on the overall efficiency appears to be small.

Note that this analysis only concerns the planetary gears in the differential. Therefore, the percentages mentioned in Figure C.2b are with respect to a straight-line-driving situation and do not reflect the total driveline efficiency.

Bibliography

[1] S. K. Gulev, P. W. Thorne, J. Ahn, F. J. Dentener, C. M. Domingues, S. Gerland, D. Gong, D. S. Kaufman, H. C. Nnamchi, J. Quaas, J. Rivera, S. Sathyendranath, S. L. Smith, B. Trewin, K. von Schuckmann, and R. S. Vose. *Climate Change 2021: The Physical Science Basis*, chapter Changing State of the Climate System, pages 287–422. Cambridge University Press, Cambridge, United Kingdom and New York, NY, USA, 2021. doi: 10.1017/9781009157896.004.

[2] IEA. Global Renewable Energy Policies and Measures Database©. Available online: https://www.iea.org/articles/global-ev-data-explorer, 2022. Accessed on 9 Feb. 2022.

[3] D. Lowell and F. Kamakaté. Urban off-cycle NOx emissions from Euro IV/V trucks and buses. *ICCT White Pap.*, (Number 18), Mar. 2012.

[4] R. Kok, R. de Groot, S. van Zyl, S. Wilkins, R. Smokers, and J. Spreen. Towards Zero-Emission Bus Transport. Technical Report TNO 2017 R10952, TNO, Sept. 2017, Available online: https://publications.tno.nl/publication/34625509/aLOfyW/.

[5] Q. Liu, Å. M. Hallquist, H. Fallgren, M. Jerksjö, S. Jutterström, H. Salberg, M. Hallquist, M. Le Breton, X. Pei, R. K. Pathak, T. Liu, B. Lee, and C. K. Chan. Roadside assessment of a modern city bus fleet: Gaseous and particle emissions. *Atmos. Environ. X*, 3(May):100044, July 2019. doi: 10.1016/j.aeaoa.2019.100044.

[6] F. Rosero, N. Fonseca, J.-M. López, and J. Casanova. Real-world fuel efficiency and emissions from an urban diesel bus engine under transient operating conditions. *Appl. Energy*, 261(October 2019):114442, Mar. 2020. doi: 10.1016/j.apenergy.2019.114442.

[7] A. Nordelöf, M. Romare, and J. Tivander. Life cycle assessment of city buses powered by electricity, hydrogenated vegetable oil or diesel. *Transp. Res. Part D Transp. Environ.*, 75(September):211–222, Oct. 2019. doi: 10.1016/j.trd.2019.08.019.

[8] E. Hawkins. ShowYourStripes.info. Available online: https://showyourstripes.info/c/globe, 2022. Accessed on 13 Mar. 2022.

[9] R. A. Rohde and Z. Hausfather. The Berkeley Earth Land/Ocean Temperature Record. *Earth Syst. Sci. Data*, 12(4):3469–3479, Dec. 2020. doi: 10.5194/essd-12-3469-2020.

[10] H. Hao, X. Ou, J. Du, H. Wang, and M. Ouyang. China's electric vehicle subsidy scheme: Rationale and impacts. *Energy Policy*, 73:722–732, Oct. 2014. doi: 10.1016/j.enpol.2014.05.022.

[11] J. Du, F. Li, J. Li, X. Wu, Z. Song, Y. Zou, and M. Ouyang. Evaluating the technological evolution of battery electric buses: China as a case. *Energy*, 176: 309–319, June 2019. doi: 10.1016/j.energy.2019.03.084.

[12] IEA. Global EV Outlook 2021. Technical report, IEA, Paris, Apr. 2021, Available online: https://www.iea.org/reports/global-ev-outlook-2021.

[13] European Commission. Directive (EU) 2019/1161 of the European Council and of the European Parliament of 20 June 2019, amending Directive 2009/33/EC on the promotion of clean and energy-efficient road transport vehicles. *Off. J. Eur. Union*, 2019(December 2018):1–15, 2019.

[14] Ministerie van Infrastructuur en Milieu. Bestuursakkoord Zero Emissie Regionaal Openbaar Vervoer Per Bus. Technical report, Ministerie van Infrastructuur en Milieu, Apr. 2016, Available online: https://www.greendeals.nl/sites/default/files/uploads/2015/04/Bestuursakkoord_Zero_OV-Bus_v3.pdf.

[15] H. Kim, N. Hartmann, M. Zeller, R. Luise, and T. Soylu. Comparative TCO Analysis of Battery Electric and Hydrogen Fuel Cell Buses for Public Transport System in Small to Midsize Cities. *Energies*, 14(14):4384, July 2021. doi: 10.3390/en14144384.

[16] S. Bakker and R. Konings. The transition to zero-emission buses in public transport - The need for institutional innovation. *Transp. Res. Part D Transp. Environ.*, 64: 204–215, Oct. 2018. doi: 10.1016/j.trd.2017.08.023.

[17] M. Schwertner and U. Weidmann. Stand und Perspektiven elektrischer Busantriebe. *Schweizer Eisenbahn-Revue*, 38(7):330–335, 2015.

[18] M. Schwertner. *Energetischer Systemvergleich von Diesel-, Hybrid- und Elektrobussen.* PhD thesis, ETH Zürich, 2017. doi: 10.3929/ethz-b-000206395.

[19] S. Tica, S. Filipović, P. Živanović, and S. Bajčetić. Development of Trolleybus Passenger Transport Subsystems in Terms of Sustainable Development and Quality of Life in Cities. *Int. J. Traffic Transp. Eng.*, 1313(4):196–205, 2011.

[20] M. Połom. Technology Development and Spatial Diffusion of Auxiliary Power Sources in Trolleybuses in European Countries. *Energies*, 14(11):3040, May 2021. doi: 10.3390/en14113040.

[21] G. Mom. *The electric vehicle : technology and expectations in the automobile age.* Johns Hopkins University Press, Baltimore SE, 2004. ISBN 0801871387.

[22] J. Wouters. *De elektische auto : Is het marktaandeel van 1914 in 2020 haalbaar?* Pepijn, Eindhoven, The Netherlands, June 2013. ISBN 9789078709220.

[23] D. A. Kirsch. *The electric vehicle and the burden of history.* Rutgers University Press, New Brunswick, N.J., 2000. ISBN 0813528097.

[24] M. Hamer. All aboard! *New Sci.*, 235(3142):35–37, Sept. 2017. doi: 10.1016/S0262-4079(17)31776-1.

[25] M. Hamer. *A Most Deliberate Swindle: How Edwardian Fraudsters Pulled the Plug on the Electric Bus and Left Our Cities Gasping for Breath.* RedDoor Publishing, 2018. ISBN 1910453420.

[26] Anonymous. The Oerlikon Electrogyro - Its development and application for omnibus service. *Automob. Eng.*, 45(13):559–566, Dec. 1955.

[27] M. Kane. MAN Presented Its First Electric Bus Some 50 Years Ago. Available online: https://insideevs.com/features/429781/man-first-electric-bus-50-years-ago/, 2020. Accessed on 18 Oct. 2021.

[28] C. Morris. Silent Rider-A Project for City Center Transport. In *Automot. Eng. Congr. Expo.*, number 750192, Detroit, Michigan, Feb. 1975. SAE International.

doi: 10.4271/750192.

[29] MCR Technology. Denver RTD range extension study : final report : task 4, recommendations. Technical Report NTIS PB83- 226050, Urban Mass Transportation Administration, US Department of Transportation, 1982.

[30] M. Hamer. Batteries for the van about town. *New Sci.*, (1517):37–38, July 1986.

[31] Sustainable-bus.com. The pandemic doesn't stop the European e-bus market: +22% in 2020. Available online: https://www.sustainable-bus.com/news/europe-electric-bus-market-2020-covid/, 2021. Accessed on 15 Mar. 2021.

[32] G. Correa, P. Muñoz, T. Falaguerra, and C. R. Rodriguez. Performance comparison of conventional, hybrid, hydrogen and electric urban buses using well to wheel analysis. *Energy*, 141:537–549, 2017. doi: 10.1016/j.energy.2017.09.066.

[33] J. Wang, I. J. M. Besselink, and H. Nijmeijer. Battery electric vehicle energy consumption modelling for range estimation. *Int. J. Electr. Hybrid Veh.*, 9(2):79, 2017. doi: 10.1504/IJEHV.2017.085336.

[34] H. Basma, C. Mansour, M. Haddad, M. Nemer, and P. Stabat. Comprehensive energy modeling methodology for battery electric buses. *Energy*, 207:118241, 2020. doi: 10.1016/j.energy.2020.118241.

[35] J. Vepsäläinen, K. Kivekäs, K. Otto, A. Lajunen, and K. Tammi. Development and validation of energy demand uncertainty model for electric city buses. *Transp. Res. Part D Transp. Environ.*, 63:347–361, Aug. 2018. doi: 10.1016/j.trd.2018.06.004.

[36] I. J. M. Besselink, J. Wang, and H. Nijmeijer. Evaluating the TU/e Lupo EL BEV performance. In *2013 World Electr. Veh. Symp. Exhib.*, pages 1–12. IEEE, Nov. 2013. doi: 10.1109/EVS.2013.6915029.

[37] L. Mauler, F. Duffner, W. G. Zeier, and J. Leker. Battery cost forecasting: a review of methods and results with an outlook to 2050. *Energy Environ. Sci.*, 14 (9):4712–4739, 2021. doi: 10.1039/D1EE01530C.

[38] K. Kivekas, A. Lajunen, F. Baldi, J. Vepsalainen, and K. Tammi. Reducing the Energy Consumption of Electric Buses With Design Choices and Predictive Driving. *IEEE Trans. Veh. Technol.*, 68(12):11409–11419, Dec. 2019. doi: 10.1109/TVT.2019.2936772.

[39] D. Göhlich, T.-A. Fay, D. Jefferies, E. Lauth, A. Kunith, and X. Zhang. Design of urban electric bus systems. *Des. Sci.*, 4:e15, Aug. 2018. doi: 10.1017/dsj.2018.10.

[40] A. Sciarretta, G. De Nunzio, and L. L. Ojeda. Optimal Ecodriving Control: Energy-Efficient Driving of Road Vehicles as an Optimal Control Problem. *IEEE Control Syst.*, 35(5):71–90, Oct. 2015. doi: 10.1109/MCS.2015.2449688.

[41] G. P. Padilla, J. C. Flores Paredes, and M. C. F. Donkers. A Port-Hamiltonian Approach to Complete Vehicle Energy Management: A Battery Electric Vehicle Case Study. In *2020 Am. Control Conf.*, volume 2020-July, pages 288–294. IEEE, July 2020. doi: 10.23919/ACC45564.2020.9147748.

[42] M. M. Hasan, M. El Baghdadi, J. Van Mierlo, and O. Hegazy. Energy management and ECO-strategies modeling of electric bus fleets in Barcelona city. In *2021 23rd Eur. Conf. Power Electron. Appl. EPE 2021 ECCE Eur.* EPE Association, 2021.

[43] R. Deng, Y. Liu, W. Chen, and H. Liang. A Survey on Electric Buses–Energy Storage, Power Management, and Charging Scheduling. *IEEE Trans. Intell. Transp. Syst.*, 22(1):9–22, Jan. 2021. doi: 10.1109/TITS.2019.2956807.

[44] Z. Gao, Z. Lin, T. J. LaClair, C. Liu, J.-M. Li, A. K. Birky, and J. Ward. Battery capacity and recharging needs for electric buses in city transit service. *Energy*, 122:

588–600, Mar. 2017. doi: 10.1016/j.energy.2017.01.101.

[45] M. Zhou, H. Jin, and W. Wang. A review of vehicle fuel consumption models to evaluate eco-driving and eco-routing. *Transp. Res. Part D Transp. Environ.*, 49 (5):203–218, Dec. 2016. doi: 10.1016/j.trd.2016.09.008.

[46] M. M. Hasan, A. Saez-de Ibarra, M. El Baghdadi, and O. Hegazy. Analysis of the peak grid load reduction using ECO-charging strategy for e-bus fleets in Gothenburg. In *2021 IEEE Veh. Power Propuls. Conf.*, volume 769850, pages 1–6. IEEE, Oct. 2021. doi: 10.1109/VPPC53923.2021.9699184.

[47] M. Rogge, S. Wollny, and D. Sauer. Fast Charging Battery Buses for the Electrification of Urban Public Transport–A Feasibility Study Focusing on Charging Infrastructure and Energy Storage Requirements. *Energies*, 8(5):4587–4606, May 2015. doi: 10.3390/en8054587.

[48] X. Tang, X. Lin, and F. He. Robust scheduling strategies of electric buses under stochastic traffic conditions. *Transp. Res. Part C Emerg. Technol.*, 105:163–182, Aug. 2019. doi: 10.1016/j.trc.2019.05.032.

[49] G. Wang, X. Xie, F. Zhang, Y. Liu, and D. Zhang. bCharge: Data-Driven Real-Time Charging Scheduling for Large-Scale Electric Bus Fleets. In *2018 IEEE Real-Time Syst. Symp.*, pages 45–55. IEEE, Dec. 2018. doi: 10.1109/RTSS.2018.00015.

[50] J. Wang, L. Kang, and Y. Liu. Optimal scheduling for electric bus fleets based on dynamic programming approach by considering battery capacity fade. *Renew. Sustain. Energy Rev.*, 130:109978, Sept. 2020. doi: 10.1016/j.rser.2020.109978.

[51] A. S. Al-Ogaili, A. Q. Al-Shetwi, H. M. K. Al-Masri, T. S. Babu, Y. Hoon, K. Alzaareer, and N. V. P. Babu. Review of the Estimation Methods of Energy Consumption for Battery Electric Buses. *Energies*, 14(22):7578, Nov. 2021. doi: 10.3390/en14227578.

[52] Y. Chen, G. Wu, R. Sun, A. Dubey, A. Laszka, and P. Pugliese. A Review and Outlook on Energy Consumption Estimation Models for Electric Vehicles. *SAE Int. J. Sustain. Transp. Energy, Environ. Policy*, 2(1):13–02–01–0005, Mar. 2021. doi: 10.4271/13-02-01-0005.

[53] T. Pamuła and D. Pamuła. Prediction of Electric Buses Energy Consumption from Trip Parameters Using Deep Learning. *Energies*, 15(5):1747, Feb. 2022. doi: 10.3390/en15051747.

[54] C. Fiori, M. Montanino, S. Nielsen, M. Seredynski, and F. Viti. Microscopic energy consumption modelling of electric buses: model development, calibration, and validation. *Transp. Res. Part D Transp. Environ.*, 98(July):102978, Sept. 2021. doi: 10.1016/j.trd.2021.102978.

[55] J. Wang, I. J. M. Besselink, and H. Nijmeijer. Battery electric vehicle energy consumption prediction for a trip based on route information. *Proc. Inst. Mech. Eng. Part D J. Automob. Eng.*, 232(11):1528–1542, Sept. 2018. doi: 10.1177/0954407017729938.

[56] C. J. J. Beckers, T. A. G. H. Geraedts, I. J. M. Besselink, and H. Nijmeijer. TU/e Microscopic Energy Consumption PRediction tOol 0.1 (TU/e MECPRO 0.1). Available online: https://doi.org/10.4121/12764732, Jan. 2021.

[57] EVERLASTING Consortium. EVERLASTING Website. Available online: https://everlasting-project.eu/, 2019. Accessed on 8 Jan. 2019.

[58] A. Deschênes, J. Gaudreault, and K. Rioux-paradis. Predicting Electric Vehicle Consumption: a Physical Model That Fits. In *EVS32 Symp.*, number 1, pages 1–7,

Lyon, France, 2019.

[59] OpenWeather ®. OpenWeatherMap.org. Available online: `https://openweathermap.org/current`, 2022. Accessed on 28 Mar. 2022.

[60] © OpenStreetMap contributors. OpenStreetMap. Available online: `https://www.openstreetmap.org/copyright`, 2022. Accessed on 28 Mar. 2022.

[61] T. G. Farr, P. A. Rosen, E. Caro, R. Crippen, R. Duren, S. Hensley, M. Kobrick, M. Paller, E. Rodriguez, L. Roth, D. Seal, S. Shaffer, J. Shimada, J. Umland, M. Werner, M. Oskin, D. Burbank, and D. Alsdorf. The Shuttle Radar Topography Mission. *Rev. Geophys.*, 45(2):RG2004, May 2007. doi: 10.1029/2005RG000183.

[62] ISO 10521-1:2006. Road vehicles – Road load – Part 1: Determination under reference atmospheric conditions. Technical report, Nederlands Normalisatie-instituut, Delft, Netherlands, Oct. 2006, Available online: `https://www.iso.org/standard/37533.html`.

[63] J. Howell. Aerodynamic Drag of Passenger Cars at Yaw. *SAE Int. J. Passeng. Cars - Mech. Syst.*, 8(1):2015–01–1559, Apr. 2015. doi: 10.4271/2015-01-1559.

[64] F. Beauducel. readhgt. Available online: `https://github.com/IPGP/mapping-matlab/tree/master/readhgt`, 2020. Accessed on 28 Feb. 2020.

[65] A. Picard, R. S. Davis, M. Gläser, and K. Fujii. Revised formula for the density of moist air (CIPM-2007). *Metrologia*, 45(2):149–155, Apr. 2008. doi: 10.1088/0026-1394/45/2/004.

[66] T. R. Oke. *Boundary Layer Climates*. Routledge, London, 2nd edition, Sept. 2002. ISBN 9781134951345. doi: 10.4324/9780203407219.

[67] I. Filippidis. OpenStreetMap Functions. Available online: `https://nl.mathworks.com/matlabcentral/fileexchange/35819-openstreetmap-functions`, 2020. Accessed on 31 Aug. 2020.

[68] A. Lajunen, K. Kivekäs, F. Baldi, J. Vepsaelaeinen, and K. Tammi. Different Approaches to Improve Energy Consumption of Battery Electric Buses. In *2018 IEEE Veh. Power Propuls. Conf.*, pages 1–6. IEEE, Aug. 2018. doi: 10.1109/VPPC.2018.8605024.

[69] T. Halmeaho, M. Antila, J. Kataja, P. Silvonen, and M. Pihlatie. Advanced Driver Aid System for Energy Efficient Electric Bus Operation. In *Proc. 1st Int. Conf. Veh. Technol. Intell. Transp. Syst.*, pages 59–64. SCITEPRESS - Science and and Technology Publications, 2015. doi: 10.5220/0005494600590064.

[70] O. A. Hjelkrem, K. Y. Lervåg, S. Babri, C. Lu, and C.-J. Södersten. A battery electric bus energy consumption model for strategic purposes: Validation of a proposed model structure with data from bus fleets in China and Norway. *Transp. Res. Part D Transp. Environ.*, 94(April):102804, May 2021. doi: 10.1016/j.trd.2021.102804.

[71] R. Al Haddad, H. Basma, and C. Mansour. Analysis of heat pump performance in battery electric buses. In *ECOS 2019 - Proc. 32nd Int. Conf. Effic. Cost, Optim. Simul. Environ. Impact Energy Syst.*, pages 1897–1909, Wroclaw, Poland, 2019.

[72] H. Basma, C. Mansour, M. Haddad, M. Nemer, and P. Stabat. Energy consumption and battery sizing for different types of electric bus service. *Energy*, page 122454, Oct. 2021. doi: 10.1016/j.energy.2021.122454.

[73] Y. Luo, Y.-P. Tan, and L.-F. Li. Study on saving energy for electric auxiliary systems of electric bus. *Energy Sources, Part A Recover. Util. Environ. Eff.*, pages 1–13, Oct. 2020. doi: 10.1080/15567036.2020.1829750.

[74] A. Lajunen and A. Kalttonen. Investigation of thermal energy losses in the pow-

ertrain of an electric city bus. In *2015 IEEE Transp. Electrif. Conf. Expo*, pages 1–6. IEEE, June 2015. doi: 10.1109/ITEC.2015.7165776.

[75] ZeEUS Consortium. ZeEUS eBus Report #2 - An updated overview of electric buses in Europe. Technical report, ZeEUS Consortium, 2017, Available online: https://zeeus.eu/uploads/publications/documents/zeeus-report2017-2018-final.pdf.

[76] M. Pihlatie, S. Kukkonen, T. Halmeaho, V. Karvonen, and N. O. Nylund. Fully electric city buses - The viable option. In *2014 IEEE Int. Electr. Veh. Conf.*, pages 1–8, Florence, Italy, Dec. 2014. IEEE. doi: 10.1109/IEVC.2014.7056145.

[77] Y. Ding, Z. P. Cano, A. Yu, J. Lu, and Z. Chen. Automotive Li-Ion Batteries: Current Status and Future Perspectives. *Electrochem. Energy Rev.*, 2(1):1–28, Mar. 2019. doi: 10.1007/s41918-018-0022-z.

[78] J. Asamer, A. Graser, B. Heilmann, and M. Ruthmair. Sensitivity analysis for energy demand estimation of electric vehicles. *Transp. Res. Part D Transp. Environ.*, 46:182–199, July 2016. doi: 10.1016/j.trd.2016.03.017.

[79] K. Sarrafan, D. Sutanto, K. M. Muttaqi, and G. Town. Accurate range estimation for an electric vehicle including changing environmental conditions and traction system efficiency. *IET Electr. Syst. Transp.*, 7(2):117–124, June 2017. doi: 10.1049/iet-est.2015.0052.

[80] R. Shankar and J. Marco. Method for estimating the energy consumption of electric vehicles and plug-in hybrid electric vehicles under real-world driving conditions. *IET Intell. Transp. Syst.*, 7(1):138–150, Mar. 2013. doi: 10.1049/iet-its.2012.0114.

[81] C. De Cauwer, J. Van Mierlo, and T. Coosemans. Energy Consumption Prediction for Electric Vehicles Based on Real-World Data. *Energies*, 8(8):8573–8593, Aug. 2015. doi: 10.3390/en8088573.

[82] L. L. Ojeda, A. Chasse, and R. Goussault. Fuel consumption prediction for heavy-duty vehicles using digital maps. In *2017 IEEE 20th Int. Conf. Intell. Transp. Syst.*, pages 1–7, Yokohama, Kanagawa, Japan, Oct. 2017. IEEE. doi: 10.1109/ITSC.2017.8317613.

[83] F. D. Hales. Computer Prediction of Power Required by Articulated Vehicles During Cornering. Technical Report TT 7901, Department of Transport Technology, Loughborough Univeristy of Technology, 1977.

[84] L. Gyenes, T. Williams, and I. C. P. Simmons. Power requirements of articulated vehicles under cornering conditions. Technical Report TRRL Supplementary Report 484, Department of the Environment Department of Transport, Crowthorne, 1979, Available online: https://trl.co.uk/sites/default/files/SR484.pdf.

[85] T. Kobayashi, E. Katsuyama, H. Sugiura, E. Ono, and M. Yamamoto. Direct yaw moment control and power consumption of in-wheel motor vehicle in steady-state turning. *Veh. Syst. Dyn.*, 55(1):104–120, Jan. 2017. doi: 10.1080/00423114.2016.1246737.

[86] Y. Ikezawa, H. Fujimoto, D. Kawano, Y. Goto, Y. Takeda, and K. Sato. Range Extension Autonomous Driving for Electric Vehicle Based on Optimal Vehicle Velocity Profile in Consideration of Cornering. *Electr. Eng. Japan*, 207(1):43–54, Apr. 2019. doi: 10.1002/eej.23088.

[87] S. Bhat, M. M. Davari, and M. Nybacka. Study on Energy Loss due to Cornering Resistance in Over-Actuated Vehicles using Optimal Control. *SAE Int. J. Veh. Dyn. Stability, NVH*, 1(2):2017–01–1568, Mar. 2017. doi: 10.4271/2017-01-1568.

[88] P. Sun, A. Stensson Trigell, L. Drugge, J. Jerrelind, and M. Jonasson. Exploring the Potential of Camber Control to Improve Vehicles' Energy Efficiency during Cornering. *Energies*, 11(4):724, Mar. 2018. doi: 10.3390/en11040724.

[89] J. Edrén, M. Jonasson, J. Jerrelind, A. Stensson Trigell, and L. Drugge. Energy efficient cornering using over-actuation. *Mechatronics*, 59(March):69–81, May 2019. doi: 10.1016/j.mechatronics.2019.02.006.

[90] B. Maclaurin. Comparing the steering performances of skid- and Ackermann-steered vehicles. *Proc. Inst. Mech. Eng. Part D J. Automob. Eng.*, 222(5):739–756, May 2008. doi: 10.1243/09544070JAUTO567.

[91] G. Rill. Reducing the cornering resistance by torque vectoring. *Procedia Eng.*, 199: 3284–3289, 2017. doi: 10.1016/j.proeng.2017.09.393.

[92] C. Chatzikomis, M. Zanchetta, P. Gruber, A. Sorniotti, B. Modic, T. Motaln, L. Blagotinsek, and G. Gotovac. An energy-efficient torque-vectoring algorithm for electric vehicles with multiple motors. *Mech. Syst. Signal Process.*, 128:655–673, Aug. 2019. doi: 10.1016/j.ymssp.2019.03.012.

[93] L. De Novellis, A. Sorniotti, and P. Gruber. Wheel Torque Distribution Criteria for Electric Vehicles With Torque-Vectoring Differentials. *IEEE Trans. Veh. Technol.*, 63(4):1593–1602, May 2014. doi: 10.1109/TVT.2013.2289371.

[94] C. J. J. Beckers, I. J. M. Besselink, and H. Nijmeijer. Modeling of Energy Losses During Cornering for Electric City Buses. In *2019 IEEE Intell. Transp. Syst. Conf.*, pages 4164–4169, Auckland, New-Zealand, Oct. 2019. IEEE. doi: 10.1109/ITSC.2019.8917232.

[95] H. B. Pacejka. *Tire and Vehicle Dynamics*. Butterworth-Heinemann, Oxford, 3rd edition, Apr. 2012. ISBN 978-0-08-097016-5.

[96] C. J. J. Beckers, I. J. M. Besselink, and H. Nijmeijer. MATLAB-scripts describing a nonlinear steady-state cornering model for an electric city bus. Available online: https://doi.org/10.4121/12717902, Mar. 2020.

[97] I. Kageyama. Steering System. In G. Mastinu and M. Ploechl, editors, *Road Off-Road Veh. Syst. Dyn. Handb.*, chapter 25, pages 919–942. CRC Press, Boca Raton, 1st edition, 2014. ISBN 978-0-8493-3322-4. doi: 10.1201/b15560.

[98] C. Howcroft, M. Lowenberg, S. Neild, and B. Krauskopf. Effects of Freeplay on Dynamic Stability of an Aircraft Main Landing Gear. *J. Aircr.*, 50(6):1908–1922, Nov. 2013. doi: 10.2514/1.C032316.

[99] P. Y. Papalambros and D. J. Wilde. *Principles of Optimal Design*. Cambridge University Press, Cambridge, 2nd edition, 2000. ISBN 9780511626418. doi: 10.1017/CBO9780511626418.

[100] European Union Parliament. Regulation (EC) No 1222/2009 of the European Parliament and of the Council of 25 November 2009 on the labelling of tyres with respect to fuel efficiency and other essential parameters. *Off. J. Eur. Union*, L 342: 46–58, Dec. 2009.

[101] A. Savitzky and M. J. E. Golay. Smoothing and Differentiation of Data by Simplified Least Squares Procedures. *Anal. Chem.*, 36(8):1627–1639, July 1964. doi: 10.1021/ac60214a047.

[102] L. Segel and X. Lu. Vehicular Resistance To Motion As Influenced By Road Roughness And Highway Alignment. *Aust. Road Res.*, 12(4):211–222, Dec. 1982.

[103] C. O. Bachmann. *Vergleichende Rollwiderstandsmessungen an Lkw-Reifen im Labor und auf realen Fahrbahnen*. PhD thesis, RWTH Aachen University, Aachen,

Mar. 2017. ISBN 978-3946019190.

[104] A. J. P. Miège and A. A. Popov. Truck tyre modelling for rolling resistance calculations under a dynamic vertical load. *Proc. Inst. Mech. Eng. Part D J. Automob. Eng.*, 219(4):441–456, Apr. 2005. doi: 10.1243/095440705X11176.

[105] T. D. Gillespie, M. W. Sayers, and L. Segel. Calibration of Response-Type Road Roughness Measuring Systems. Technical Report 228, Transportation Research Board, National Research Council, Dec. 1980, Available online: https://trid.trb.org/view/165815.

[106] D. Karnopp. Power Requirements for Traversing Uneven Roadways. *Veh. Syst. Dyn.*, 7(3):135–152, Sept. 1978. doi: 10.1080/00423117808968558.

[107] S. A. Velinsky and R. A. White. Vehicle Energy Dissipation Due to Road Roughness. *Veh. Syst. Dyn.*, 9(6):359–384, Dec. 1980. doi: 10.1080/00423118008968630.

[108] X. P. Lu and L. Segel. Vehicular Energy Losses Associated with The Traversal of an Uneven Road. *Veh. Syst. Dyn.*, 15(sup1):342–352, Jan. 1986. doi: 10.1080/00423118608969146.

[109] X. P. Lu and L. Segel. Vehicular Energy Losses Associated with the Traversal of an Uneven Road. *Veh. Syst. Dyn.*, 14(1-3):166–171, June 1985. doi: 10.1080/00423118508968823.

[110] D. A. Crolla and A. M. A. Abouel Nour. Power losses in active and passive suspensions of off-road vehicles. *J. Terramechanics*, 29(1):83–93, Jan. 1992. doi: 10.1016/0022-4898(92)90016-D.

[111] M. A. A. Abdelkareem, L. Xu, M. K. A. Ali, A. Elagouz, J. Mi, S. Guo, Y. Liu, and L. Zuo. Vibration energy harvesting in automotive suspension system: A detailed review. *Appl. Energy*, 229(April):672–699, Nov. 2018. doi: 10.1016/j.apenergy.2018.08.030.

[112] M. C. Smith and S. J. Swift. Power dissipation in automotive suspensions. *Veh. Syst. Dyn.*, 49(1-2):59–74, Feb. 2011. doi: 10.1080/00423110903427421.

[113] J. Wallaschek. Dynamics of non-linear automobile shock-absorbers. *Int. J. Non. Linear. Mech.*, 25(2-3):299–308, Jan. 1990. doi: 10.1016/0020-7462(90)90059-I.

[114] C. Surace, K. Worden, and G. R. Tomlinson. On the Non-Linear Characteristics of Automotive Shock Absorbers. *Proc. Inst. Mech. Eng. Part D J. Automob. Eng.*, 206(1):3–16, Jan. 1992. doi: 10.1243/PIME_PROC_1992_206_156_02.

[115] S. J. Elliott, M. G. Tehrani, and R. S. Langley. Nonlinear damping and quasi-linear modelling. *Philos. Trans. R. Soc. A Math. Phys. Eng. Sci.*, 373(2051):20140402, Sept. 2015. doi: 10.1098/rsta.2014.0402.

[116] S. Boere, I. L. Arteaga, A. Kuijpers, and H. Nijmeijer. Tyre/road interaction model for the prediction of road texture influence on rolling resistance. *Int. J. Veh. Des.*, 65(2/3):202, 2014. doi: 10.1504/IJVD.2014.060815.

[117] C. Hoever and W. Kropp. A model for investigating the influence of road surface texture and tyre tread pattern on rolling resistance. *J. Sound Vib.*, 351:161–176, Sept. 2015. doi: 10.1016/j.jsv.2015.04.009.

[118] O. E. Lundberg, A. Nordborg, and I. Lopez Arteaga. The influence of surface roughness on the contact stiffness and the contact filter effect in nonlinear wheel–track interaction. *J. Sound Vib.*, 366:429–446, Mar. 2016. doi: 10.1016/j.jsv.2015.12.026.

[119] Y. Huang and H. Chen. Review of rolling resistance influence on fuel consumption of trucks. In *13th ITS Eur. Congr.*, pages 1–12, Brainport, The Netherlands, 2019. ERTICO.

[120] J. A. Ejsmont, G. Ronowski, B. Świeczko-Żurek, and S. Sommer. Road texture influence on tyre rolling resistance. *Road Mater. Pavement Des.*, 18(1):181–198, Jan. 2017. doi: 10.1080/14680629.2016.1160835.

[121] G. Svenson and D. Fjeld. The impact of road geometry and surface roughness on fuel consumption of logging trucks. *Scand. J. For. Res.*, 31(5):526–536, July 2016. doi: 10.1080/02827581.2015.1092574.

[122] G. Rill. *Road Vehicle Dynamics*. Ground vehicle engineering series. CRC Press, Sept. 2011. ISBN 9781439897447. doi: 10.1201/9781439897447.

[123] A. J. C. Schmeitz. *A Semi-Empirical Three-Dimensional Model of the Pneumatic Tyre Rolling over Arbitrarily Uneven Road Surfaces.* PhD thesis, TU Delft, Delft, 2004.

[124] Mathworks. Solver. Available online: https://nl.mathworks.com/help/simulink/gui/solver.html, 2022. Accessed on 3 Feb. 2022.

[125] P. Johannesson and I. Rychlik. Modelling of road profiles using roughness indicators. *Int. J. Veh. Des.*, 66(4):317, 2014. doi: 10.1504/IJVD.2014.066068.

[126] ISO 8608:2016. Mechanical vibration – Road surface profiles – Reporting of measured data. Technical report, Koninklijk Nederlands Normalisatie-instituut, Delft, Netherlands, Nov. 2016, Available online: https://www.iso.org/standard/71202.html.

[127] Algemeen Hoogtebestand Nederland. AHN.nl. Available online: https://www.ahn.nl/, 2021. Accessed on 27 Nov. 2021.

[128] P. Welch. The use of fast Fourier transform for the estimation of power spectra: A method based on time averaging over short, modified periodograms. *IEEE Trans. Audio Electroacoust.*, 15(2):70–73, June 1967. doi: 10.1109/TAU.1967.1161901.

[129] Michelin. The tyre - Rolling resistance and fuel savings. Technical report, Sociéte de Technologie Michelin, Clermont-Ferrand, 2003.

[130] F. Meishner and D. Uwe Sauer. Technical and economic comparison of different electric bus concepts based on actual demonstrations in European cities. *IET Electr. Syst. Transp.*, 10(2):144–153, June 2020. doi: 10.1049/iet-est.2019.0014.

[131] P. Sahlholm and K. Henrik Johansson. Road grade estimation for look-ahead vehicle control using multiple measurement runs. *Control Eng. Pract.*, 18(11):1328–1341, Nov. 2010. doi: 10.1016/j.conengprac.2009.09.007.

[132] H. A. Yavasoglu, Y. E. Tetik, and K. Gokce. Implementation of machine learning based real time range estimation method without destination knowledge for BEVs. *Energy*, 172:1179–1186, Apr. 2019. doi: 10.1016/j.energy.2019.02.032.

[133] J. Yao and A. Moawad. Vehicle energy consumption estimation using large scale simulations and machine learning methods. *Transp. Res. Part C Emerg. Technol.*, 101:276–296, Apr. 2019. doi: 10.1016/j.trc.2019.02.012.

[134] MIRIAM Consortium. Rolling Resistance – Basic Information and State-of- the-Art on Measurement methods. Technical Report MIRIAM_SP1_01, MIRIAM, 2011, Available online: https://www.diva-portal.org/smash/get/diva2:674026/FULLTEXT02.pdf.

[135] Y. Ma, I. J. M. Besselink, and H. Nijmeijer. Impact of elevation data quality on power request modelling accuracy for electric vehicles. In *ITS Eur. Congr. 2019*, pages 1–12, Eindhoven, The Netherlands, July 2019. ERTICO.

[136] S. Han and C. Rizos. Road Slope Information from GPS-Derived Trajectory Data. *J. Surv. Eng.*, 125(2):59–68, May 1999. doi: 10.1061/(ASCE)0733-

9453(1999)125:2(59).

[137] K. Jo, J. Kim, and M. Sunwoo. Real-Time Road-Slope Estimation Based on Integration of Onboard Sensors With GPS Using an IMMPDA Filter. *IEEE Trans. Intell. Transp. Syst.*, 14(4):1718–1732, Dec. 2013. doi: 10.1109/TITS.2013.2266438.

[138] J. Jauch, J. Masino, T. Staiger, and F. Gauterin. Road Grade Estimation With Vehicle-Based Inertial Measurement Unit and Orientation Filter. *IEEE Sens. J.*, 18(2):781–789, Jan. 2018. doi: 10.1109/JSEN.2017.2772305.

[139] H. Liu, H. Li, M. O. Rodgers, and R. Guensler. Development of road grade data using the United States geological survey digital elevation model. *Transp. Res. Part C Emerg. Technol.*, 92(August 2017):243–257, July 2018. doi: 10.1016/j.trc.2018.05.004.

[140] K. Oda, H. Takeuchi, M. Tsujii, and M. Ohba. Practical Estimator for Self-Tuning Automotive Cruise Control. In *1991 Am. Control Conf.*, pages 2066–2071. IEEE, June 1991. doi: 10.23919/ACC.1991.4791762.

[141] M. Würtenberger, S. Germann, and R. Isermann. Modeling and Parameter Estimation of Nonlinear Vehicle Dynamics. *Transp. Syst.*, 44:53–63, 1992.

[142] P. Lingman and B. Schmidtbauer. Road Slope and Vehicle Mass Estimation Using Kalman Filtering. *Veh. Syst. Dyn.*, 37(sup1):12–23, Jan. 2002. doi: 10.1080/00423114.2002.11666217.

[143] H. S. Bae and J. C. Gerdes. Parameter Estimation and Command Modification for Longitudinal Control of Heavy Vehicles. Technical Report UCB-ITS-PRR-2003-16, Stanford University, Apr. 2003, Available online: https://escholarship.org/uc/item/6s35h1ch.pdf.

[144] A. Vahidi, A. Stefanopoulou, and H. Peng. Recursive least squares with forgetting for online estimation of vehicle mass and road grade: theory and experiments. *Veh. Syst. Dyn.*, 43(1):31–55, Jan. 2005. doi: 10.1080/00423110412331290446.

[145] H. K. Fathy, Dongsoo Kang, and J. L. Stein. Online vehicle mass estimation using recursive least squares and supervisory data extraction. In *2008 Am. Control Conf.*, pages 1842–1848, Seattle, WA, June 2008. IEEE. doi: 10.1109/ACC.2008.4586760.

[146] X. Zhang, L. Xu, J. Li, and M. Ouyang. Real-Time Estimation of Vehicle Mass and Road Grade Based on Multi-Sensor Data Fusion. In *2013 IEEE Veh. Power Propuls. Conf.*, pages 1–7. IEEE, Oct. 2013. doi: 10.1109/VPPC.2013.6671743.

[147] D. Alegre, R. de Lemos Peroni, E. da Rosa Aquino, and F. Dille. A method to assess haul roads rolling resistance using dispatch system data. *Min. Technol.*, 130(3):1–12, June 2021. doi: 10.1080/25726668.2021.1935098.

[148] R. Wragge-Morley, G. Herrmann, P. Barber, and S. Burgess. Gradient and Mass Estimation from CAN Based Data for a Light Passenger Car. *SAE Int. J. Passeng. Cars - Electron. Electr. Syst.*, 8(1):2015–01–0201, Apr. 2015. doi: 10.4271/2015-01-0201.

[149] C. E. Tannoury, S. Moussaoui, F. Plestan, N. Romani, and G. Pita-Gil. Synthesis and Application of Nonlinear Observers for the Estimation of Tire Effective Radius and Rolling Resistance of an Automotive Vehicle. *IEEE Trans. Control Syst. Technol.*, 21(6):2408–2416, Nov. 2013. doi: 10.1109/TCST.2012.2232669.

[150] A. K. Sharma, M. Bouteldja, and V. Cerezo. High gain and sliding mode adaptive observers comparison: estimation of tire rolling resistance. In *2018 6th Int. Conf. Control Eng. Inf. Technol.*, number October, pages 1–7. IEEE, Oct. 2018. doi: 10.1109/CEIT.2018.8751889.

[151] D. Zhang, A. Ivanco, and Z. Filipi. Model-Based Estimation of Vehicle Aerodynamic Drag and Rolling Resistance. *SAE Int. J. Commer. Veh.*, 8(2):433–439, Sept. 2015. doi: 10.4271/2015-01-2776.

[152] F. Andriaminahy, A. Amamou, S. Kelouwani, N. Zioui, A. Ghobadpour, and K. Agbossou. Comparative Study of Vehicle Aerodynamic and Rolling Resistance Coefficients Estimation Methods. In *2019 IEEE Veh. Power Propuls. Conf.*, pages 1–5. IEEE, Oct. 2019. doi: 10.1109/VPPC46532.2019.8952491.

[153] Z. Yi and P. H. Bauer. Adaptive Multiresolution Energy Consumption Prediction for Electric Vehicles. *IEEE Trans. Veh. Technol.*, 66(11):10515–10525, Nov. 2017. doi: 10.1109/TVT.2017.2720587.

[154] Royal Netherlands Meteorological Institute (KNMI). Hourly Observations. Available online: https://www.daggegevens.knmi.nl/klimatologie/uurgegevens, 2019. Accessed on 10 Jan. 2019.

[155] OpenStreetMap Wiki. Key:name — OpenStreetMap Wiki, 2021. URL https://wiki.openstreetmap.org/w/index.php?title=Key:name&oldid=2194005. Accessed on 25 Oct. 2021.

[156] OpenStreetMap Wiki. Key:highway — OpenStreetMap Wiki, 2021. URL https://wiki.openstreetmap.org/w/index.php?title=Key:highway&oldid=2156966. Accessed on 25 Oct. 2021.

[157] OpenStreetMap Wiki. Key:junction — OpenStreetMap Wiki, 2020. URL https://wiki.openstreetmap.org/w/index.php?title=Key:junction&oldid=2034421. Accessed on 25 Oct. 2021.

[158] J. H. Friedman. Multivariate Adaptive Regression Splines. *Ann. Stat.*, 19(1):1–67, Mar. 1991.

[159] L. Ljung and T. Söderström. *Theory and Practice of Recursive Identification.* MIT Press, Cambridge, MA, USA, 1983. ISBN 9780262620581.

[160] K. J. Keesman. *System Identification.* Advanced Textbooks in Control and Signal Processing. Springer London, London, 2011. ISBN 978-0-85729-521-7.

[161] K. Kivekäs, J. Vepsalainen, K. Tammi, and J. Anttila. Influence of Driving Cycle Uncertainty on Electric City Bus Energy Consumption. In *2017 IEEE Veh. Power Propuls. Conf.*, pages 1–5, Belfort, France, Dec. 2017. IEEE. doi: 10.1109/VPPC.2017.8331014.

[162] S. Sautermeister, F. Ott, M. Vaillant, and F. Gauterin. Reducing range estimation uncertainty with a hybrid powertrain model and online parameter estimation. In *2017 IEEE 20th Int. Conf. Intell. Transp. Syst.*, pages 1–6. IEEE, Oct. 2017. doi: 10.1109/ITSC.2017.8317633.

[163] Y. Li, H. He, and J. Peng. An Adaptive Online Prediction Method With Variable Prediction Horizon for Future Driving Cycle of the Vehicle. *IEEE Access*, 6:33062–33075, 2018. doi: 10.1109/ACCESS.2018.2840536.

[164] J. Hou, D. Yao, F. Wu, J. Shen, and X. Chao. Online Vehicle Velocity Prediction Using an Adaptive Radial Basis Function Neural Network. *IEEE Trans. Veh. Technol.*, pages 3113–3122, Apr. 2021. doi: 10.1109/TVT.2021.3063483.

[165] J. Vepsäläinen, A. Ritari, A. Lajunen, K. Kivekäs, and K. Tammi. Energy Uncertainty Analysis of Electric Buses. *Energies*, 11(12):3267, 2018. doi: 10.3390/en11123267.

[166] A. Lajunen. Energy-optimal velocity profiles for electric city buses. In *2013 IEEE Int. Conf. Autom. Sci. Eng.*, pages 886–891. IEEE, Aug. 2013. doi:

10.1109/CoASE.2013.6653956.

[167] A. Kontou and J. Miles. Electric Buses: Lessons to be Learnt from the Milton Keynes Demonstration Project. *Procedia Eng.*, 118:1137–1144, 2015. doi: 10.1016/j.proeng.2015.08.455.

[168] J. Vepsäläinen. Driving Style Comparison of City Buses: Electric vs. Diesel. In *2017 IEEE Veh. Power Propuls. Conf.*, volume 2018-Janua, pages 1–5, Belfort, France, Dec. 2017. IEEE. doi: 10.1109/VPPC.2017.8330942.

[169] G. Li, S. E. Li, B. Cheng, and P. Green. Estimation of driving style in naturalistic highway traffic using maneuver transition probabilities. *Transp. Res. Part C Emerg. Technol.*, 74:113–125, Jan. 2017. doi: 10.1016/j.trc.2016.11.011.

[170] D. V. Ngo. *Gear Shift Strategies for Automotive Transmissions*. PhD thesis, Eindhoven University of Technology, Eindhoven, 2012. ISBN 9789038632223. doi: 10.6100/IR735458.

[171] G. Saldaña, J. I. San Martín, I. Zamora, F. J. Asensio, and O. Oñederra. Analysis of the Current Electric Battery Models for Electric Vehicle Simulation. *Energies*, 12(14):2750, July 2019. doi: 10.3390/en12142750.

[172] A. Fotouhi, D. J. Auger, K. Propp, S. Longo, and M. Wild. A review on electric vehicle battery modelling: From Lithium-ion toward Lithium–Sulphur. *Renew. Sustain. Energy Rev.*, 56:1008–1021, Apr. 2016. doi: 10.1016/j.rser.2015.12.009.

[173] X. Hu, S. Li, and H. Peng. A comparative study of equivalent circuit models for Li-ion batteries. *J. Power Sources*, 198:359–367, Jan. 2012. doi: 10.1016/j.jpowsour.2011.10.013.

[174] Z. Khalik, M. C. F. Donkers, J. Sturm, and H. J. Bergveld. Parameter estimation of the Doyle–Fuller–Newman model for Lithium-ion batteries by parameter normalization, grouping, and sensitivity analysis. *J. Power Sources*, 499(January): 229901, July 2021. doi: 10.1016/j.jpowsour.2021.229901.

[175] G. P. Padilla, C. Pelosi, C. J. J. Beckers, and M. C. F. Donkers. Eco-Driving for Energy Efficient Cornering of Electric Vehicles in Urban Scenarios. *IFAC-PapersOnLine*, 53(2):13816–13821, 2020. doi: 10.1016/j.ifacol.2020.12.891.

[176] P. Li, Y. Zhang, Y. Zhang, Y. Zhang, and K. Zhang. Prediction of electric bus energy consumption with stochastic speed profile generation modelling and data driven method based on real-world big data. *Appl. Energy*, 298(March):117204, Sept. 2021. doi: 10.1016/j.apenergy.2021.117204.

[177] H. Abdelaty, A. Al-Obaidi, M. Mohamed, and H. E. Z. Farag. Machine learning prediction models for battery-electric bus energy consumption in transit. *Transp. Res. Part D Transp. Environ.*, 96(May):102868, July 2021. doi: 10.1016/j.trd.2021.102868.

[178] Y. Chen, Y. Zhang, and R. Sun. Data-driven estimation of energy consumption for electric bus under real-world driving conditions. *Transp. Res. Part D Transp. Environ.*, 98(July):102969, Sept. 2021. doi: 10.1016/j.trd.2021.102969.

[179] F. C. Barbosa. Pure Electric Bus Traction Technology Overview - A Path Towards Enhanced Environmental Performance and Efficiency for Transit Bus Fleets. In *SAE Tech. Pap.*, number October, Sept. 2014. doi: 10.4271/2014-36-0205.

[180] J.-Q. Li. Battery-electric transit bus developments and operations: A review. *Int. J. Sustain. Transp.*, 10(3):157–169, Mar. 2016. doi: 10.1080/15568318.2013.872737.

[181] F. C. Barbosa. Bus' system electrification review – A technological operational comparative assessment. In *SAE Tech. Pap.*, number September, Sept. 2018. doi:

10.4271/2018-36-0095.

[182] M. Pagliaro and F. Meneguzzo. Electric Bus: A Critical Overview on the Dawn of Its Widespread Uptake. *Adv. Sustain. Syst.*, 3(6):1800151, June 2019. doi: 10.1002/adsu.201800151.

[183] F. J. R. Verbruggen, A. Hoekstra, and T. Hofman. Evaluation of the state-of-the-art of full-electric medium and heavy-duty trucks. In *31st Int. Electr. Veh. Symp. Exhib.*, Kobe, Japan, Sept. 2018.

[184] C. J. J. Beckers, I. J. M. Besselink, and H. Nijmeijer. The State-of-the-Art of Battery Electric City Buses. In *34th Int. Electr. Veh. Symp. Exhib.*, Nanjing, China, June 2021.

[185] Chinabuses.org. China Sold 150,637 Units Buses & Coaches in 2020. Available online: http://www.chinabuses.org/analyst/2021/0115/article_12287.html, 2021. Accessed on 15 May 2021.

[186] W. Chatrou. Development of alternative drivelines 2012-2020 western-europe + poland gvw 8t. Available online: https://www.sustainable-bus.com/news/europe-electric-bus-market-2020-covid/, Feb. 2021.

[187] Mordor Intelligence LLP. North America Electric Bus Market - Growth, Trends, and Forecast (2020-2025). Technical Report 5986874, Mordor Intelligence LLP, Telangana - 500008 India, Oct. 2020, Available online: https://mordorintelligence.com/industry-reports/north-america-electric-bus-market.

[188] Prescient & Strategic Intelligence Private Limited. India Electric Bus Market Overview. Technical report, Prescient & Strategic Intelligence Private Limited, Delhi- 110096 India, May 2019, Available online: https://www.psmarketresearch.com/market-analysis/india-electric-bus-market.

[189] BYD Company Limited and Alexander Dennis Limited. BYD ADL Enviro400EV. Available online: https://www.evbus.co.uk/products/byd-adl-enviro400ev/, 2021. Accessed on 29 Sept. 2021.

[190] Anhui Ankai Automobile Co.,Ltd. Ankai latest 12M electric city bus. Available online: https://www.ankaiglobal.com/ankai-latest-12m-electric-city-bus_p41.html, 2021. Accessed on 29 Sept. 2021.

[191] BYD Motors Inc. The BYD K9 - 40' Transit. Available online: https://en.byd.com/wp-content/uploads/2019/07/4504-byd-transit-cut-sheets_k9-40_lr.pdf, 2021. Accessed on 29 Sept. 2021.

[192] CaetanoBus. e.City Gold - Specification. Available online: https://caetanobus.pt/en/buses/e-city-gold-2/#especificacoes, 2021. Accessed on 29 Sept. 2021.

[193] Ebusco. Ebusco 3.0. Available online: https://www.ebusco.com/electric-buses/ebusco-3-0/, 2021. Accessed on 29 Sept. 2021.

[194] GAZ Global. All-Electric City Bus. Available online: https://gazglobal.com/buses/electrobus/, 2021. Accessed on 29 Sept. 2021.

[195] EvoBus GmbH. Mercedes-Benz eCitaro - Download technical brochures. Available online: https://www.mercedes-benz-bus.com/en_DE/buy/services-online/download-technical-brochures.html, 2021. Accessed on 29 Sept. 2021.

[196] Olectra Greentech Limited. . Electric Bus K9 highlights. Available online: https://olectra.com/electric-bus-k9/, 2021. Accessed on 29 Sept. 2021.

[197] Otokar. e-KENT C. Available online: https://commercial.otokar.com.tr/bus/

`city/e-kent-c-bus`, 2021. Accessed on 29 Sept. 2021.

[198] Proterra. The Proterra ZX5 Electric Transit Bus. Available online: `https://www.proterra.com/vehicles/zx5-electric-bus/`, 2021. Accessed on 29 Sept. 2021.

[199] Scania CV AB. Fully Electric Low Floor - Scania Citywide. Available online: `https://www.scania.com/content/dam/scanianoe/market/master/products-and-services/buses-and-Coaches/novali/brochures/product-brochure-scania-citywide-bev.pdf`, 2021. Accessed on 29 Sept. 2021.

[200] Solaris Bus & Coach sp. z o.o. Urbino 15 LE electric. Available online: `https://www.solarisbus.com/en/vehicles/zero-emissions/new-u15le-electric`, 2021. Accessed on 29 Sept. 2021.

[201] Tata Motors Limited. STARBUS EV: Tata 4/12m Low Entry AC Electric bus. Available online: `https://www.buses.tatamotors.com/products/brands/starbus/starbus-ev-tata-4-12m-low-entry-ac-electric-bus/`, 2021. Accessed on 29 Sept. 2021.

[202] TEMSA Skoda. Avenue Electron. Available online: `https://www.temsa.com/eu/en/city/avenue-electron`, 2021. Accessed on 29 Sept. 2021.

[203] VDL Bus & Coach bv. Citea Electric > Technical specifications. Available online: `https://web.archive.org/web/20190611183354/http://www.vdlbuscoach.com/Producten/Openbaar-vervoer/Citea-Electric/Technische-specificaties.aspx`, 2019. Accessed on 29 Sept. 2021.

[204] Volvo Bus Corporation. Volvo 7900 Electric. Available online: `https://www.volvobuses.com/content/dam/volvo/volvo-buses/master/bre/our-offering/documents/Brochure_7900E_EN.pdf`, 2021. Accessed on 29 Oct. 2021.

[205] YUTONG. E12. Available online: `https://en.yutong.com/products/ZK6128BEVG.shtml`, 2021. Accessed on 29 Sept. 2021.

[206] Sileo GmbH. Technical Specification Sileo S25. Available online: `https://www.sileo-ebus.com/fileadmin/user_upload/service/download/datenblaetter/Sileo_Datenblatt_S25_EN.pdf`, 2021. Accessed on 16 Sept. 2021.

[207] Chariot Motors. 12m ultracapacitor Chariot e-bus. Available online: `https://chariot-electricbus.com/cmproduct/12m-ultracapacitor-chariot-e-bus/`, 2021. Accessed on 20 Oct. 2021.

[208] Sustainable-bus.com. France, 92 ecitaro ordered in rennes. the star network prepares for the transition. Available online: `https://www.sustainable-bus.com/news/rennes-electric-bus-mercedes-ecitaro-star/`, 2020. Accessed on 6 May 2021.

[209] electrive.com. Paris public transport operator orders 109 electric buses by Bluebus. Available online: `https://www.electrive.com/2021/01/09/146625/`, Jan. 2021. Accessed on 17 Sept. 2021.

[210] D. Berjoza and I. Jurgena. Effects of change in the weight of electric vehicles on their performance characteristics. *Agron. Res.*, 15(Special Issue 1):952–963, 2017.

[211] European Environment Agency. Occupancy rates of passenger vehicles. Available online: `https://www.eea.europa.eu/data-and-maps/indicators/occupancy-rates-of-passenger-vehicles/occupancy-rates-of-passenger-vehicles`, 2015. Accessed on 6 May 2021.

[212] I. C. Borbujo, P. G. Pereirinha, J. A. del Valle, M. G. Vega, D. A. Gonzalez, and J. C. V. Perez. International and European Legislation and Standards for Battery

Electric Buses. In *2020 IEEE Veh. Power Propuls. Conf.*, pages 1–6, Gijon, Spain, Nov. 2020. IEEE. doi: 10.1109/VPPC49601.2020.9330865.

[213] Union Internationale des Transports Publics. UITP SORT & E-SORT brochures. Available online: https://www.uitp.org/publications/uitp-sort-e-sort-brochures/, 2021. Accessed on 15 May 2021.

[214] Transport For London. London Exhaust Emissions Study. Available online: http://content.tfl.gov.uk/london-exhaust-emissions-study-drive-cycle-development.pdf, 2016.

[215] D. Jefferies and D. Göhlich. A Comprehensive TCO Evaluation Method for Electric Bus Systems Based on Discrete-Event Simulation Including Bus Scheduling and Charging Infrastructure Optimisation. *World Electr. Veh. J.*, 11(3):56, Aug. 2020. doi: 10.3390/wevj11030056.

[216] Anhui Ankai Automobile Co.,Ltd. Ankai 12M electric double decker sightseeing bus. Available online: https://www.ankaiglobal.com/ankai-12m-electric-double-decker-sightseeing-bus_p40.html, 2021. Accessed on 20 Oct. 2021.

[217] B. Nykvist, F. Sprei, and M. Nilsson. Assessing the progress toward lower priced long range battery electric vehicles. *Energy Policy*, 124(September 2018):144–155, Jan. 2019. doi: 10.1016/j.enpol.2018.09.035.

[218] N. Rietmann and T. Lieven. How policy measures succeeded to promote electric mobility – Worldwide review and outlook. *J. Clean. Prod.*, 206:66–75, Jan. 2019. doi: 10.1016/j.jclepro.2018.09.121.

[219] M. Nilsson. Electric vehicles: The phenomenon of range anxiety. Technical Report Task 1300, ELVIRE Consortium, 2011, Available online: http://e-mobility-nsr.eu/fileadmin/user_upload/downloads/info-pool/the_phenomenon_of_range_anxiety_elvire.pdf.

[220] Z. Khalik, G. P. Padilla, T. C. J. Romijn, and M. C. F. Donkers. Vehicle Energy Management with Ecodriving: A Sequential Quadratic Programming Approach with Dual Decomposition. In *2018 Annu. Am. Control Conf.*, volume 2018-June, pages 4002–4007. IEEE, June 2018. doi: 10.23919/ACC.2018.8431544.

[221] M. T. Sebastiani, R. Luders, and K. V. O. Fonseca. Evaluating Electric Bus Operation for a Real-World BRT Public Transportation Using Simulation Optimization. *IEEE Trans. Intell. Transp. Syst.*, 17(10):2777–2786, Oct. 2016. doi: 10.1109/TITS.2016.2525800.

[222] T. Halmeaho, P. Rahkola, K. Tammi, J. Pippuri, A.-P. Pellikka, A. Manninen, and S. Ruotsalainen. Experimental validation of electric bus powertrain model under city driving cycles. *IET Electr. Syst. Transp.*, 7(1):74–83, Mar. 2017. doi: 10.1049/iet-est.2016.0028.

[223] N. Mohan. *Electric Machines and Drives.* John Wiley & Sons, Feb. 2011. ISBN 978-1-118-07481-7.

[224] P. Kokke, J. Wang, I. J. M. Besselink, and H. Nijmeijer. TU/e Lupo EL Powertrain Efficiency Experiments. In *Eur. Electr. Veh. Congr.*, pages 1–7, Brussels, Belgium, Dec. 2014.

[225] E. Pennestrì and P. P. Valentini. A Review of Formulas for the Mechanical Efficiency Analysis of Two Degrees-of-Freedom Epicyclic Gear Trains. *J. Mech. Des.*, 125(3):602, 2003. doi: 10.1115/1.1587157.

[226] D. Yu and N. Beachley. On the Mechanical Efficiency of Differential Gearing. *J. Mech. Transm. Autom. Des.*, 107(1):61–67, Mar. 1985. doi: 10.1115/1.3258696.

Dankwoord

Dit proefschrift markeert voor mij het eind van een meer dan vier jaar durend project. In deze tijd ik veel mensen mogen ontmoeten, die allemaal - bewust of onbewust - hebben bijgedragen aan dit werk. Enkelen van hen wil ik hier bedanken.

Allereerst gaat mijn dank uit naar mijn twee promotoren Henk Nijmeijer en Igo Besselink. Henk, jij hebt gedurende mijn promotie altijd een wetenschappelijk oog in het zeil gehouden maar mij ook aangespoord om vooral zelf de koers te bepalen. Tijdens onze gesprekken wist je altijd vrij snel tot de kern van het probleem te komen; iets wat het resultaat ten goede kwam. Ik ben je humor, gekenmerkt door gepast sarcasme, gaan waarderen. Bedankt voor de prettige samenwerking en al je advies. Igo, bedankt voor alle technische discussies en je kritische commentaar. Jouw aanstekelijk enthousiasme was voor mij, vooral gedurende de huiswerkperiode, een belangrijke motivator. Tevens heb ik altijd met interesse meegekeken naar de vriendelijke doch directe manier waarop je studenten begeleidt. Als wetenschapper heb je een scherp oog voor 'novelty'. Zo zijn meerdere hoofdstukken in dit proefschrift tot stand gekomen nadat jij zei: "Misschien moet je dáár eens naar kijken."

Furthermore, I would like to extend this gratitude to the chair Anton van Steenhoven and the members of the doctorate committee: Kari Tammi from Aalto University, Omar Hegazy from Vrije Universiteit Brussel, Maarten Bonnema from Universiteit Twente, Theo Hofman from Eindhoven University of Technology, and Pieter Blom from VDL ETS. Thank you for taking the time to read my thesis and providing valuable feedback that improved the quality of the work.

This research is part of EVERLASTING, and I want to thank everyone involved in this project. It was insightful and informative to learn about all the partners' interests and visit their labs in the cities of Aachen, München, and Lyon. Thanks to Carlo Mol from Vito for demonstrating a well-organized project. Thanks to Mario Paroha from Voltia for the support in conducting the eVan measurements. Also, thanks to the colleagues from the CS-group: to Will Hendrix for teaching me the internal politics of an EU project, to Tijs Donkers for the enthusiasm that he brought to the general assembly meetings, and to Paul Padilla for the many insightful discussions, one of which has materialized in a journal publication. Thanks to Matthieu Ponchant from Siemens for involving me in their work, which

resulted in a conference contribution.

I sincerely thank VDL ETS for the fruitful collaboration that has arisen within the EVERLASTING project. The results presented in this thesis could only be achieved by combining theoretical research with practical vehicle tests, to which VDL contributed greatly. Especially thanks to Anouk Hol and Pieter Blom for their guidance and for allowing me to move freely within their organization. Thanks to the controls engineering team: Juan, Rahul, Koen, Roshni, Oswin, Stijn, Arda, Bregje, and Chris for making me feel part of their team by inviting me to their many potlucks, bowling events, and housewarmings. Also thanks to the people from the test department, including Nick, Frank, Edwin, Gökman, and Wim, who provided practical insights and helped to conduct many of the measurements presented in this thesis.

To all the students I had the pleasure of working with: Jules, Kaustav, Mark, Tim, Oswin, Kevin, Achyuthan, David, and Loek. Your input has directly or indirectly contributed to the results presented in this thesis, and I am grateful for that. I also thank Rudolf Huisman from DAF for the pleasant collaboration in supervising one of these projects.

Next, I would like to thank all the (ex-)colleagues from the D&C and CST groups. It is precious to work in an environment where scientific discussions are easily mixed with informal leisure activities, such as the Benelux Meetings, D&C outings, bowling events, and Friday afternoon drinks. I will highlight just a few of you: Thanks to Michiel, Mark, Frans, Robert, Lennart, Ruud, and Leroy for showing us how its done, to Daniël, Rob, Geertje, Bas, Jari, Viral, Farhad, Wouter, Luuk, Ruud, and Brandon for keeping the vrijmibo alive during lockdowns, to Yuhze, Wouter, and Viral for the collaboration during the vehicle dynamics courses, to Erwin, Wietse, Gerard, and Marvin for helping me out in the AES-lab, and to Geertje and Anouk for being the organizational center of the D&C group and for contributing to a great group atmosphere. Also, I want to thank the next-door neighbors: Noud, Nard, Nick, Max, Masahiro, and Wataru, for the timely coffee breaks. Lastly, thanks to Brandon for the many early-morning train rides together.

Dan mijn kantoorcollega's: Fahim en Joey. Ondanks dat onze projecten inhoudelijk verschilden, heb ik veel aan jullie gehad; presentaties oefenen in een Center Parks bungalow of samen fietsen in Meijel. Er heerste een gemoedelijke gezelligheid op kantoor, waarin goed gewerkt kon worden, maar ook zeker ruimte was voor onzin en ontspanning. Ik zal dit gaan missen. Joey, bedankt voor je aanmoedigingen om af en toe "nou eens gewoon door te werken!" en voor je nuchtere kijk op problemen. Fahim, bedankt voor al je advies, zowel academisch als daarbuiten, en voor alle discussies over gitaarspelen, fietsen, en wat nu écht belangrijk is in het leven.

Aan alle vrienden buiten Eindhoven: bedankt voor alle fietsavonturen, klusmiddagen, bordspelavonden, gezellige etentjes en filmmarathons. Dit waren voor mij momenten waarop ik af kon schakelen en kon ontspannen. Bovendien dank

aan Falco Creemers en Martijn Merks voor het reviewen van vroege versies van delen van dit proefschrift. Bedankt aan de kerels van Das Haus, waar ik het eerste jaar van mijn promotie nog heb gewoond, maar me ook daarna nog altijd welkom heb gevoeld.

Pap, mam, Karlijne en Jasper. Het is onbeschrijfelijk belangrijk om een thuishaven te hebben waar je weet dat je altijd terecht kunt, al is het maar voor een relativerend gesprek of warme kop soep. Jullie hebben mij altijd gesteund en m'n eigen keuzes laten maken. Bedankt voor alles.

Mijn laatste dank gaat uit naar mijn allerliefste: Roos. Jouw steun en begrip zijn belangrijker dan je beseft. Je hebt me op de juiste momenten gemotiveerd om de schouders eronder te zetten, of juist om wat afstand te nemen. Ik ben blij dat ik jou naast me heb, en ik zie uit naar de rest van ons leven samen. Ik hou van je.

Camiel Beckers
Roermond, mei 2022

About the author

Camiel Beckers was born in Enschede on April 18, 1993. He obtained his bachelor's degree in mechanical engineering in 2014 and his master's degree in mechanical engineering in 2017, both with great appreciation, at Eindhoven University of Technology (TU/e). From 2014 to 2016, Camiel worked part-time at student team InMotion on the simulation, design, and construction of a battery electric formula race car. His graduation project, under the supervision of Rob Fey and Nathan van de Wouw, entitled 'Bifurcation-based shimmy analysis of landing gears using flexible multibody models,' was performed in close collaboration with Siemens PLM Software and Fokker Landing Gear.

In December 2017, Camiel started his Ph.D. research in the Dynamics & Control (D&C) group at the Mechanical Engineering department of Eindhoven University of Technology under the supervision of Igo Besselink and Henk Nijmeijer. This research is part of the research project 'Electric Vehicle Enhanced Range, Lifetime And Safety Through INGenious battery management (EVERLASTING),' financed by the European Union's Horizon 2020 research and innovation program. The research focuses on energy consumption modeling of battery electric vehicles through the use of physics-based and vehicle-dynamics-related methods, with application to battery electric city buses. The main results of this research are presented in this thesis.